University of Liège - Faculty of Applied Sciences
Academic year 2014-2015

LASER CLADDING FINITE ELEMENT MODELLING. Application to Ti6Al4V.

Master's thesis submitted in partial fulfillment of the requirements for the degree of Master in Civil Engineering

Conducted by Romain Brusten

Jury composition :
J-P. Jaspart, president (Ulg)
A-M. Habraken, thesis supervisor (Ulg)
R. Carrus, member (Sirris)
L. Duchêne, member (Ulg)
J. Lecomte-Beckers, member (Ulg)
J-P. Ponthot, member (Ulg)

Author

Mr. R. Brusten
Master's student in Civil Engineering
University of Liège, Belgium
Romain.Brusten@student.ulg.ac.be

Jury members

Mrs A-M. Habraken, supervisor
Research Director FNRS
ArGEnCo Department - MS^2F Division
University of Liège, Belgium
Anne.Habraken@ulg.ac.be

Mr. J-P. Jaspart, president
Professor
ArGEnCo Department - MS^2F Division
University of Liège, Belgium
Jean-Pierre.Jaspart@ulg.ac.be

Mr. R. Carrus, member
Senior Engineer Additive Manufacturing
Sirris - Collective Center for the Belgian technology industry
Liège, Belgium
Raoul.Carrus@sirris.be

Mr. L. Duchêne, member
Lecturer
ArGEnCo Department - MS^2F Division
University of Liège, Belgium
L.Duchene@ulg.ac.be

Mrs. J. Lecomte-Beckers, member
Professor
LTAS Department - MMS Division
University of Liège, Belgium
Jacqueline.Lecomte@ulg.ac.be

Mr. J-P. Ponthot, member
Professor
LTAS Department - $MN2L$ Division
University of Liège, Belgium
JP.Ponthot@ulg.ac.be

Abstract

This master's thesis outlines the development of a numerical model for laser cladding as a repair technology. This model reproduces an experimental study (submitted article) of a laser cladding application for the Ti6Al4V alloy : H.Paydas, A.Mertens, R.Carrus, J.Lecomte-Beckers and J.Tchoufang Tchuindjang: "*Laser cladding as a repair technology for Ti6Al4V alloy: influence of building strategy on micro-structure and hardness.*" In this study, only the thermal phenomena are reproduced and analysed, nonetheless, the changes required to transform the current thermal model into a thermal-mechanical model are provided.

This work contains a technological review, in which the different additive manufacturing technologies are introduced and compared. The alloy properties, as well as the finite element code LAGAMINE used in this simulation, are also detailed. The model design is then explained in depth, including the design of the mesh, the modelling of the laser heat flux, the thermal laws and boundary conditions used. All model parameters are provided and compared to other literature values. To simulate the cladding of new material, activation of elements has been applied within the model. Two activation strategies have been studied, a complex element-by-element strategy, as well as a simpler layer-by-layer activation strategy. Calibration was carried out on a 3-D model, based on the experimental results of H.Paydas et al. The model was calibrated using the flux value absorbed by the work-piece during cladding. Given the nominal laser power, the calibration led to the identification of a dimensionless absorptivity coefficient β, ratio between the absorbed energy and the laser input energy, equal to 0,33. In order to simplify the model and reduce computation time, a 2-D model was developed for result analysis. The simplifications made when transitioning from a 3-D to a 2-D model are listed in the work.

A series of observations have been provided, using the calibrated 2-D model. These observations include a study of the temperature distribution (temporally and spatially) in the piece, a study of the melt-pool observed and an analysis of the heat flux distribution during cladding. The influence of the pre-heating and building strategies was also analysed. All numerical results have been compared to experimental observations. The main takeaways of the numerical results are summarised hereafter:

- Comparison of constant track length (CTL) and decreasing track length (DTL) building strategies shows that hot temperature zone is more concentrated in the middle of the clad and reaches higher value for DTL.
- A Widmanstätten micro-structure is numerically predicted for all points with all building strategies. Experimentally, a Widmanstätten was observed in all cases except at the extremities of the clad for the decreasing track length strategy, where a martensite microstrucuture was observed.
- The higher the pre-heating temperature, the higher the maximal temperature observed but the lower the cooling rate and temperature spatial gradient are. Therefore, the risks of cracks due to thermal related stresses can be reduced by increasing pre-heating temperature.

For all results, the shapes and profiles numerically obtained are coherent with the experimental results, however, the absolute values, especially in terms of temperature, have been overestimated. The causes and potential solutions to overcome this problem are detailed in the work. This paper represents the first step towards building a complete thermal-mechanical model to help industry better understand the laser cladding process, and *in-fine* to optimise laser cladding operating procedures, in order to produce well-mastered pieces. This model is under development at the ArGenCo department within the University of Liège, under the supervision of FNRS research director A-M Habraken and with the help of their industrial partner, Sirris.

Résumé

Cette thèse de Master présente le développement d'un modèle numérique simulant l'utilisation du *laser cladding* comme technologie de réparation de pièces endommagées. Le modèle reproduit une étude expérimentale (article soumis) sur l'application du *laser cladding* à l'alliage Ti6Al4V menée par H.Paydas, A.Mertens, R.Carrus, J.Lecomte-Beckers and J.Tchoufang Tchuindjang et intitulée : "*Laser cladding as a repair technology for Ti6Al4V alloy: influence of building strategy on micro-structure and hardness.*" Dans ce travail, seuls les phénomènes thermiques seront intégrés au modèle, néanmoins, les modifications nécessaires pour transformer le modèle thermique réalisé en un modèle thermomécanique sont détaillées.

Ce travail contient en outre un état de l'art, dans lequel les différents processus de fabrication additive seront introduits et comparés. Les propriétés de l'alliage de titane utilisé ainsi que le code élément fini LAGAMINE, utilisé dans le cadre de ce projet, seront aussi introduit. La conception du modèle est détaillé et comprend notamment : la conception du maillage, la modélisation de la source de chaleur, le détail des lois thermiques utilisées ainsi qu'une description des conditions limites appliquées. La calibration du modèle numérique est menée sur un modèle 3-D et basée sur les résultats expérimentaux de Paydas et al. La valeur du flux de chaleur absorbée par la matière est utilisée comme variable de calibration. Etant donné la puissance nominale du laser utilisé, fournie par le constructeur, la calibration mène à la détermination du coefficient d'absorptivité β, rapport entre l'énergie absorbée par la pièce et l'énergie fournie par le laser. La valeur identifiée après calibration est de 0,33. Afin de simplifier l'utilisation du modèle et réduire le temps de calcul, un modèle 2-D a été développé et est utilisé pour l'analyse des résultats. Les simplifications engendrées par le passage du 3-D vers le 2-D sont répertoriées dans ce travail.

Une série d'observations a été réalisée sur ce modèle 2-D, celles-ci comprennent : une étude de la distribution de température dans la pièce (spatialement et temporellement), une étude de la zone de fusion (*melt-pool*) ainsi qu'une analyse des flux de chaleur. L'influence des stratégies de construction et de préchauffage est aussi analysée. Les principaux enseignements tirés des résultats numériques sont synthétisés ci-dessous:

- La comparaison des deux stratégies de construction, *constant track length* (CTL) et *decreasing track length* (DTL), montre une concentration de la zone de haute température au centre de la pièce pour la stratégie DTL.
- Une micro-structure de Widmanstätten est prédite numériquement en chaque point et pour les deux stratégies de constructions. Expérimentalement, la Widmanstätten est observée partout sauf aux extrémités du clad pour le cas DTL, ou une micro-structure de martensite est observée.
- Si on augmente la température de pré-chauffage, la température maximale observée augmente mais la vitesse de refroidissement et le gradient spatial de température diminuent. Par conséquent, le risque de fissures peut être réduit en augmentant la température de pré-chauffage.

Pour tous les résultats, les profils et formes obtenus sont cohérents avec les résultats expérimentaux mais les valeurs obtenues, particulièrement en ce qui concerne la température, sont surestimées par le modèle numérique. Les causes et solutions potentielles pour surmonter ce problème sont détaillées. Ce document constitue un premier pas vers le développement d'un modèle thermomécanique complet capable d'aider les industriels á mieux comprendre le procédé du *laser cladding* et, *in fine* permettre l'optimisation des paramètres de fonctionnement. Cela afin de permettre la fabrication de pièces maitrisées, avec les propriétés recherchées. Ce modèle est en développement au département ArGEnCo de l'Université de Liège, sous la supervision de A-M. Habraken.

Acknowledgement

First of all, I would like to thank my master's thesis supervisor Anne-Marie Habraken (research director F.N.R.S, ArGenCo, University of Liege) for the time she took to guide me in my work and help me tackle the challenges faced during the course of the thesis. I would also like to thank her for having put me in excellent working conditions in the ArGenCo department.

I would also like to thank the people that helped me overcome the numerous issues I faced while developing the numerical model presented in this thesis. G.Gilles, for his help in LAGAMINE as well as for his availability and insightful inputs on various subjects. N.Hashemi and R.Jardin, for their productive exchange of information about laser cladding numerical modelling. T.Hoang Son for his support on numerical matters. H.Paydas and A.Mertens for taking the time to explain to me their experimental work on laser cladding and helping me with Ti6Al4V properties. I would also like to acknowledge prof. F.Collin and B.Pardoen for their help in tackling software related issues.

I am also grateful to Sirris[1], and especially to J.Magnien for helping me with operating parameters and procedures, as well as showing me their installations.

I would also like to thank my jury: R.Carrus, L.Duchene, J.Lecomte-Beckers and J-P Ponthot for their remarks during the intermediate presentation or their help in numerical modelling.

Finally I would like to thank Joanna Huddleston for her support during the whole thesis, her indispensable English language correction and her ability to get me to work when my good will was not sufficient.

[1]Sirris is the collective center for and by the technological industry. Their facilities are located in Sart-Tilman, Liege, Belgium.

Contents

List of Figures

List of Tables

Chapter 1

Introduction

Laser cladding is an additive manufacturing process based on the use of a laser beam as a heat source. Laser cladding is able to process a large variety of alloys and unlike other additive manufacturing technologies, laser cladding can be used on uneven substrates, these particularities make laser cladding a promising technology for the repair or coating of existing pieces. Nevertheless, the technology is not yet mastered. Industries experimenting with this technology face various problems, including apparition of cracks and difficulty to produce net shapes. A potential solution to tackle these problems is the development of a numerical model for process simulation.

This master's thesis work addresses this problem. It consists in the design of a thermal numerical model able to simulate, as accurately as possible, the use of laser cladding as a repair technology for a Ti6Al4V alloy piece. Concretely, the designed numerical model reproduces one of the experiments described in the submitted article of H.Paydas, A.Mertens, R.Carrus, J.Lecomte-Beckers and J.Tchoufang Tchuindjang: "*Laser cladding as a repair technology for Ti6Al4V alloy: influence of building strategy on micro-structure and hardness*"[46].

A numerical model based on a non-linear finite elements code will be developed to model the process. The work presented in the following chapter contains a brief introduction to additive manufacturing most commonly used processes, with an emphasis on laser cladding. The finite elements method will then be introduced, as well as the software used for the computation, particularly LAGAMINE, the non-linear finite element code used. The material used for modelling will also be depicted. The model designed will be described extensively in chapter 5, including the design of the mesh, the heat source, the thermal and mechanical laws applied, the boundary conditions, as well as the calibrations of different parameters. Each of these sub-sections contains a bibliographical study, the description and justification of the choices made for the model design and the limitations induced. The results obtained based on this design will be described in chapter 6. This chapter contains an analysis of the temperature profile, spatially and temporally, the resulting heat flux in the work-piece[1], a description of the thermally affected depth, a micro-structure analysis as well as an sensitivity study of operating parameters such as the pre-heating or the building strategy. For each set of results a comparison with the experimental results will be provided. Finally, the limitations will be synthesised and potential solutions to overcome them will be described and tested in chapter 7.

The model as presented in this work is a first step toward a complete and accurate thermal-mechanical model that will allow industries involved in laser cladding to better master this technology. The results presented in this work should be read while keeping in mind the current model limitations.

[1] Defined as the substrate and cladded layers

Chapter 2

Additive manufacturing

In this chapter, additive manufacturing (AM) processes will be introduced. The focus is put on processes applicable to the printing of metallic alloys, while these represent just a fraction of the AM technology, they are more closely related to the topic of this master thesis.

The main processes identified are selective laser melting (SLM), electron beam melting (EBM) and laser cladding. Each of these processes will be introduced, explained and examples of industrial applications will be provided. Since the laser cladding process is at the heart of this thesis, this process will be detailed in-depth and the takeaway information from a visit of the laser cladding facility at Sirris[1] will be given. Other less commonly used processes will be also be introduced at the end of this chapter.

As the main objective of this thesis is the design of a thermal model to numerically simulate the process of laser cladding, current technology descriptions provided here under will be voluntarily brief. Most of the bibliographical work has been directed towards the finding of the different model parameters. Those findings will be detailed in chapter 5.

2.1 Selective laser melting

2.1.1 Method

Selective laser melting (SLM) also called selective laser sintering[2] (SLS) or laser beam melting (LBM), is one of the most rapidly growing additive manufacturing processes. It has the ability to create metal parts with complex shapes and well-defined properties. The mechanical properties that can be obtained with SLM are potentially higher than with the traditional processes as reported by H.Attar[4] for Cp-Ti parts. Furthermore, they offer other competitive advantages compared to traditional technologies: shorter time to market, versatility, high part accuracy, etc[64].

In SLM, layers in the shape of finite 2-D cross-sections of the 3-D model are built one after the other[21]. Each individual layer consists in atomised metal powder spread on a substrate plate. The slices are then fused by selectively melting the powder using a laser as heat source. In other words, the laser beam scans a surface on which a thin layer of powder has previously been deposed. This process is described here below in a visually comprehensive form given by J.Hart[25]:

[1] Sirris is the collective center for and by the technological industry. Their facilities are *inter alia* located in Sart-Tilman, Liege, Belgium.

[2] Depending on the power of the laser

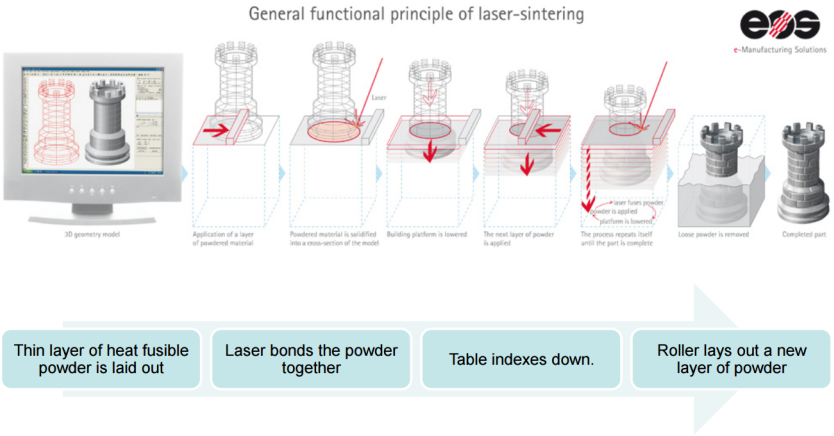

Figure 2.1: Selective laser melting process as explained by J.Hart, MIT.[25]

The building temperature in this process is relatively low, around 200°C. An argon flux is used to prevent oxidation near the laser beam[50].

2.1.2 Applications

The SLM can be used to produce geometrically complex lightweight components[8].

The main potential of SLM Ti6Al4V pieces lies in the aerospace[48], the automobile and the biomedical industries[65]. One of the most interesting biomedical applications is the the use of SLM to build prostheses or implants. The complex tailored geometry can then be modelled in 3-D with an interconnection of the porosity and features that allows biological processes[8]. An example of such a complex tailor-made implant is provided in Figure 2.2. This example was observed at Sirris facilities.

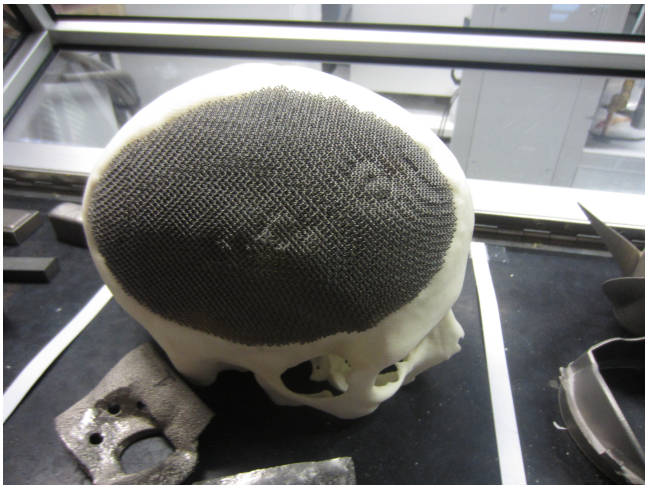

Figure 2.2: Tailor-made prostheses built by selective laser melting. Sirris, Sart-Tilman, Belgium.

The limitations of SLM currently are the surface quality of the end-product as well as the materials that can currently be used for the process. It is also not always possible to predict the surface chemistry which is a critical need for the biomedical applications[60]. Most implants are thus coated with biocompatible materials.

2.1.3 Advantages and drawbacks

The advantages of LSM as stated by Sirris are the following[50]: The flexibility for new material development is very high, it is also possible to work with a wide variety of powders (up to $< 10\mu m$). Powder can be easily removed from the parts since there is no pre-sintering.

From a production point of view, the short time between 2 production batches is relatively low due to short cooling times (about 2 hours). There is also the possibility to restart an interrupted job. The quality of the piece can also be controlled during the process, either by eye inspection or using an optical camera.

However, this technology also have its drawbacks: the process is not suitable for sizeable parts and its applications are therefore limited. Elaborated cutting tools must be used to release the part from its build plate and the quality of the product at that time is often not sufficient due to high internal stresses. An additional annealing of the part is thus often needed. Finally, the process requires strong supports during the building phase and the build plates must be made of the same material as the powder, making this a costly process when working with expensive alloys such as Ti6Al4V.

2.2 Electron beam melting

2.2.1 Method

Electron beam melting (EBM) is another type of additive manufacturing. It uses a similar process to laser metal deposition except that for EBM, an electron beam is used as the power source. It was initially developed by Arcam[3]. The process starts by designing the 3-D part with a CAD software. The part is then divided into a series of layers. As in SLM, the thin layers of metal powder (from 0.05 to 0.2 mm thick [32]) are deposited and then selectively melted by an electron beam in the case of EBM. The complete 3-D product is thus built layer-by-layer. The process usually takes place in a vacuum (ususally $< 5.10^{-4} mBar$ [32]) and at a high temperature, that allows stress relief in the part produced[3].

The electron beam as used in the EBM process has typical power density of $100 W/m^2$ making it possible to obtain temperatures exceeding the evaporation temperature of all materials at the beam spot. The build temperature used for this technology is usually between 680°C and 720°C [50]

2.2.2 Applications

Fields of application of EBM are globally similar those for SLM including the aerospace, the automotive and the biomedical industries. The EBM process is also used for manufacturing electronic alloys. An example of porous Ti6Al4V part built by EBM is presented in Figure 2.3:

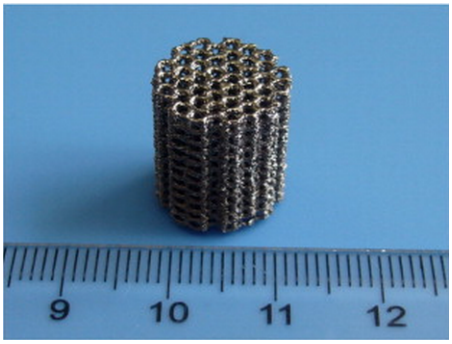

Figure 2.3: Example of porous Ti6Al4V part fabricated by EBM [32].

2.2.3 Advantages and drawbacks

The advantages of EBM are numerous according to Sirris[50]: It offers high productivity and is suitable for the production of sizeable parts. The processing conditions: high temperature and vacuum limits the development of internal residual stresses and prevents any kind of gas contamination. The supports needed are reduced compared with other technologies and there is a possibility to stack parts on top of each other. Finally, the results obtained with Ti6Al4V by EBM are very good in terms of mechanical and fatigue results.

The drawback of this technology are the following: only conductive materials can be used which limits the applications of this technology. Once the powder is sintered, it is challenging to remove it. Working with fine powder is, in a general way, a source of problems. It must also be noted that the maintenance of the EBM machinery is expensive and that the time in between two productions is high due to the long cooling time (about 8 hours)[50].

A comprehensive comparison of the two technologies here above (EBM and SLM) is also provided by Sirris[50] and presented in Figure 2.4.

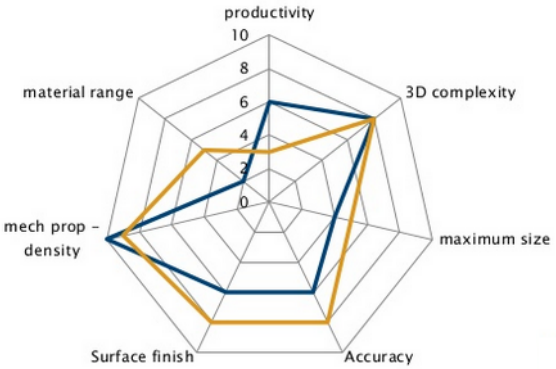

Figure 2.4: Comprehensive comparison of SLM and EBM technologies developed by Sirris [50]

The more technical details are listed by Sirris in Table 2.1:

Table 2.1: Sirris detailed technical comparison of SLM and EBM technologies [50]

	SLM	EBM
Size [mm]	250x250x350[3]	210x210x350[4]
Layer thickness [μm]	30-60	50
Minimum wall thickness [mm]	0.2	0.6
Accuracy [mm]	± 0.1	± 0.3
Build rate [cm^3/h]	5-20	80
Surface roughness [μm]	5-15	20-30
Materials	Stainless steel, Titanium, Aluminium, ...	Conductive materials only.

2.3 Laser cladding

2.3.1 Method

Laser cladding is an additive manufacturing metal deposition technology based on the use of a laser as a heat source and a deposition material. Laser cladding is referred to under several different names across the world, the most common being "Laser Coating"[51], "Laser powder deposition"[11] and "Laser Surfacing"[55]. Other less common appellations are "Laser engineered net shaping"[24],"Direct Metal deposition"[35], "Laser Powder Fusion"[28], "Laser direct casting"[37] or "Directed light fabrication"[34]. All these names refer to the same method, with occasional variations in application fields. This method will be explained in detail in the following sections and its numerical modelling will represent the core of this paper.

In the laser cladding process, a 3-D end-product is generated by adding tracks, also called clads, to the already existing structure or on the substrate. The powder flux is here included in the laser nose and not deposited in layers as in EBM or SLM. The energy of the laser is partly[5] absorbed by the powder and the clad material, creating a melt pool. The melted powder is then added to the melt pool. As the laser passes by, the melt pool is cooled by a combination of convection, radiation and conduction through the workpiece forming a solid clad. The physics of this operation is described in Figure 2.5.

[5]An absorptivity coefficient must be used while representing laser cladding. The value of this absorptivity coefficient will be studied in section 5.3.

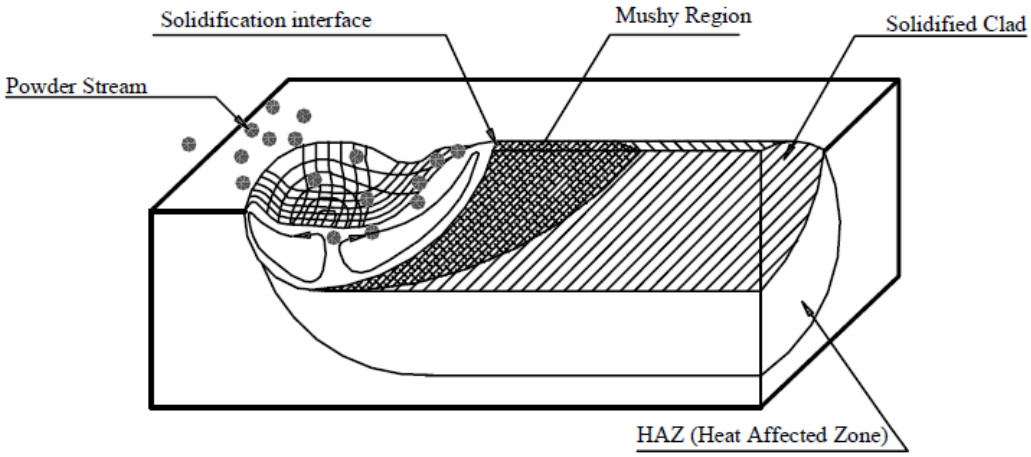

Figure 2.5: Description of different physical phenomena during laser application [58]

2.3.2 Applications

Laser cladding has numerous industrial applications[58]. The different applications can be categorised as such:

Coating: It consists of a thin deposition of material over the surface of another selected material. The new coated material becomes a composite material with generally enhanced surface properties by increasing its resistance to corrosion, increasing the load bearing capacity, etc. A wide variety of metals and alloys such as copper, nickel[18], titanium[63], cobalt[47], chrome and so on can be used as coatings depending on the sought after properties. The fields of application of laser cladding coating are the aerospace, bio-medical and automotive industries.

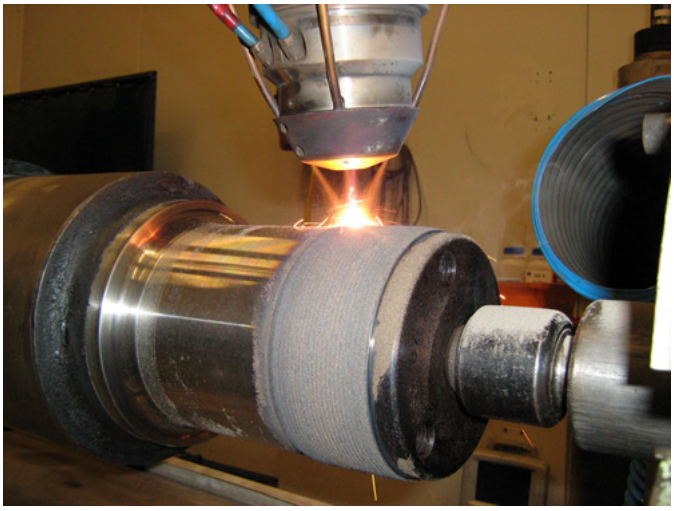

Figure 2.6: Example of laser cladding used for a coating application [54]

Laser cladding as a repair technology: Laser cladding has various advantages over the traditional repair method when it comes to repairing high value components. The temperature is applied precisely and the substrate is therefore not damaged. The heat affected zone is small, solidification is quick and the process can be precisely controlled. Over the other selective metal

deposition methods, laser cladding offers the advantages of not needing a plane substrate as well as being potentially performed on a large range of metals and alloys. The industries currently using this technology are jet engine applications in aerospace, turbine blades in power generation, naval industry, etc.

2.3.3 Advantages and drawbacks

The advantages of laser cladding over SLM and EBM are the following: Laser cladding can be used on uneven surfaces and is therefore easily used as a repair technology. Furthermore, the technology works with a wide variety of alloys as the different metals can be mixed into the powder before being cladded.

- Part reparation is made possible by the use of an integrated laser and powder flux. Unlike the other technologies, it does not require a flat surface platform and can be used to fill gaps and cracks of various geometry. Compared to traditional repair technologies such as welding, Laser cladding offers a non-destructive solution with limited machinery errors and an increased lifetime for the repaired structure.

- The variety of metals used for the deposition process is virtually unlimited. The powder can consist of a wide variety of alloys. The metal powder used in the process can consist of any possible mix. Nowadays, the process is mostly used with common alloys for which the properties are better known.

Laser cladding technology is not yet mastered. As an interdisciplinary technology, it implies a large number of interrelated parameters of different kinds. Those parameters are sensitive to operating conditions and have an effect on the geometry and other properties of the end-product[2]. The quality of the cladded material remains uncertain and varies between different samples as well as within a sample. The optimal parameters of the laser cladding machine (including laser speed and intensity, powder rate or pre-heating of the substrate) are not precisely known. This drawback highlights the need for the development of advanced numerical models to predict those optimum parameters for different geometries and alloys.

The effects of the thermal stresses on the mechanical and metallurgical properties of the end-product can also be problematic. Indeed, contraction caused by the thermal strains results in deformation and thus residual stresses that can lead to delaminations or cracks[2]. Laser claddding is therefore usually completed with thermal post-treatment. The high cost of the machinery needed is also problematic.

2.3.4 Key takeaways - Visit at Sirris

On the 10th of March 2015, I had the opportunity to visit the laser cladding facilities of Sirris, a non-profit organisation specialised in high technology services for industry. In this section, I will explain how the laser cladding process works based this visit.

The configuration of the machinery and the experiment observed were the following: a laser nominal power of 1100W, with potential 5-D movement:three for the laser (X-Y-Z) and two for the substrate (rotation along X and Y). The platform holding the substrate (made in aluminium) and the laser are shown in Figure 2.7.

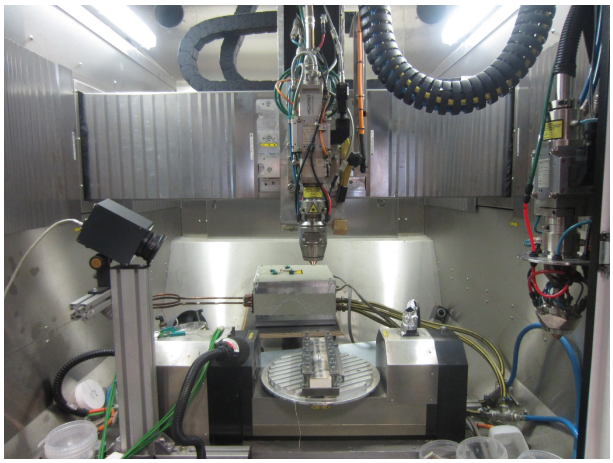

Figure 2.7: Configuration of Sirris installation in Sart-Tilman, Belgium

In the demonstration observed at Sirris, laser cladding was used as a repair technology on a Ti6Al4V substrate. The substrate was designed to simulate a defect which will be filled by laser cladding with Ti6Al4V alloy. The substrate will be fixed at only one of its extremities and the deformation of the substrate due to thermal stresses will be studied.

1. The origin of the axis (X, Y and Z) are calibrated manually. The distance between the substrate and the laser's nozzle is manually set at 10 mm, thanks to a 10 mm high object. The X and Y axis are then set thanks to an optical camera situated on the axis of the laser.

2. The powder flux is then controlled. Before every use of the laser the powder flux is controlled thanks to a mass measurement over a 5 minute period. The powder is sprayed (with the laser being deactivated) in a recipient which is weighed before and after. The powder flux per second can thus be computed as a global average. The powder flow is controlled by a machine provided by the laser manufacturer. This machine is illustrated in Figure 2.8 .It consists of a wheel turning at a defined speed on a disk and providing the laser a powder flux as constant as possible. The powder inside the recipient is heated so that it remains completely dry.

3. The shape of the powder flux is then controlled optically by lighting the powder flux and visual observation. It is important that there is as little powder dispersion as possible. If needed, adjustments are performed manually. The lighted powder flux as seen during the adjustment is presented in Figure 2.9.

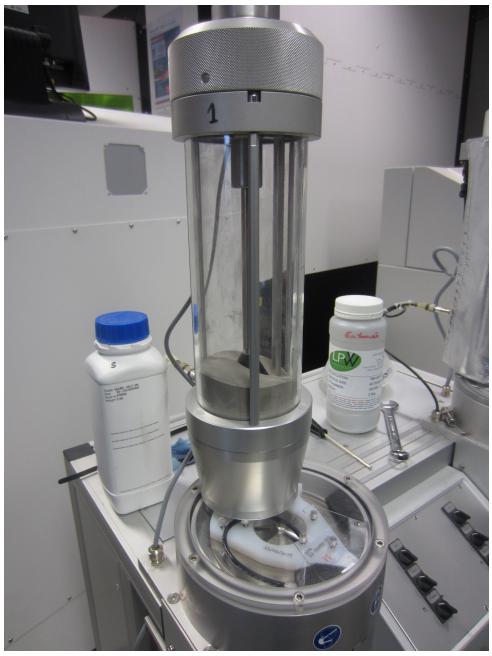

Figure 2.8: Machine controlling the powder flux.

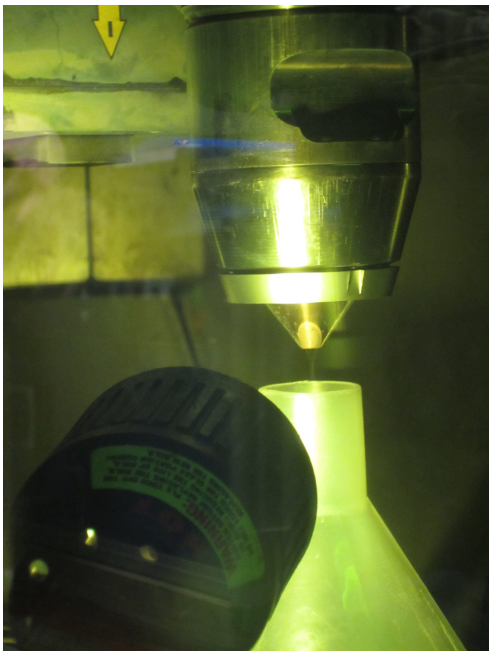

Figure 2.9: Controlling the shape of the powder flux.

The nozzle used in Sirris is a coaxial nozzle, another possibility for the powder influx is a lateral nozzle. Figure 2.10 shows the difference between these two types of nozzles.

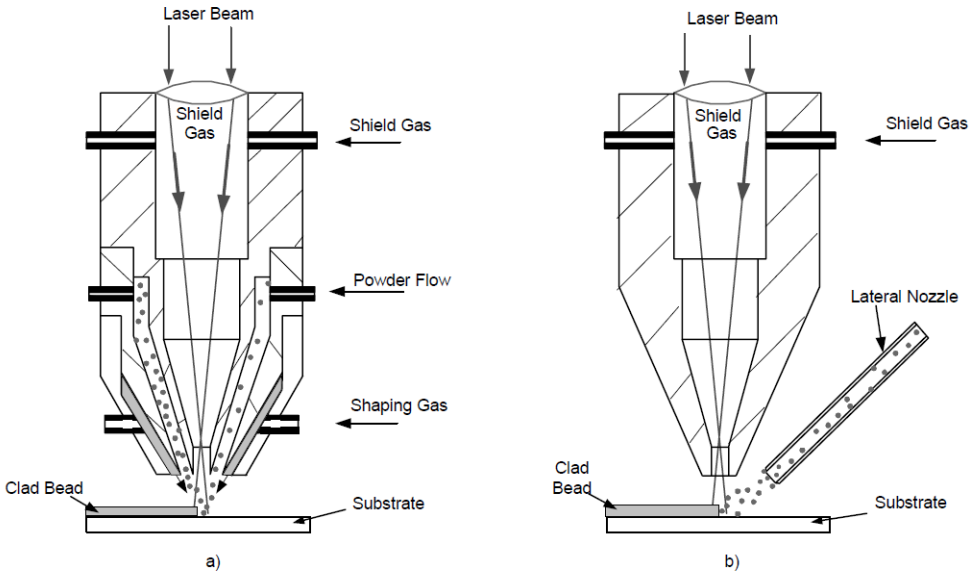

Figure 2.10: Different nozzle configurations. a: coaxial nozzle and b: lateral nozzle [58].

4. The temperature distribution during the cladding is controlled by a thermocouple and a thermal camera. During the observed experiment, only the thermal camera will be used. It is calibrated according to the expected temperature range. For this experiment, the range chosen will be 100-600°C. Screen shots from the thermal camera while the laser is active are shown in Figure 2.11.

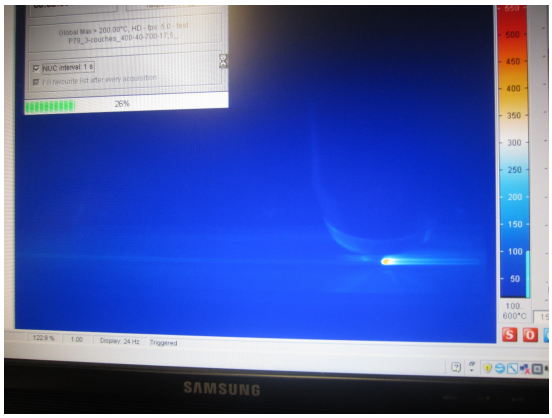

Figure 2.11: View of the thermal camera control screen during cladding

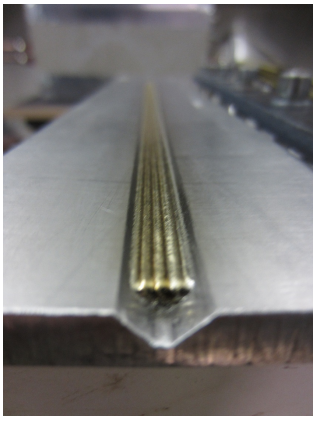

Figure 2.12: Finite product - Laser cladding as a repair technology

5. The laser cladding phase can begin. The temperature inside the cladding area is monitored but not modified. The changes of temperature in the cladding atmosphere due to the laser operation can be neglected and remain around room temperature between 20 and 23°Celsius. In the case of this experiment, 3 layers were clad for a total of 10 laser passes: 3 passes for the two first layers and 4 for the last one. A picture of the finite product are presented in Figure 2.12. These pieces will then be sent to the laboratory for further analysis.

2.4 Other AM processes

Other processes of additive manufacturing, less in line with the main topic of this master's thesis, exist. Several of these technologies, as well as very brief descriptions, will be added to the technologies generic names listed below. Further description of these technologies as well as a classification of the different additive manufacturing technologies is available in literature[12].

- Wire extrusion processes. Work by heating a metallic wire through a nozzle and deposit the metal in fusion on the substrate. The process can also be applied to non-metallic wire.

- 3-D printing. Layers of heated materials are laid down on top of each other. The technology can use a moving platform or a moving nozzle and is mostly used with plastic, wax or with other more exotic materials such as chocolate.

- Stereolithography (SL): The combination of ultraviolet beams sets the liquid polymer into its solid form. The UV beams browse the piece, layer per layer, to create the desired geometry.

These technologies, largely covered in literature and more recently in the media, will not be further detailed in the case of this master's thesis.

Chapter 3

Finite element method modelling

3.1 Linear and non-linear FEM

The following section will describe the finite element method, which was used to develop a numerical model for this thesis. The finite element method will be introduced, followed by an introduction to non-linear finite element method. In the course of this master's thesis, I followed the GrasMech Class of A.M. Habraken (University of Liège) about non-linear finite element methods. As such, the article of Z.Fan and L.Liou, "*Numerical modeling of the additive manufacturing (AM) processes of titanium alloys*"[17], will be analysed in the light of the principles learned in class in a distinct work.

3.1.1 Linear FEM

The finite element method is a numerical method used for determining approximate solutions to a large variety of problems by discretising a structure into several elements and reducing the partial differential equations into linear equations. The continous physical problem is therefore transformed into a discretised finite element problem. The physical phenomena must be expressed by a series of governing equations and boundary conditions[14]. These governing equations and boundary equations relative to our thermal analysis of laser cladding will be expressed in section 3.2.

The solution of a problem by Finite element method (FEM) can be approximated by the following step-by-step approach as described by R.W Lewis[31].

1. Discretise the continuum. The solution region must be divided into non-overlapping elements. A wide variety of element shapes is possible. In the case of our model, we will favour a quadrangular shape[1]. Each element is formed by the connection of a certain number of nodes.

2. Select interpolation functions. The interpolation functions approximate the field variables over the element.

3. Form element equations. The matrix equations expressing the properties of each individual element are built. Different approaches exist to perform this step like the variational[40] or the Galerkin method.

4. Assemble the element equations. The local elements equations need to be combined in a global matrix $\mathbf{K}$ such that:

[1] In the non-linear finite element code LAGAMINE, the most complex codes are developed for quadrangular finite elements

$$[\mathbf{K}].\{\mathbf{T}\} = \{\mathbf{f}\} \tag{3.1}$$

With $\mathbf{K}$, the global system matrix, $\{\mathbf{T}\}$ the global unknown vector and $\{\mathbf{f}\}$ the global load vector.

5. Solve the system of equations to obtain the nodal values.

6. Compute additional results. For many problems, we are interested in additional parameters. For example, in a mechanical problem, the finite element method will traditionally provide the displacement. The strains and corresponding stresses have to be computed afterwards.

3.1.2 Non-linear FEM

The linear approach offer provides sufficient results for a large number of applications but two sources of non-linearity can affect the results:

1. Material non linearity. Most materials have non-linear compartmental laws. For example, the stress-strain law of Ti6Al4V alloy, as well as its thermal laws are non-linear.

2. Geometrical non-linearity. The finite element method relies on a global equilibrium. Whether this equilibrium is expressed in the deformed geometry or the initial one, makes a substantial difference in the case of large deformations.

In the case of our simulations, we are uniquely affected by material non-linearities. These linearities are even enhanced by the changes of state that occur during the laser cladding process. Indeed, the temperature range needed for our simulation includes a transition of micro-structure and a transition from the solid to liquid state[2]. The profile of the apparent heat capacity is thus highly non-linear in the case of our analysis. The different material laws are described in sections 5.4 and 5.5 for the thermal laws and mechanical laws respectively.

Since the displacement of all nodes of our model are blocked, the initial geometry is exactly equal to the deformed one. Therefore we are not affected by geometrical non-linearities.

3.2 FE modelling application to laser cladding

In order to better understand the laser cladding process (temperature profile inside the workpiece, residual stresses distribution, micro-structure predictions) and be able to objectify the influence of various parameters (pre-heating strategy, laser power or speed) numerical models are required. Several mathematical or finite element models of laser cladding have been developed, usually focusing on specific topics: the shape of the melt pool[53], the clad geometry[16], or the dissolution of powder [36]. The influence of the different processing parameters, such as the powder rate or the laser speed, has also been studied in some articles[57].

In line with the objective of this thesis, general numerical modelling of the laser cladding process, we will focus here on the main physical phenomena affecting the process. In order to

[2]Where the liquidus temeprature of Ti6Al4V is 1923°K [7].

numerically model the laser cladding process, the physical phenomena involved must be mathematically represented. This chapter introduces the corresponding equations as they are described in literature and as they will be used in our model through the modelling and the use of LAGAMINE's implemented laws.

3.2.1 Governing equations

The first mathematically modelled phenomenon is the temperature distribution through the work piece. The following is the equation of conduction and it is given[2] for the 2-D case by:

$$\frac{\partial}{\partial x}\left(k\frac{\partial T}{\partial x}\right)+\frac{\partial}{\partial y}\left(k\frac{\partial T}{\partial y}\right)+Q=\frac{\partial(\rho c_p T)}{\partial t} \tag{3.2}$$

And similarly for the 3-D case:

$$\frac{\partial}{\partial x}\left(k\frac{\partial T}{\partial x}\right)+\frac{\partial}{\partial y}\left(k\frac{\partial T}{\partial y}\right)+\frac{\partial}{\partial z}\left(k\frac{\partial T}{\partial z}\right)+Q=\frac{\partial(\rho c_p T)}{\partial t} \tag{3.3}$$

With $T(x,y,z,t)$ [°K] the transient temperature, $k(T)$ $[W.m^{-1}.K^{-1}]$ the thermal conductivity[3], $c_p(T)$ $[J.Kg^{-1}.K^{-1}]$ the apparent heat capacity, $\rho(T)$ $[kg.m^{-3}]$ the density, Q $[W.m^{-3}]$ the power generated per volume in the work-piece and t $[s]$ the time.

The effect of the Latent heat of fusion L_f and vaporisation L_e is integrated in the definition of c_p. Indeed, for our model, we consider the apparent heat capacity as described in Figure 5.29. The integration of the Latent heat of fusion and vaporisation into the heat capacity is detailed in the appendix (A.8.2).

The effect of adding material on the work-piece is done through the activation of elements. This critical part of the model is described in section 5.6.

3.2.2 Expressing initial and boundary conditions

Initial conditions are defined for the temperature on our model. This initial condition is defined as such:
In 2-D:

$$T_0 = T(x,y,0) \tag{3.4}$$

And in 3-D:

$$T_0 = T(x,y,z,0) \tag{3.5}$$

In the case of our model, the initial temperature T_0 is given by the experimental conditions as described in section 5.4 and is equal to $T_0 = 328,89$°K. The influence of the pre-heating temperature and the different ways to implement it into the model will be discussed in section 6.5.

Convection and radiation boundary conditions must also be defined. The surfaces or lines on which this boundary condition is applied are detailed in the section 5.4. The mathematical expression of this condition is given[2] by:

$$-K.(\nabla T.\mathbf{n}) = -h(T-T_0)-\varepsilon\sigma(T^4-T_0^4) \tag{3.6}$$

[3]The value of those parameters for our finite element model is given in section 5.4.

It is applied on the surface defined in Figure 5.33. With $\mathbf{n}$, the normal vector on the surface, $\varepsilon(T)$ [/] the emissivity, $h(T)$ $[W.m^{-2}.K^{-1}]$ the convection coefficient and σ $[W.m^{-2}.K^{-4}]$ the Stefan-Boltzmann constant. All those parameters are described for the case of our model in section 5.4.

The laser flux should also be represented through the boundary conditions in the case of our model. It is defined through the use of a loading file,where the laser is modelled by imposing a flux at a group of nodes. This mathematical modelling of the laser flux is described extensively in section 5.3.

A general formulation of the heat flux in the boundary condition, as it is done in other studies[17][2] is given here under. The boundary condition mathematical expression becomes:

$$-K.(\nabla T.\mathbf{n}) = q_{laser} - h(T - T_0) - \varepsilon\sigma(T^4 - T_0^4) \tag{3.7}$$

Where q_{laser} $[W.m^{-2}]$ is the energy flux from the laser. The mathematical expression for q_{laser} can take a wide variety of forms as described in the section 5.3. The most common one being[2]:

$$q_{laser} = \beta \cdot I(x, y, z, U, t) \tag{3.8}$$

Where β is the absorption factor,I $[W/m^2]$ is the laser energy distribution on the piece and U $[m/s]$ is the velocity of the laser in the x, y and z directions respectively.

The expression of the intensity profile is often considered Gaussian TEM_{00} [2][57][45][13]. We have:

$$I(r) = \frac{2 \cdot P_1}{2 \cdot \pi} \cdot exp(\frac{-2 \cdot r^2}{r_1^2}) \tag{3.9}$$

Where r_1 [m] is the laser beam radius, r [m] the distance from the center of the beam and P_1 [W] the average laser power. However, other shapes can be considered for the laser intensity profile as detailed in the corresponding section.

Other physical phenomena such as the Marangoni flow or the effect of the angle of influence as considered in [2] are not numerically modelled in the course of this master thesis.

3.3 Software

3.3.1 LAGAMINE

Code description

The finite element code LAGAMINE will be used to perform the mathematical simulation. The code has been developed in-house at the departement ArGenCo of the University of Liege since 1982. It was initially designed to simulate the rolling process[30].

It is a non-linear Lagrangian code that can carry out thermal, mechanical and metallurgical simulations. The general flowchart of the finite element code LAGAMINE is presented in Figure 3.1.

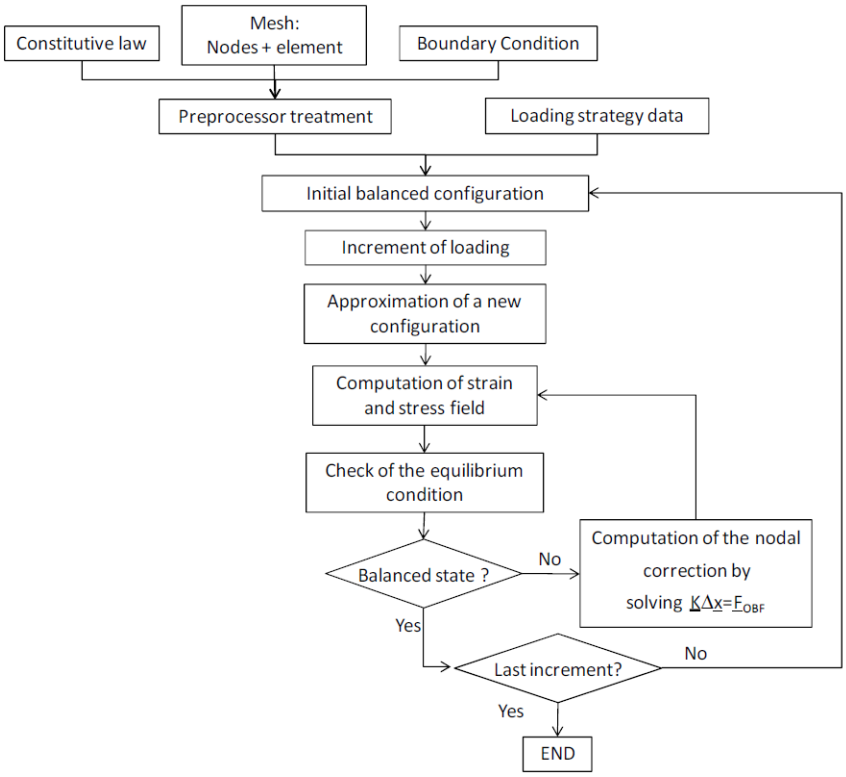

Figure 3.1: General flowchart of LAGAMINE as described by C.Lequesne [30]

In order to get familiar with this finite element code, I followed during the course of this master's thesis a LAGAMINE training with the help and advices of Dr.Ir. Gilles, University of Liège.

Parameters used

In the case of our simulation, the solid element used (BLZ2T and BLZ3T respectively for the 2-D and 3-D simulation) are based on the variation principle of Hu-Washizu[62]. They use one point of integration in order to reduce the computation time.

The temporal integration scheme chosen for our simulation is the implicit scheme[4]. The 2-D thermal simulation will be performed in plane strain state while the 3-D thermal analysis will

[4]Other schemes will be tested (Galerkin, Cranck-Nicolson) and a comparison with the implicit scheme will be provided in section A.4.

naturally be performed in 3-D state. The computation of the inverse tangent stiffness matrix is performed using a direct solver with LU factorisation and skyline storage. The tangent stiffness matrix will be computed analytically.

The heat source is modelled in LAGAMINE's. The LOA file is described in the 5.3 section. Finally the precision for convergence on displacements increments and the precision for out-of-balance forces will both be set at $p = 1, 0.10^{-3}$

3.3.2 Gmsh

Gmsh is a software developed by C.Geuzaine and J.F. Remacle[20]. The source code and pre-compiled versions are available for download (Windows, Mac and Unix) from http://geuz.org/gmsh/. It is a 3-D finite element grid generator with an integrated post processor. It allows the construction of complex 3-D or 2-D models in a bottom-up approach. First, the points are defined, then oriented lines, oriented surfaces[5] and volumes. A mesh can then be defined in those surfaces and volumes. Gmsh allows the use of a wide variety of element shapes. However, in the case of this master's thesis, only quadrangular elements will be generated. The mesh generated for our modelling is mostly a structured mesh, with some exceptions[6].

The use of Gmsh rather than the GMAIL mesh generator built in LAGAMINE can be justified by the high complexity of the 3-D geometry. Gmsh offers a comprehensive interface with intuitive commands and allows any modification of the geometry to be easily performed.

The mesh algorithm used to create the quadrangular mesh: the Delaunay Quad Algorithm (DelQuad) created a few challenges that have been tackled and detailed in section 5.2.

3.3.3 Others

Three other software were used for model development:

1. *Notepad ++* in order to manage the large input file needed by LAGAMINE as well as to identify errors in the input files. It is a free source code editor and Notepad replacement. It is available from http://notepad-plus-plus.org.
2. *Matlab* in order to create the input file for LAGAMINE. This included: the generation of the .LOA file, modelling the movement of the laser on the workpiece, the generation of the .SWI file and modelling the activation of the cladded material. As well as the generation of the .LAG file, that converts the mesh generated by Gmsh into a LAGAMINE readable file that defines the nodes coordinates, the elements types and definition, the thermal laws, etc. All the *Matlab* code used have been developed in the course of this master's thesis. Some of those codes (laser and activation modelling) are now used by other researchers modelling laser cladding for different applications. *Matlab* is available for download from www.mathworks.com.
3. *Excel* spreadsheets were used to analyse the results. The figures highlighting the different results and phenomena will also be generated via *Excel*.

[5] When using LAGAMINE with a mesh generated by Gmsh, it is necessary that every surface has an orientation coherent with the element definition as given in LAGAMINE user guide.

[6] The mesh properties are detailed in the section 5.2.

Chapter 4

Ti6Al4V Alloy

4.1 Applications

Ti6Al4V is the most common titanium alloy. Alone it accounts for 45% of the total titanium alloy production. In the following part of this master's thesis, it will be also named TA6V or Ti64. Its main advantages are the following: high strength to weight ratio, good corrosion resistance, biocompatibility and good fatigue behaviour. Ti6Al4V is a superplastic material allowing it to undergo large strain before failure[61].

Ti6Al4V is used in a wide range of industrial sectors including the aerospace, automotive, biomedical or petrochemical industries[22]. A series of applications for Ti6Al4V is provided by [7] and includes engine components, airframe and space equipment, prostheses and implants.

4.2 Chemical composition

Ti6Al4V is a titanium based alloy and contains, as its name implies, around 6% of aluminium and 4% of vanadium. The exact proportion of alloying elements as well as the concentration in other elements such as oxygen, carbon, nitrogen, hydrogen or iron vary in the different studies. A comparison of the chemical composition used in the modelled experiment and the ASTM standard is given in Table 4.1.

Table 4.1: Experimental and ASTM Ti6Al4V powder chemical composition

Ti6Al4V Powder	Ti [Wt%]	Al[Wt%]	V[Wt%]	O[Wt%]	Fe[Wt%]	H[Wt%]	C[Wt%]	N[Wt%]
Experimental	Bal	6.3	4.1	0.09	0.06	0.0036	0.01	0.01
ASTM Standard B348 Gd23	Bal.	5.5-6.5	3.5-4.5	Max 0.13	Max 0.25	Max 0.0125	Max 0.08	Max 0.03

4.3 Phases and micro-structures

Ti6Al4V is a two-phase α+β alloy. The α phase consists of an hexagonal closed packed (HCP) microstructure while the β phase is body centered cubic (BCC). A comparison of those two phases is given in Figure 4.1

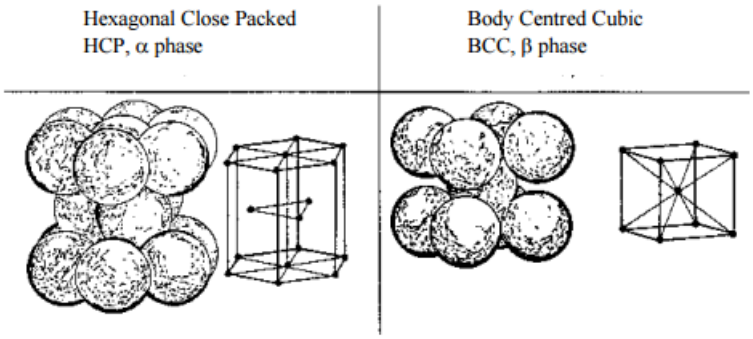

Figure 4.1: Crystal structure of the α and β phases

The transition from the α to the β phase occurs at around 995°C or 1268°K in the case of Ti6Al4V[22]. The volume fraction of the different phases changes depending on the thermal treatment but the β phase usually accounts for less than 10%.

Besides those two phases, some other crystal formation can be observed under particular thermal conditions such as α' or HCP martensite. It has acicular or fine lamellar micro-structure and can be obtained with a rapid cooling of the material from above 900°C. Such cooling conditions can be observed during quenching. α", ω orα_2 phases can also be obtained under specific conditions detailed in [61].

The thermal treatment has thus a great influence in determining the phases, but it also has a big influence on the micro-structure. The influence of thermal treatment on the micro-structure is synthesised in Figure 4.2.

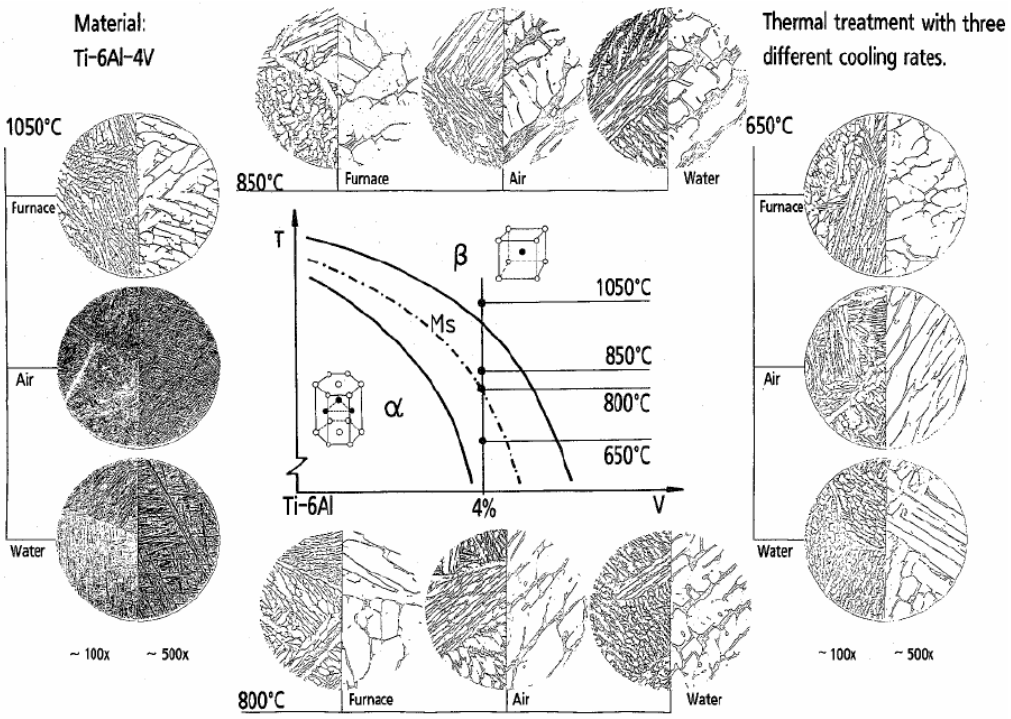

Figure 4.2: Influence of thermal treatment and cooling rate on microstructure of Ti6Al4V [61]

Three classes of micro-structures are usually considered [22][7][61]: lamellar structures, equiaxed structure and a mix of both. A model determining the micro-structure of the Ti6Al4V according to its cooling rate has been develloped by T.Ahmed[1] and is detailed in Figure 6.13. This model was also used as a reference for H.Paydas findings.

Chapter 5

Laser cladding of Ti6Al4V modelling

5.1 Experiment modelled

The objective of this thesis is to build a laser cladding finite element model applied to Ti6Al4V. More specifically, the model reproduces an experimental study (submitted article) on Ti6Al4V performed by H.Paydas, A.Mertens, R.Carrus, J. Lecomte-Beckers and J.Tchoufang Tchuindjang named: "*Laser cladding as a repair technology for Ti6Al4V alloy: Influence of building strategy on micro-structure and hardness[46].* Some of the key inputs, such as the type of material, the geometry, the laser properties or the calibration reference, used for our modelling come from this article. A brief description of the experimental study key findings followed by the inputs used for the model design are given in this section.

The work describes investigations on Ti6Al4V set up by laser cladding to simulate a repair work on a Ti6Al4V substrate. The experiment was performed at Sirris Research Center, Sart-Tilman, Belgium. The effect of the building strategy[1] is studied on the Ti6Al4V samples. On the other hand, the effect of the incident energy[2] have been studied too but will not be modelled in this numerical simulation. The pictures of the clad samples with different strategies and lasers are presented in Figure 5.1. With sample (a), the experiment performed with the meso-clad, that will not be considered in our modelling, sample (b) was perfomred using the macro-clad and a decreasing track length (DTL) building strategy, finally, sample (c) was performed using the macro-clad and a constant track length (CTL) strategy.

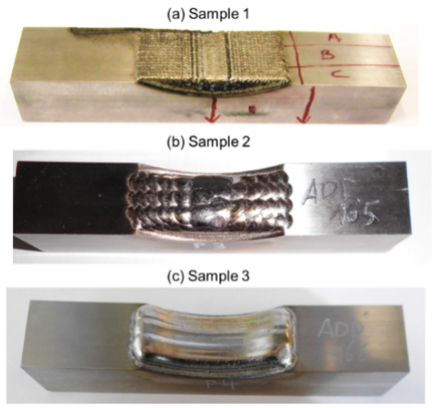

Figure 5.1: The three samples built during the experiment [46]

[1] Two different building strategies are studied: a decreasing track length and a constant track length strategy

[2] Two different lasers are used in the experiment, the MesoClad and the MacroClad, with nominal power of 210 and 1100W respectively

For each of those samples, the following characteristics were investigated:

- The macro and micro-structure are analysed through optical and scanning electron microscopes.

- The hardness of the work-piece is studied and a hardness cartography of the material in the form of a 2-D hardness map is provided.

- The temperature evolution of the substrate during the process was recorded with a thermocouple and thermal imaging cameras.

The result of the analysis is synthesised in a simplified thermo-metallurgic diagram. This diagram allows a rapid understanding of the influence of the different parameters and provides a tool to quickly identify the nature of the phase based on the hardness value and related micro-structure. This simplified diagram is presented in Figure 5.3

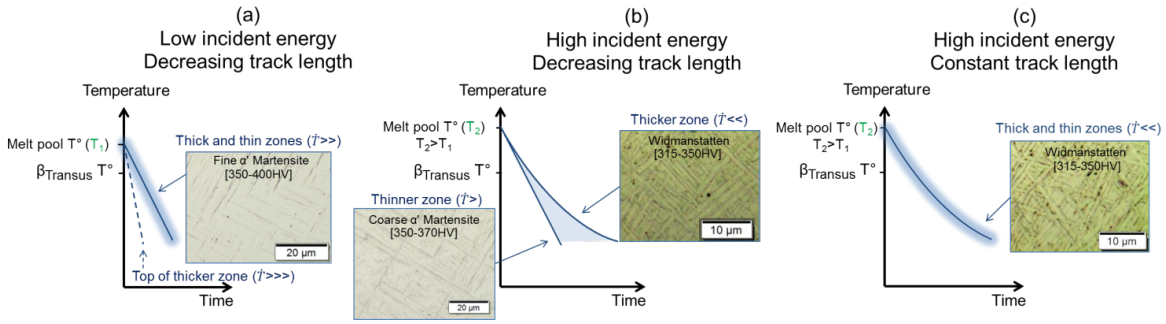

Figure 5.2: Simplified thermo-metallurgic diagram proposed by H.Paydas [46]

In the course of this thesis, the geometry, laser properties, building strategies and material properties used by H.Paydas will be modelled and unknown parameters will be fitted so that numerical results are coherent with the observations for one of the experimental conditions (MacroClad laser, constant track length building strategy). The temperature profile, the welding depth and the micro-structure observed will be compared. The fitted model will then be applied for another experimental condition (MacroClad Laser, decreasing track length strategy).

The experimental conditions as described in H.Paydas paper are listed here below:

The material used for the substrate and cladding material is Ti6Al4V. The specific characteristics of the powder are the following: grain size range from 45 to 78 μm and the chemical composition is given in Table 4.1. The thermal and mechanical properties of the material are described in the sections 5.4 and 5.5. A general overview of Ti6Al4V is also given in the corresponding section (4).

The substrate geometry is meant to represent a damaged titanium piece. It was extracted from Ti6Al4V standard roll bar and was machined to create a cup in its center. The geometry given is provided in Figure 5.3:

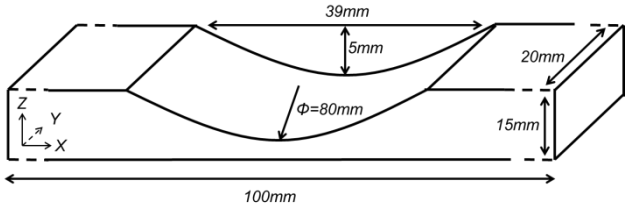

Figure 5.3: Geometry of the machined substrate [46]

The lasers used in the experiment are both Nd-YAG lasers. The MesoClad laser, used for the low incident energy of the simulation has a nominal power of $210W$ and the MacroClad has a nominal power of $1100W$. In the case of this work, only the MacroClad laser will be modelled. Other laser and processing parameters are given in table 5.1 and 5.3:

Table 5.1: Other processing properties

Laser type	Building Strategy	Number of layers	Total building time [min]
MacroClad	Decreasing track length	10	5.4
MacroClad	Constant track length	10	8.1

Experimental results used for calibration and comparison: firstly, the temperature profile at the thermocouple is presented, when using a constant track length strategy and a MacroClad laser. These experimental results will be used to calibrate the 3-D simulation and determine the value of the flux absorbed by the work-piece. The thermocouple temperature profile is provided in Figure 5.5.

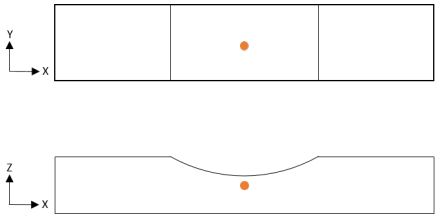

Figure 5.4: Position of the thermocouple

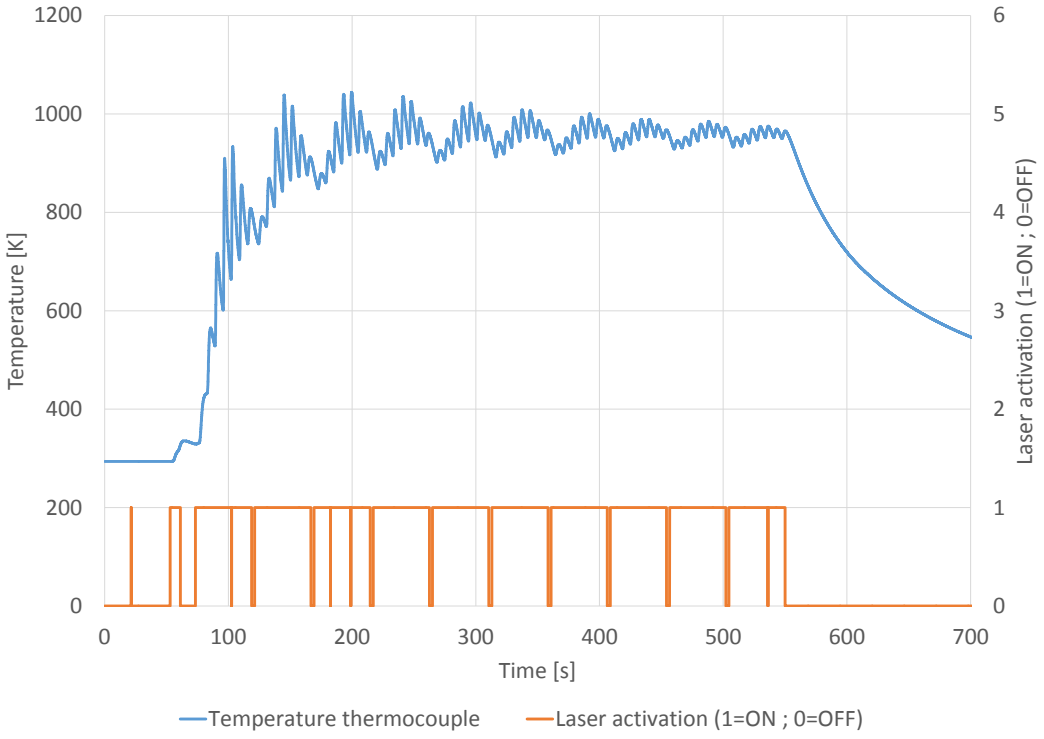

Figure 5.5: Experimental temperature profile at the thermocouple

In Figure 5.5, each group of peaks represents the printing of one layer of material, with a total of ten layers. Each group of peaks is composed of 8 individual peaks, accounting for the different passes. The laser activation graph corresponds to the activation of the laser. It is equal to 1 when the laser is on, 0 when it is off.

A second factor for result comparison is given by the depth of the fusion for the last layer[3]. It will be used to evaluate the quality of the designed model by comparing this value to the experimental one (chapter 6). This fusion depth can be deducted from the optical micrograph provided in H.Paydas's article. A more detailed interpretation of this figure will be provided in section 6.4. The given optical micrograph is show in Figure 5.6.

[3]When using a constant track length strategy and the MacroClad laser

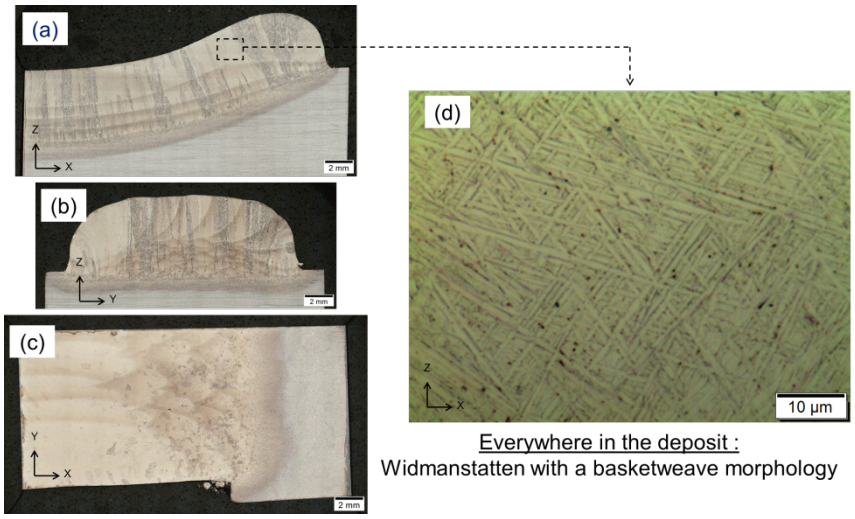

Figure 5.6: Heat affected zone and micro-structure - CTL

The micrograph shows that the heat affected zone (HAZ) is situated at an average depth of $2.75mm$ for the cladding of layer 10. The observed micro-structure is also identified, in this case as Widmanstätten. An analysis of the cooling speed in the numerical simulation will allow us to predict the type of micro-structure. It will be compared to the micro-structure obtained empirically. This analysis will be performed in section 6.4.

5.2 Mesh design

5.2.1 Methodology

A wide variety of geometry types have been created in the course of this master's thesis to best represent the experimental phenomena, from a simplified 2-D stack of elements to a complete multi-pass 3-D geometry. In this section, we will study how we can build the best geometry to represent the experimental work-piece (Figure5.3)and the processing conditions we are interested in. The mesh precision and type will be discussed, as well as a specific tool used when modelling incremental forming: the activation of elements[4]. Finally, the choices made will be highlighted and justified.

5.2.2 2-D simple pile

In order to apprehend the challenges of finite element modelling of complex phenomena, the first mesh designed is a simple pile of elements. This will allow us to observe the effect of an applied flux on a structure. It will be our first model of a Ti6Al4V object subjected to a heat flux.

The geometry designed consists of a a pile of 10 cm high. The height of the element varies in the pile with the position from the top, finer at the top, where the flux is applied, and coarser at the bottom. The height of the fine elements (at the top) varies from $h = 100\mu m$ to $h = 1000\mu m$. In a given pile, the biggest coarse elements have a height equal to five times the height of the finest elements. The width of the stack was set such that the dimensions of the element along the X and Y axes remain close in order to avoid additional numerical problems. A factor of maximum 5 between the height and the width was chosen making every element

[4]The activation/dis-activation of element is generally used when modelling cases when material is added or removed from the initial geometry. Tunnel digging simulation is another example of the activation/dis-activation of elements in engineering.

of the pile $w = 500\mu m$ wide. This geometry, generated by a *Matlab* routine was translated directly into a text file to be used as an input of the non-linear finite element program LAGAMINE.

The parameters used for this first simple simulation will be given without further explanation, as they are similar to the ones extensively described in the next sections. The properties of Ti6Al4V are used[5]. Convection and radiation are taken into account at the boundaries (sides and top of the pile). The simulation is purely thermal and realised in plain strain state. A first study was realised on this pile to understand the influence of the mesh height on the temperature profile for different mesh heights. The initial temperature in the pile is set at $298,15K$ and a flux of $41412W/Node$[6] is brutally applied to the top two nodes to simulate a thermal shock and will be applied for a total time of 2 seconds.

To assess the influence of the element height on the convergence of the code, the temperature profiles obtained with the different element heights will be analysed, temporally and spatially.

Temporally, we observe the temperature profile under the laser beam for different depths for the different piles. Piles with element heights of $h = 100, 250, 500 \quad and \quad 1000\mu m$ will be numerically tested. The temperature profiles will be analysed at the top of the pile (depth=0) and 1 mm under the top of the pile. The results are presented in Figures A.1, A.2 and A.3 in the appendix. From those figures, we can deduce that the smaller the element height, the smaller is the chance of observing oscillations. The intensity of theses oscillations also increases with the element height. Their origin will be explained at the end of this section. Figure A.3 shows that an element height of $h = 250\mu m$ is a good compromise between the limitation of oscillations and computation time.

Spatially, an analysis is performed for three time steps, $t = 0.001s, t = 0.01s \quad and \quad t = 2s$. For each of these time steps, the temperature distribution in the piece is analysed. As it can be seen in Figures A.4, A.5 and A.6 found in the appendix, the bigger the time step considered, the smaller the oscillations. We also clearly see that the bigger the element height, the bigger the oscillations and the the longer they affect the results. In this case, the element height $h = 500\mu m$ and $h = 1000\mu m$ are clearly too coarse to represent our operating conditions. Element heights $h = 100\mu m$ and $h = 250\mu m$ produce small oscillations for the first time-steps (t=0.001s and t=0.01s). This can be seen in Figure A.7 in the appendix. The oscillations decreased rapidly in amplitude with the time as shown in Table 5.2 below:

Table 5.2: Spatial oscillations amplitude study

Element height [mm]	Amplitude at t=0,001s [%]	Amplitude at t=0,01s [%]	Amplitude at t=2,0s [%]
0,10	14,08	4,75	0,00
0,25	122,82	28,79	0,00
0,50	259,70	75,75	0,00
1,00	355,43	403,49	0,01

In order to perform a representative simulation with an acceptable computation time, an element height of $h = 250\mu m$ will be accepted for our thermal model. However, the presence of oscillations of high amplitudes for small time-steps, must be taken into account when considering a thermal-mechanical model. One possible solution to do so would be to start the mechanical

[5]Detailed in sections 5.4 and 5.5.

[6]Corresponding to the surface flux represented by the laser detailed in sections 5.3 and 5.7.

model slightly[7] after the thermal one to avoid the oscillations of the first time-steps.

The origins of the oscillations can be explained theoretically; they are due to a sudden application of a high flux, resulting in a steep slope and strong curvature in the temperature profile. This curvature has to be represented on a finite number of elements. On one element, this variation in temperature[8] is represented as an average which can result in values significantly different from the analytical solution at the extremity of the element (the nodes). In the next element, its average solution will be computed and the solution in this second element will be linearised given the results at the extremity of the previous element, leading to the apparition of an oscillation[9]. A comprehensive figure illustrating this phenomenon is presented in the appendix (A.45). Depending on the importance of the curvature and the precision of the mesh, this phenomenon can influence the results over a certain distance. As shown in Table 5.2, refining the mesh decreases the amplitude of these oscillations.

5.2.3 2-D geometry design

Interest

In order to limit the computing time of the simulation, it was decided that the Laser cladding finite element model would be a 2-D model. The 3-D model described in the next section was uniquely used to calibrate the applied flux. It is thus crucial to design the 2-D mesh in a efficient way.

In order to do so, the mesh precision will vary depending of its position. The parts subjected to the heat source will be refined while the extremity of the substrate will be made as coarse as possible. To build such a differentiated mesh, the software Gmsh[20] is used. It allows the definition of physical zones inside a single mesh that allows a customisation of the mesh by physical zone. The 2-D mesh with the different physical zones is presented in Figure 5.7

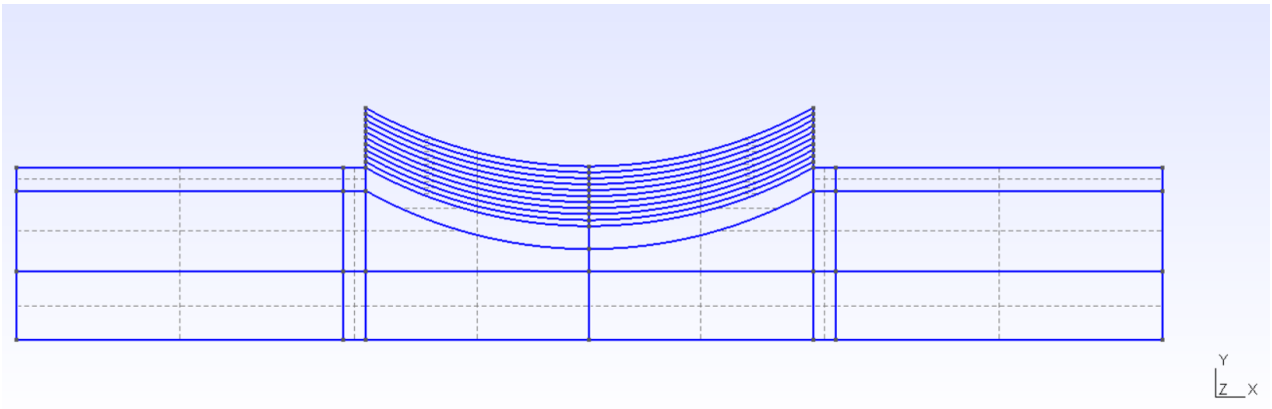

Figure 5.7: 2-D geometry and physical groups - CTL

Constraints and optimisation

The precision of the mesh in the different physical groups is defined to respect several constraints:

In the clad material physical group, that is the 10 layers situated above the substrate, the main constraints defining the mesh size are the following: the laser beam profile, the risk of

[7] If the mechanical model starts 0,1s after the thermal one, the oscillation for $h = 250\mu m$ already have an amplitude of 0,0% of the initial temperature and can therefore be neglected

[8] Highly non-linear due to the strong curvature.

oscillation, the height of one layer of clad material and the limitation of the computing time to a reasonable extend. Each of those constraints are described here below:

- Laser beam profile: the exact modelling of the laser beam will be developed in section 5.3. Here we focus on its impact on the mesh size. The laser beam intensity profile will be modelled as a $1.5mm$ wide rectangle, moving along the X axis. In order to represent accurately its movement, it was decided to choose a mesh length of 1/6 of the laser beam length in the X axis, that is $250\mu m$. In literature, a mesh length equivalent to the length of the laser beam is recommended[10]. We have chosen a finer mesh in our simulation in order to best represent the movement of the laser along the work-piece.

- Oscillation limitation: oscillations, as highlighted on the 2-D pile example, can occur when the mesh is too coarse, in an area where a thermal shock may occur. That is typically the case under the laser beam. The element size (both height and width) must therefore be kept to a reasonable range. In our case, as shown by the 2-D pile example, a $100\mu m$ length for any of the dimensions is acceptable given the flux order of magnitude value, and oscillations become problematic for a mesh size of around $500\mu m$.

- Layer height: the height of a single layer of clad material is $520\mu m$. That is given by the laser increment along the Y axis and presented in Table 5.3.

- Limitation of computing time: although it is a constraint for every numerical simulation, in this particular region of our model, the priority is to best represent the reality. Therefore, respecting the constraints described here above is thus more important.

The size of the element in the clad material physical group is chosen, in respect with the constraints described here above, to be of $250\mu m$ over $260\mu m$ in the horizontal(X-Axis) and vertical(Y-Axis) respectively.

The fine physical group, that is the part of the substrate situated up to $2mm$ under the cup, is highlighted in Figure5.8. This area includes the thermocouple, used for the calibration of the model and will be directly affected by the heat flux during the cladding of the first layer.

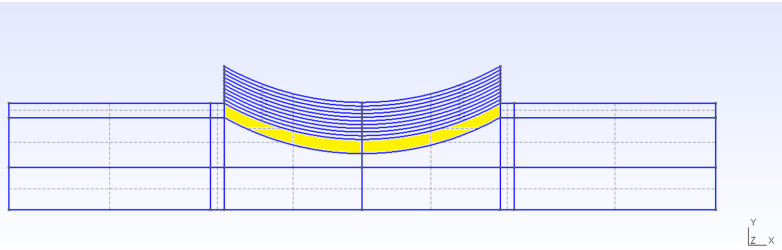

Figure 5.8: Fine physical group - highlighted in yellow

The constraints on the element size for this group are similar to the constraints relative to the clad material physical group[9].

The size of the element in the physical group is therefore chosen similar to the element size of the clad material physical group. The values are chosen so that the dimension of the element will be the same along the horizontal and vertical axis at $250 \quad by \quad 250\mu m$.

[9] All constraints for the two physical groups are the same except for the layer height, which is of no use for the fine mesh physical group

The coarse and transition physical group, that is the rest of the substrate, are presented in Figure 5.9 and 5.10. Here the mesh size is essentially driven by three constraints: the limitation of the computing time, a good coherence of the mesh and a regularity in the shape of the mesh generated. The coarse mesh physical group is situated at the external part of the work-piece. It is subjected to boundary conditions but is situated far enough from the heat flux to not be affected by numerical oscillations due to thermal shock. The transition mesh ensures the link between the coarse and the fine mesh. The mesh in this particular physical group is irregular and is generated by Gmsh algorithm[10].

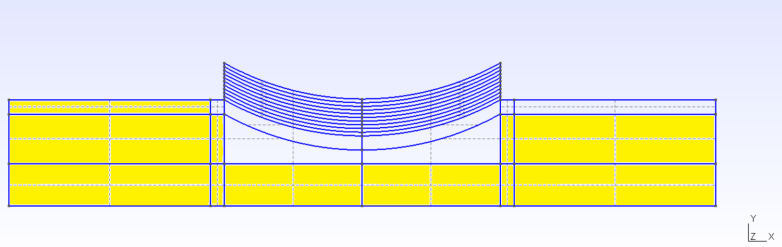

Figure 5.9: Coarse physical group

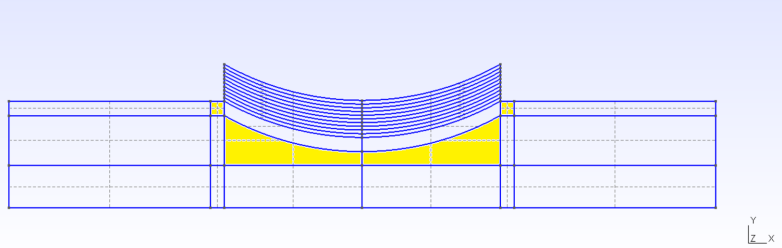

Figure 5.10: Transition physical group

- Limitation of computing time : In the case of the coarse mesh, the main objective is the reduction of the computing time. The temperature profile in this zone is not subjected to a thermal shock and can reasonably take values up to $2000\mu m$ in both directions.

- Coherence of the mesh : the coherence of the mesh has to be checked in the transition area. Due to a too coarse mesh in the coarse physical group, the mesh generated by Gmsh in the transition zone is unable to create the necessary transition elements. It can lead to a non-coherent mesh as depicted in Figure 5.11. The solution to avoid a non-coherent mesh problem is to increase the mesh precision in the coarse physical group.

[10] A description of the algorithm used by Gmsh to generate this transition mesh is given at the end of this section.

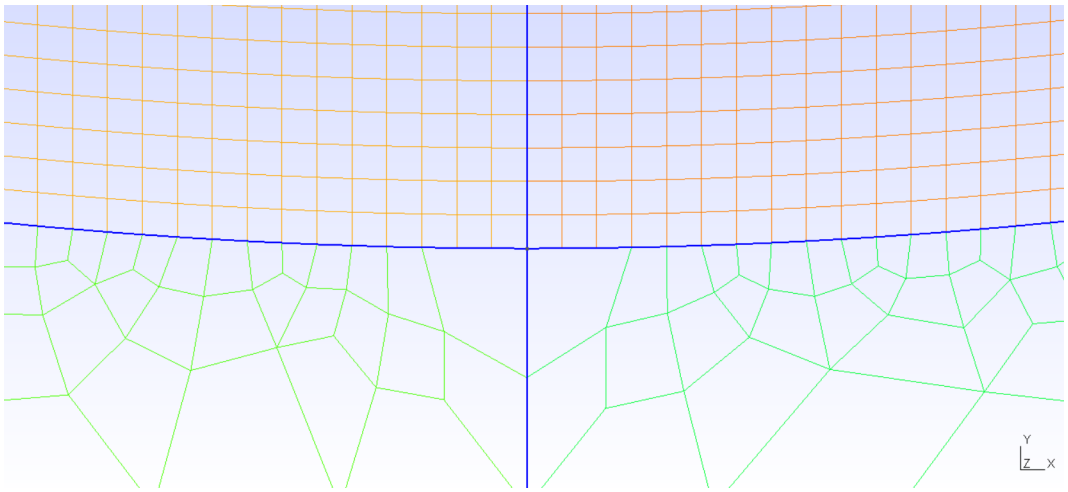

Figure 5.11: Example of a non coherent mesh in the transition physical group

- Quadrangles only : another potential issue observed in the transition mesh is the generation by Gmsh of triangular elements, despite the use of a quadrangle element generation code. This occurs when Gmsh is unable to create a quadrangle only mesh in the transition physical group because the difference in precision between the coarse and the fine mesh is too large, as can be seen in Figure 5.12.

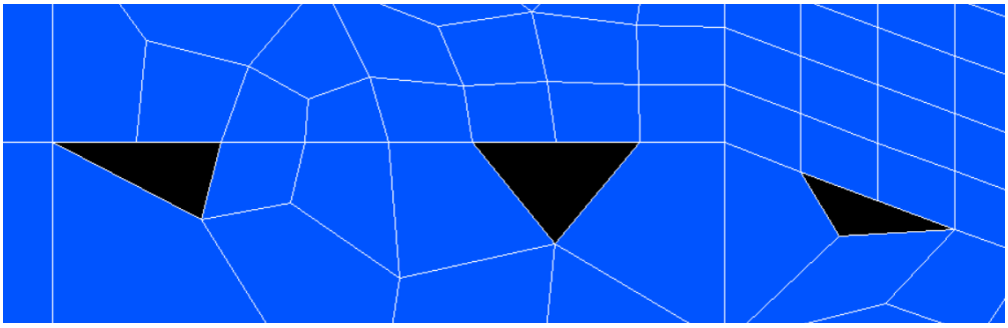

Figure 5.12: Example of non-coherent triangular mesh generated in the transition physical group

This phenomenon is problematic as the type of finite element algorithm (BLZ) used in this simulation only works with quadrangular elements.

The size of the element chosen for the coarse area varies from $1000\mu m$ to $2000\mu m$ in both direction depending on the situation in the work-piece. The coarser mesh is applied to the area with the most distance from the fine mesh.

The mesh algorithm used to generate quadrilateral mesh is the Delaunay for quads algorithm (DelQuad). As described in the Gmsh tutorial guide: "It is a triangulation algorithm that enables to create right angle almost everywhere."[20]. Once the mesh has been generated, it is translated into a readable file for LAGAMINE (.Lag). This translation is performed through the use of *Matlab* routines developed for the purpose of this master's thesis.

Type of element in 2-D

For the inside of the piece, the type of element chosen in Lagamine is BLZ2T with one integration point. This element is based on the variational principle of Hu Washizu[62].

This choice of element was made to reduce the computation time of the simulation. Compared to the classical finite element based on the virtual work principle (type CPL2D in Lagamine), finite element based on the variational principle, are theoretically able to process much faster, as they resolve the displacement, strain and stress fields simultaneously, instead of one after the other.

Convection and radiation elements are also placed on the boundary of the work-piece. In LAGAMINE, we will use the CONRA element. Each of them is composed of 2 nodes from the work-piece and a third node to represent the atmosphere. The atmosphere is set at a constant temperature of $298.15K$[11]

The 2-D work-piece and the 10 clad layers are modelled by a total of 5488 nodes, 5327 solid BLZ2T elements and 1662 convection and radiation elements for a total of 6989 elements. The 2-D mesh, implemented in LAGAMINE is presented in the appendix, in Figure A.15.

Limitations

The 2-D model will be used for most of the simulations, but in order to fit the applied flux, a 3-D model is needed. Indeed, the most accurate information available for the calibration is the temperature evolution at the thermocouple. This thermocouple is situated in the middle of the work-piece (for the two horizontal axis) and $2mm$ under the center of the cup. As showed in Figure 5.13. A 2-D simulation of the thermocouple temperature evolution cannot provide the sought after curve and cannot therefore be used as a calibration tool.

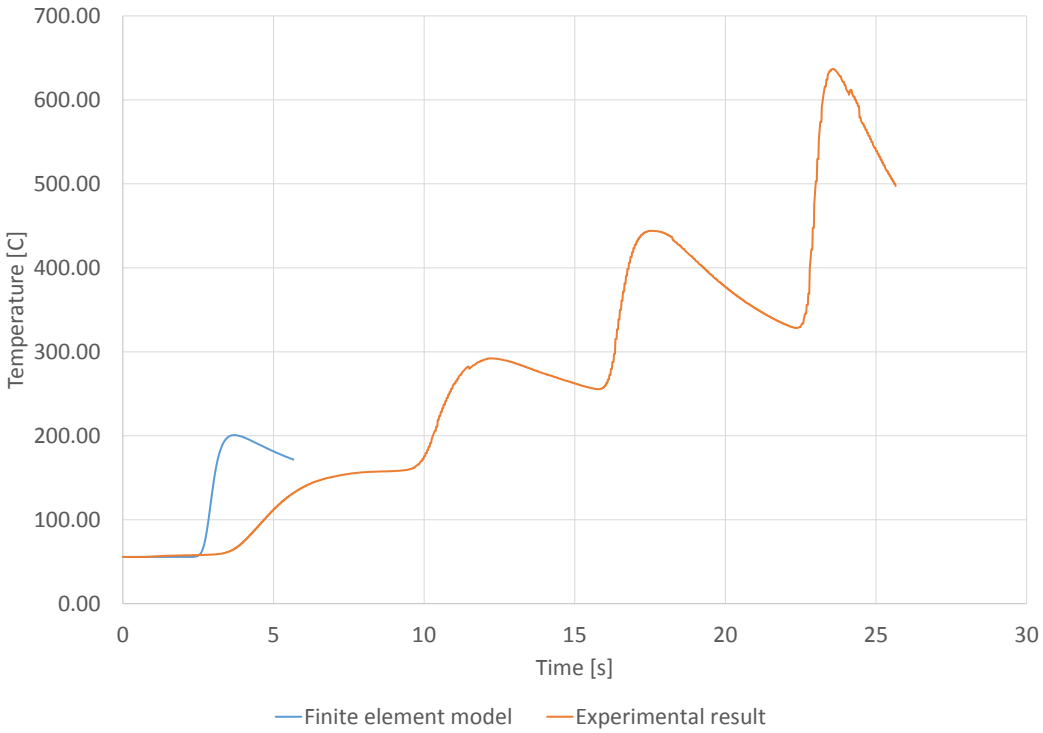

Figure 5.13: 2-D model unable to provide a thermocouple curve that can be used for calibration

[11] This was the outside temperature during the experiment witnessed at Sirris. The change of temperature in the cladding atmosphere during the cladding operation will be neglected.

5.2.4 3-D geometry design

Single and multi-pass design

In order to provide a model to calibrate the applied flux, a 3-D model is needed. The base for the 3-D model consists in the 2-D model. An extrusion will then be realised in order to model the 3-D piece. Two different 3-D models are built: a 3-D geometry simulating the first pass and another simulating the first two passes.

The software Gmsh[20] was used to perform the extrusion. The number of elements along the depth axis (or Z axis) is to be defined. The width of a pass is $2.1mm$ as given by the laser width increment in Table 5.3. In order to limit the computing time, particularly high[12] for a 3D simulation, an element width of $2.1mm$[13] is chosen. This allows us to apply the flux on one row of the element.

The depth of the elements next to the clad layer is reduced to $1.05mm$ in order to limit oscillations[14]. As it is the case in the experimental procedure, a layer of $1.6mm$ width on each side of the workpiece will not be clad. An axonometry of the single pass model and of the multi-pass model are presented in Figure 5.14.

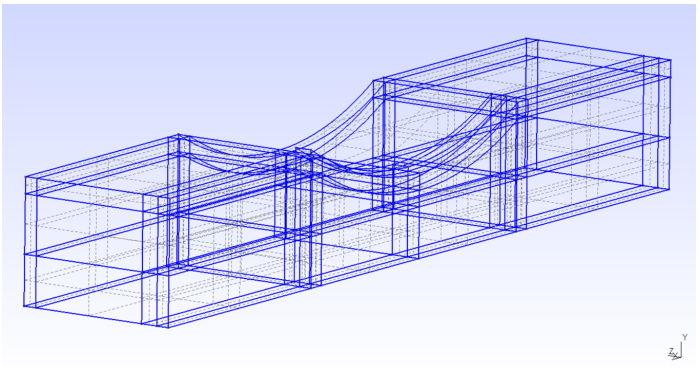

Figure 5.14: 3-D geometry for one cladding pass

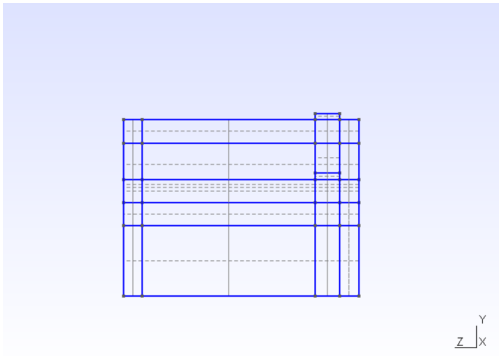

Figure 5.15: View in the Y-Z plan

The mesh is then realised by Gmsh using the 3D DelQuad algorithm. The mesh structure is presented in Figure 5.16 for the two-pass case.

[12] Around 2 hours with a personal laptop and optimal parameters
[13] That is more than 8 times the dimension of the element in the other axis
[14] This refining operation of the mesh will not be sufficient to completely reduce the oscillations.

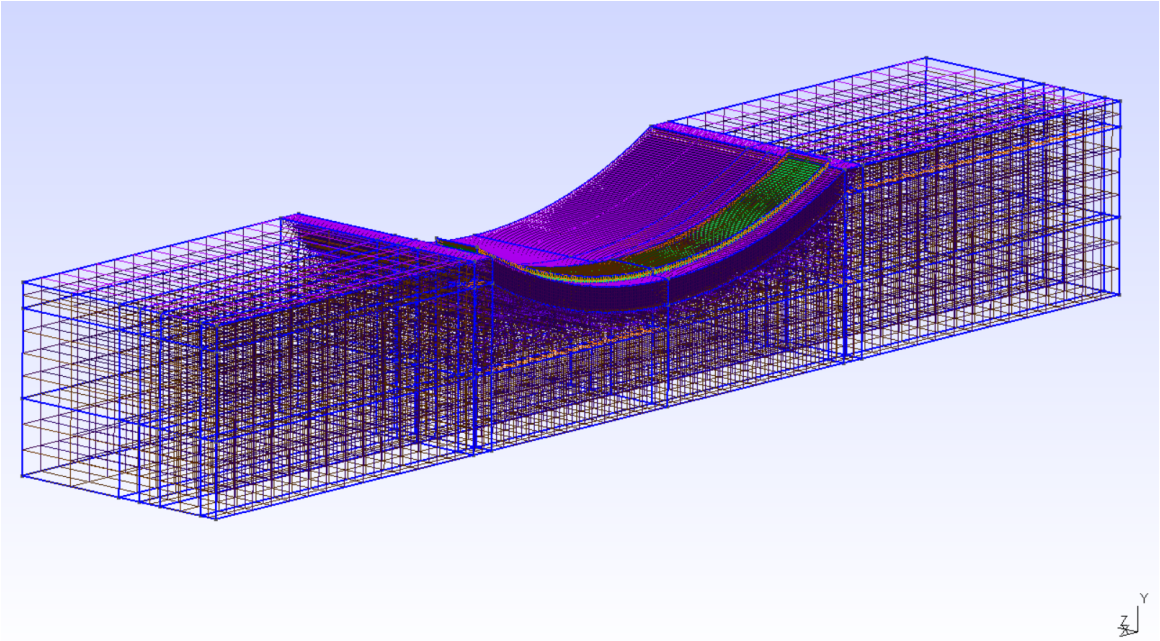

Figure 5.16: Axonometry of the meshed 3-D two-pass geometry

The .msh file generated by Gmsh is then translated into a file readable by the non-linear finite element code LAGAMINE. This translation is done through a *Matlab* routine.

Type of element in 3-D

Similarly to the 2-D case, elements based on the variational principle of Hu-Washizu[62] will be chosen. In LAGAMINE, those elements are called BLZ3T. As for the 2-D analysis, one integration point will be used.

The convection and radiation elements will consist of a quadrangle plane surface with an external point representing the atmosphere. As for the 2-D analysis, the external temperature will be set at $298.15K$ according to the observations of the Sirris experimental procedure. The temperature of this external point is fixed during the simulation. In LAGAMINE, the 3-D convection and radiation elements are called CORA3.

While the computation is performed normally by LAGAMINE, the viewer (DESFIN) struggles to represent the CORA3 elements for big simulations[15]. Indeed each CORA3 element seems to be connected to element 1, as we can see in Figure A.19, presented in the appendix. The point 1 in the picture is the point that all CORA3 elements seem to have in common. By reviewing the different input files, geometry and processing, no mistakes were found concerning the element definition. The problem is thus considered to be a displaying problem of the viewer Desfin, with no impact on the simulation.

The 3-D work-piece and the two clad passes are modelled by a total of 24393 nodes, 20469 solid elements (BLZ3T) and 6522 convection and radiation elements (CORA3) for a total of 26991 elements. The 3-D geometry, as can be seen by the viewer DESFIN, is presented in Figure A.16, found in the appendix.

[15]Simulations with up to three CORA3 elements do not lead to that display problem.

Limitations

The main limitations with the 3-D model is the presence of oscillations in the temperature evolution along the depth axis. These oscillations are due to the fact that the precision along the depth axis is low compared to the other axes. At $2100\mu m$ compared to $250\mu m$ and $260\mu m$ along the horizontal and vertical axes respectively.

Spatial oscillations along the depth axis impact the temperature evolution at the thermocouple, which reduces the accuracy of the model calibration. The oscillations are highlighted in the appendix in Figure A.17, which consist of a horizontal view of the work-piece at a height of $8mm$[16] and at $t = 3s$, that is approximately at the middle of the first layer cladding.

These oscillations affect the temperature profile at the thermocouple. For the printing of one layer of material, the observed temperature profile is given in Figure 5.17. The oscillation observed can be quantified as such:

$$\varepsilon = \frac{\delta_{oscillation}[K]}{T_{initial}[K]} = 0.3\% \tag{5.1}$$

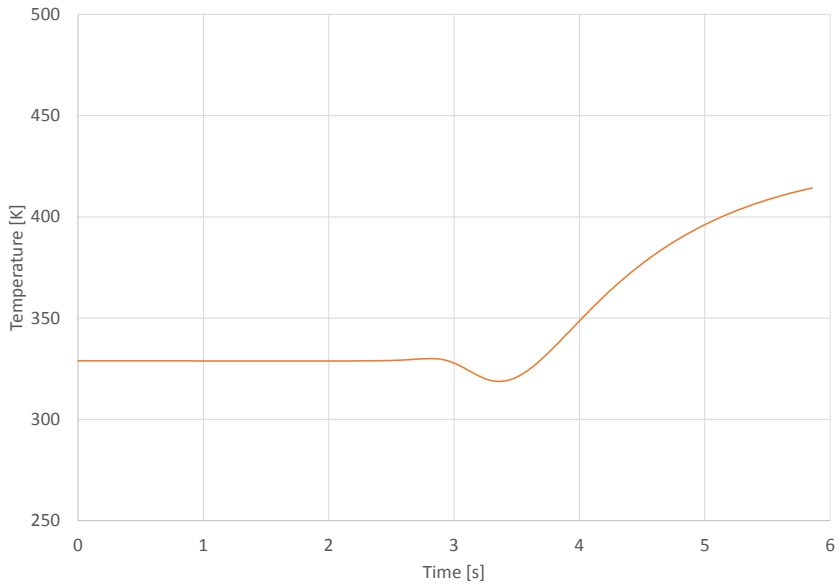

Figure 5.17: Oscillation observed at the thermocouple

To verify that a too coarse mesh along the depth axis is the cause of the oscillations, a modified 3-D geometry was built. The structure is unchanged but the coordinates along the depth axis are divided by 5, leading to a maximal element size along the depth axis of $420\mu m$. This modified geometry was not used for simulation or calibration of the results but only to confirm the cause of the oscillations observed in the temperature profile. The flux applied on the nodes was reduced to maintain the same surface flux in $[W/m^2]$. The same view as for the 3-D accurate geometry is provided in Figure A.20, found in the appendix, the figure provides a horizontal view of the modified piece at a height of $8mm$ and at $t = 3s$.

[16] That is the height of the thermocouple in the work-piece

No oscillation can be observed along the depth axis. A display of the temperature profile at the thermocouple also proves the absence of thermal oscillations at this point. To overcome this oscillation issue, the solution is thus to increase the mesh precision along the depth axis. Nevertheless, this solution will not be applied in the case of this master's thesis. The computation time for such a simulation will increase drastically, making the simulation too complex to run on a personal laptop.

5.2.5 Element Renumbering

In order to enhance the computation speed, one possible solution is to proceed to a renumbering of the equations' numbers in the finite element code. Renumbering does not change the node numbers but only the equation numbers corresponding to the degrees of freedom[17] of these nodes.

Different strategies exist for the renumbering. First the directions must be ranked according to the number of nodes in their direction. It gives X-Y for the 2-D case and X-Y-Z for the 3-D model.

The renumbering strategy must then be chosen. Different methods have been developed and will not be detailed in this master's thesis work. The different methods applicable in LAGAMINE are the following: maximum bandwidth optimisation, mean bandwidth optimisation and directional optimisation.

These three methods will be used on the 2-D model for the modelling of one layer. The computation time needed will then be compared to the time required to perform the same simulation without any renumbering strategy. The results of this analysis are provided in Figure 5.18:

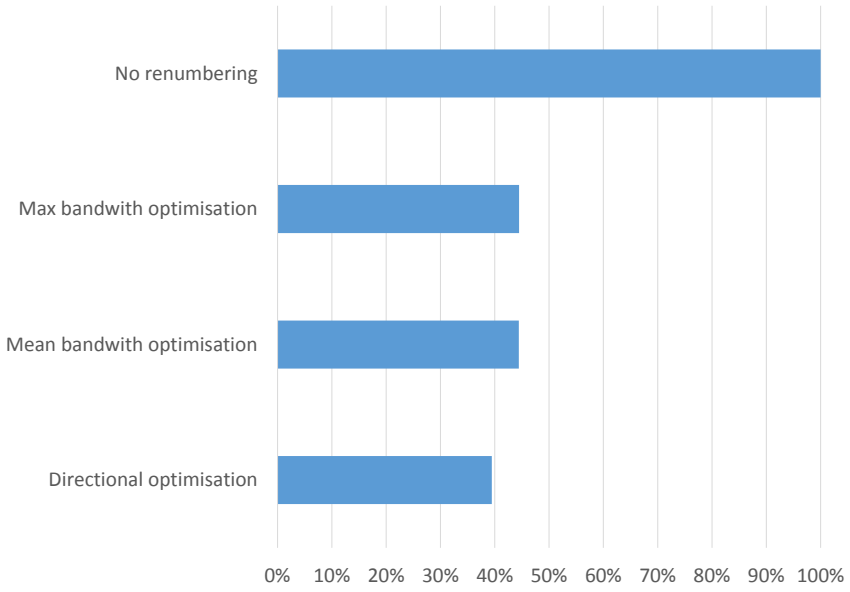

Figure 5.18: Comparison of the different renumbering strategies in terms of computation time.

The results show that the most time-efficient renumbering strategy is the directional optimisation strategy. By using this strategy, the computation time needed in this specific case was

[17] In our case the degrees of freedom concerning the temperature, that is degree number 3 in 2-D and degree number 4 in 3-D

equal to only 39% of the computation time needed for the same simulation without any renumbering strategy. Therefore, for all results producing models, a directional optimisation strategy will be used.

5.3 Heat source modelling

The heat source modelling, or laser modelling, is based on the laser properties. Laser properties were provided by Sirris in order to perform the numerical modelling of the experiment. The following information was provided[46]:

Table 5.3: Laser Properties

type	Height increment	Width increment	Power	Speed	Powder rate
Macro clad	520 um	2,1 mm	1100 W	400 mm/min	4%

The laser will be modelled by a flux applied to certain nodes of the structure. The value of the flux and the path of the laser on the solid must then be determined. The combined results will be given in the form of a list of times. For each instance of time, a list of nodes affected by the laser will be provided and the determined flux will be applied to them. In this section, a study is presented on how these factors can be numerically modelled to simulate the path of the laser as it happens in the experiments. A focus will be given to the technical characteristics: the increments, the power, the speed and the shape of the laser. The powder rate is not relevant to the simulation as the layer height is considered fixed.

In other studies, a different approach is followed [2]: the effect of the laser is modelled through the boundary conditions under the form:

$$\beta \cdot I(x, y, z, U, t) \tag{5.2}$$

where β is the absorption factor,I $[W/m^2]$ is the laser energy distribution on the piece and U [m/s] is the velocity of the laser in the x, y and z directions respectively[18].

5.3.1 Height and width increment

The height increment has been already used to define the height of the element in the clad region, resulting in an element height of $260\mu m$. This characteristic has no additional effects on the modelling of the laser as only the flux is imposed on top of the clad material to simulate the laser action. The actual laser position in the vertical axis is therefore of no use.

The width increment has already been used in defining the total width to be printed as well as in defining the precision of the mesh along the width axis. It will be used in this section to define the laser path. The width increment determines the movement of the laser along the width axis (Or Y axis in 3-D) when the laser moves from printing one line to another. This change of line is done without stopping the laser and must be taken into account in the modelling.

[18]More information about this approach is given in section 3.2.

5.3.2 Speed

The laser speed is $400mm/min$, that is $0.00667m/s$. This is the maximal speed that is reached by the laser after a brief phase of acceleration that will not be modelled[19]. The speed given is an absolute speed. As the laser is moving on a curved surface, the speed can be divided into a vertical and a horizontal speed. When determining the path history of the laser, only the horizontal speed is needed. In a first estimation, the horizontal speed was assumed to be equal to the absolute speed of the laser[20]. Considering the length of the element in the clad area ($250\mu m$), we can compute the time step required for the laser flux to advance one element along its path. This first time step is given by:

$$TimeStep = (250\mu m)/(0.00667m/s) = 0.0375s \tag{5.3}$$

We can also compute the total time required to simulate one entire line of cladding. We compute a total time of $5.625s$[21]. It corresponds to 150 time steps per line of clad material. The advantage of this hypothesis is that it results in a constant time step, facilitating the execution strategy[22]. However, it is not an acceptable simplification. The laser is moving in a curve and therefore its speed has a vertical compound. The difference with the simplified hypothesis was computed and gives the following results:

Table 5.4: Influence of the vertical speed

	$V_{extreme}$	V_{centre}	V_{mean}
$V_{Horizontale}[m/s]$	0.0058	0.0067	0.0064
$V_{abs}[m/s]$	0.0067	0.0067	0.0067
Difference [%]	12.69	0.00	4.27

The average difference is just below 5% but increases to greater than 12% near the extremities where the vertical component is of importance. To allow the simulation to take this into account, it was thus decided to change the time step at each time interval, to better represent the horizontal speed of the laser. To determine these time steps, simple geometrical and trigonometric rules have been used and are described here under for the case of the extremities.

[19] The acceleration phase coincides with the laser power increase and is therefore difficult to fit into the model as the parameters are unknown. Neglecting this phase is assumed to have a limited impact on the model accuracy.

[20] This hypothesis will be challenged and a more sophisticated hypothesis will be formulated.

[21] Obtained by considering the laser starting already on the cladding surface and not on the substrate.

[22] The time step by which the finite element model must be solved has to be defined in the execution file. A constant time step significantly eases this definition.

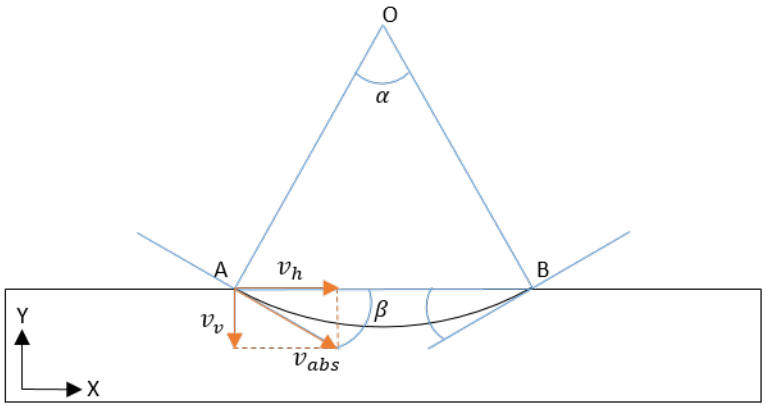

Figure 5.19: α angle

We have from the geometry definition:$Stringlength = 39mm \quad and \quad ArcDiameter = 80mm$ Therefore we can compute:

$$\alpha = 2 * ArcSin(Stringlength/Diameter) = 1.004 \quad rad. \tag{5.4}$$

The β angle can then be obtained, knowing that the sum of a triangle angle is equal to π:

$$\alpha + 2 \cdot (\frac{\pi}{2} - \beta) = \pi$$

$$\pi - \alpha = 2 \cdot (\frac{\pi}{2} - \beta)$$

$$\beta = \alpha/2 = 0.509 \quad rad \tag{5.5}$$

The horizontal component of the laser speed is then given by:

$$V_h = V_{abs} * cos(\beta) = 0.0058 \quad m/s \tag{5.6}$$

5.3.3 Shape

To model the laser intensity profile, several studies have been published in recent years. Models can be as simple as considering a uniform flow such as in Rosenthal [52]. This first level of complexity will be used in our model as the goal is not to focus on the heat source but on the overall laser cladding process. It is possible to select a more developed intensity profile such as a circular Gaussian TEM_{00} shaped intensity profile as used in [2][57][45] or [13]:

$$I(r) = \frac{2 \cdot P_1}{2 \cdot \pi} \cdot exp(\frac{-2 \cdot r^2}{r_1^2}) \tag{5.7}$$

where r_1 [m] is the laser beam radius, r [m] the distance from the center of the beam and P_1 [W] the laser average power.

A more complex model has been developed by Goldak et al.[23]. It consists of a double ellipsoidal power density distribution. Such a complex profile is difficult to model from a numerical point of view as it requires a very precise mesh. Such complex models are then often used when only the melt pool or the laser beam itself are being modelled.

The laser intensity profile was provided by Sirris and is described hereafter:

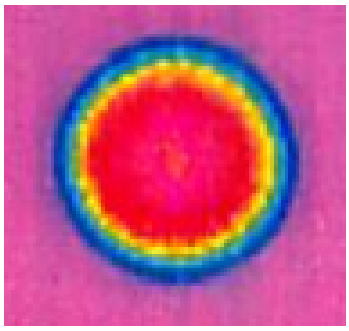

Figure 5.20: Laser beam thermal image

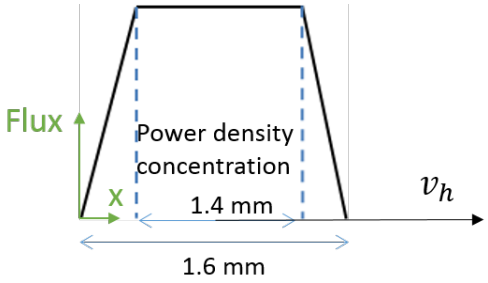

Figure 5.21: Laser intensity modelling

The maximum value of the heat source modelled here above will be discussed in the next section.

In most simple laser cladding simulations, the size of the heat source is of the same order of magnitude as the surface element size. Since the usual mesh size used to represent laser-clad pieces is too coarse compared to the laser beam size, the mesh density is thus usually refined near the heat source[10]. This methodology was applied in our modelling, and in the 2-D case the mesh is set to be 6 times smaller than the laser beam size, allowing a representative modelling of the heat flux, as well as a precise representation of its movement along the work-piece. For the 3-D simulation, along the width (Z) axis, the mesh width is set equal to the laser beam width to avoid drastically increasing the number of nodes and elements.

As we assume that the laser is providing a constant energy flux, the heat flux must at all times provide the same total energy to the work-piece. In order to do so, and given the precision of the mesh, simplification hypotheses are applied to guarantee this applied energy conservation:

The shape of the heat flux applied is given by:

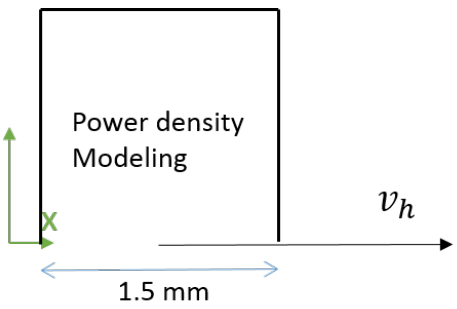

Figure 5.22: Simplified energy source heat flux profile

This simplification allows us to replace the shape of Figure 5.21 by an energy equivalent

rectangle. Such a hypothesis was needed as modelling the $100\mu m$ long slopes on both sides of the profile was impossible to do on $250\mu m$ elements.

Since the flux is applied on the nodes and not on the elements, the shape of the heat flux has to be discretised. The surface flux $[W/m^2]$ are reported on the 2 adjacent nodes or the 4 adjacent nodes for the 2-D or 3-D simulations respectively. The discrete heat source applied in our model is presented in Figure 5.23 for the 2-D case.

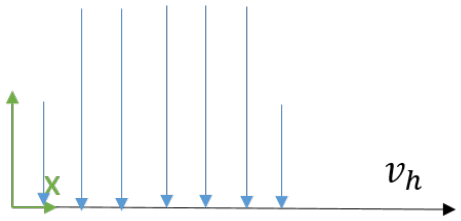

Figure 5.23: Heat flux applied to nodes

5.3.4 Power

When modelling the heat source, "The only accurate input data is the power of the laser" says Chiumenti [13]. The laser nominal power is indeed given by the laser manufacturer. In the case of our finite element modelling of laser cladding, the laser power properties are given in[46] and were $1100W$ for the MacroClad laser and $210W$ for the MesoClad laser. Unfortunately, these values cannot been used as such for the value of the flux applied to the work-piece. In fact, only a portion of the laser energy is absorbed by the work-piece. Only a few studies exist on the absorption phenomena given its complex nature. An indirect method for calculating the absorptivity coefficient (β) has been developed by Yang[66] for a Gaussian intensity profile. The absorptivity coefficient β is given by:

$$\beta = \frac{k\Delta T}{2 \cdot P} \cdot \sqrt{\frac{\pi^3 b^3 U}{2 \cdot a}} \tag{5.8}$$

Where ΔT is the temperature on the top of the work-piece as given by Dahorte [13].k is the thermal conductivity and a the thermal diffusivity. P is the nominal laser power, b the value of the beam radius and U the laser velocity. According to this model, the average absorptivity of a Ti6Al4V plate work-piece is equal to 0,34. This value was obtained using Mills data for Ti6Al4V [41].

For this thesis, the value of the flux applied, thus indirectly the value of the absorptivity β coefficient will be used as a calibrating factor. As presented in the results section, the absorptivity coefficient numerically obtained is equal to 0,33. Close to the value recommended by Yang [66]. Given the nominal power of the laser, 1100 W, we can compute the value of the flux to apply and obtain 363,51 W.That corresponds to a flux of 15,15 W/node.

A sensitivity study of the temperature profile obtained in the work-piece, depending on the given flux, was realised for the 3-D model. The sensitivity study was performed for 5 different flux values. This analysis is presented in appendix A.2.

5.3.5 Integrated Modelling

By combining the modelling hypothesis section described here above, an input file can be generated for our finite element model.

In the 2-D modelling, it takes the form of seven punctual flux applied to the nodes. The value of the flux applied to each node, obtained after calibration is of $9599\,W$ for the two outside nodes and $19200\,W$ for the 5 middle ones. These applied flux move along the X axis at a speed of one node every time step. This time step changes continuously according to the analysis made in section 5.3.2.

This laser modelling in the 2-D case is modelled in Figure 5.24:

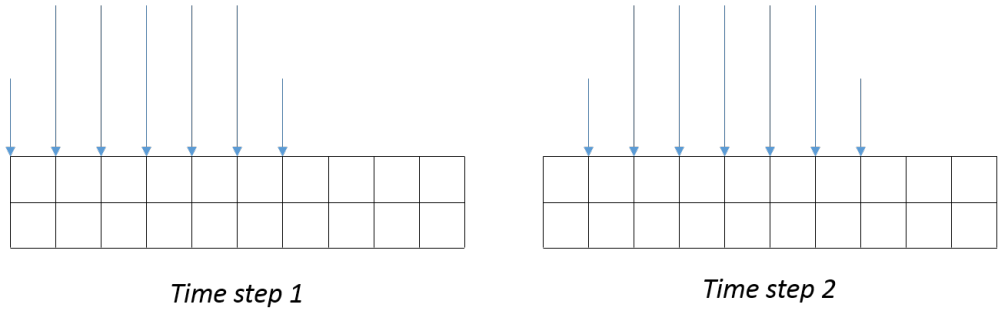

Figure 5.24: Applied Flux for two successive time steps

In the case of the 3-D simulation, the method is similar. The flux applied on one element is reported on 4 nodes with a value of $15.15W$ per node. The factors applied to convert the 3-D flux into the 2-D flux will be explained in subsection 5.7.2.

Another difference with the 2-D simulation lies in the definition of time between layers. This time between layers (TBL), is initially defined as the time for the laser to go from one pass to another. Given the space between the passes ($2.1mm$) and the horizontal speed of the laser, this time was first estimated at:

$$TBL_{firstestimate} = \frac{0.0021m}{0.0067m/s} = 0.315s \tag{5.9}$$

by applying this TBL to our multi-pass 3-D simulation, the temperature profile numerically observed at the thermocouple was different from the experimental temperature recorded. The peak was appearing too soon in the numerical simulation, due to an underestimated TBL. Figure 5.25 shows the early appearance of the second layer peak of temperature at the thermocouple with $TBL_{firstestimate} = 0.315s$:

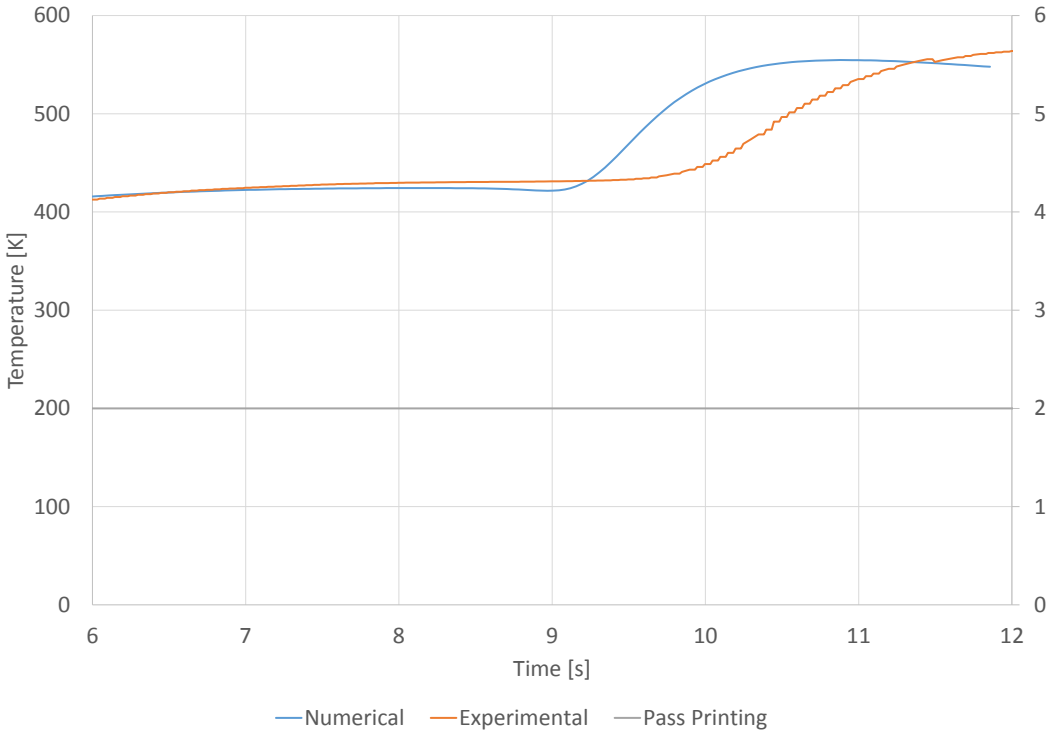

Figure 5.25: Early appearance of the temperature peak for $TBL = 0.315s$

The value of the TBL was thus modified to take into account that difference between the finite element model and the experimental records. The beginning of both peaks were identified. In the case of our model, we consider the beginning of the peak when:

$$\frac{\Delta T}{0.1s} > 10 \quad K/s \tag{5.10}$$

By applying this criteria, an additional time of $0.413s$ is added to the previous TBL to give:

$$TBL = TBL_{firstestimate} + 0.413 = 0.728s \tag{5.11}$$

Applying this time between layers allows an equal appearance in time of the temperature peaks at the thermocouple in both the numerical observation and the experimental data.

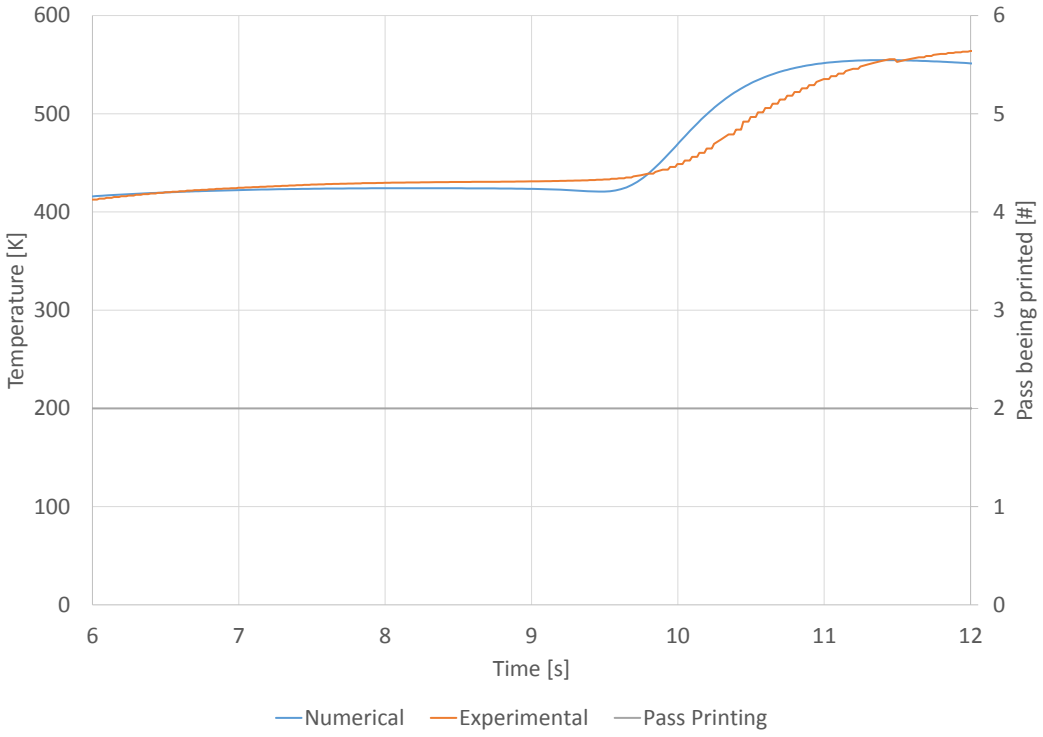

Figure 5.26: Appearance of the temperature peak for the corrected TBL

The combined parameters explained in this chapter were written into an input file readable by LAGAMINE (.Loa file). A *Matlab* routine was developed and used to generate the .Loa file.

5.4 Thermal law modelling

The thermal laws used for the simulation are of two kinds: an internal heat transfer law that characterises heat transfer by conduction and accumulation in the solid, and an external heat transfer law that characterises the heat transfer between the solid and the external world by convection and radiation.

The law THNL-S will be used for internal heat transfer. It takes into account heat transfer by conduction as well as heat accumulation in solids. The two parameters used in this law are the conductivity of the material and its apparent heat capacity, both these properties will be given for different temperature values. It is important that the range of temperatures for which the parameters are given is sufficiently wide to cover the expected range of temperatures of the experiment, that is from ambient temperature (298,15°K) to the evaporation temperature of Ti6Al4V (3533°K [7]). In order to represent heat transfer between the solid and the external world by convection and radiation, the RACO law will be used. It requires as input the convection coefficient h and the emissivity ε given for a wide range of temperatures. It also uses the Stefan-Boltzmann's constant given by:

$$\sigma = 5,670373.10^{-8} \quad [W.m^{-2}.K^{-4}] \tag{5.12}$$

It is also important to note that because of discontinuities in the apparent heat capacity definition, the enthalpy formulation of the heat problem[23] will be used in our simulation.

[23] By opposition to the classical formulation of the heat problem

5.4.1 Parameters definition

Heat conductivity

The thermal conductivity is the property to transfer heat by conduction. It represents the heat energy transferred by unit of surface and time under a gradient of temperature of 1°C/s. The heat conductivity of Ti6Al4V as a function of temperature is given by a wide variety of scientific articles and reports. The most relevant, including the model of Z. Fan and F.Liou[17] used in this simulation, will be briefly described and a comparison of the given values will be performed.

A.Mertens and H.Paydas, in an experimental test of Ti6Al4V set up by laser cladding analysed the apparent conductivity for the range [100-1000 °Celsius][38]. The measure precision is about 7% and was performed on three samples. As shown on Figure 5.27, a significant peak of conductivity appears at the α to β micro-structure[24] transition temperature. This α to β transition occurs at 882°C.[19].

A. Neira Arce provides in his thesis polynomial functions to describe the conduction of Ti6Al4V as a function of temperature, where temperatures range from 23 to 2700 °Celsius. However, the peak for the α to β transition is not represented. Conductivity increases drastically at the liquidus temperature (1923 °K [41]). Thermal conductivity values are also given by K.C. Mills[41]. These values are provided in Table 5.5, alongside the values relative to heat capacity:

Table 5.5: Thermal conductivity and heat capacity of Ti6Al4V alloy according to K.C. Mills [41]

Temperature [°C]	Thermal conductivity $[W.m^{-1}.K^{-1}]$	Specific heat $[J.kg^{-1}.K^{-1}]$	Density $[kg.m^{-3}]$
25	7.0	546	4420
100	7.4	562	4406
200	8.7	584	4395
300	10.1	606	4381
400	11.3	629	4366
500	12.6	651	4350
600	14.2	673	4336
700	15.5	694	4324
800	17.8	714	4309
900	20.2	734	4294
995	19.3	641	4282
1100	21.0	660	4267
1200	22.9	678	4252
1300	23.7	696	4240
1400	24.6	714	4225
1500	25.8	732	4205
1600	27.0	750	4198
1650	28.4	759	4189
Uncertainties	± 10%	± 3%	± 3%

Based on this data, Z.Fan and F.Liou have developed polynomial functions to approach the

[24]For more information about the α to β micro-structure transition please refer to chapter 4

thermal conductivity as functions of temperature[17]. Finally M.Boivineau et al. conducted experiments on two different resistive pulse heating devices at CEA Valduc and TU-Graz to provide thermal conductivity values for Ti6Al4V at solid and liquid states[5].

A graphical comparison of the different studies is provided in Figure 5.27. The thermal conductivity is given in $W.m^{-1}.K^{-1}$.

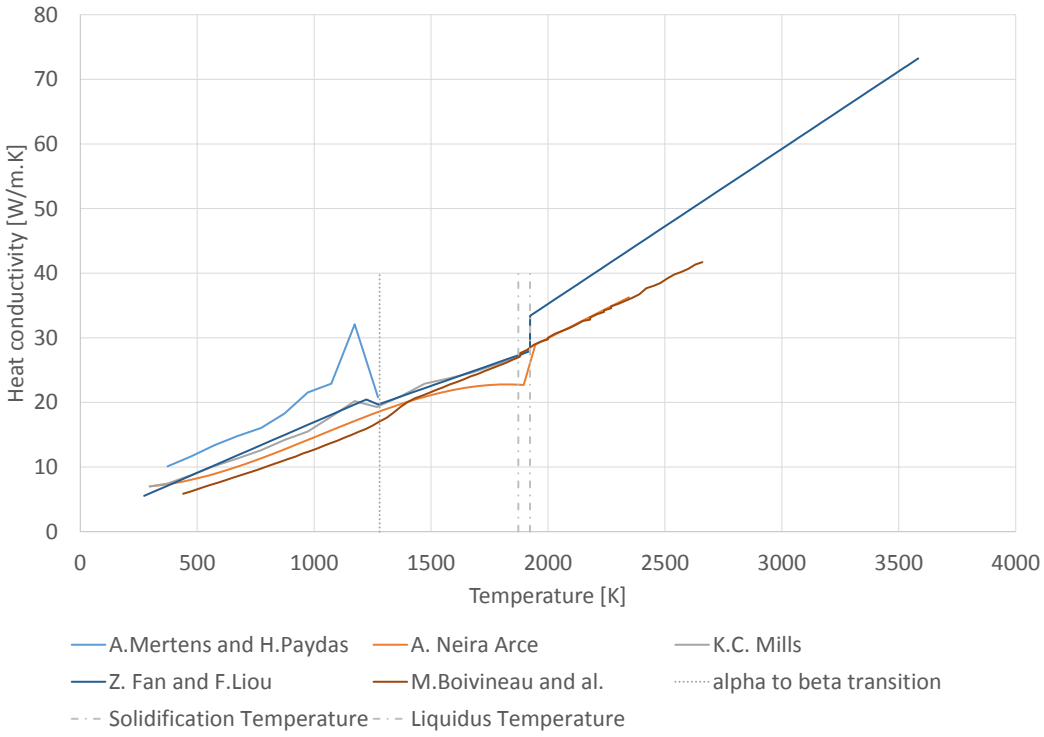

Figure 5.27: Thermal conductivity - A graphical comparison of existing models. [38][43][41][17][5]

A zoom of the comparison for data below 2000°K is provided in Figure 5.28. The α to β transition as well as the transition from a solid to a liquid phase are here made more clear.

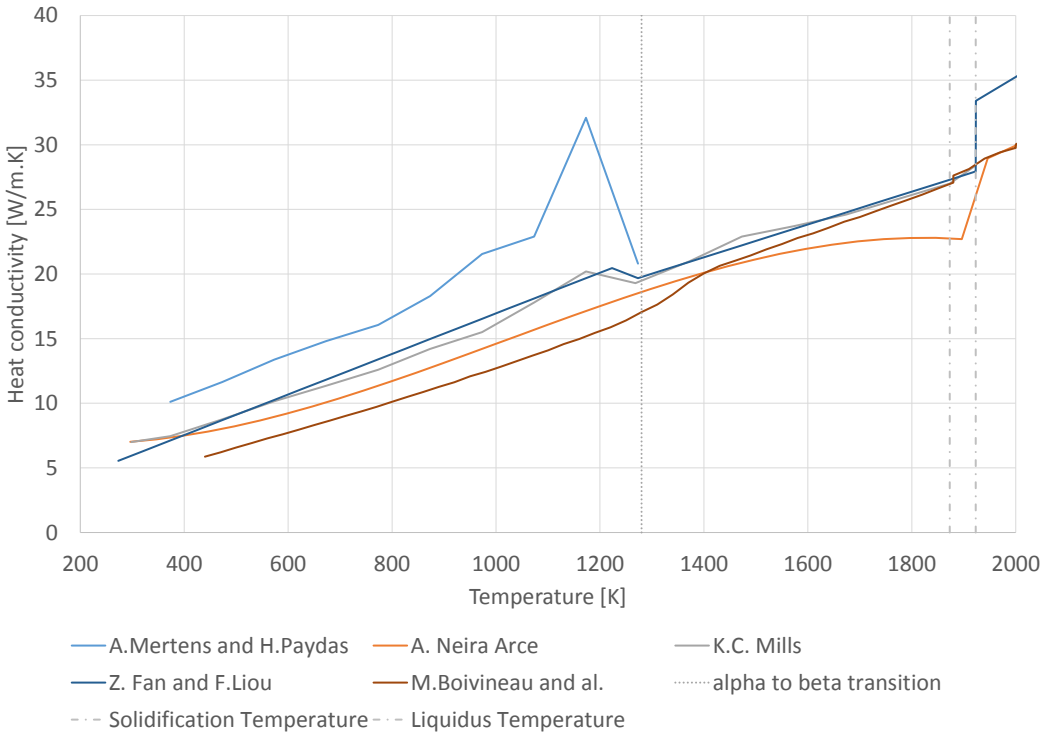

Figure 5.28: Thermal conductivity of Ti6Al4V. Zoom below 2000°K [38][43][41][17][5]

In the case of our simulation, the model of Z.Fan and F.Liou, based on the initial findings of K.C. Mills has been selected. The thermal conductivity in this model is given for the widest range of temperatures [293 - 3533°K]. It also represents the α to β transition as well as the transition from solid to liquid state.

Heat capacity

The volumetric heat capacity or volume-specific heat capacity of a material is its capacity to accumulate heat given its volume. It is defined by the quantity of heat needed to increase the temperature of one meter cube of material by 1°C. It can be obtained by taking the product of the specific heat capacity and the density. The heat capacity analysis will be performed in a similar fashion to the thermal conductivity analysis. The most relevant articles will be shortly detailed and a graphical comparison of the given values will be provided. Two important notions about the heat capacity detailed here after must be specified:

- The heat capacity used by our model and compared hereafter is the apparent heat capacity. It takes into account the latent heat of fusion(L_f) and vaporisation(L_e). These two values are given by K.C. Mills : $L_f = 2,86.10^5 J.Kg^{-1}$ and $L_e = 9,83.10^6 J.Kg^{-1}$[41].
- The heat capacity per unit volume is used in our model. Since most of the heat capacity values are given for unit of mass, the density as a function of the temperature has to be studied as well.

A.Mertens and H.Paydas, in their experimental study, give values for both the density and the apparent heat capacity for the range of temperatures [100-1000 °Celsius][38]. The measurement precision is about 3% and was performed on two samples. The heating rate during the experiment was 10°C per minute. Once again, a peak of apparent heat capacity appears at the α to β transition temperature. The peak starts at a temperature of 825 °Celsius, reaching a

maximum at 930 °Celsius.

A. Neira Arce provides polynomial functions to approach the density and heat capacity evolution of TA6V. Those polynomial functions are defined for given temperature intervals. When analysing the A.Neira Arce curves on Figure 5.30, we notice that the peak for the α to β transition is not represented. the heat capacity increases until the liquidus temperature (1923 °K [41]) and slowly decreases afterwards.

K.C. Mills[41] provides other data which has been provided in the Table 5.5. Here again, Z.Fan and F.Liou have developed polynomial functions to approach TA6V density and heat capacity as a function of temperature[17].

M.Boivineau gives other values based on its experiments at CEA Valduc and TU-Graz [5]. Finally, E.Kaschnitz provides some results for the heat capacity of Ti6Al4V alloy over the temperature range 1400 to 2300 °K. The measurements are taken, as for M.Boivineau, by microsecond pulse heating[27]. Since E.Kaschnitz measured the heat capacity per unit of mass and does not provide a density evolution of Ti6Al4V with temperature, the heat capacity per unit of volume has been obtained by multiplying the density as given by K.C.Mills and available in Table 5.5 to the heat capacity per unit of mass of E.Kaschnitz.

A graphical comparison of the different studies is provided in Figure 5.27. The apparent heat capacity is given in $J.m^{-3}.K^{-1}$.

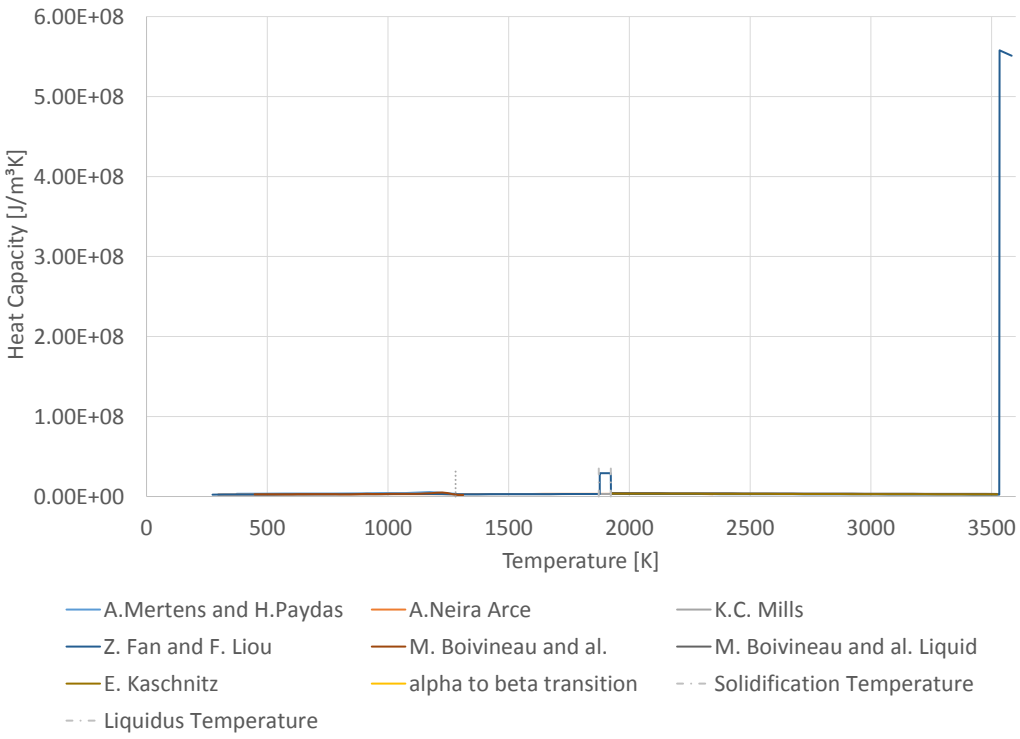

Figure 5.29: Apparent heat capacity - A graphical comparison of existing models. [38][43][41][17][5][27]

Figure 5.29 shows how the Latent heat L_f and especially L_e influence the profile of the apparent heat capacity. The figure therefore highlights their relative importance in heat accumulation

in the cladding process. In order to see what happens in the heat capacity profile outside the peaks due to the latent heat of fusion and vaporisation, a zoom is provided in Figure 5.30. It shows the profile of the heat capacity below 1400°K.

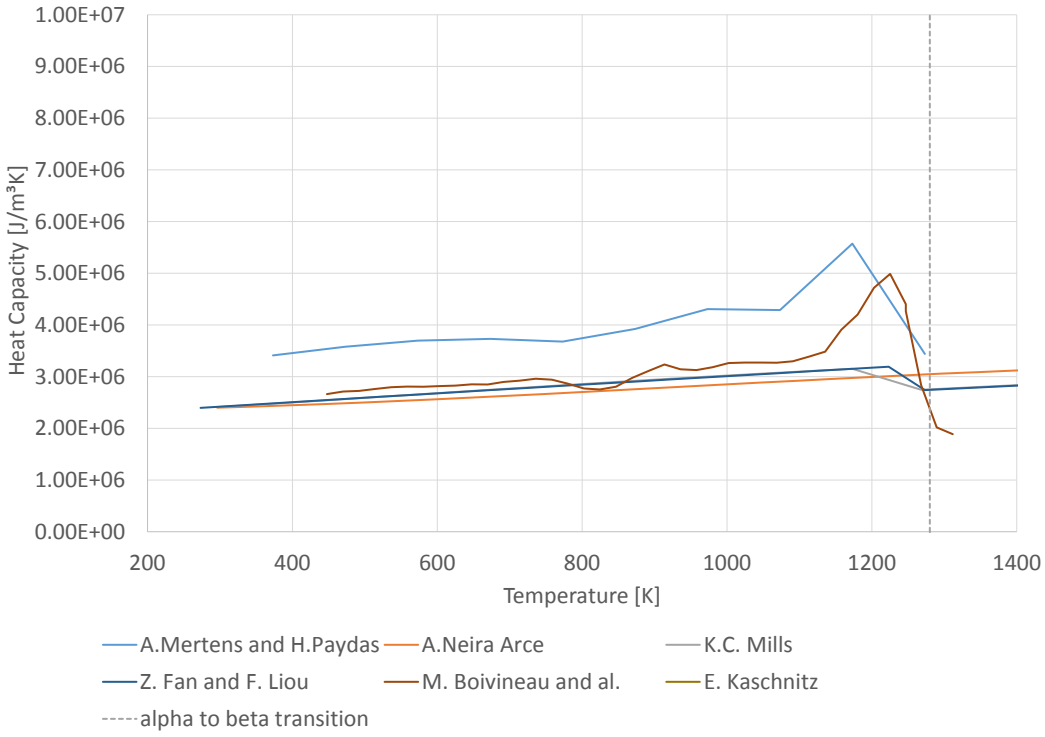

Figure 5.30: Apparent heat capacity of Ti6Al4V. Zoom below 1400°K. [38][43][41][17][5][27]

The heat capacity chosen for our model is the one proposed by Z.Fan and F.Liou, based on the initial data of K.C. Mills. This analysis once again provides data for a wide range of temperatures with a good coherence with the other heat capacity models.

Emissivity

The emissivity of a material is a dimensionless number that characterises its capacity to transfer heat by thermal radiation. It is defined by the ratio between the energy radiated by the material and the heat radiated by an ideal black surface at the same temperature. Therefore, a black body has an emissivity of $\varepsilon = 1$ while any real material has an emissivity of $\varepsilon < 1$.

Different studies directly or indirectly relative to the emissivity of Ti6Al4V have been compared in order to select the most appropriate value for our model. The most relevant will be briefly explained and a graphical comparison of their findings will be presented. In the case of our model, the value proposed by A.Neira Arce[43] was used in our simulation.

A. Mohammadi in his study on incremental forming considered a value of 0.94[42]. Z.Fan and F.Liou[17], using data from T.Lips and B.Fritsche[33] have developed a polynomial function of temperature given by:

$$\varepsilon = 0,1536 + 1,8377.10^{-4}.(T(K) - 300) \tag{5.13}$$

A.Neira Arce gives different values according to the part of the piece studied. From 0.83 in the contact area to 0.4 at the melt pool for high temperatures[43]. M.Boivineau also provides some data for high temperatures starting at 0.4 at the fusion point and decreasing with increasing temperature [5]. M.Labudovic in his simulation of laser surface nitriding of Ti6Al4V, has used a different set of values for the emissivity[29]. Finally, J.Yhang experimentally measured a relatively steady emissivity with the temperature around 0.25 until 900°C, before drastically increasing to values close to 1 [66].

All the findings described here above are drawn and compared in Figure 5.31:

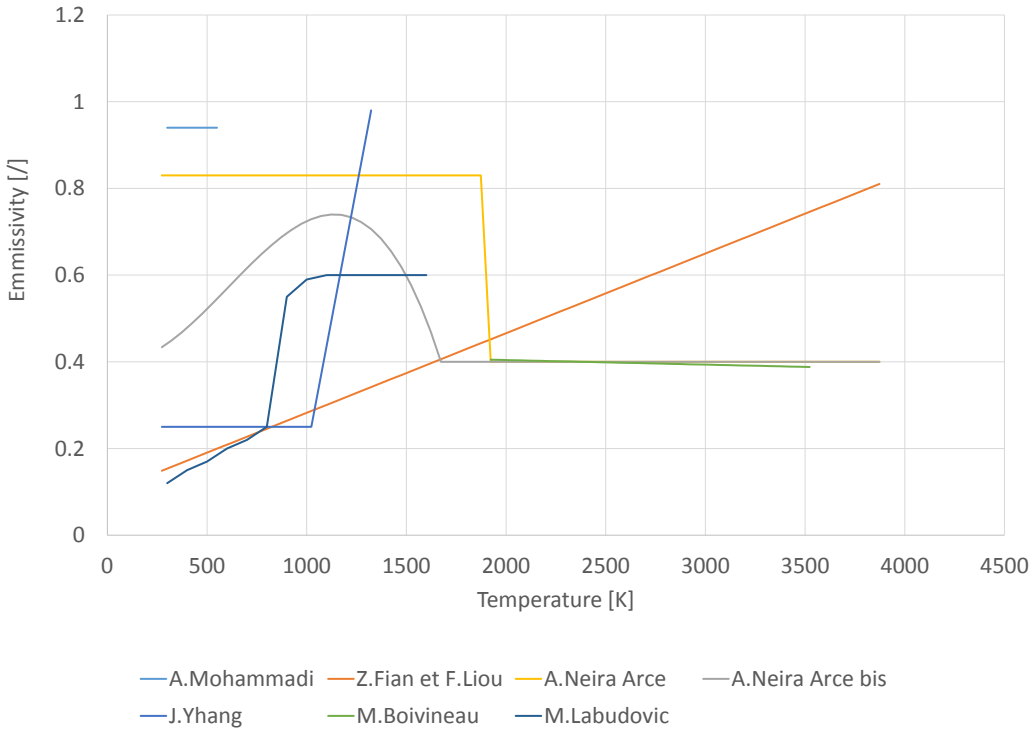

Figure 5.31: Emissivity - A graphical comparison of existing models. [42][17][43][5][29][66]

As can be seen, the various models and experimental measurements conducted provide rather different values for the emissivity. In the case of our model, it has been chosen to select the model of A.Neira Arce with a constant value of emissivity for the solid state at $\varepsilon = 0.83$ and another value for the liquid state at $\varepsilon = 0.4$. This simplistic model has the advantage of being easy to implement and is one of the most coherent with the other emissivity studies.

In our model, a radiation coefficient is entered instead of the emissivity. This radiation coefficient is obtained by multiplying the emissivity by the Stefan-Boltzmann constant:

$$r_c = \sigma.\varepsilon \quad [W.m^{-2}.K^{-4}] \tag{5.14}$$

with $\sigma = 5,670373.10^{-8} \quad [W.m^{-2}.K^{-4}]$, the Stefan-Boltzmann constant.

Convection coefficient

The convection coefficient of a material quantifies the heat transfer by convection. It is defined in $W.m^{-2}.K^{-1}$

Only a few studies about the convection coefficient are available for Ti6Al4V. One experimental study by A.Mohammadi providing values of h for a restricted range of temperatures (from 300 to 550°K.)[42]. In other articles detailing the numerical modelling of Ti6Al4V, the convection coefficient used in their simulation is given, without explanation of the origin of the value. Z.Fan and F.Liou[17] used $h = 10 \quad W.m^{-2}.K^{-1}$ and J.Yhang[66] used $h = 50 \quad W.m^{-2}.K^{-1}$. A comparison of the convection coefficient given in the different articles in presented in Figure 5.32.

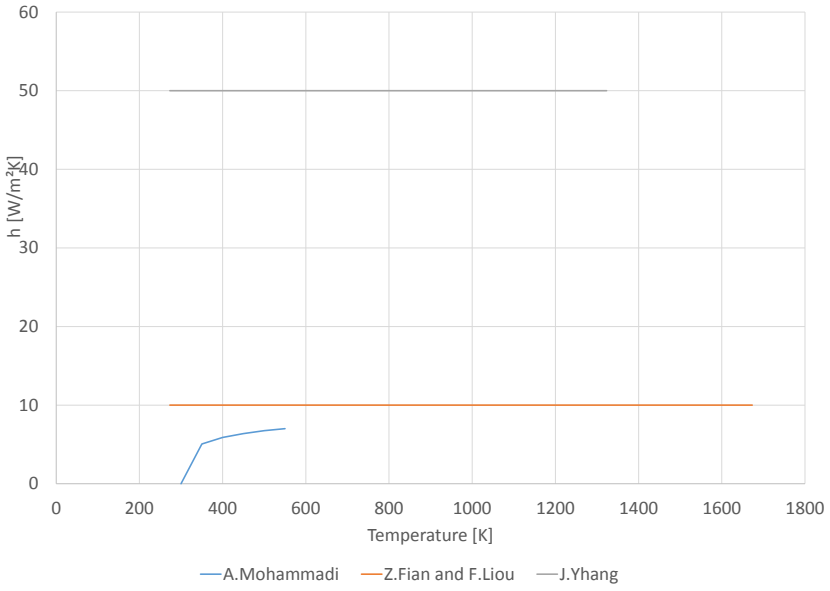

Figure 5.32: Convection coefficient h - A graphical comparison of existing models.[42][17][66]

The value proposed by Z.Fan and F.Liou will be used in our model. That is $h = 10 \quad W.m^{-2}.K^{-1}$. Several limitations linked to this choice of value for the convection coefficient will be stated in the limitations subsection hereafter.

5.4.2 Boundary conditions

In some studies[2], the boundary conditions imposed on the model includes heat transfer with the external world as well as the heat source representing the laser. As stated in section 5.3, the heat source will not be modelled as part of the boundary conditions. This is due to LAGAMINE file structure that made it easier to impose a flux to nodes rather than changing boundary conditions locally.

The boundary conditions as used in our model will thus consist of the heat exchange with the external world. It will be modelled through the CONRA element using the RACO law described here above[25]. The boundary able to exchange heat with the external world must then be defined. They are presented in Figure 5.33.

[25] As a reminder, the RACO law characterises the heat transfer between the solid and the external world by convection and radiation.

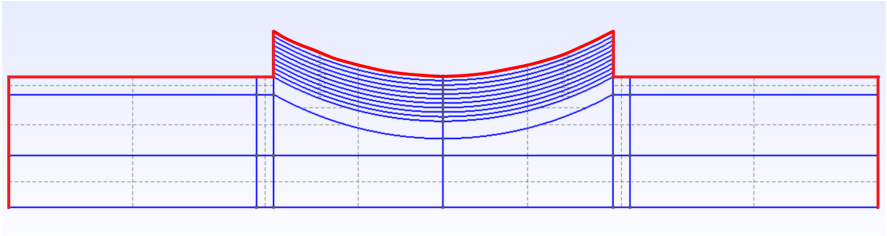

Figure 5.33: Boundary conditions application used in the model. Represented in red. The limitations of this approach are described hereafter.

In a first modelling attempt, it was assumed that a piece of insulator was situated under the work-piece, limiting the heat exchange on this surface to a negligible value. This was proven to not be the case in the real experiment. The difference in boundary conditions between the numerical model and the experimental conditions will be detailed in the limitations subsection. The means to overcome these limitations will be developed in chapter 7.

In 3-D modelling, the boundary conditions used in our model are similar to those used in the 2-D model, the difference is being that surfaces are used instead of lines. It is also important to note that heat exchange by convection and radiation on the lateral surfaces is taken into account in the 3-D model and not in the 2-D model. In the 2-D model, the cooling of the structure via convection and radiation on the lateral faces is neglected.

5.4.3 Limitations

The main limitations of our thermal model are of two kinds:

- A non-accurate value for the convection coefficient h.

- A difference in the boundary conditions used in the numerical model and in the experimental conditions.

The first limitation can be explained as such: the literature on convection coefficient of Ti6Al4V is limited and unable to properly represent our experimental conditions. The convection coefficients were all given for a Ti6Al4V-Air contact surface while most of the cladding operations in our case are performed under an argon atmosphere. The speed of the gas flux also plays an important role in the value of the convection coefficient and was not considered in the case of our modelling. In the experimental conditions, an argon forced flux is applied near the cladding area. This flux allows the cladding operation to be done under a controlled atmosphere and helps quickly cool down the melt pool. Such a flux was not modelled in this simulation. Due to the argon forced flux at the laser alone, at other points of the work-piece, there is no longer an argon but an air atmosphere. Ideas to model the resulting complex heat transfer by convection will be stated in chapter 7.

The boundary conditions used in our model do not efficiently represent the experimental conditions. Indeed, in the numerical model, the hypothesis made was that the work-piece was lying on an insulator piece. In fact, it was discovered during an exchange with the team from Sirris that the piece was held in the air by two metallic supports as represented in Figure A.36. This implies three major underestimations of heat transfer with the external world:

1. There is a flux of air under the work-piece that should be modelled with CONRA elements and RACO law. The heat transfer under the work-piece by convection and radiation is currently not modelled.

2. In the 2-D model, convection and radiation transfer through the lateral faces are not considered.
3. There is heat transfer by conduction happening in the metal pieces holding the work-piece in the air. Due to the high conductivity of the metallic pieces, this heat transfer by conduction should not have been neglected.

Unfortunately, these limitations in the convection coefficient definition and boundary conditions were discovered too late in the course of this master's thesis to correct the model and perform the complete analysis again. The corrections to be applied to the model in order to improve its representation of the experimental conditions are listed in chapter 7 and a corrected version of the model is presented in A.7.

5.5 Mechanical law modelling

In this chapter, the different parameters used for the definition of the mechanical laws will be defined. In this model, laws will be used that are applicable both for the 2-D and the 3-D model and that can be coupled with the thermal laws defined here above. The appropriate law in LAGAMINE is ARBTH. It is an elasto-plastic constitutive law with thermal effects for solid elements at variable temperatures.

In the course of this master's thesis, however, since the goal is to produce a thermal model, the mechanical behaviour of Ti6Al4V will be reduced to its elastic state and will remain constant with temperature. Each node will be blocked in every direction and the stresses inside the material will not be studied. Setting up an accurate mechanical law will be needed in the case of a coupled thermal-mechanical model that will not be performed in this work. The parameters presented were selected after a bibliographical study and have already been implemented in the model.

5.5.1 Parameters definition

Thermal expansion coefficient

The thermal expansion coefficient measures the relative change in volume of a system when the temperature increases or decreases. The thermal expansion coefficient is given for a constant pressure. This coefficient is relevant both for solid and fluid states. In the case of the laser cladding model, Ti6Al4V is considered as an isotropic material, the thermal expansion coefficient will thus be equal in the different directions.

Two main definitions of the thermal expansion coefficient exist in literature and are: the classic thermal expansion coefficient α_c and the partial expansion coefficient α_p. The definition of these two parameters is given by C.Bouffioux [6] and is described in the appendix (A.3). In the appendix, it is also proven that LAGAMINE uses the partial expansion coefficient α_p. This should be kept in mind when looking for thermal expansion coefficient in literature. Here under, some studies determining the thermal expansion coefficient for Ti6Al4V are briefly explained and compared:

A.Mertens and H.Paydas have measured experimentally in [38] the thermal expansion coefficient of Ti6Al4V set up by laser cladding. The samples were heated at a rate of 20°C per 20 seconds from the ambient temperature to around 1000°C. The results in Figure 5.34 shows a change in the slope sign. Numerically, this will lead to some convergence problems when implementing such a law. Alternatively, P.Rangaswamy has conducted similar tests and arrives at

slightly different results[49].

R.Boyer and G.Welsh propose a wide range of relations between temperature and the thermal expansion coefficient. The value taken from this reference will be the average thermal expansion coefficient, given for the wider range of temperatures, that is $\alpha_p = 1,1.10^{-5} \quad [m.m^{-1}.K^{-1}]$[7]. In their model, Z.Fan and F.Liou use the same value[17][41]. Figure 5.34 shows a comparison of the different thermal expansion coefficient values given by existing models.

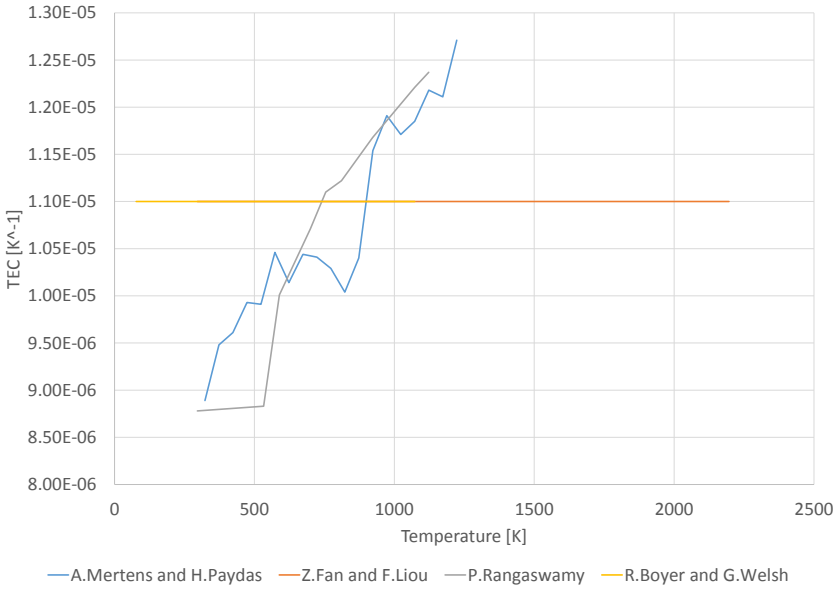

Figure 5.34: Thermal expansion coefficient - A graphical comparison of existing models[38][49][7][17].

In the light of this comparative study and for the sake of simplicity in the mechanical law parameters[26], a constant value of the thermal expansion coefficient will be chosen at $\alpha_p = 1,1.10^{-5} \quad [m.m^{-1}.K^{-1}]$ such in [7][17].

Youngs' modulus

Young's modulus or elasticity modulus is the constant that links stresses and strains in an elastic isotropic material. The hypothesis of an elastic isotropic material is made as in the case of this thermal model, a change in the Young's modulus has no effect on the results. Nevertheless, a comparative study was performed and the results are given hereafter:

R.Boyer and G.Welsh propose a decreasing value of Young's modulus with increasing temperature. The values are given in a range from -196°C to 800°C[7]. P.Rangaswamy also propose a decreasing value of the Young's modulus with increasing temperature. In his model, the Young's modulus becomes as small as 5 GPa for a temperature of 1123°K. On the other hand, Z.Fan et F.Liou use a constant value of the Young's modulus equal to 113,8 GPa. This value is supposed constant with time until the liquidus temperature of the alloy. A comparison of these values is given in Figure 5.35.

[26]These parameters have no effect on the current model since at this stage we are only interested in a thermal analysis of the laser cladding process

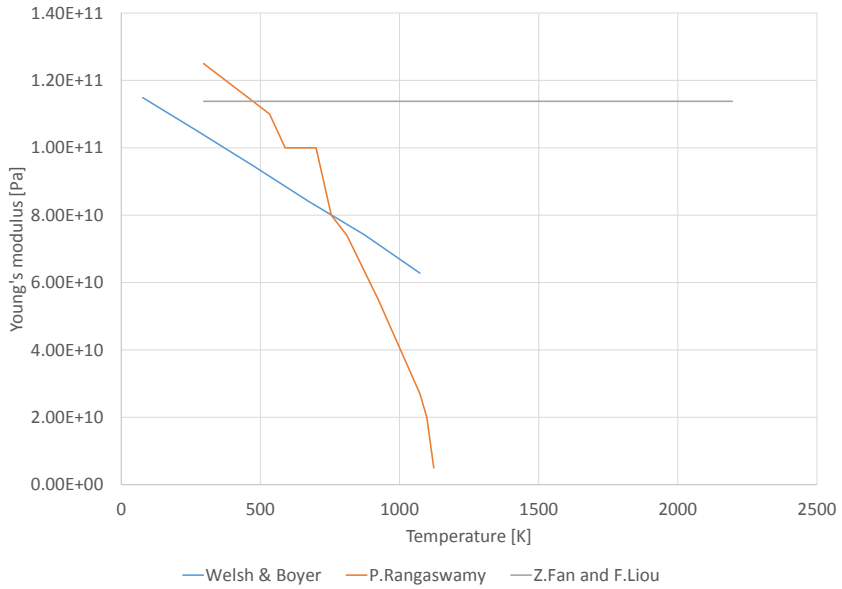

Figure 5.35: Young's modulus - A graphical comparison of existing models. [49][7][17].

For the sake of simplicity, the value proposed by Z.Fan et F.Liou (113,8 GPa) was chosen and applied for the complete range of temperatures considered. That is from ambient temperature (293°K) to the evaporation temperature of TA6V (3533°K). This simplification would not be accurate in the case of a coupled mechanical and thermal model, however, in the case of our purely thermal model, the Young's modulus value does not impact the results.

If a coupled thermal and mechanical model was to be built, a decreasing value of the Young's modulus should be chosen to better represent the behaviour of the material. Beyond the liquidus temperature (1923°K), one way to model the material without switching to a liquid modelling phase would be to reduce the Young's modulus to a low value in order to allow the material to undergo the large strain caused by the thermal variation without reaching the yield criteria. Such a detailed modelling of the Young's modulus will not be performed in this work. Information can be found in literature [44].

Poisson coefficient

The Poisson's coefficient characterises the expansion (respectively reduction) of the material in the directions perpendicular to the applied compression (respectively traction). It is given by:

$$\nu = -\left(\frac{d\varepsilon_{transversal}}{d\varepsilon_{axial}}\right) \tag{5.15}$$

Where $d\varepsilon_{transversal}$ is the strain in the transversal direction and $d\varepsilon_{axial}$ is the strain in the axial direction, that is parallel to the force applied.

In literature, the value of Poisson's coefficient for Ti6Al4V varies slightly with temperature[7]. However, this property will be neglected and a unique value of the Poisson's coefficient will be considered, for the entire range of the simulation. Different values are presented in literature, from $\nu = 0.23$ proposed by R.Boyer[7], $\nu = 0.31$ by P.Rangaswamy[49] or $\nu = 0.342$ by ASM[26].

In the course of this model, the value proposed by R.Boyer will be used, that is $\nu = 0.23$. If a thermal-mechanical model is considered, in order to represent the low compressibility of molten Ti6Al4V, the value of the Poisson coefficient ν should be set at 0,5 when Ti6Al4V is in its liquid phase[44].

5.5.2 Limitations

The limitations of the mechanical laws and properties described in this chapter are numerous:

1. Ti6Al4V has been assumed as an isotropic material. The impact of anisotropy on the mechanical behaviour of Ti6Al4V have been studied by V.Tuninetti and A.M.Habraken[59].

2. For the different parameters given, single value was applied across the whole temperature range. This is a important hypothesis that will greatly impact the quality of the results in the case of a coupled thermal-mechanical model.

3. Only a continuous solid phase has been considered for the temperature range from 293°K to 3533°K. The liquid phase starting at 1923°K is therefore neglected in the parameters definition. In order to properly model the behaviour of molten Ti6Al4V, the model should be coupled with a fluid model for the liquid phase. In order to avoid this level of complexity, an approximation would be to model the fluid by changing the solid parameters (low Young's modulus, incompressibility of the Ti6Al4V fluid, etc.). Such a modelling is presented by F.Pascon[44].

4. The hypothesis that Ti6Al4V is infinitely elastic was made. In a proper mechanical or coupled model, the yield criteria should be defined as well.

In the case of this master's thesis, however, as this model is purely thermal, the limitations stated here above have little impact on the results obtained.

5.6 Activation of element modelling

In order to represent the cladding of new materials during the simulation, the model will include the activation of elements. This is made possible in LAGAMINE by the use of the sub-routine "Switch". When elements are deactivated, their stresses and stiffness matrix terms are set to zero. The elements will be activated to simulate the cladding of new layers.

The idea behind the activation of an element is straightforward: as the heat flux moves along the work-piece, elements are activated and the heat flux is applied on the newly activated element. The elements are activated slightly before the heat flux application to avoid the application of the flux on a deactivated node. In order to improve the convergence of the code, the elements will be activated one time-step before the flux is applied to them. Figure 5.36 illustrates this strategy.

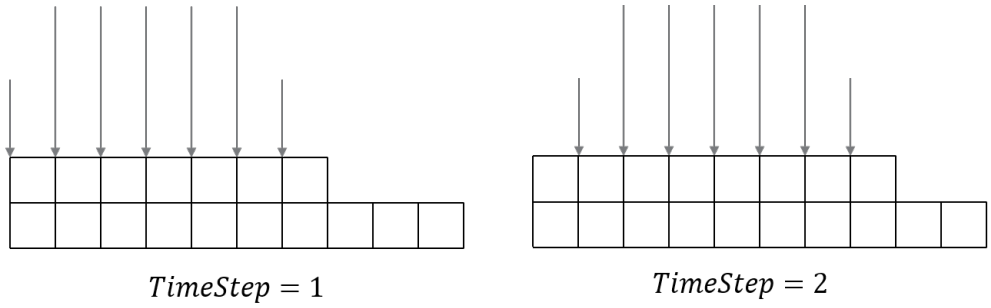

Figure 5.36: Flux application and element activation for the first two time-steps.

The routine used in the LAGAMINE code consists of a definition of the time intervals, for which an activation/deactivation will occur, followed by a list of nodes to be activated or deactivated. A *Matlab* routine has been written to create a "Switch" input file for the different models: 2-D or 3-D, single or multi-pass. Several modifications of the LAGAMINE source code have been made to allow the activation of the elements to a much larger extend than it was originally designed for. Among these changes, the number of time steps for which an activation is possible has been increased. The changes in the source code were performed by G.Gilles.

Two different strategies are used to model the activation of elements. The activation of elements as the heat flux moves along the surface of the work-piece is the most accurate way to represent the printing of new material. It will be later referred to as the element-by-element activation strategy. Nevertheless, as the number of layers or passes to print increases, the file becomes overly complex and reached several LAGAMINE limitations[27], which were later overcome. An alternative is to activate the elements by pass or by layer for the 3-D and 2-D cases respectively. That is, in the 2-D case, when a layer of material has been printed, a second layer of the element is activated and so on. This will later be referred to as the layer-by-layer activation strategy. This simplified method has two main advantages:

- It allows the use of element activation for a large number of layers, despite LAGAMINE former inherent limitations.
- It decreases the computation time of the code.

With one main drawback:

The temperature profile observed with a layer-by-layer activation strategy is different than the one observed with an element-by-element strategy. The difference between these two methods is highlighted in Figure 5.37 that shows the temperature profile at the thermocouple using both strategies for the printing of one layer.

[27] The maximum number of time intervals that can be defined was 150 before code modification.

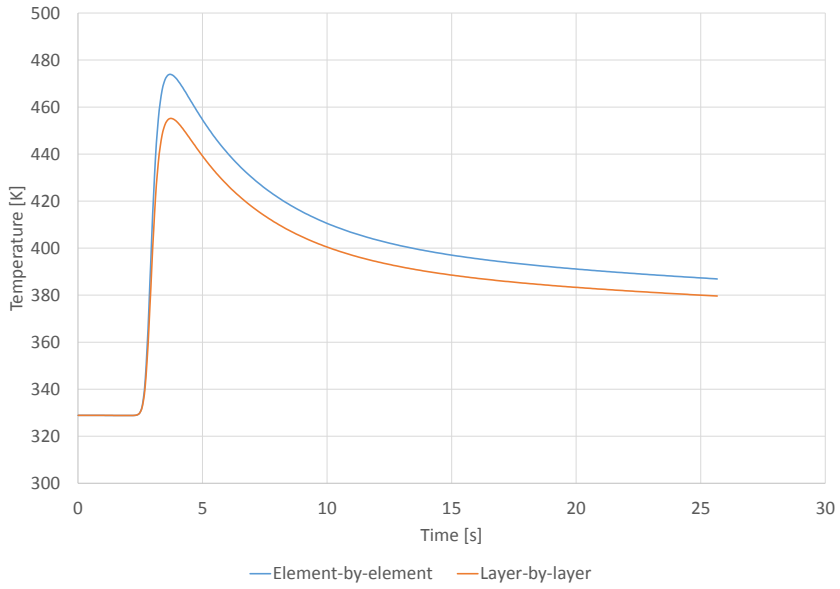

Figure 5.37: Difference in the temperature profile at the thermocouple observed with the two activation strategies

This difference can be quantified by: $\varepsilon_{max} = 4.08\%$ and $\varepsilon_{mean} = 1.83\%$

In a first approach, the layer-by-layer strategy will be used for the simulations. The results and the calibrations were done using this simplified activation strategy. To refine the model, it is necessary to perform a proper element-by-element activation strategy. Now that the LAGAMINE limitations have been overcome, the element-by-element strategy can be applied to the most complex model, that is the 2-D simulation with 10 layers or the 3-D simulation with 2 passes. An element-by-element activation code has been developed for those complex cases with the help of Tran Hoang Son.

Another issue with the activation of elements comes from the thermal effect induced when activating elements at their initial temperature on a heated surface. It creates an inverted flux, from the substrate to the surface that is not coherent with reality. In the case of a layer-by-layer activation strategy, this phenomenon is clearly visible on the temperature profile near the surface. When the next layer is activated, at an initial temperature, an exchange of temperature occurs with the previously heated layer. Such a phenomenon is highlighted in Figure 5.38, that represents the temperature profile at the top of layer one (Figure 5.39).

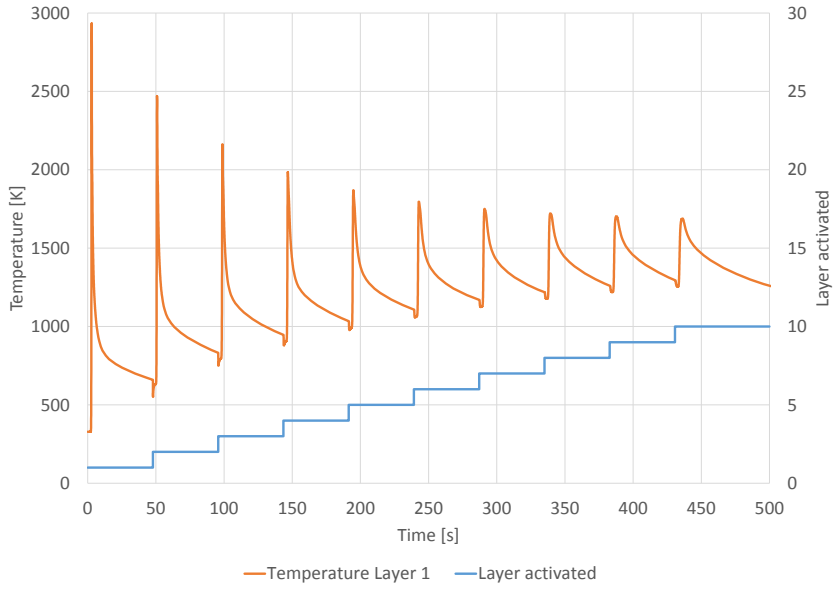

Figure 5.38: Temperature profile at the top of layer one (Figure 5.39) affected by layer activation

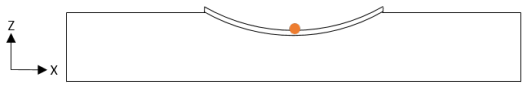

Figure 5.39: Top of layer one - middle of the work-piece, 2-D

As we can see on Figure 5.38, every time a new layer is activated, the temperature at the top of layer one decreases. It is especially marked in the activation of the second and third layers, where the heat flux from layer one to the newly activated layers is the highest. Potential solutions to solve this issue are presented in the perspectives (chapter 7).

5.7 Calibration of the model

The calibration of the model is a decisive step in the model building process. The main parameter that will vary to best fit the model to the experimental results will be the power of the flux applied. As referred to in section 5.3, the power of the laser is known, however, the proportion of the laser's power that is actually absorbed by the work-piece remains uncertain.

To perform the calibration, it is important to rely on consistent experimental data. This data is given by the temperature profile at the thermocouple (Figure 5.5). With a 2-D model, it is not possible to represent this thermocouple, located at the middle of the work-piece, 2 mm under the cup as described in Figure 5.4. When using a 2-D model, the peaks for the first passes are always too steep, because there is no heat conduction along the Y axis[28].

In order to better represent the heat transfer within the full 3-D work-piece, it is therefore necessary to perform the calibration of the heat flux on a 3-D numerical model[29].

[28]The calibration attempt of the 2-D model is presented in Figure 5.13. As can be seen in Figure 5.13, when printing one layer of elements, the peak obtained at the thermocouple in a 2-D model is too steep.
[29]Such a model was developed and presented in section 5.2.

In this 3-D calibration, the flux applied in the numerical model is modified until obtaining the same maximum temperature[30] at the thermocouple for the cladding of the first layer. The profile of the curve will also be studied. The cladding of a second layer was then added to check the coherence of the calibration. This operation is detailed in subsection 5.7.1

A correction was then performed to transfer from the 3-D to the 2-D model. As all heat transfer effects are not simulated in the 2-D model, the flux obtained in the calibration of the 3-D model cannot be used as such. A correction factor (f_{flux}) is thus determined to apply to the 3-D flux obtained by the calibration. The value of this correction factor will be determined by making the hypothesis of a similar maximal temperature in the melt pool in both the 2-D and the 3-D models. This operation is detailed in the subsection 5.7.2

The two calibration steps described hereafter will be performed with a constant track length strategy. The limitations of this calibration method will be listed and possible solutions to overcomes them will be proposed.

5.7.1 Calibration of the 3-D model

The objective of this calibration is to obtain numerically, at the thermocouple, the same first peak[31] of temperature (Figure 5.5) between the numerical model and experimental results. The initial temperature in the work-piece was set at a uniform value in the numerical model, equal to the temperature at the thermocouple, just before the start of the cladding. That is $T_0 = 328,89°\text{K}$. This hypothesis and its implications are discussed in subsection 5.7.3.

The simulation of the cladding of one pass is then performed with various flux values, as described in the subsection 5.3.4. The different values tested and the corresponding absorptivity coefficient are given in Table A.1. For those different values of the applied flux, we look at the maximum temperature observed at the thermocouple. These points are graphically represented on an applied flux - maximum temperature graph presented in Figure 5.40.

[30] That is the same value as the one obtained by the experimental study performed by H.Paydas [46].

[31] The first peak of temperature is due to the cladding of the first pass

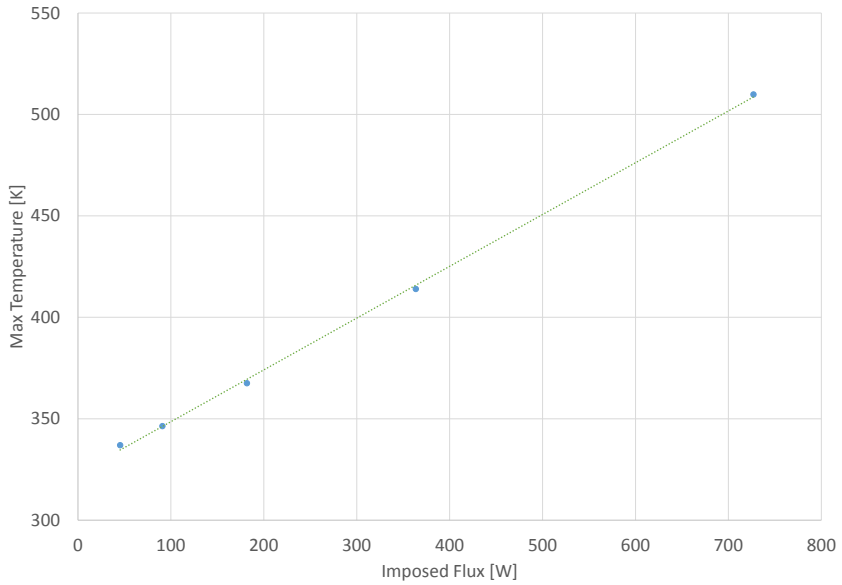

Figure 5.40: Maximum temperature observed at the thermocouple after the cladding of one pass for different values of imposed flux.

A linear correlation is observed with the different results. The corresponding coefficient being $R^2 = 0.999$. By using the equation of the corresponding line and knowing the maximum temperature observed experimentally at the thermocouple, we find:

$$T_{Max} = 0,2553.Flux_{imposed} + 323,02 \tag{5.16}$$

$$T_{Max,experimental} = 416 \quad [K] \tag{5.17}$$

$$\Rightarrow Flux_{imposed} = \frac{1}{0,2553}(T_{Max,experimental} - 323,02) = 363,5 \quad [W] \tag{5.18}$$

This flux value, as described in section5.3, corresponds to an absorptivity coefficient $\beta = 0.33$. The characteristics of the calibrated flux are synthesised in Table 5.6.

Table 5.6: Calibrated Flux details

Nominal Laser Flux [W]	1100
Calibrated Applied Flux [W]	363,5
Calibrated Applied Flux [MW/m^2]	57,7
Absorptivity Coefficient β	0,33
Absorptivity Coefficient β in literature[17][66]	0,34-0,4

As described in Table 5.6, given the nominal power of the laser and the value of the calibrated applied flux, a value for the absorptivity coefficient β can be determined. The use of this coefficient is extensively described in section 5.3. The value numerically obtain is $\beta = 0.33$. This value is coherent with the value for the absorptivity coefficient used in other numerical models of laser cladding. Z.Fan and F.Liou [17] use a value of $\beta = 0,4$ while J.Yang and al. [66] use a value of $\beta = 0,34$.

The calibration of the flux was performed using the maximum temperature after the cladding of one pass. The temperature profile during the cladding of this pass is also studied. The

temperature profile at the thermocouple is provided in Figure 5.41. It is compared to the experimental value.

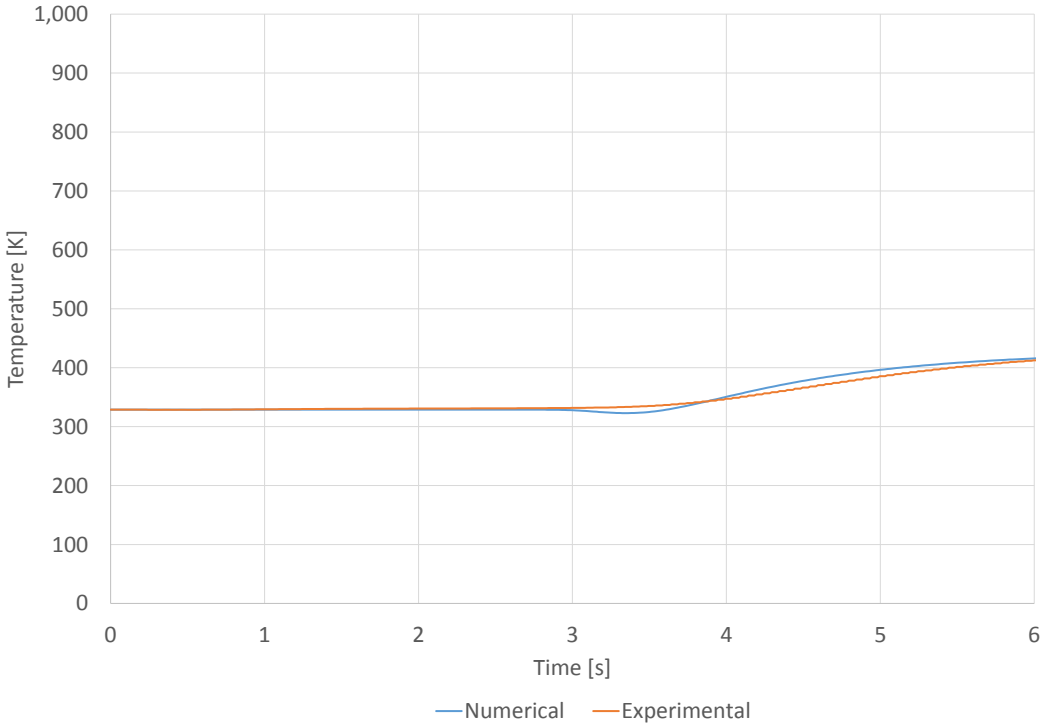

Figure 5.41: Temperature profile at the thermocouple. Comparison of the experimental and numerical results - One pass clad

The difference between the curves can be quantified, with a maximum relative difference of 4,8% and a mean relative difference of 1,33%. An oscillation is also visible before the increase in temperature and is explained in the section 5.2. Despite those two differences, the numerical curves fit well with the experimental results and the calibration will be accepted for the printing of one pass.

It is also useful to simulate the cladding of the second pass to see if the results remain accurate. The results for the cladding of a second pass are provided in Figure 5.42 with information on which pass is being clad.

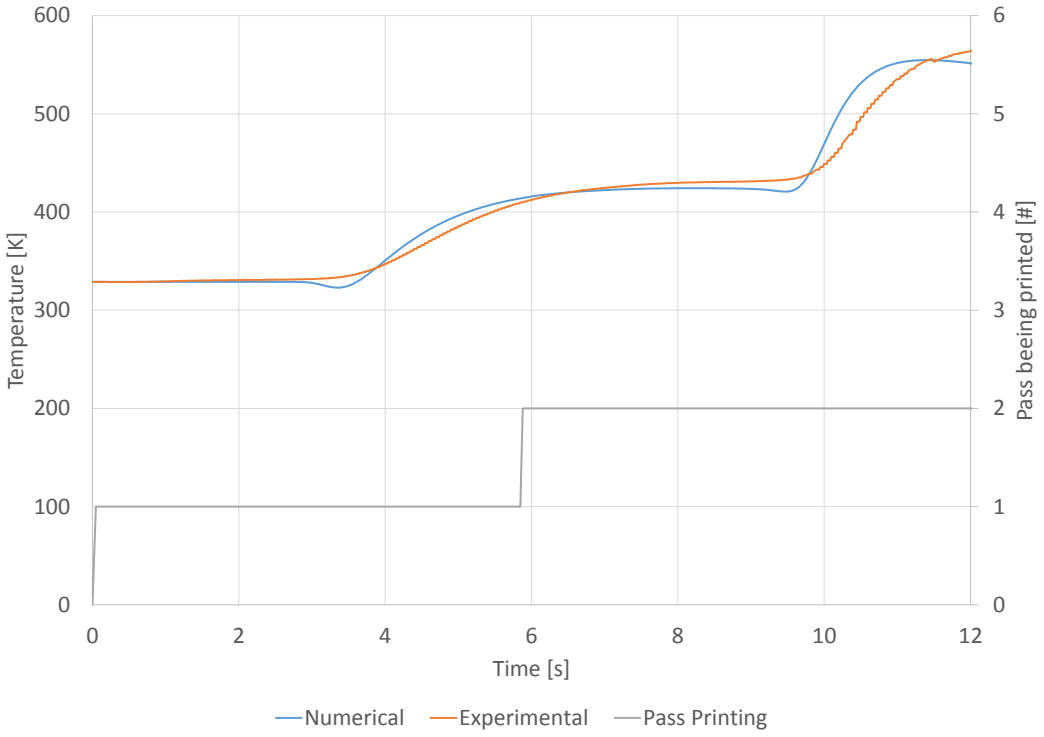

Figure 5.42: Temperature profile at the thermocouple. Comparison of the experimental and numerical results - two passes clad

The takeaways of this "two-passes" simulation are the following: firstly the temperature profile is different between the experimental and numerical results, the numerical curves being much steeper than the experimental ones. Secondly, the difference between the two curves, for both the mean and the maximum values, is bigger than for the cladding of one pass. The maximum relative difference is 8,9% when the mean relative difference is 1,5%. The difference between the numerical and experimental results for the one and two passes models are synthesised in Table 5.7.

Table 5.7: Difference between numerical and experimental results - Temperature profile at the thermocouple analysis.

	One pass simulation	Two passes simulation
Mean relative difference [%]	1,3	1,5
Maximum relative difference [%]	4,8	8,9

This issue of having a less representative model for the cladding of the second pass, and potentially the following ones, will be discussed in section 5.7.3.

5.7.2 From 3-D to 2-D

The flux calibrated in section 5.7.1 cannot be used as such on the 2-D model. Thermal effects such as 3-D conduction in the piece, convection and radiation on certain surfaces (see section 5.4.2) are not considered. In 2-D, the heat source is applied in a way such that the thermal behaviour in the piece is the same across the whole width. Therefore, a correction factor must be applied on the 3-D flux to be used in the 2-D model. To determine this correction factor, we make the hypothesis that the temperature in the melt-pool is the same in the 3-D and 2-D model, when subjected to the laser flux. The maximum temperature at the top of pass one and

layer one will be considered respectively for the 3-D and 2-D models as described in Figure 5.43 and 5.44.

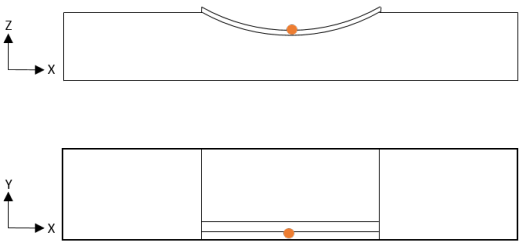

Figure 5.43: Top of pass one - 3-D model

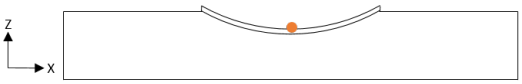

Figure 5.44: Top of layer one - 2-D model

The passage from 3-D to 2-D will thus consist of the definition of a correction factor f_{flux} such as:

$$Flux_{imposed,2D} \quad [W/m^2] = Flux_{imposed,3D} \quad [W/m^2].f_{flux} \tag{5.19}$$

This dimensionless factor f_{flux} will be most likely larger than 1, as in 3-D, the conduction along the Y-Axis tends to decrease the temperature in the melt-pool faster than in the 2-D model. To define the correction factor f_{flux}, the maximum temperature in the melt-pool observed with the 2-D model with different values of f_{flux} will be compared to the maximum temperature in the melt-pool observed with the 3-D model. Those results are presented on Figure 5.45.

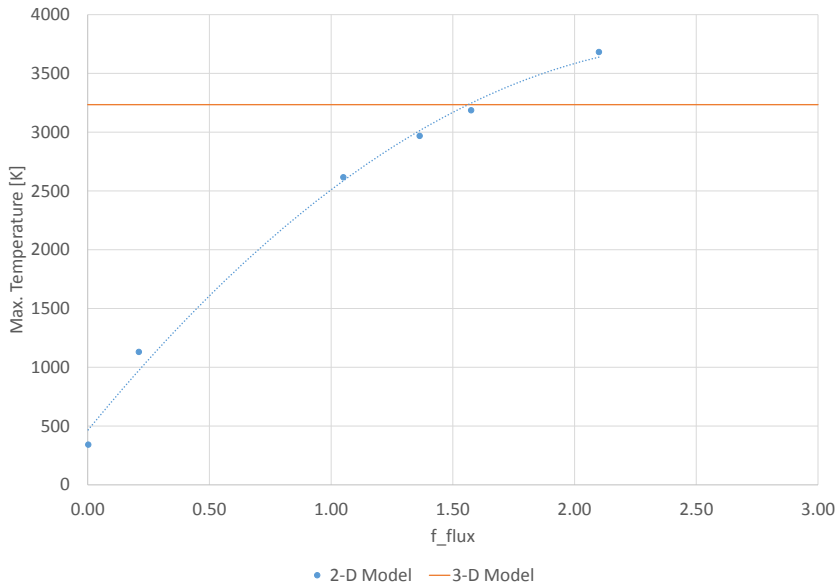

Figure 5.45: Max temperature obtained in the melt-pool for different f_{flux} correction factors, 2-D model. Comparison with results of the 3-D model.

Where the horizontal line represents the maximum temperature observed in the melt pool with the 3-D model. The points on the graph represent the different couples f_{flux} -max. temperature observed in the melt pool with the 2-D model. Each point corresponds to one simulation performed with another f_{flux} correction factor. The summary of theses simulations is presented in table 5.8.

Table 5.8: Maximum temperature observed in the melt-pool with various values of f_{flux} - 2-D model

f_{flux}	Max.Temperature [°K]
0,002	342
0,210	1130
1,050	2616
1,364	2968
1,575	3182
2,100	3682

The most precise maximum temperature of the melt-pool for the 3-D model is the one resulting from the 3-D simulation with an element-by-element activation strategy (See section 5.6). The temperature obtained with this model is given by 3234,32°K. By interpolating the value obtained for different values of the correction factor f_{flux}, we can find the intersection with this temperature. as follows:

$$T_{Max,2D} = -468,38.f_{flux}^2 + 2533,6.f_{flux} + 562,56 \tag{5.20}$$

$$T_{Max,2D} = T_{Max,3D} = 3234,32 \quad K \tag{5.21}$$

$$\Rightarrow f_{flux} = 1,435^{32} \quad [/] \tag{5.22}$$

Since the flux is applied on the nodes and the 2-D model is defined for a unitary depth, a geometrical factor must also be applied in order to have the same surface value [W/m^2]. This means that the surface flux applied in 2-D and 3-D must be equivalent after having taken into account the correction factor f_{flux}. In order to keep coherent surface flux [W/m^2], the flux applied per node [W/node] must be multiplied by a factor f_geo. Starting from equation 5.19 we obtain:

$$Flux_{imposed,2D} \quad [W/m^2] = Flux_{imposed,3D} \quad [W/m^2].f_{flux} \tag{5.23}$$

$$\Leftrightarrow Flux_{imposed,2D} \quad [W/node] = Flux_{imposed,3D} \quad [W/node].f_{flux}.f_{geo} \tag{5.24}$$

with f_{geo} such that:

$$f_{geo} = \frac{Surface_{element,2-D} \quad [m^2]}{Surface_{element,3-D} \quad [m^2]} = \frac{250.10^{-6}.1}{2100.10^{-6}.250.10^{-6}} = 476,19 \quad [/] \tag{5.25}$$

Different characteristics have been neglected when transitioning from the 3-D to the 2-D model. These characteristics will be developed along with their potential solutions in the following subsection (5.7.3).

5.7.3 Limitations

The calibration stage, as performed for this master's thesis, has two major limitations:

1. **Initial temperature set up**. The initial temperature is set uniform in the whole work-piece, equal to the temperature at the thermocouple before the beginning of the cladding phase. This is an approximation since the work-piece was not uniformly pre-heated. Different strategies of pre-heating exist: using the laser for a short time period, the use of an oven or the use of induction heating. Depending on the type of pre-heating used, the temperature distribution will

[32] The other solution of this quadratic equation (4) is excluded for not being realistic according to Figure 5.45

vary but in none of the pre-heating strategies is the temperature constant in the whole work-piece. The influence of the initial temperature and the different methods to simulate it in our current model will be detailed in section 6.5.

2. **One pass represented.** In the 2-D model, only the impact of the different layers is considered as if they were printed in one pass. In the cladding process however, a layer is made up of 8 layers in order to fill the cavity on the whole horizontal surface. The 2-D model is based on the approach that one pass is done per layer. The temperature profile in the work-piece is therefore not precisely represented in the model. For example, an analysis of the temperature profile at the thermocouple equivalent in 2-D is presented in (Figure 5.46).

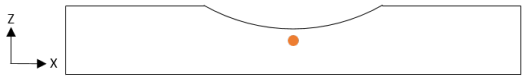

Figure 5.46: Equivalent position of the thermocouple in the 2-D simulation.

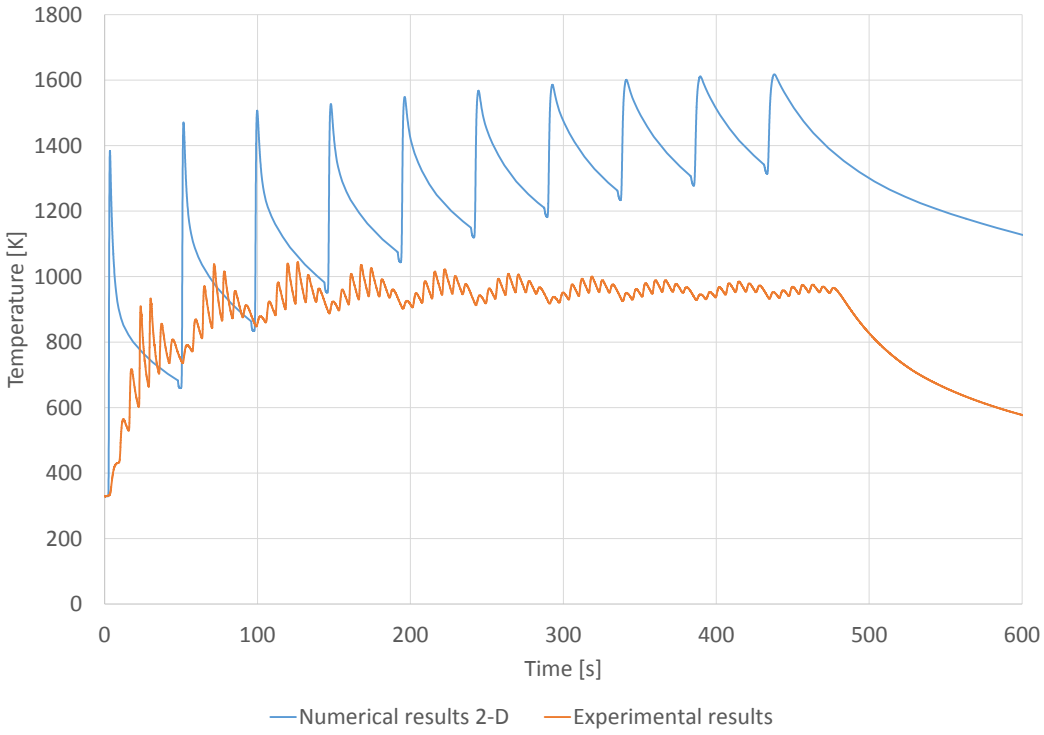

Figure 5.47: Temperature profile at the equivalent 2-D thermocouple

Figure 5.47 highlights this limitation. When compared to Figure 5.5, we can clearly see that the group of peaks representing the cladding of one layer have been replaced by one single peak in the 2-D model. Furthermore, the absolute values of temperature are significantly higher in the equivalent 2-D thermocouple than in the experimental thermocouple. Meaning the global equilibrium between energy entering and leaving the work-piece is not obtained similarly for the numerical and experimental results, with values of the temperature up to 60% higher. The high difference of temperature at the thermocouple, when printing a large number of layers (≥ 3), can be explained by an underestimation of the convection coefficient and an inaccurate descrip-

tion of the boundary conditions[33]. The 2-D model as it is now, calibrated for the temperature in the melt-pool, is thus unable to represent the temperature profile deeper inside the work-piece.

This is a strong limitation that impacts the accuracy of the thermal results to characterise the resulting mechanical stresses or the micro-structure.

3. **3-D calibration for the first pass**. As seen in the calibration of the 3-D model, the calibration was performed based on the maximum temperature at the end of the cladding of the first pass. Even for that first pass, the temperature profile was slightly different (See Table 5.7.) For the second pass, the difference between the numerical and experimental model keeps on increasing. Simulations have not been performed for more than two passes, however, it is possible that the difference will keep on increasing.

Nevertheless, the current model, with its inaccuracies, is used to produce the results presented in Section 6. Solutions to the current limitations will be given in chapter 7.

5.8 Validation of the model

The designed model was tested on another experiment in order to assess its efficiency for the modelling of the laser cladding process.

In order to keep the value of flux obtained by the calibration, it is decided to keep an experiment with the same laser beam (Nd:Yag Macroclad of Sirris.) and the same substrate geometry. The second experiment, as described in [46], uses a decreasing track length strategy to refill the cup of the substrate, as opposed to a constant track length strategy for the calibration case. The finished clad pieces for both building strategies are presented in Figure 5.1.

In this chapter, the new building strategy will be presented, as well as the changes performed on the activation of elements and the heat flux application in order to fit the new building strategy. The consistency of the results will be briefly presented[34]. Finally, the limitations corresponding to that model will be stated and described, along with the solutions to overcome them.

5.8.1 Changes in the model

New geometry. Both the geometry of the substrate and the mesh remain the same for both experiments. By keeping the same meshing, it is possible to keep the same node and element numbering than for the constant track length strategy (CTL). This reasoning will be carried forward for to the geometry of the cladding region. The geometry designed for the constant track length strategy, as described in Figure 5.7 will be kept as such. Element that are never active, in the decreasing track length strategy (DTL), will remain permanently deactivated.

Permanently deactivated elements are determined following the idea that the level (along axis Y) of the clad material should not be lower than the the level of the substrate, assuming that the decrease in the length of the clad is constant[35]. Given these two key hypotheses and the precision of the mesh, unchanged compared to the calibration model, we find that the track length should be decreased at every layer of 8 elements[36], that is 2 mm along the X axis of length

[33] Respectively discussed in section 5.4 and section 5.4.2.
[34] A complete analysis of results with both building strategies is presented in chapter 6.
[35] This hypothesis will be challenged in section 5.8.3.
[36] Four elements, or 1 mm on both sides

reduction.

The obtained geometry is presented in Figure 5.48, with the previous constant track length (CTL) configuration in the background. Figure 5.49 shows the isolated decreasing track length (DTL) configuration.

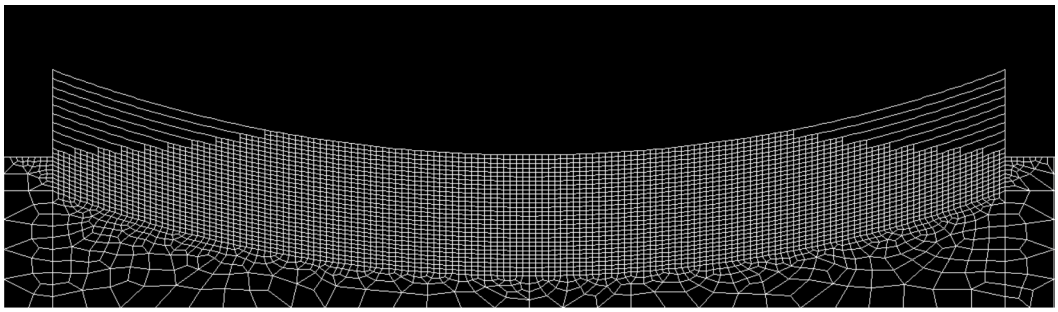

Figure 5.48: DTL vs. CTL geometry

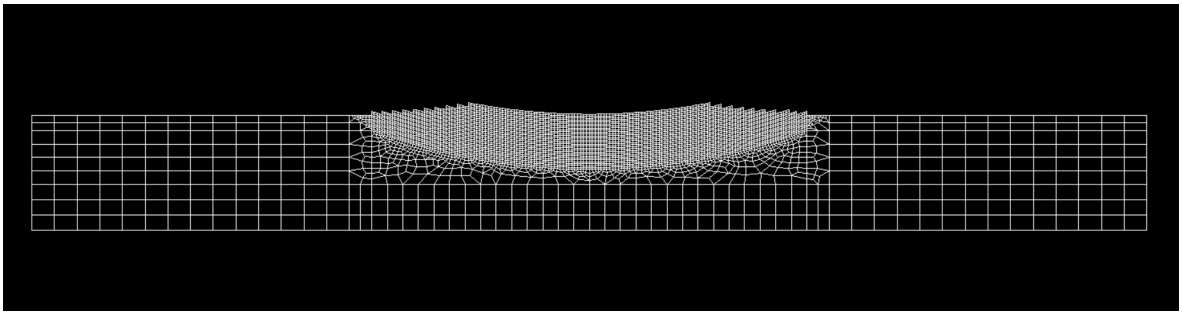

Figure 5.49: Isolated decreasing track length geometry and mesh

New activation of elements strategy: The activation strategy has been modified to take into account the permanently deactivated elements. A layer-by-layer activation strategy is used as was the case for the constant track length strategy. An element-by-element strategy, developed for the constant track length strategy but not yet properly applied, can be fitted to the validation model with a few modifications. The new .SWI file in LAGAMINE, containing the activation strategy is made more complex by the permanent deactivation of elements.

New heat flux application: The heat flux application is modified. Firstly, the list of the nodes on which the flux is applied is modified and reduced for the printing of each layer compared to the constant track length strategy. The timing is also reduced. Based on the laser history properties, we are able to determine the time taken for the printing of each layer of clad, as presented in Table 5.9.

Table 5.9: Cladding time of the different layers based on laser data. decreasing track length strategy

Layer	Cladding time[37] [s]
1	47,86
2	45,08
3	42,19
4	39,14
5	35,92
6	32,43
7	28,59
8	24,17
9	18,66
10	10,00

In the the constant track length strategy, the time required by the laser to perform the cladding of one layer and re-position for the next one was constant at 47,86 s.

The other factors described in section 5.3, such as the laser intensity, beam shape or speed, remain unchanged. A *Matlab* routine has been developed to produce the loading file used in LAGAMINE (.LOA file) specific to this case.

5.8.2 Consistency of results

Two results will be studied in this section, in order to check if the model produces valid results with the decreasing track length building strategy. The other results, such as the depth of the melt-pool or micro-structure prediction analysis will be later studied in chapter 6. The two results studied hereafter are the temperature obtained in the melt-pool and the temperature profile at the thermocouple. These two results should be consistent with the calibration model results described respectively in Figure A.11 and Figure 5.47.

The temperature at the melt-pool, if we look at a the middle of the last layer clad (Figure 5.39, shows a similar profile to the melt-pool obtained for the constant track length simulation. The space between the temperature peaks is naturally smaller as the time between the cladding of successive layers is reduced. The temperature profile at the middle of the last layer clad is presented for both strategies in Figure 5.50.

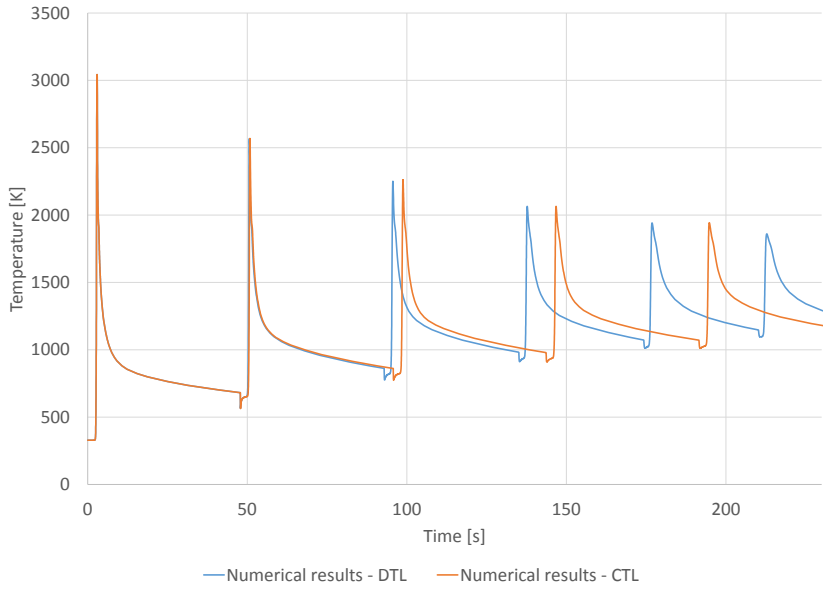

Figure 5.50: Numerical temperature profile in the melt-pool for 5 passes - CTL and DTL

The temperature profile at the thermocouple can also be studied and compared to the experimental data, as done in section 5.7.3 for the constant track length strategy. Similarly for the decreasing track length strategy, we find a significant difference between the two curves as shown in Figure 5.51.

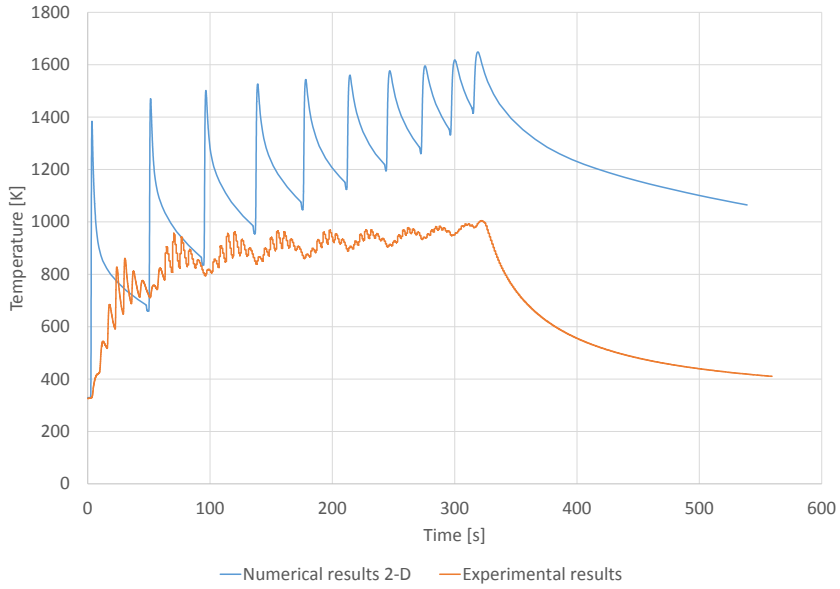

Figure 5.51: Numerical and experimental temperature profile at the thermocouple - DTL

The temperature difference between the thermocouple experimental data and the numerical results are similar to those obtained with the constant track length strategy. The cause of this difference is explained in section 5.7.3.

5.8.3 limitations

The limitations introduced by the development of this new model are as follows:

1. This modified model in itself cannot be used as a proper calibration model, as a proper calibration would require a more significantly different configuration in order to assess the model's behaviour under different configurations. Variables for a validation model must be significantly different than the one used for the calibration, as suggested by B.Thacker[56]. In our case however, the variables used, such as the flux value or the cladding geometry, are too similar, therefore providing results that are also very similar. This modified model is thus more an application of the model on a slightly modified case rather than a proper validation of the model.

2. The geometry of the clad used for the calibration model is simplified when compared to the one described in the operating procedure. The hypothesis made for the decreasing track length model have produced a different clad geometry than that observed in the experiment. It was assumed that there was a constant reduction of cladding length of 8 elements that is 2 mm along the X-axis, at each layer. Sirris does the following calculation, based on a modified version of Figure 5.19, we have:

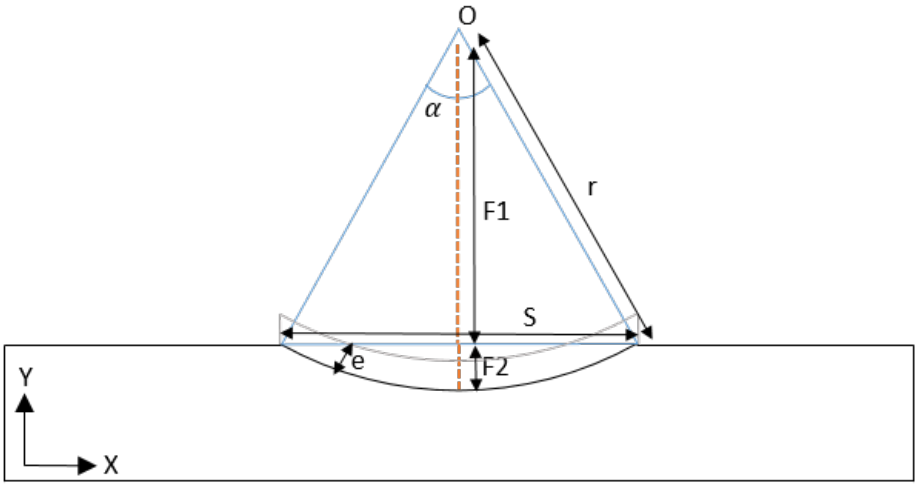

Figure 5.52: Schematic representation of the laser path

For the first layer, F1 is measured (4,8mm) as well as r (40,6mm). The string length can be obtained from:

$$c = 2.\sqrt{(2r - F2)F2} \tag{5.26}$$

We can also compute the value of F1 given by:

$$F1 = r - F2 \tag{5.27}$$

The angle α can then be determined by trigonometric relation.

$$\alpha = 2.arctan(\frac{S/2}{F1}) \tag{5.28}$$

The length of the laser path for the first layer can therefore be computed and is equal to:

$$l_{clad} = \alpha.r \tag{5.29}$$

For the following layers, the length can be obtained in a similar manner, by subtracting e from F2 and r.

Chapter 6

Results analysis

This chapter outlines the main results obtained by the laser cladding model. The results presented include the temperature profile, the thermal fluxes, the depth of the re-melted zone, as well as the micro-structure prediction. Sensitivity studies will also be performed to assess the impact of the pre-heating strategy or the building strategy. The impact of the integration scheme (A.4) will be discussed in the appendix. The results will be analysed in light of the corresponding literature and compared to the experimental results [46].

6.1 Temperature profile analysis

The temperature profile is given by the model at every point and at every time step. After a brief analysis of the spatial temperature distribution in the work-piece for different selected times, a time-dependent analysis will be performed for a selected number of points.

6.1.1 Spatial temperature distribution

The analysis will be performed for various times, for both the constant track length strategy and the decreasing track length strategy. The results will be illustrated by screen shots form DESFIN, LAGAMINE's viewer. The time selected for the analysis will be the middle and the end of the first layer printing, as well as the middle and the end of the last (10th) clad layer. On top of that, the temperature profile will be provided one minute after the end of the cladding. For each analysis, a results description will be performed, giving the maximum temperature observed and the particularities. A comparison between the two building strategies will also be completed.

The different moments described here above correspond to different times if the constant track length (CTL) or decreasing track length (DTL) strategy is considered, provided below:

Table 6.1: Cladding time of the different layers based on laser data.

Moment considered	Time with CTL [s]	Time with DTL [s]
Middle of clad 1	2,91	2,91
End of clad 1	5,86	5,86
Middle of clad 10	433,98	315,55
End of clad 10	436,89	317,03
End cooling period	779,00	377,03

The temperature profiles for the moments described in table 5.9 are given in appendix A.5. The profiles come from the viewer DESFIN and are given in the appendix in order to allow the reader to have good quality figures with a visible scale. The description of the different profiles

will be performed in this section, with a reference to the appropriate figure in the appendix.

Constant track length strategy - Temperature spatial distribution:
The result for the moments "middle" and "end of clad one" are given in Figure A.21 and A.22 respectively. We can see in Figure A.21 that the maximum temperature reached is just above 3000°K, situated just under the laser beam, at the middle of the clad. The minimum temperature is 306°K, smaller than the initial temperature but higher than the atmospheric temperature (respectively 329 and 298°K). On the left side of the laser application, the piece that has been heated by the laser beam is progressively cooling down, with temperature remaining high at above 900°K on most of the heated surface.

Figure A.22 shows a similar pattern, with an overheated point at the extremity with temperature rapidly rising to 3571°K under the laser beam. The newly clad layer also clearly transfers a large part of its energy downwards in the work-piece and the diffusion of temperature in the work-piece continues to spread. Two singularities are also visible in Figure A.22: right of the laser beam, a zone of low temperature can be observed, with a minimum of 234°K[1]. The other singularities are visible at the bottom of the work-piece, due to an inaccurate definition of the boundary conditions, no dissipation of energy is permitted under the work-piece. The cause of those singularities are explained in chapter 7.

In Figure A.23, temperature profile at the middle of clad 10, we can see that the temperature in the work-piece has increased at every-point, with the minimum temperature in the piece being 1131°K. Following the laser path, the temperature is also high in the last clad layer and overall the work-piece tends to dissipate less energy than it receives. Figure A.24 confirms this trend, with a maximum temperature at the extremities far above the evaporation point of Ti6Al4V at 3609°K ($>$ 3533°K). At the end of the cooling period, the temperature is distributed in the work-piece in a coherent way given the different boundary conditions. The temperature is higher for areas more distant from the convection and radiation boundary.

Decreasing track length strategy - Temperature spatial distribution:
For the cladding of layer 1, the profile is exactly the same for the constant track length and the decreasing track length strategy. For the cladding of the first layer, there is no difference between the two building strategies.

For the cladding of layer 10, Figures A.26 and A.27 show similar results to Figures A.23 and A.24 respectively. The geometry is modified to represent the decreasing track length strategy and the temperature in the piece is more concentrated in the middle of the piece, given the reduced time of the building strategy. The building strategy reduces the time for the piece to cool down in between each layer and the laser beam is applied on an increasingly restricted area. As such, the temperature is concentrated in the center of the work-piece. During the cooling period (Figure A.28), the temperature decreases faster in the regions close to a convection boundary.

The results presented here-above bring additional information concerning temperature distribution in a piece repaired by laser cladding. Experimentally, it is difficult to perform such a fine spatial analysis of the temperature distribution. The information about the temperature profile shape and value obtained are thus useful data to better understand the process of laser cladding. However, the results must be read by keeping in mind the limitations of the model, further developed in chapter 7.

With this current model, the results show the trends in the temperature spatial distribution

[1]This numerical oscillation occurs at the boundary between the fine mesh and the coarse mesh.

and allow comparison of time-step or models together. It was numerically observed that the hot temperature zone, in the case of the decreasing track length strategy, is more concentrated in the middle of the work-piece than it is in the constant track length strategy. If we focus on comparing situations within the same model, we can also conclude that the end of the cladding of a layer results in higher temperature under the laser beam than at the middle of the layer.

6.1.2 Time-dependent analysis in selected points

The temperature evolution will be studied at 6 points[2] situated respectively at the beginning, middle and end of layer 1 and 10. These points are represented in Figure 6.1 for the constant track length strategy and Figure 6.2 for the decreasing track length strategy.

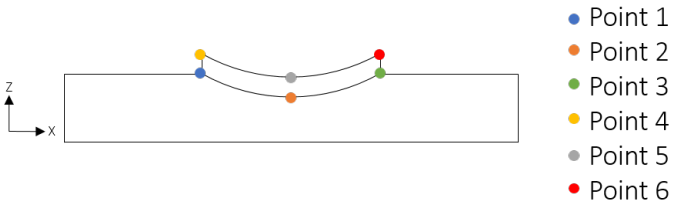

Figure 6.1: Points analysed - Constant track length strategy

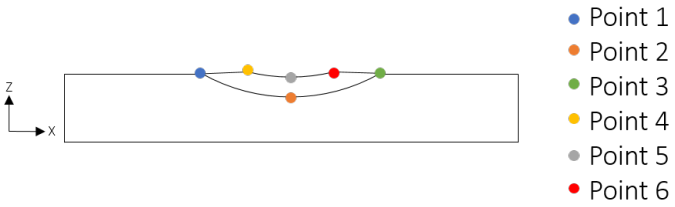

Figure 6.2: Points analysed - Decreasing track length strategy

Temporal analysis: points 1,2 and 3:
Points 1 to 3 are analysed for the constant track length strategy in Figure 6.3 and a zoom for the cladding of the first layer is available in Figure 6.4.

[2]These 6 points do not include the thermocouple. The temperature profile has already been established at the thermocouple (Figure 5.46) and compared to the experimental results respectively in Figure 5.47 for the constant track length strategy and Figure 5.51 for the decreasing track length strategy.

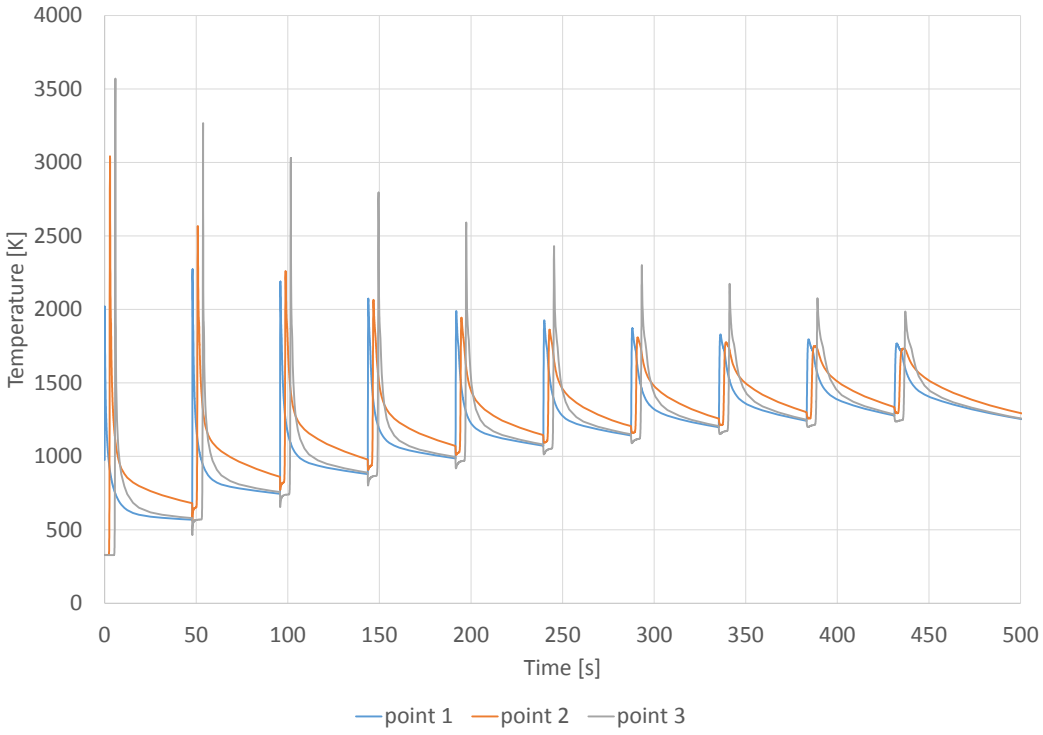

Figure 6.3: Numerical temperature profile in points 1,2 and 3 - CTL

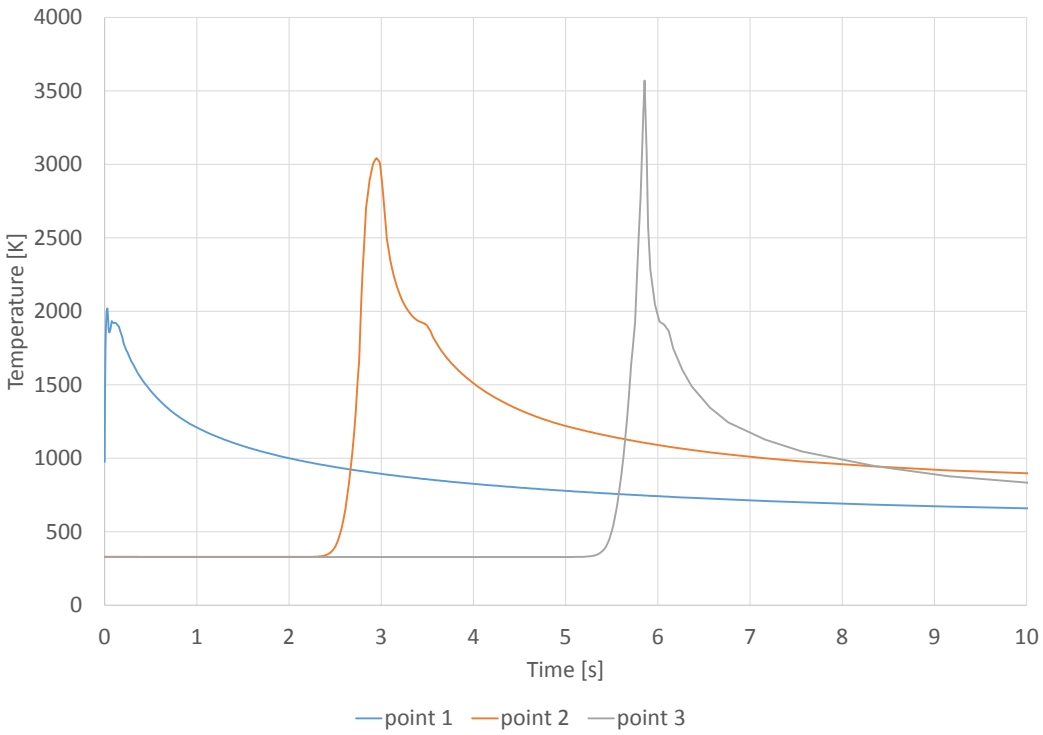

Figure 6.4: Numerical temperature profile in points 1,2 and 3 - CTL - Zoom

Figure 6.3 shows the impact of the cladding of the different layers, 10 in total, on the temper-

ature profiles. The peaks slightly differ due to the time that it takes the laser beam to go from point 1 to 2 and then 3. We can see in this graph that point 2, in the middle of the clad, has a less steep cooling rate. This is due to the fact that on the left of point 1 and on the right of point 3, there is a bigger unheated mass of Ti6Al4V in which the energy can more easily dissipate to than for point 2. Point 2 being in the center of the cladding, its energy can only be dissipated by convection and radiation at the top and conduction in the volume of material under it where the volume of substrate is the smallest.

In Figure 6.4, the time offset of the peaks is made clearer and the maximum temperature also varies. The further the point is along the laser path, the hotter the maximum temperature will be. The maximum temperature observed at these points for the cladding of the whole 10 layers is given in Table 6.2. Another point to discuss is the irregularity in the peaks caused by the latent heat of fusion of Ti6Al4V. While it does not seem to affect the heating up of the nodes, it clearly affects their cooling down. The phenomenon is particularly marked for points 2 and 3. In the case of point 1, the fusion point has just been reached and the latent heat of fusion seems to create a small oscillation.

Table 6.2: Maximum temperature observed in point 1,2 and 3. CTL.

	Point 1	Point 2	Point 3
Max.Temperature [K]	2273	3043	3570

According to the model, the evaporation temperature of Ti6Al4V (3533°K) is also locally reached in node 3, with the limitations described in chapter 7.

If we now look at points 1, 2 and 3 for the decreasing track length building strategy, we find the following results:

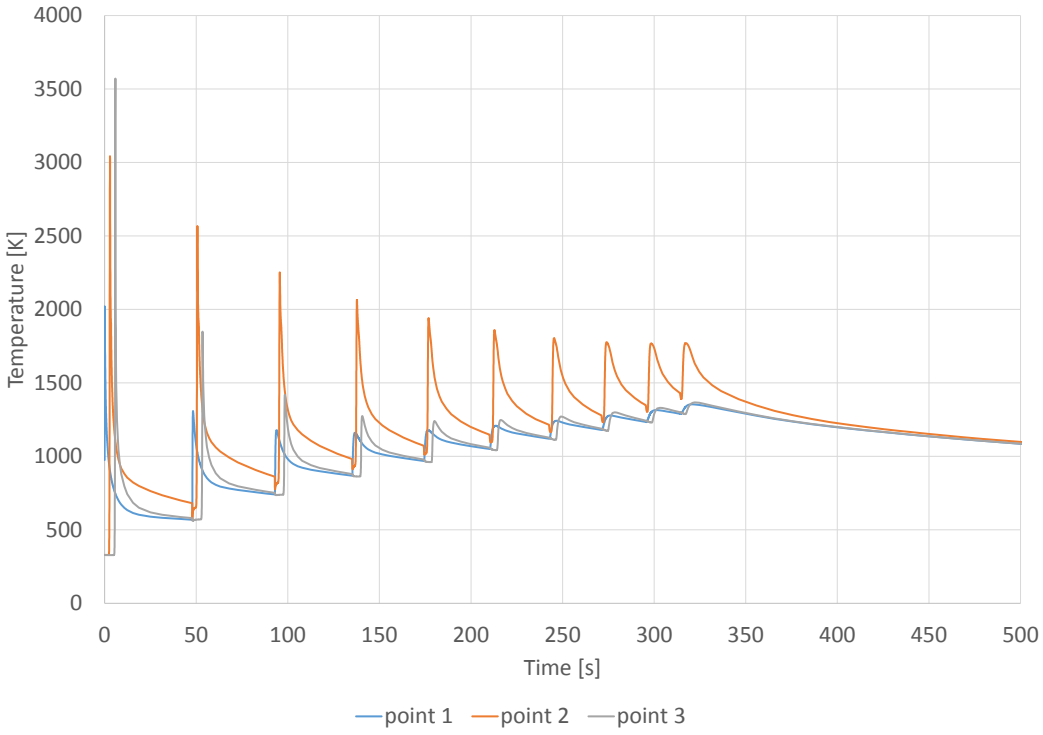

Figure 6.5: Temperature profile in points 1, 2 and 3 - DTL

Figure 6.5 being similar to 6.3, with the difference of the peaks being more close to each other. The maximum temperature observed also slightly increases, we find:

Table 6.3: Maximum temperature observed in points 1, 2 and 3. DTL.

	Point 1	Point 2	Point 3
Max.Temperature [K]	2019	3043	3570

In Table 6.3, the only change compared to Table 6.2 is the temperature at point 1, which in the case of the constant track length strategy, was more affected by the printing of layer 2 than with the decreasing track length strategy. The difference in the cooling rate between points 2 and points 1 and 3 is also more marked in the decreasing track length example. The peaks being more close to each other, the dissipation of energy by convection and radiation is reduced in the case of the decreasing track length strategy, while the energy influx at that points remains unchanged. Except for these differences, the temperature profiles have a similar shape, both with a singularity before the solidification temperature during the cooling, due to the latent heat of fusion.

Temporal analysis: Points 4,5 and 6:
The analysis of points 4, 5 and 6 is conducted in a similar way. The complete temperature profile is described in Figure 6.6.

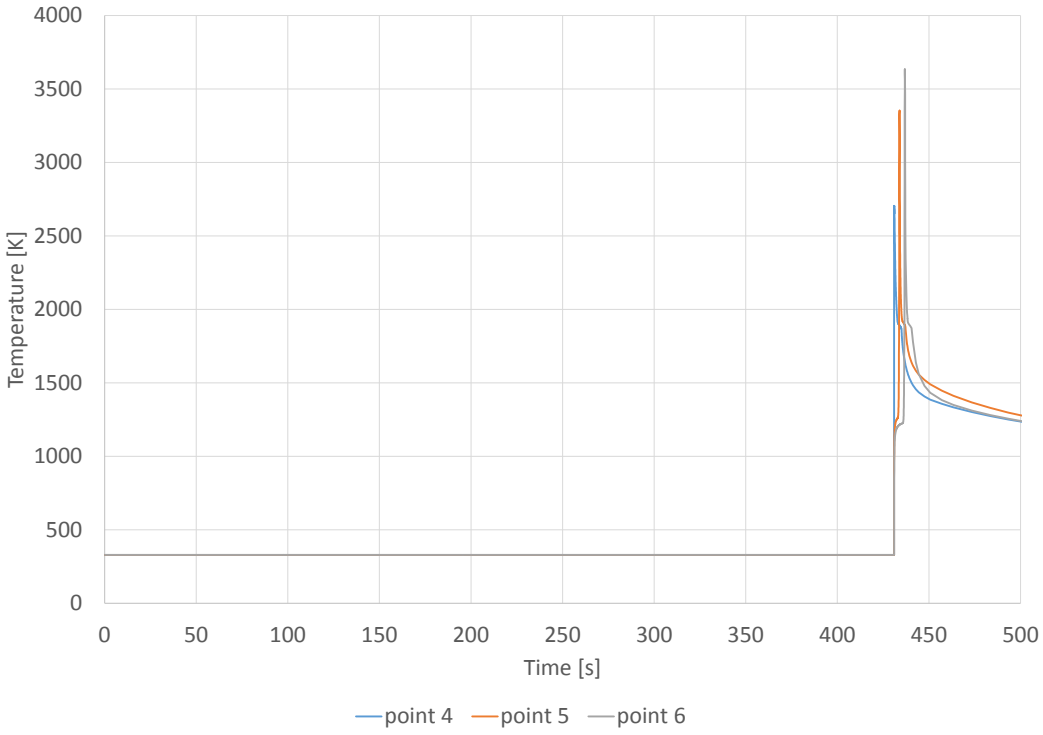

Figure 6.6: Temperature profile in points 4, 5 and 6 - CTL

We can see that the temperature at these points remain constant during most of the simulation, equal to the initial temperature of 328,89°K. This is due to the fact that these elements are only activated just before the cladding of the 10th and last layer[3].

More information can be obtained by looking only at the results for the time frame of the cladding of layer 10, as provided in Figure 6.7 and 6.8 respectively for the constant track length (CTL) and the decreasing track length (DTL) building strategies.

[3]The activation strategy is described in section 5.6.

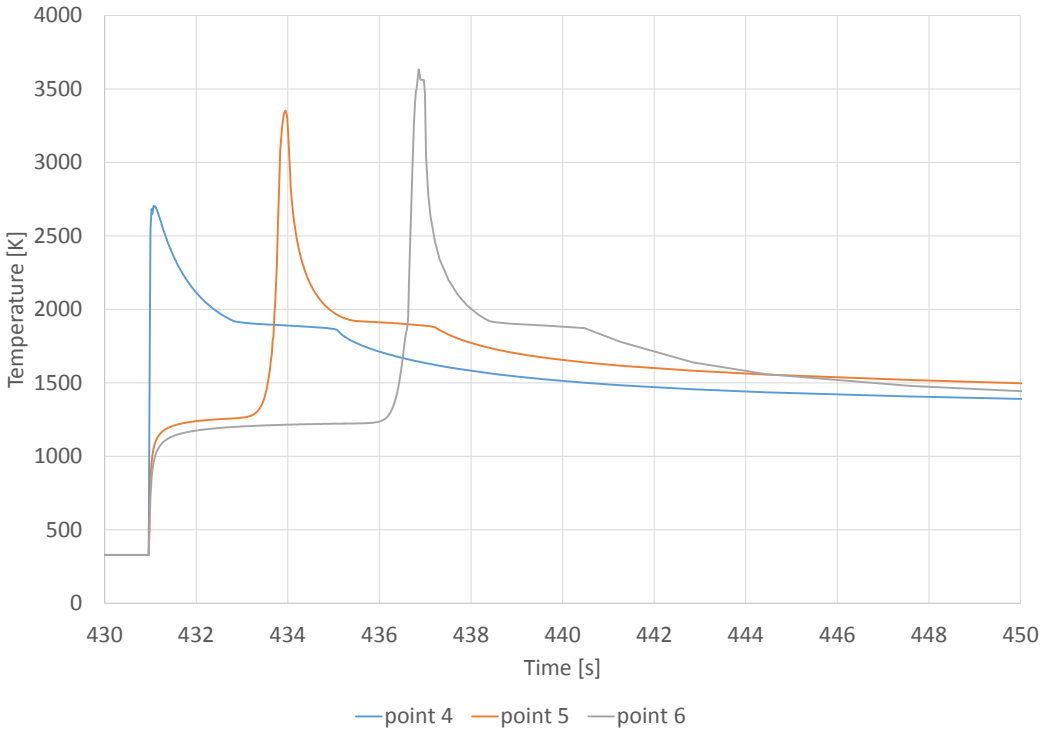

Figure 6.7: Temperature profile in points 4, 5 and 6 - CTL

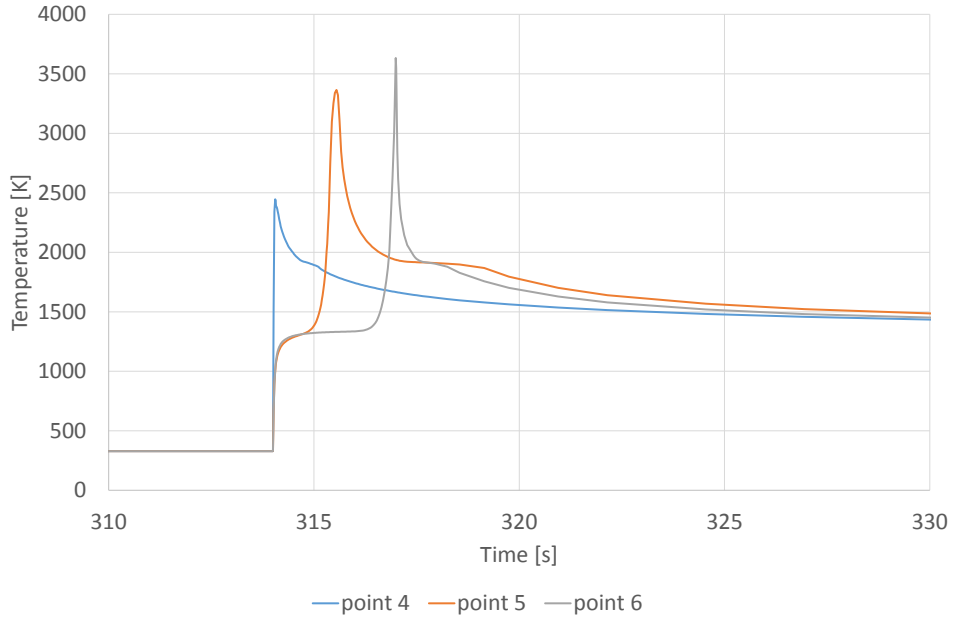

Figure 6.8: Temperature profile in points 4, 5 and 6 - DTL

In Figure 6.7, we can see around 433s a strong discontinuity due to the activation of the 10th

layer. This new layer is going to absorb heat energy from the elements under it and will rapidly rise in temperature. The laser then follows its path along the work-piece, producing the three successive peaks in 4, 5 and then 6. As for the cladding of layer 1, the peaks have a greater intensity at the end of the cladding. The effect of the latent heat of fusion is, in the case of the 10th layer, highlighted in the results, with a steep decrease in temperature for high temperatures and a steady temperature evolution between the solidification and liquidus temperatures[4]. When the temperature is lower than the solidification temperature of Ti6Al4V the cooling rate briefly increases again, then reaches a relatively constant cooling rate described in detail in section 6.4.

The comparison between 6.7 and 6.8 show several differences. The peaks are closer to each other with the decreasing track length strategy, due to the reduced time for cladding layer 10 compared to constant track length strategy. We can also see that at the middle of the clad (point 5), is cooling more slowly than in the decreasing track length strategy, compared to the point situated at the extremity. This can be explained by the capacity of those points at the extremity to dissipate energy through the top and sides of the piece.

6.2 Thermal Flux analysis

The thermal flux distribution in the work-piece during cladding can be studied based on the current results. The viewer DESFIN allows us to represent the thermal flux in the piece. In this section, the flow distribution in particular cases is analysed, the figures described in this section are available in the Appendix (A.5). The flux analysis has been performed for the constant track length strategy, the results in the case of the decreasing track length strategy are not significantly different. The flux distribution is analysed when the laser beam is at the beginning and at the end of one layer. A comparison between the flux distribution obtained with an element-by-element or a layer-by-layer activation strategy will also be provided.

In all simulations, the flux distribution is concentrated around the laser beam application nodes. The flux observed is important in these elements compared to other parts of the work-piece. This concentration of heat flux near the laser beam is presented in Figure A.29. Figure A.29 shows the flux distribution in the work-piece after 2,91s, that corresponds to the middle of the cladding of layer 1. A zoom near the laser beam application is available in Figure A.30. The maximum flux observed at this time step is equal to $7,88.10^7$ $[W/m^2]$ in the element situated just under the laser beam.

The heat flux distribution becomes more concentrated, reaching higher values, when the laser beam reaches the end of the clad, as can be seen in Figure A.31 for the end of layer 1. The flux path to reach the substrate is indeed more complex, leading to more significant flux concentration in the elements under the laser beam. For the element at the extreme right, a heat flux value of $1,01.10^8$ $[W/m^2]$ is reached.

The flux distribution is also analysed in the case of the cladding of layer 10. The results obtained can be compared with the values observed in the decreasing track length strategy. These findings are synthesised in Table 6.4.

[4] 1877°K and 1923°K respectively

Table 6.4: Maximum heat flux numerically observed in the work-piece

Moment	flux in CTL $[W/m^2]$	flux in DTL $[W/m^2]$
Middle of clad 1	$7,88.10^7$	$7,88.10^7$
End of clad 1	$1,01.10^8$	$1,01.10^8$
Middle of clad 10	$7,89.10^7$	$7,84.10^7$
End of clad 10	$4,53.10^7$	$3,54.10^7$

Where we can see that the heat flux in the decreasing track length (DTL) strategy are smaller or equal (for the cladding of layer 1) to the one obtained in the constant track length (CTL) strategy. This is due to the fact that the temperature is higher under the laser beam in the case of DTL strategy, leading to reduced flux in the material.

The activation strategy has an impact on the flux distribution in the work-piece[5]. The impact of the choice of activation strategy can be studied by comparing Figures A.30 and A.32. The flux in the more complex element-by-element strategy follows a different path and cannot be directed towards the elements that have not been activated yet. This flux distribution is nevertheless more realistic than the one obtained with the layer-by-layer activation strategy.

6.3 Thermally affected depth

At the cladding of every layer, the work-piece is heated and the liquidus temperature is reached and exceeded on a certain depth under the laser beam. This vertical distance (along Y) at which the liquidus temperature is exceeded will be later called the re-melting depth. It can be studied by looking at the temperature distribution within the piece and setting a different color for when the temperature is higher than the liquidus temperature, or lower.

By looking at the micrography from the experimental paper[46], we can estimate where the heat affected zone is. By its different color on the micrography, this heat affected zone is clearly visible and is provided in Figure 6.9 and 6.10 for respectively the constant track length (CTL) strategy and the decreasing track length (DTL) strategy.

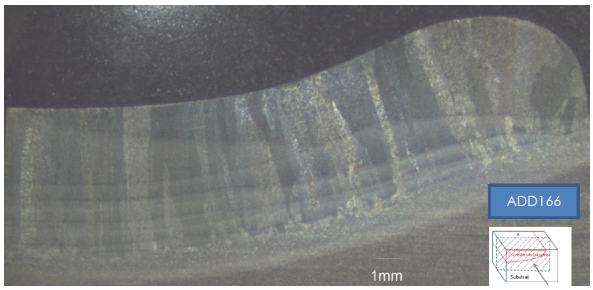

Figure 6.9: Micrography - CTL

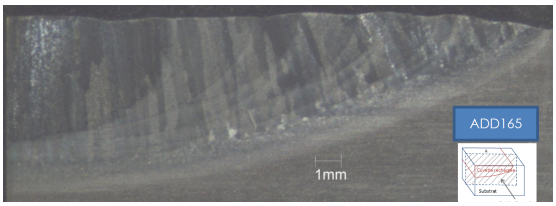

Figure 6.10: Micrography - DTL

In Figures 6.9 and 6.10, we can see different layers of material with a very varied depth, the top one being the biggest by far. This is due to the fact that during the cladding of each layer, the previously clad layers are also affected by the laser beam. The separation between these layers is the heat affected zone (HAZ), the distance between the HAZ and the surface will be called the thermally affected depth. It is not yet sure that this thermally affected depth is equal to re-melting depth but this is the current assumption. By looking at Figures 6.9 and 6.10, the depth of the thermally affected zone can be graphically determined and is given in Table 6.5.

[5]The two activation strategies, layer-by-layer and element-by-element are presented in section 5.6.

Table 6.5: Thermally affected depth (TAD) obtained experimentally [46].

Building strategy	TAD [μm]
Constant track length	2750
Decreasing track length	3000

The results obtained with the numerical model are observed for the cladding of the last layer, the only layer that can be compared with experimental results. By looking at the temperature profile and graphically highlighting the area where the temperature is higher than the liquidus temperature, we find the shape of the melt-pool[6] This melt-pool prediction is given at 433,98 s. and 315,55 s. respectively for the constant track length strategy and the decreasing track length strategy. These times correspond to the application of the laser at the middle of clad 10 based on Table 5.9. The results are shown in Figures A.33 and A.34, available in the appendix.

The first remark from these figures is the large size of the melt-pool. According to Sirris, and based on observation of the different laser cladding experiments, such a large melt-pool is not possible, refer chapter 7.

The thermally affected depth can also be more precisely determined using the temperature at the nodes. A polynomial interpolation of the temperature in the clad material as a function of the depth allows us to find the depth where the temperature in our model is higher than the liquidus temprature of Ti6Al4V. This interpolation is performed right in the middle of the work-piece[7].

The results are given for the constant track length strategy:

[6]Chapter 7 details the limitation of the model explaining this shape.
[7]From point 5 to point 2 on Figures 6.1 and 6.2.

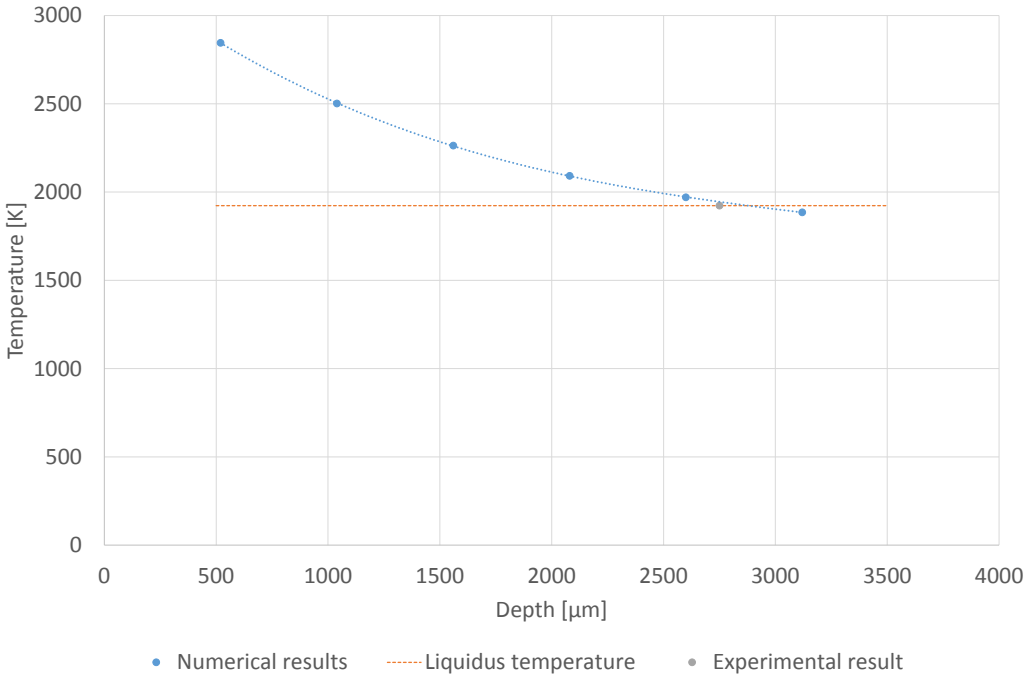

Figure 6.11: Temperature observed as a function of depth - CTL

The numerical results can then be interpolated, by using a third order polynomial equation, we have a determination R^2 coefficient of 0,999. The interpolation, performed via *Matlab*, gives the following equation:

$$T = -2,56.10^{-8}Z^3 + 2,56.10^{-4}Z^2 - 1,00Z + 3,30.10^3 \tag{6.1}$$

Where Z is the thermally affected zone (TAD) in [μm] and T is the temperature in [°K]. Using this strategy, a TAD of 2876 μm is found. When compared to the experimental TAD obtained graphically, we find a difference of 4,58%.

Similarly, for the decreasing track length strategy, we can produce the same graph and the same calculation to find the corresponding TAD.

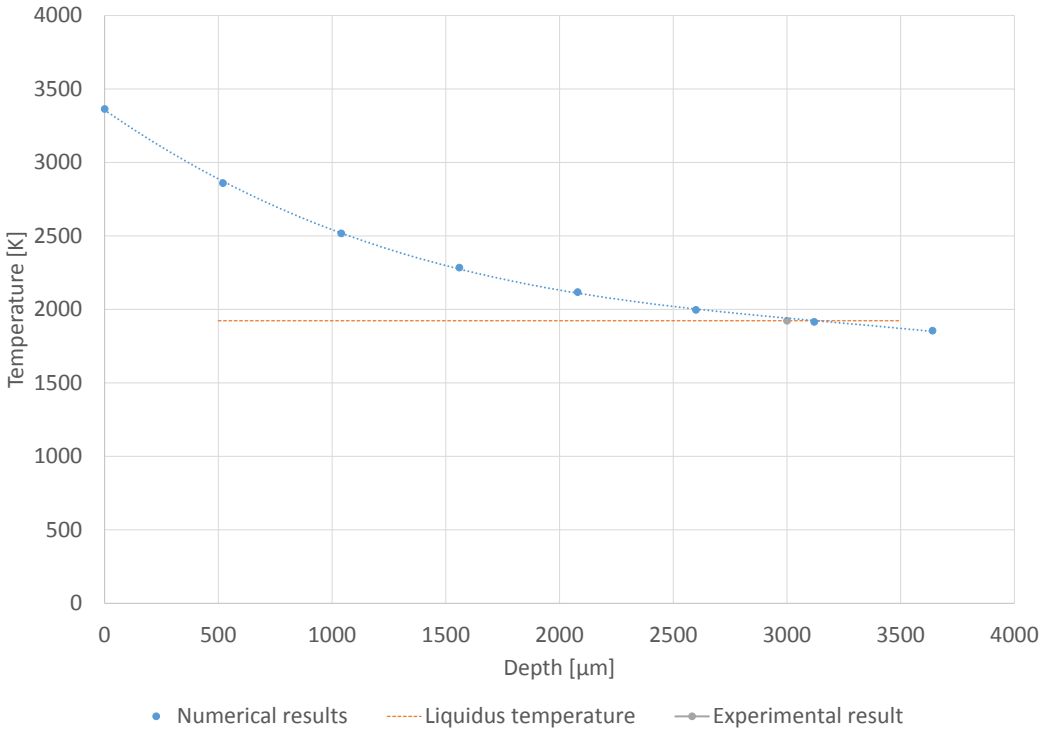

Figure 6.12: Temperature observed as a function of the depth - DTL

The numerical results are interpolated, by using a third order equation, we have a once again a determination R^2 coefficient of 0,999. The interpolation, performed via *Matlab*, gives the following equation:

$$T = -3,04.10^{-8}Z^3 + 2,93.10^{-4}Z^2 - 1,08Z + 3,36.10^3 \tag{6.2}$$

Where Z is the thermally affected zone (TAD) in [μm] and T is the temperature in [°K]. We found a TAD of 3126 μm[8], with a difference of 4,22% compared to the experimental results.

The different results are synthesised in the table hereafter:

Table 6.6: Synthesised result of thermally affected depth

	Constant track length	Decreasing track length
Numerical TAD [μm]	2876	3126
Experimental TAD [μm]	2750	3000
Difference [%]	4,58	4,22

Globally, we can see that the model highlights a difference between the two building strategies, adapting the size of the thermal affected zone. We can also see that the depth of the thermally affected zone is overestimated compared to the experimental results. The definition of this thermal affected zone is also important to keep in mind : it is taken as the zone where the temperature exceeds the liquidus temperature of Ti6Al4V for the numerical results and as the zone situated above the heat affected zone (HAZ) in the case of the experimental observations. There is no certainty that these two definitions exactly coincide. This assumption was made as no other usable data, other than the micrography, was available to assess the thermal affected zone.

[8]The two other solutions of this third degree equation being unrealistic.

6.4 Microstructure analysis

A complete and separate micro-structure study was performed in two specific areas of the work-piece, at the middle of the cup and at the right end extremity (Figure 6.15 and 6.21 respectively). The temperature profile and the cooling rate are established for different depths and the expected micro-structure was then determined studying the cooling rate at the β-transus temperature. Finally, the predicted micro-structure was compared to the one obtained in the experimental tests led H.Paydas et al.

The micro-structure that should be obtained considering the cooling rate from the β phase range is given by T.Ahmed[1] and is presented in Figure 6.13.

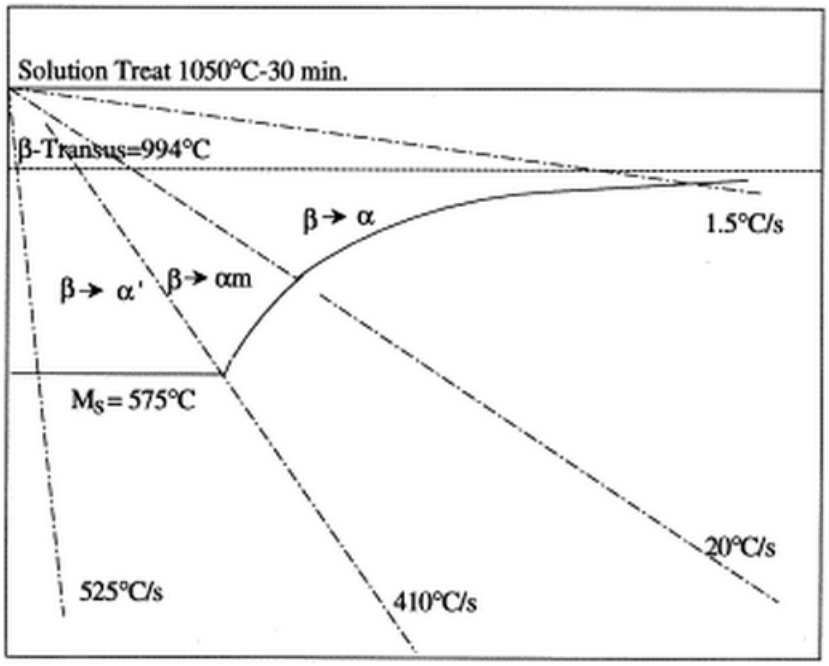

Figure 6.13: Schematic cooling diagram for Ti6Al4V [1]

Figure 6.13 can be interpreted such that: if the cooling rate from the β-transus temperature is lower than 20°C/s, an α Widmanstätten microstructure is formed. On the other hand, when the cooling rate is greater than 410°C/s, a fully α' martensitic microstructure is observed. In between these cooling rate values, a mixed micro-structure of martensite and Widmanstätten is formed with different grain formations according to the cooling rate. The different types of grain formations are presented in Figure 6.14.

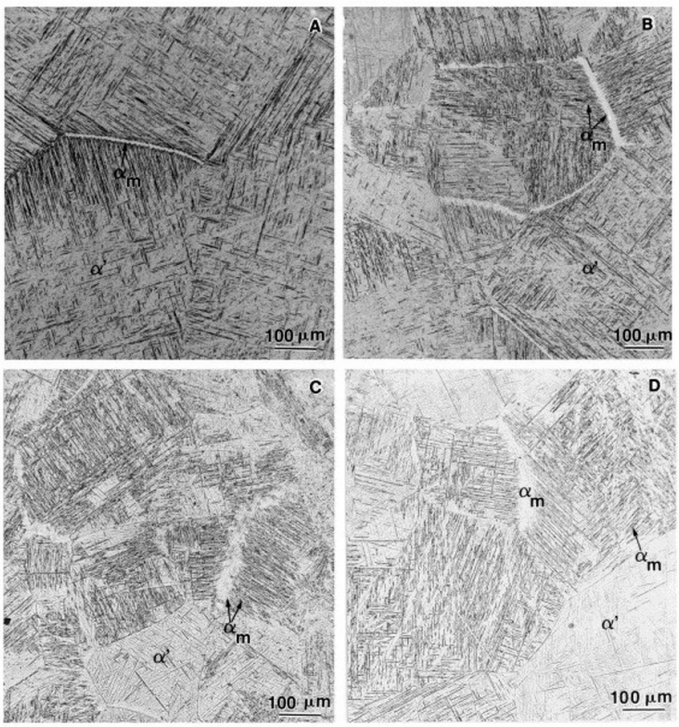

Figure 6.14: Type of microstructure formation observed for different cooling rates: 410°C/s (A), 275°C/s (B), 175°C/s (C) and 20°C/s (D)[1].

H.Paydas also provides a comprehensive tool in order to determine the micro-structure of Ti6Al4V according to the cooling rate[46]. This thermo-metallurgical scheme is provided in Figure 5.2.

Analysis at the middle of the cup. The numerical results obtained with our model are given for three different depths, situated at the middle of the work-piece, as shown in Figure 6.15 for the constant track length building strategy. The position of the points with the decreasing track length strategy are the same.

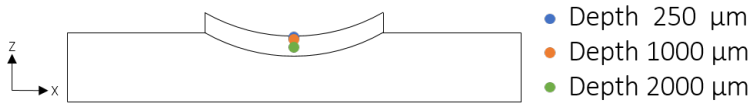

Figure 6.15: Analysis for three points with different depth in the work-piece.

Firstly, the temperature profiles were studied at these points for the constant track length strategy case. Then, the cooling speed was determined and analysed precisely during the final cooling down of the work-piece[9]. The temperature profile of the three points is given in Figure 6.16.

[9]The most critical time for the micro-structure determination. It includes the moment when the temperature goes from above the β-transus temperature to room temperature.

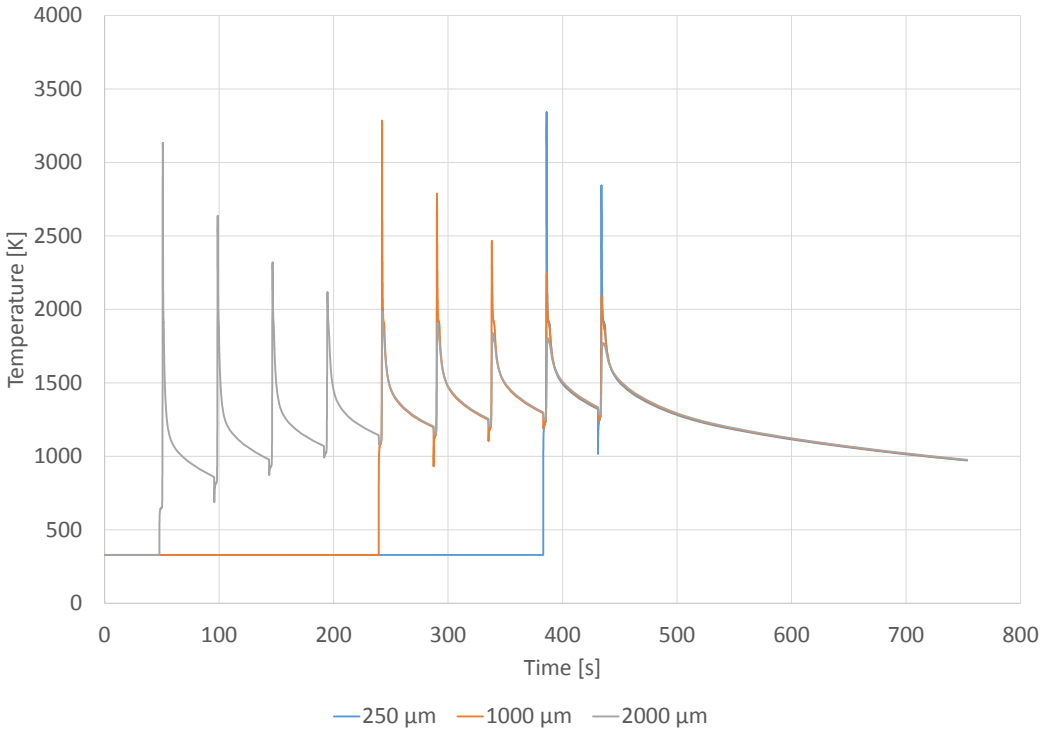

Figure 6.16: Temperature profile for three different depths - CTL

As we can see in Figure 6.16, the temperature profiles in these points undergo a number of peaks. Each peak corresponds to the printing of one layer of material. Before the first peak - respectively before 50 seconds for 2000 μm, 220 seconds for 1000 μm and 380 seconds for 250 μm - the temperature is equal to the initial temperature, 328.9°K. The intensity of the different peaks varies with their proximity to the heat source. The closer to the surface of the work-piece, the higher the intensity of the peak. The oscillations due to the activation of the layers are also visible before each peak[10].

If we look at the cooling of the piece after the last peak, the temperature profile seems similar for the three different depths. By looking at this cooling rate on another scale, as in Figure 6.17, we can see that the curves follow similar patterns, with small disparities. It can be observed that the upper node (250 μm depth) has the highest cooling rate until around 550°K. The β-transus temperature is also represented. The difference in cooling rates will be later quantified.

[10]These oscillations have been explained in section 5.6.

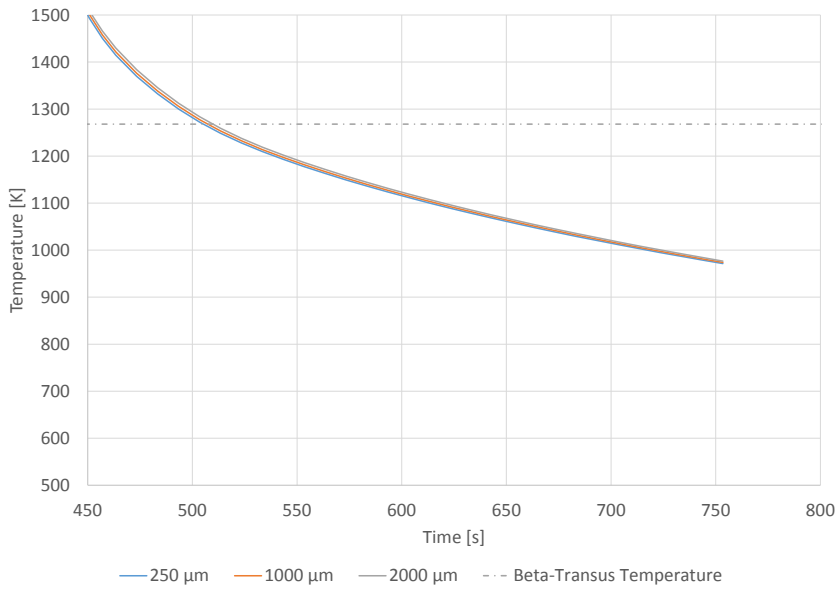

Figure 6.17: Temperature profile for three different depths - Zoom on final cooling - CTL

For decreasing track length strategy (DTL), and considering the same points as described in Figure 6.15, we find:

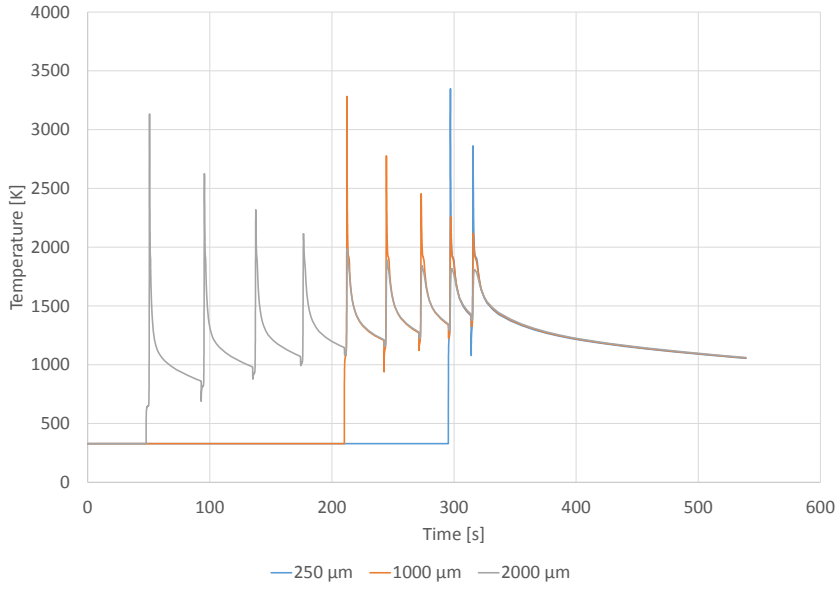

Figure 6.18: Temperature profile for three different depths - DTL

Where the temperature profiles obtained are similar to Figure 6.16. The difference being the duration of the printing and the decreasing times between the peaks, reduced in the case of the decreasing track length strategy.

In terms of cooling rate in [°K/s], and focusing on the final cooling rate of the work-piece, we can compute the cooling rate as a function of the temperature for both the constant track length strategy and the decreasing track length strategy, we find:

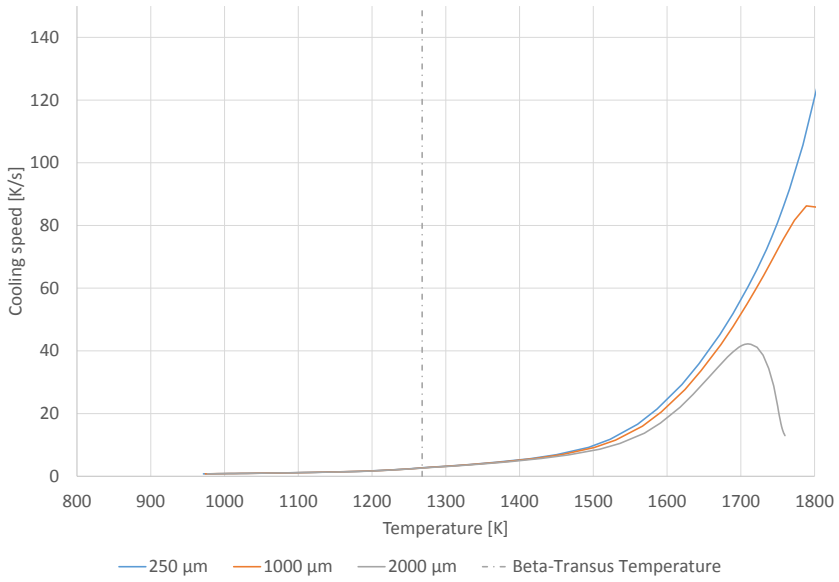

Figure 6.19: Numerically observed cooling rate as a function of temperature - CTL

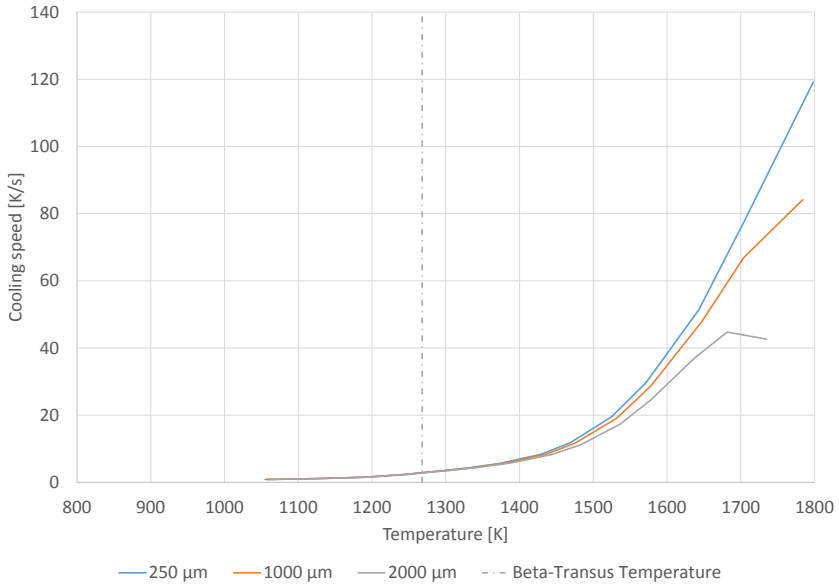

Figure 6.20: Numerically observed cooling rate as a function of temperature - DTL

The cooling rate at the β-transus temperature can thus be studied for both strategies. The values obtained allow us to predict the micro-structure at these points and compare them to the experimental results. The results obtained are synthesised in Table 6.7.

Table 6.7: Cooling rate at β-transus. Comparison of the different strategies at the middle of the cup

Depth [μm]	Cooling rate - CTL [°K/s]	Cooling rate - DTL [°K/s]
250	2,71	2,93
1000	2,65	2,85
2000	2,59	2,77

The main takeaways from these results are the following:

- The cooling rate decreases with depth, all other parameters unchanged. That means the deeper in the work-piece, the lower is cooling rate. The chance of seeing martensitic formation is thus higher near the extremity.
- The cooling rate is significantly higher for the decreasing track length strategy. The chance of observing martensitic formation is thus higher.
- In all the points studied, the cooling rate is low, under 3°C/s. The micro-structure expected according to [1] is thus pure α Widmanstätten.

These results are consistent with H.Paydas' experimental findings. In the case of constant track length strategy, only a Widmanstätten micro-structure was observed (α). With a maximum cooling rate of 2,71°K/s in that case near the surface, and according to T.Ahmed[1], only an α micro-structure should be observed with that cooling rate. In the case of a decreasing track length strategy, H.Paydas has observed at those points a pure α micro-structure as well. Therefore, for points situated in the middle of the work-piece, the numerical results are consistent with the experimental observations.

Analysis at the extremity. For this analysis, two depths will be considered, situated at the right extremity of the cup[11] as described in Figure 6.21.

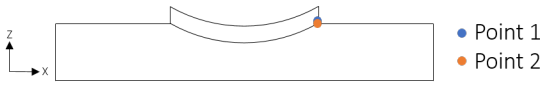

Figure 6.21: Analysis for two points with different depths at the right extremity.

Using a similar methodology as for the points in the middle of the work-piece, the temperature profiles and cooling speeds are computed for both the constant track length and the decreasing track length building strategy. The main results are synthesised in Table 6.8

Table 6.8: Cooling rate at β-transus. Comparison of the different strategies at the right extremity of the cup

Distance from the substrate [μm]	Constant track length strategy [°K/s]	Decreasing track length strategy [°K/s]
0	2,51	2,34
520	2,55	2,35

The values obtained at the extremity are not coherent with the experimental results. H.Paydas observed different types of micro-structures for the two building strategies: an Widmanstätten

[11] The exact position of the nodes is at the extreme right of the clad at heights of 520 μm and 0μm above the level of the initial substrate.

formation for the constant track length strategy and a mixed Widmanstätten and martensitic formation for the decreasing track length strategy. This is highlighted on Figures 6.22 and 6.23.

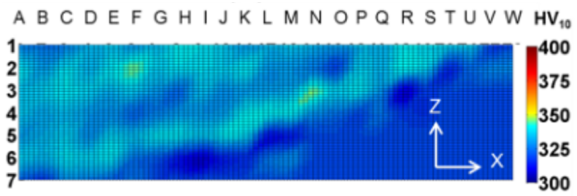

Figure 6.22: Hardness map - CTL [39]

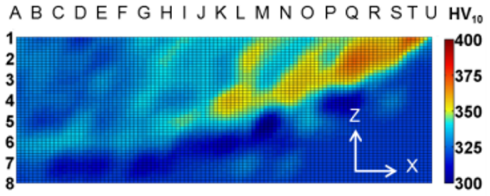

Figure 6.23: Hardness map - DTL [39]

The above figures are hardness maps of the clad material performed experimentally and described in the original study[46]. The hardness map highlights the difference in micro-structure. The presence of a martensitic formation improves the hardness of the material (in red). With the numerical model however, we do not predict the formation of martensite at those points. This incoherence is most likely due to an underestimation of heat transfer to the external world, as described extensively in chapter 7[12].

6.5 Influence study - Pre-heating strategy

One of the problem faced by industries using laser cladding is the apparition of cracks during the process. The solution to tackle this problem, experimentally determined, is to pre-heat the material. Different pre-heating strategies exist such as the use of an oven[13] or the use of an induction heating device. For some pieces, no pre-heating is needed. Numerical models could be used to assess the impact of pre-heating on the work-piece and could eventually determine the optimal pre-heating strategy for a specific work. In this section, firstly, the impact of different pre-heating temperatures, set uniform in the substrate, has been studied. Secondly, a more representative model to simulate the pre-heating strategy used in the experiment has been detailed and the results compared to the simplified model[14].

Temperature set uniform in the substrate. The effect of the initial temperature, set uniformly in the whole substrate, was studied. The numerical simulation was performed with three different values of the initial temperature: 298,15°K, corresponding to the ambient temperature and therefore simulating the process without any pre-heating. 328,89°K, the temperature experimentally obtained at the thermocouple right before the beginning of the cladding, used in the model presented. Finally, 473,15°K, corresponding to a pre-heating temperature of 200°C, that is the target pre-heating temperature in the case of the experiment modelled.

The comparison of the results with the different initial temperatures is provided at the 2-D equivalent of the thermocouple (Figure 5.46). The temperature profiles obtained are detailed in Figures 6.24, for the whole experiment time frame, and in Figure 6.25 for a zoom on the first clad layer.

[12] The corrected model, presented in A.7, does not have this problem.
[13] This pre-heating strategy is the one used in the case of the modelled experiment[46]
[14] That is the model presented in chapter 5 using a uniform initial temperature in the substrate.

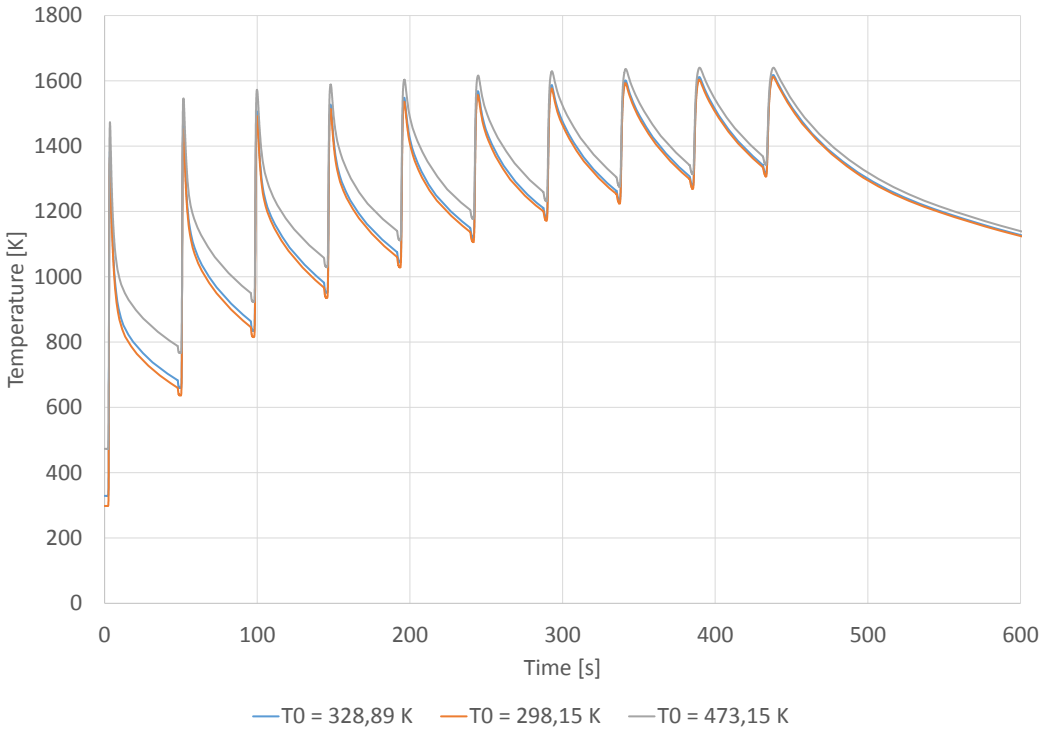

Figure 6.24: Temperature profiles at the thermocouple for different initial temperatures

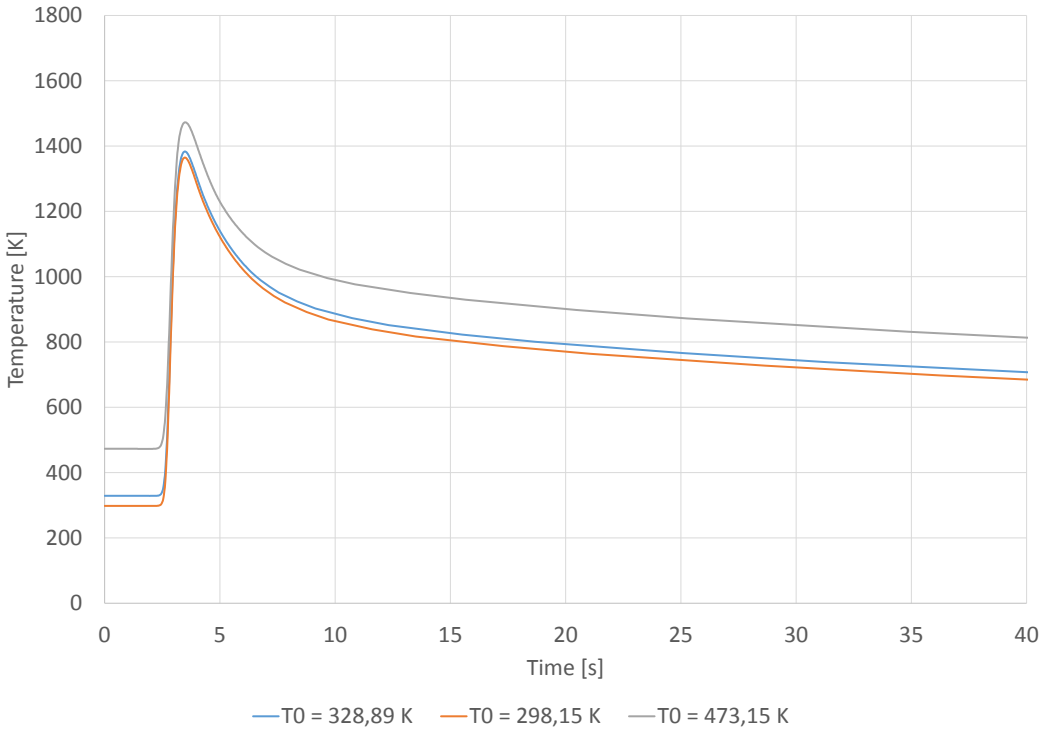

Figure 6.25: Temperature profiles at the thermocouple for different initial temperatures - first layer

In Figure 6.24 we observe that the higher the initial temperature, the higher the temperature during the whole operation. Even if the differences tend to be smaller with time, the impact of the initial temperature is still noticeable at the end of the cooling period. The difference is indeed smaller, at the beginning of the simulation ($t = 0$), the relative difference in temperature between the two extreme cases[15] is 37,0% and decreases to 1,0% at the end of the cooling ($t = 779s$). Figure 6.25 also shows that the initial temperature does not influence the global shape of the temperature profile which is consistent with the expected results, the higher the initial temperature, the higher the heat energy in the piece. During the experiment and the cooling period, this extra energy will be dissipated by convection and radiation, this explains the smaller difference in temperature after cooling.

A quantitative analysis allows us to have a better understanding of the influence of the initial temperature. The main numerical results are given in Table 6.9.

Table 6.9: Impact of the initial temperature. Analysis at the thermocouple

Initial temperature T_0 [°K]	Max. temperature observed [°K]	Max. increase in temperature [°K/s]	Max. decrease in temperature [°K/s]
298,15	1612	2247	212
328,89	1618	2207	210
473,15	1640	2002	206

As can be seen in Table 6.9, the maximum temperature observed during the simulation increases with initial temperature. We also notice that the maximum gradient of temperature observed, for the heating or the cooling of the piece, is lower when the initial temperature is high, all other parameters unchanged. If we analyse graphically the maximum increase of temperature as a function of initial temperature, we find:

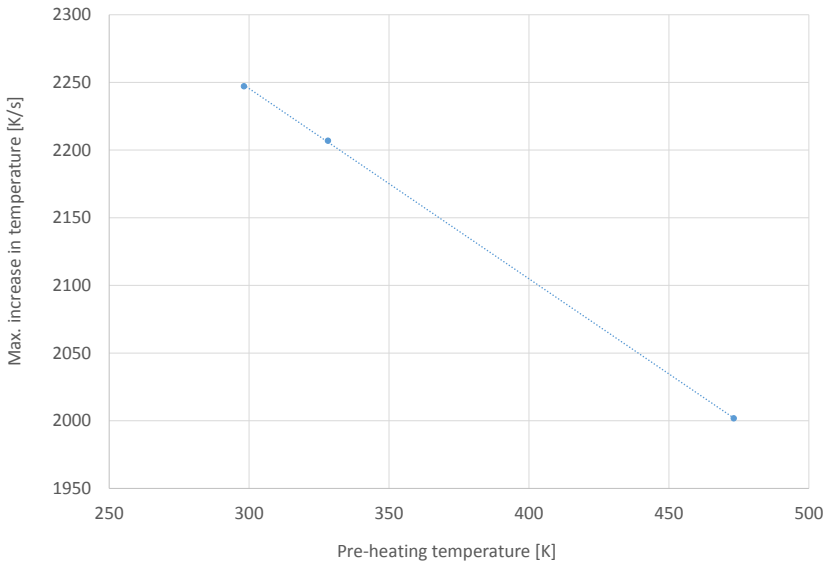

Figure 6.26: Maximum increase in temperature as a function of the initial temperature

Where Figure 6.26 tends to show a linear relationship between these values. This shows that the choice of an high initial temperature reduces the temporal thermal gradient, however, more

[15]Simulations with $T_0 = 298,15$°K and $T_0 = 493,15$°K.

simulations are required to confirm this trend.

In order to assess the impact of pre-heating on the formation of cracks, it is necessary to study the spatial temperature gradient in the work-piece. The spatial temperature gradient induced a gradient of thermal deformation in the piece and therefore induced stresses, that can eventually lead to cracks. The spatial temperature gradient between the middle of clad one and the middle of clad 10[16], provide the following:

Table 6.10: Impact of the initial temperature. Spatial temperature gradient in the clad

Initial temperature T_0 [°K]	Max. temperature gradient observed spatially [°K/mm]
298,15	366,45
328,89	365,68
473,15	360,75

As can be seen in Table 6.10, the higher the temperature, the smaller the spatial temperature gradient. Therefore we can conclude that the thermal related strains and stresses are lower if we increase the initial temperature. In order words, increasing pre-heating reduces the risk of cracks.

Refined model with pre-heating. In order to further represent the impact of pre-heating, other than a uniform temperature in the work-piece, a modified version of the model was developed. This model simulates the experiment performed at Sirris, in which a pre-heating oven was used[17]. The oven temperature is set up at 200°C or 473°K. The piece is then manipulated and set in place, allowing it to cool-down before the start of the experiment. In a first approximation, the manipulation time has a duration of two minutes[18].

By modelling these operating conditions and comparing the results between this realistic modified model and the results obtained with a uniform initial temperature of 473,15°K, we find the following results:

[16]Situated respectively in points 2 and 5 Figures 6.1.

[17]The oven has been replaced since then by an induction heating system that will not be considered in the case of this work.

[18]This manipulation time is set at 5 minutes in the case of the most up-to-date model presented in A.7.

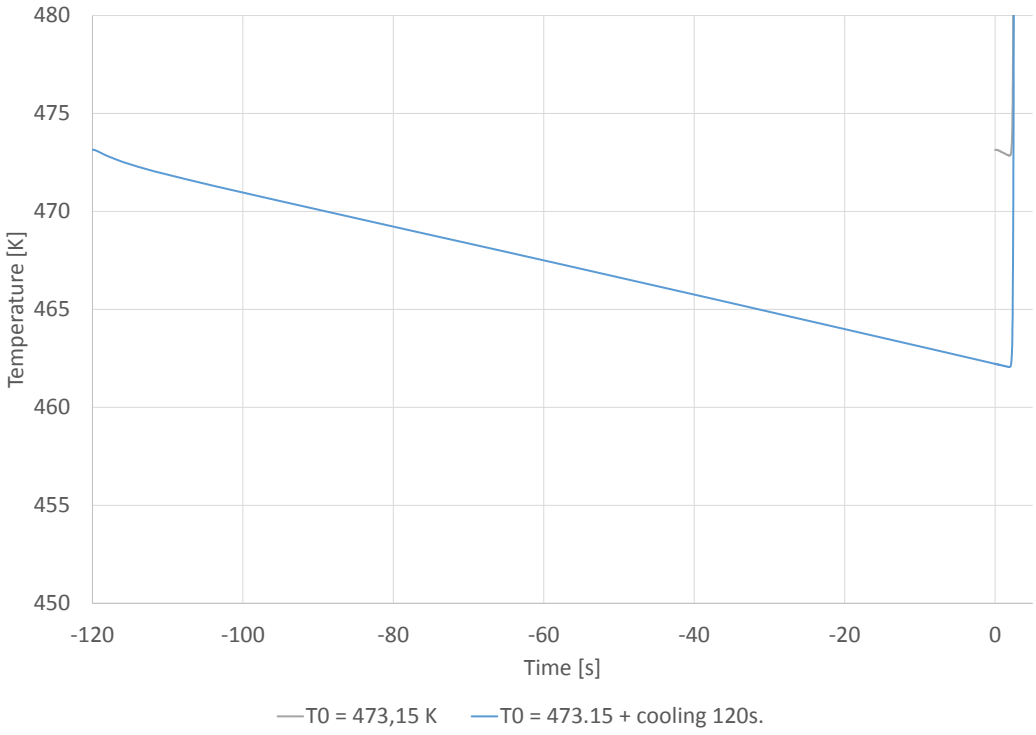

Figure 6.27: Cooling down of the work-piece after the oven

Where we can see in Figure 6.27 that the temperature in the piece decreases immediately after leaving the oven, before the cladding begins. At the instant before cladding, the temperature at the thermocouple with the hypotheses describes here-above is 462,22°K. This is much higher than the 328,89°K observed experimentally, which means that the manipulation time has been underestimated and a manipulation time of 5 min would have been more representative given the cooling rate[19]. This decrease of temperature is not uniform within the work-piece, the temperature distribution in the piece just before the cladding is presented in figure A.35.

This non-uniform temperature distribution has of course an impact on the temperature spatial and temporal distribution in the piece. This impact is nevertheless difficult to quantify. By looking at the same indicators as previously we find:

Table 6.11: Impact of the pre-heating model on the results

Pre-heating modelling	Max. temperature observed [°K]	Max. increase in temperature [°K/s]	Max. decrease in temperature [°K/s]
T_0=473,15°K	1640,4	2002	206
T_0=473,15°K + 120s cooling	1639,7	2032	206

In Table 6.11, we can see the difference in the parameters studied at the thermocouple is small, with a maximum difference of 1,5% for the increase in temperature gradient. The simplified model is therefore acceptable to simulate the process unless the focus is put on the impact of the pre-heating strategy.

[19]Cooling rate that is underestimated in the current model, as described in chapter 7

Chapter 7

Potential improvements

7.1 Limitations synthesis

A synthesis of all limitations is proposed in this chapter, followed by recommendations to tackle the most challenging ones. Table7.1 provides a list of the model current limitations [1]. Limitations are here ranked by their potential influence on the results obtained.

Limitation ranking	**Section**	**Description**
1	5.4.3	The heat transfer through the metallic support is neglected. Therefore reducing the cooling rate in all points and resulting in inaccurate heat flux distribution in the workpiece.
2	5.7.3	One pass per layer is simulated for the 2-D model. Therefore the temperature history in the piece differs from experimental data as shown in Figure 5.47.
3	5.4.3	Non-accurate value for the convection coefficient h. The value selected is too small according to the comparison with experimental results, therefore reducing the cooling rate near the surface of the workpiece. Furthermore, the forced argon flux near the laser head is not modelled.
4	5.4.3	Non-accurate boundary conditions: convection and radiation boundaries are incomplete. Under the work-piece, convection and radiation should be considered as well, as shown in Figure A.36. Furthermore, the convection and radiation transfer via the lateral faces are neglected in the 2-D model.
5	5.7.3	The calibration of the 3-D model is performed for the printing of one pass and takes into account the maximum temperature at the thermocouple. An increasing difference between the numerical model and the experimental data can be observed when looking at the temperature for the cladding of two passes.

[1] Model limitations have been detailed in their corresponding chapters, that is section 5.4.3 for the thermal law limitations, section 5.5.2 for the mechanical law limitations, section 5.2 for the mesh limitations, and respectively sections 5.7.3 and 5.8.3 for the calibration and validation.

6	5.6	The newly activated elements have a too low temperature at $T_0 = 328,89$. This causes non-realistic heat fluxes in elements near the cladding region.°K.
7	5.6	A simplified layer-by-layer activation strategy has been used to produce the results. Figure 5.37 shows the difference between a layer-by-layer activation strategy and a more realistic element-by-element strategy
8	5.2	There are oscillations in the temperature profile along the Y axis. These oscillations affect the numerical results of the 3-D model, used for the flux calibration.
9	5.3.3	The simplification of the laser intensity profile. Due to the choice of mesh size, the shape of the intensity profile has been simplified.
10	5.7.3	The initial temperature in the work-piece is considered constant at $T_0 = 328,89$. In fact, the initial temperature varies in the work-piece and depends on the pre-heating strategy.°K.
11	5.5.2	Ti6Al4V is assumed infinitely elastic causing little impact on a purely thermal model but critical if a thermal-mechanical model is the objective.
12	5.5.2	Only the solid phase of Ti6Al4V is considered.
13	5.5.2	Mechanical properties are considered constant with temperature.
14	5.5.2	Ti6Al4V is considered isotropic.

Table 7.1: Synthesis of the model limitations

7.2 Potential solutions

The aforementioned limitations currently restrict the utility of the numerical model. However, every limitation previously mentioned has a potential solution to overcome it. By applying these modifications, the model will become more accurate in representing the laser cladding process. The potential solutions to solve the current issues are listed in Table 7.2. Solutions are provided for issues 1 to 10, whereas issues 11 to 14 relate to limitations of the mechanical model, which is not a priority when developing a working thermal model. Additional detail about how to solve these limitations is provided in Table 7.2 of the appendix.

Lim. ranking	**Potential solution(s)**	**ref. for details**
1	Design of a new geometry to represent the support. The support will be connected at one end to the work-piece and on the other end to a large piece designed to dissipate the energy transferred by conduction. This new geometry will be made of steel and not Ti6Al4V. The coherence of the mesh at the contact surface will need to be performed precisely.	A.6.1

2	Firstly, it is possible to simulate the cladding of the other passes on the 2-D model by adding additional heat flux of reduced intensity on the newly activated element. The number of passes to simulate is still to be determined. A good compromise between accuracy and an acceptable complexity must be found. The influence of the second flux has been studied and the value of the secondary flux to apply can be estimated. Secondly, the influx of energy into the work-piece coming from the cladding of the other passes can be simulated by decreasing the time between layers. This time is initially set up based on laser data but can be reduced in the model to virtually take into account that influx of energy. A good and accurate model will most likely combine both of these solutions.	A.6.2
3	The value of the convection coefficient used for the Ti6Al4V-air exchange surface should be increased to better fit the numerical model to the experimental results. Furthermore, the forced argon flux near the laser beam should be modelled as well to determine a more realistic melt-pool size. It is possible to set a different value for the convection coefficient when the laser is close by making the convection coefficient dependent on temperature. The value of the convection coefficient given for high temperatures being the estimated Ti6Al4V-Argon h value.	A.6.3
4	To complete the boundary conditions to best represent the operating conditions as shown in Figure A.36, convection and radiation (CONRA) should be added below the piece. Although this will not have a large impact on the temperature profile for the first pass, it will eventually increase the cooling rate of the work-piece.	A.6.4
5	An alternative to calibrating the flux would be to use another criteria. Two alternatives seem more suitable but would require a more complex 3-D model. The first alternative consists of keeping the maximum temperature obtained at the thermocouple as the calibration criteria, but using its value after the cladding of 8 passes of layer 1. The other alternative involves minimising the difference in the temperature profile obtained numerically and experimentally. In that second case too, a model based on the cladding of more than one pass would be more accurate.	A.6.5
6	The solution to this point is to increase the temperature of the activated element. This can be done by modifying the initial temperature of the element at $T_0 = T > 328,89°\text{K}$. with T a temperature that would need to be defined but could be taken equal to the liquidus temperature[2] as a first approach. Along with an increase in temperature, the flux would need to be re-calibrated, as a part of the laser beam heat will be provided by the activated elements at a high temperature.	A.6.6

7	A full element-by-element activation strategy could be developed for complex models. The code itself has been developed after having overcome some inherent limitations of LAGAMINE, now modified.	5.6
8	Oscillation along the Y axis in the 3-D model can be reduced and even completely removed by increasing the precision of the mesh along the Y axis. Increasing the mesh precision has the drawback of increasing the computation time of an already complex simulation	5.2.4
9	The laser intensity profile can be represented in more details if the mesh precision is increased near the surface.	5.2.3
10	To change the initial temperature, a complete study of the different pre-heating strategies must be performed. More accurate assumptions could also be made, like a linear distribution of temperature from the center of the workpiece to the extremities and so on.	

Table 7.2: Potential solutions for problematic limitations

After applying the corrections listed in Table 7.2, the different steps performed in section 5.7 and 5.8 would need to be performed again, before being able to properly use the results of the model.

A modified version of the model, with the application of some of the solutions described here above is available in the appendix (A.7).

Chapter 8

Conclusion

This work has outlined the basis for numerically modelling the process of laser cladding applied to Ti6Al4V. A thermal model has been created to reproduce the experiment of Paydas et al. [46] to simulate the use of laser cladding as a repair technology. In this work, the material properties and the finite element code used are detailed, followed by a complete description of the model. The mesh design, heat source modelling, thermal and mechanical laws applied as well as boundary conditions used are explained. For each of these sections, the choices made for the model are justified and compared with other sources. The activation of elements strategy as implemented in the model is also described.

The model is calibrated based on the experimental results of H.Paydas. For this calibration, a 3-D model was developed to enable the comparison with the experimental results. As a result of this calibration, a laser absorptivity coefficient of $\beta = 0.33$ was numerically identified. This value is close to the values given in literature, ranging from $0,34$ to $0,4$ [17][66]. This calibrated model was then transitioned to a 2-D model.

The results obtained with the calibrated numerical model have been analysed. The analyses include a spatial and temporal study of the temperature profiles in the work-piece, a study of the melt-pool and re-melting depth as well as an analysis of the heat flux distribution in the work-piece during cladding. The micro-structure numerically obtained was also studied. For all results, a comparison was performed between the two building strategies used in H.Paydas study, the constant track length (CTL) and the decreasing track length (DTL) building strategies. The main takeaways from the numerical results are outlined below:

- The spatial temperature distribution analysis shows a concentration of the high temperature zone in the center of the cup when using the decreasing track length strategy, when compared with the constant track length strategy. This phenomenon is highlighted when comparing Figures A.23 and A.26.
- The maximum temperature observed during the cladding of a layer is observed at the very end of the layer. The maximum temperature observed at that time is situated under the laser beam and sometimes exceeds the vaporisation temperature of the alloy (3533°K [7]).
- The latent heat of fusion reduces the cooling rate of Ti6Al4V when its temperature is between the solidus and liquidus temperatures (respectively 1877°K and 1923°K [5][7].)
- The temperature in the middle of the clad decreases more slowly than the the temperature at its extremities. Furthermore, this phenomenon is more important for the decreasing track length strategy than for the constant track length strategy.
- The heat flux distribution in the piece is concentrated below the laser beam. The flux observed are larger or equal when using the constant track length strategy. The activation

strategy also impacts the flux distribution in the piece, with higher flux observed with the element-by-element activation compared to the simplified layer-by-layer activation strategy.

- The thermally affected depth (TAD), defined by the depth under the surface where Ti6Al4V is melted by the laser beam flux, is close to the value observed experimentally. TAD of 2876 and 3126 μm are found numerically for the constant track length strategy and the decreasing track length strategy respectively. This leads to an overestimation of the TAD of less than 5% when compared to the experimental observations.

- A Widmanstätten micro-structure is predicted by the numerical model in every point of the piece, for all building strategies. Experimentally, a Widmanstätten micro-structure is observed in the whole piece for the constant track length strategy except with the decreasing track length strategy, the presence of a partial martensite formation is observed at the extremities of the clad.

- The pre-heating temperature affects the maximum temperature and the cooling rates observed in the piece. Numerically, it is found that the higher the pre-heating temperature, the higher the maximum temperature and the lower the cooling rate observed in the piece are.

- The pre-heating temperature affects the spatial gradient of temperature in the piece. Numerically, it is found that the higher the pre-heating temperature, the lower the temperature gradient in the clad. This shows that the risk of cracks due to thermal related stresses can be reduced by increasing the pre-heating temperature.

Generally, it is found that all numerical results, trends, profiles or shapes in temperature or heat flux are consistent with the experimental results, however, the absolute values obtained, especially in terms of temperature, are overestimated in the numerical simulations. The causes of these temperature overestimations are detailed, along with the other limitations of the model, resulting mainly from an underestimation of the heat transfer to the atmosphere. In the final chapter of this paper, for each limitation, potentials solutions are proposed to increase the model accuracy. The results obtained with a corrected version of the model are presented in the appendix A.7.

To conclude, the model presented in this paper, while not complete enough at this stage to be used in industrial applications, is an important first step toward the development of a complete model to simulate the laser cladding process. Despite current imperfections, the modelling steps performed and tools developed, will facilitate the development of further models. These tools include *inter alia*:

- The development of routines to simulate the laser beam movement on the work-piece.

- The development of routines to simulate the activation of finite elements as they are clad on the substrate.

- The identification of thermal and mechanical laws to best represent the process of laser cladding.

- The identification of the different parameters necessary for the application of these laws to Ti6Al4V alloy.

- The development of a calibration method that can be reproduced for other simulations.

These tools, as well as the problems that have been tackled and the unexpected difficulties faced, will help other laser cladding model developers in building a more representative and accurate model.

An updated model, taking into account the thermal and mechanical effects, should help industry to better understand the impact of different parameters, such as pre-heating, laser speed and power or building strategy. Indirectly, a finished model should allow the optimisation of operating procedures to produce optimal quality pieces. If these objectives are fulfilled, laser cladding as a technology would become more efficient, with a potential increase in its industrial use and competitive advantages compared to classical manufacturing and other additive manufacturing technologies.

Bibliography

[1] T. Ahmed and H. Rack. Phase transformation during cooling in alpha + beta titanium alloys. *Materials Science and Engineering*, A243:206–211, 1998.

[2] M. Alimardani, E. Toyserkani, and J. Huisson. A 3d dynamic numerical approach for temperature and thermal stress distributions in multilayer laser freeform fabrication process. *Optics and Laser in Engineering*, 2007.

[3] ARCAM. Electron beam melting. in the forefront of additive manufacturing, 2015.

[4] H. Attar, M. Calin, L. Zhang, et al. Manufacture by selective laser melting and mechanical behaviour of commercial pure titanium. *Materials of science and Engineering A*, 593:170–177, 2014.

[5] M. Boivineau, C. Cagran, D. Doytier, et al. Thermophysical properties of solid and liquid ta6v alloy. *International Journal of Thermophysics*, 27(2):507–529, March 2006.

[6] C. Bouffioux. Comparaison des coefficients de dilatation thermique classique et partiel. Rapport intermediaire 35, Region wallonne, Septembre 2002.

[7] R. Boyer, G. Welsch, and E. Collings. *Materials properties handbook: titanium alloys*. ASM International, 978-0-87170-481-8 Materials Park, OH, 1994.

[8] S. Campanelli, N. Contuzzi, A. Ludovico, et al. Manufacturing and characterization of ti6al4v lattice compontents manufactured by selective laser melting. *Materials Open Access Journals*, 7:4803–4822, 2014.

[9] R. Charlier. *Methodes numeriques non-lineaires- Partie 2*. University of Liege, 2012. Notes de cours.

[10] M. Chiumenti, M. Cervera, A. Salmi, and C. Agelet de Saracibar. Finite element modmodel of multi-pass welding and shaped metal deposition processes. *Computer Methods in Applied Mechanics and Engineering*, 199:2343–2359, 2010.

[11] S. Corbin, E. Toyserkani, and A. Khajepour. Cladding of fe-al coating on mild steel using laser assisted powder deposition. *Journal of MateriaJournal of Materials Science, Vol. 354, n.1-2, pp.48-57*, 2003.

[12] CRC, Advanced, and Manufacturing. *Additive manufacturing categories processes and materials*, August 2012.

[13] N. Dahorte and S. Harimkar. Laser fabrication and machining of materials. *Spring Science+ Business Media*, pages 42–43, 2007.

[14] O. de Weck. *Finite Element Method - Engineering Design and Rapid Prototyping*. Massachussetts Institute of Technology, January 2004.

[15] H. El Cheikh and B. Courant. 3d finite element simulation to predict the induced thermal field in case of laser cladding process and half cylindrer laser clad. *Photonics and Optoelectronics*, 1(3):55–59, October 2012.

[16] H. El Cheikh, B. Courant, S. Branchu, et al. Analysis and prediction of single laser tracks geometrical characteristics in coaxial laser cladding process. *Optic and Laser Engineering*, 50(3):413–422, 2012.

[17] Z. Fan and F. Liou. Numerical modelling of the additive manufacturing (am) processes of titanium alloy. *Titanium alloys - Towards Achieving Enhanced Properties for Diversified Applications*, 2012.

[18] J. Feng, M. Ferreira, and R. Vilar. steel cladding of ni-cr/al2o3 composite ccoating on aisi 304 stainless steel. *Surface and coating technology, vol.88, n.1-3, pp.212-218*, 1997.

[19] F. Frascati. *Etude et comportement des emaux lors du matricage finition des aubes en alliage de titane.* PhD thesis, Ecole Nationale Superieure des Mines de Paris, 2003.

[20] C. Geuzaine and J.-F. Remacle. Gmsh: a three-dimensional finite element mesh generator with built-in pre- and post-processing facilities. *International Journal for Numerical Methods in Engineering*, 79(11):1309–1331, 2009.

[21] I. Gibson, D. Rosen, and B. Stucker. *Additive manufacturing technologies.* Springer US, Boston, MA, 2010.

[22] G. Gilles. *Experimental study and modeling of the quasi-static mechanical behavior of Ti6Al4V at room temperature.* PhD thesis, University of Liege, March 2015.

[23] J. Godalk, A. Chakravarti, and M. Bibby. A new finite element model for welding heat source. *Metall. Trans.*, 15B:299–305, 1984.

[24] M. Griffith, J. Keicher, D.L. and. Romero, et al. Laser engineering net shaping for the fabrication of metallic components. *American Society of Mechanical Engineers, Materials Division, Advanced Materials: Development, Characterization Processing, and Mechanical behavior. Vol.74, pp. 175-176*, 1996.

[25] J. Hart. *Additive manufacturing.* Massachussets Institue of Technology, December 2013.

[26] A. S. M. Inc. Titanium ta6v annealed, 2015.

[27] E. Kaschnitz, P. Reiter, and J. McClure. Thermophysical properties of solid and liquid 90ti6al4v in the temperature range from 1400 to 22300 measured by millisecond and microsecond pulse-heating techniques. *International Journal of Ther*, 23(1):267–275, January 2002.

[28] D. Kaser. Laser powder fusion welding. *Huffman corporation Technical Report*, 2001.

[29] M. Labudovic and R. Kovacevic. Modelling of the laser surface nitriding of ti-6al-4v alloy. analysis of heat transfer and residual stresses. *Proceedings of the institution of Mechanical Engineers*, 2001.

[30] C. Lequesne. *Modeling of fractures in heavy steel welded beam-to-column connection submitted to cyclic loading by finite elements.* PhD thesis, University of Liege, 2009.

[31] R. Lewis, K. Morgan, H. Thomas, and K. Seetharamu. The finite element method in heat transfer analysis. *John Wiley and Sons Ltd, Baffins Lane, Chichester*, 1996.

[32] X. Li, C. Wang, W. Zhang, and Y. Li. Fabrication and characterization of porous ti6al4vparts for biomedical applications using electron beam melting process. *Materials Letters*, 63(3-4):403–405, February 2009.

[33] T. Lips and F. B. A comparison of commonly used re-entry analysis tools. *Acta Astronautica*, 57(2-8):312–323, 2005.

[34] R. Mah. Dircomponents fabrication. *Advanced Materials and Processes, vol.151, n.3, pp.31-33*, 1997.

[35] J. Mazumder, D. Dutta, N. Kikuchi, and A. Ghosh. Closed-loop direct metal deposition: Art to part. *Optic and Laser Engineering, vol.34, pp.397-414*, 2000.

[36] J. Mazumder and A. Kar. Solid solubility in laser cladding. *Journal of Materials*, 39:18–23, 1987.

[37] M. McLean, G. Shannon, and W. Steen. Laser direct casting high nickel alloy components. *Advances in Powder Metallurgy and Particulate Materials, vol.3, pp.21-3-21-16*, 1997.

[38] A. Mertens and H. Paydas. Caractérisation thermophysique d'un échantillon de ti6al4v mis en oeuvre par laser cladding. Rapport d'essai, Avril 2013.

[39] A. Mertens, S. Reginster, H. Paydas, et al. Mechanical properties of alloy tial4v and stainless steel 316l processed by selective laser melting: influence of out-of-equilibrium microstructures. *Powder Metallurgy*, 57(3):184–189, 2014.

[40] S. Mikhlin. *Variational methods in mathematical physics.* Oxford, New York, Pergamon Press, 1964.

[41] K. Mills. *Recommended Values of Thermophysical Properties for Selected Commercial Alloys.* Antony Rowe Ltd, 1st ed, Wiltshire, England, 2002.

[42] A. Mohammadi, H. Vanhove, A. Van Bael, and J. Duflou. Toward accuracy improvement in single point incremental forming of shallow part formed under laser assisted conditions. *International Journal of material Forming*, 2010.

[43] A. Neira Arce. *Thermal Modelling and Simulation of Electron Beam Melting for Rapid Prototyping on Ti-6Al-4V Alloys.* Materials science and engineering, Raleigh, Noth Carolina, 2012.

[44] F. Pascon. *2D1/2 thermal-mechanical model of continous casting of steel using finite element method.* PhD thesis, University of Liege, 2003.

[45] V. Pavelec, R. Tanbakuchi, O. Uyehara, and P. Myers. Welding. *Welding Journal*, 48:295–305 suppl, 1969.

[46] H. Paydas, A. Mertens, R. Carrus, J. Lecomte Beckers, and J. Tchoufang Tchuindjang. Laser cladding as a repair technology for ti6al4v alloy: influence of building strategy on micro-structure and hardness. Submitted to Journal of Materials and Design.

[47] D. Peidao, L. Jianglong, F. Ducoin, et al. Laser surface allalloy of a low alloy steel with cobalt. *Journal of Materials Technology, vol.58, n.1, pp.131-135*, 1996.

[48] I. Polmaer. *Light Alloys: From traditional alloys to nanocrystals.* Elsevier/Butterworth-Heinemann: Amsterdam, 2006.

[49] P. Rangaswamy, H. Choo, E. Prime, et al. High temperature stress assessment in scs-6/ti-6al-4v composite using neutron diffraction and finite element modeling. In *Thermec 2000 - International Conference on Processing and Manufacturing of Advanced Materials*, 2000.

[50] O. Rigo and C. Engel. *Etat actuel des fabrication aadditive pour les applications metalliques.* Sirris, November 2013.

[51] U. Ritter, W. Kahrmann, R. Kupfer, and R. Glardon. Laser coating proven in practice. *Sulzer technical review. Vol. 73, n.3, pp18-20*, 1991.

[52] D. Rosenthal. Mathematical theory of heat distribution during welding and cutting. *Welding Journal*, 20(5):220–234, 1941.

[53] D. Rosenthal. Mathematical theory of moving sources of heat and its application to metal treatments. *Tans ASME*, 68:849–866, 1946.

[54] M. Soodi. Hacladding engineering is now equipped with state-of-the-art laser processing facility, 2015.

[55] K. Tam, F. Cheng, and H. Man. Laser surfacing of brass with ni-cr-al-mo-fe using various laser processing parameters. *Materials of science and Engineering A, Vol.325, n.1-2, pp.365-374*, 2003.

[56] B. Thacker, S. Doebling, et al. *Concepts of Model Verification and Validation.* Los Alamos national laboratory, charmian schaller edition, Otober 2014.

[57] E. Toyserkani, A. Khajepour, and S. Corbin. 3-d finite element modeling of laser cladding by powder deposition: Effects of powder feed rate and travel speed on the process. *Journal of Laser Applications*, 15(3):153–160, 2004.

[58] E. Toyserkani, A. Khajepour, and S. Corbin. *Laser Cladding.* Library of Congress Cataloging-in-Publication Data, 2005.

[59] V. Tuninetti Vasquez and A. Habraken. Impact of anisotropy and viscosity to model the mechanical behavior of ti-6al-ti alloy. *Materials Science & Engineering, A*, 605:39–50, 2014.

[60] J. Vaithilingam, S. Kilsby, R. Goodbridge, et al. Functionalisation of ti6al4v components fabricated using selective laser melting with bioactive compound. *Materials Science and Enginnering*, 46(1):52–61, January 2015.

[61] M. Vanderhasten. *Ti-6Al-4V: Deformation map and modelisation of tensile behaviour.* PhD thesis, Belgian Royal military Academy and Katholieke Universiteit Leuven, December 2007.

[62] K. Washizu. Variational methods in elasticity and plasticity. *Pergamon Press*, 1982. 3rd edition.

[63] X. Wu. In situ formation by laser cladding of a tic composite coating with gradient distribution. *Surface and coating technology, vol. 115, n.2, pp.111-115*, 1999.

[64] I. Yadroistev, P. Bertrand, and I. Smurov. Parametric analysis of the selective laser melting process. *Applied rface Science*, 253(19):8064–8069, July 2007.

[65] I. Yadroistev, P. Krakhlmalev, and I. Yadroitsava. Selective laser melting of ti6al4v alloy for biomedical applications: Temperature monitoring and microstructural evolution. *Journal of Alloys and Compounds*, 583:404–409, 2014.

[66] J. Yang, S. Sun, W. Brandt, and W. Yan. Experimental investigation and 3d finite element prediction of the heat affected zone during laser assisted machining of ti6alti alloy. *Journal of Materials Processing Technology*, 210:2215–2222, 2010.

Appendix A

Appendix

A.1 2-D Pile of elements - Oscillation study

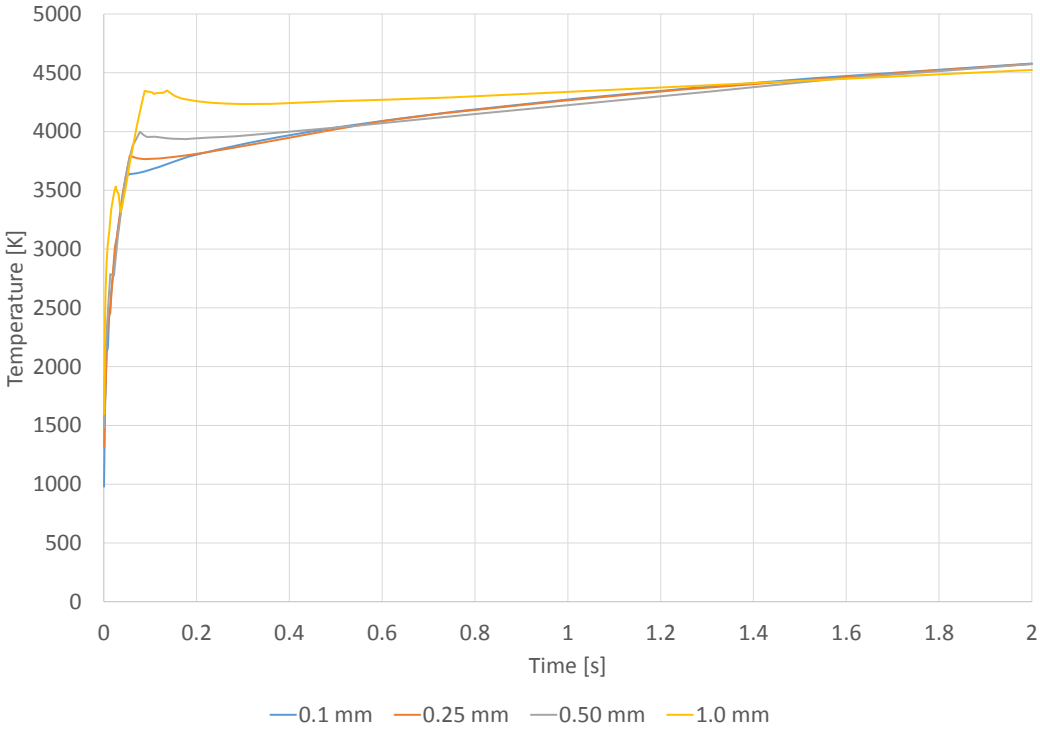

Figure A.1: Temperature profiles at the top of the pile for the different element heights

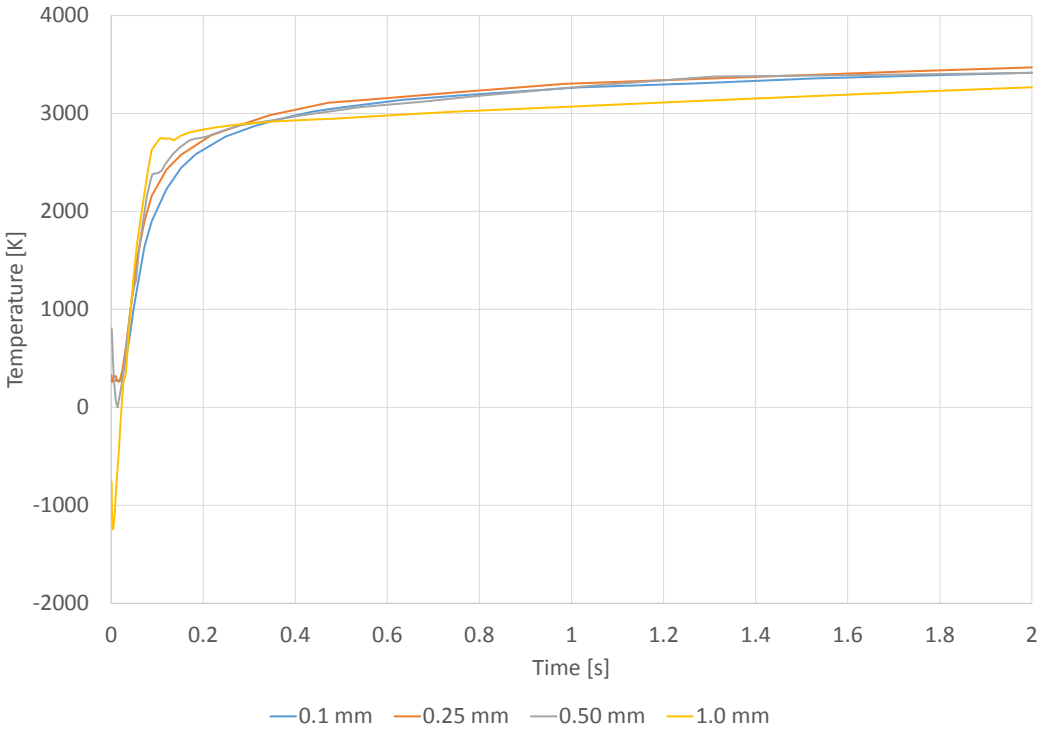

Figure A.2: Temperature profiles 1 mm under the top of the pile for the different element heights

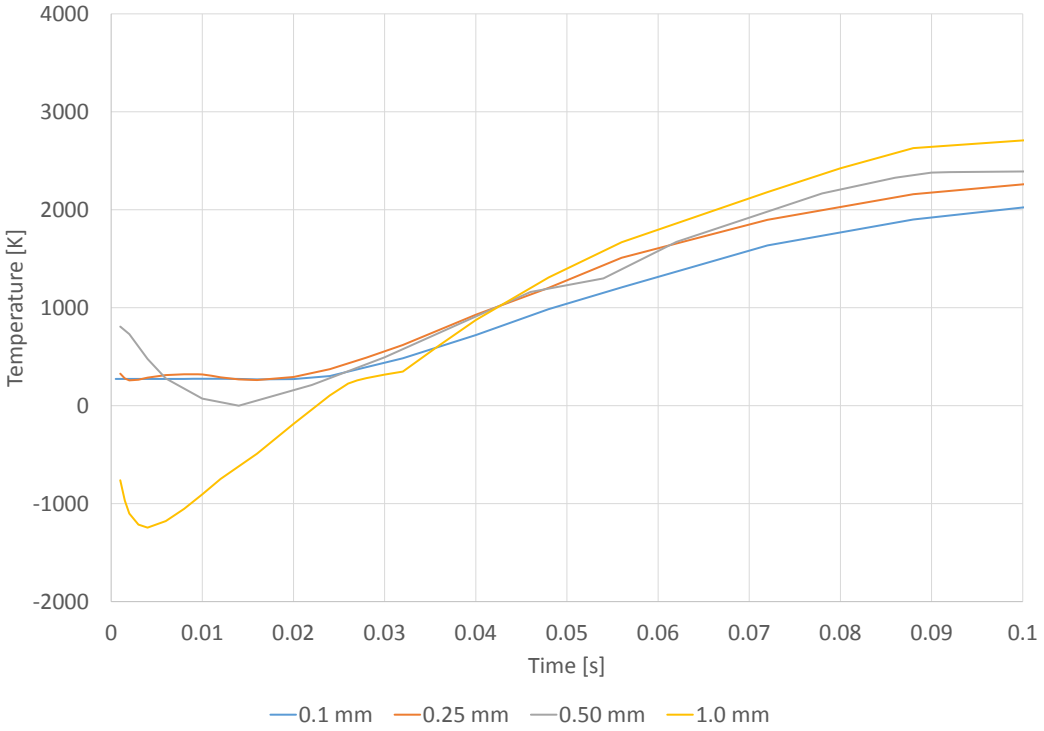

Figure A.3: Temperature profiles 1 mm under the top of the pile for the different element heights - Zoom for beginning of flux application

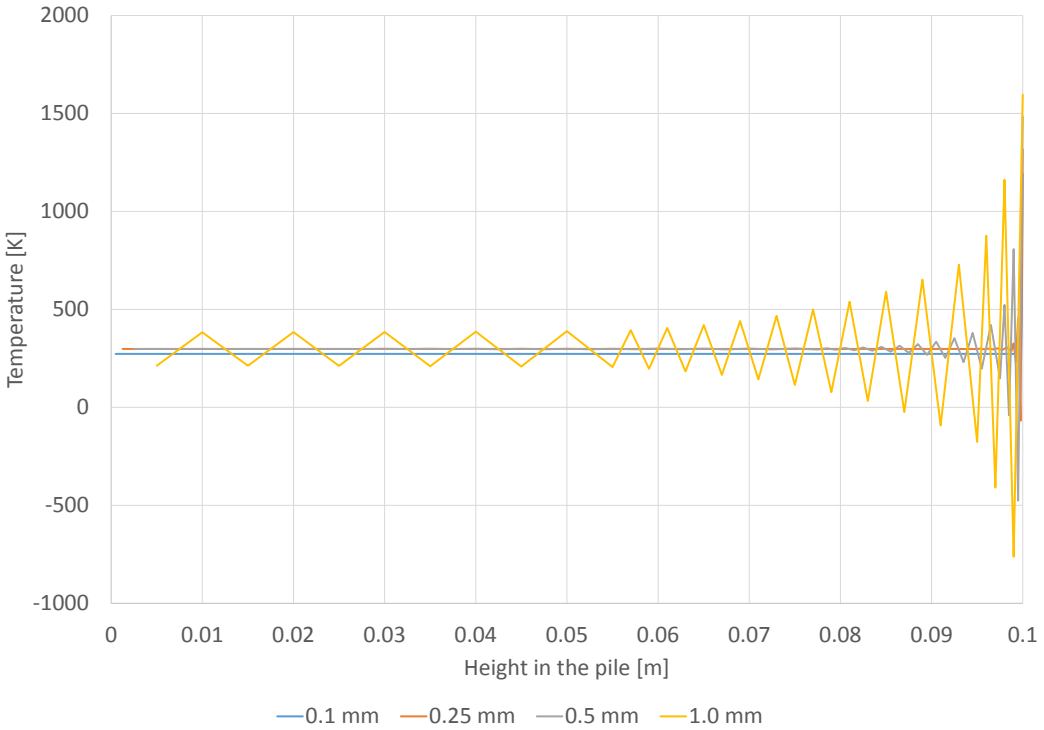

Figure A.4: Spatial temperature distribution in the pile for the different element heights - t=0,001s

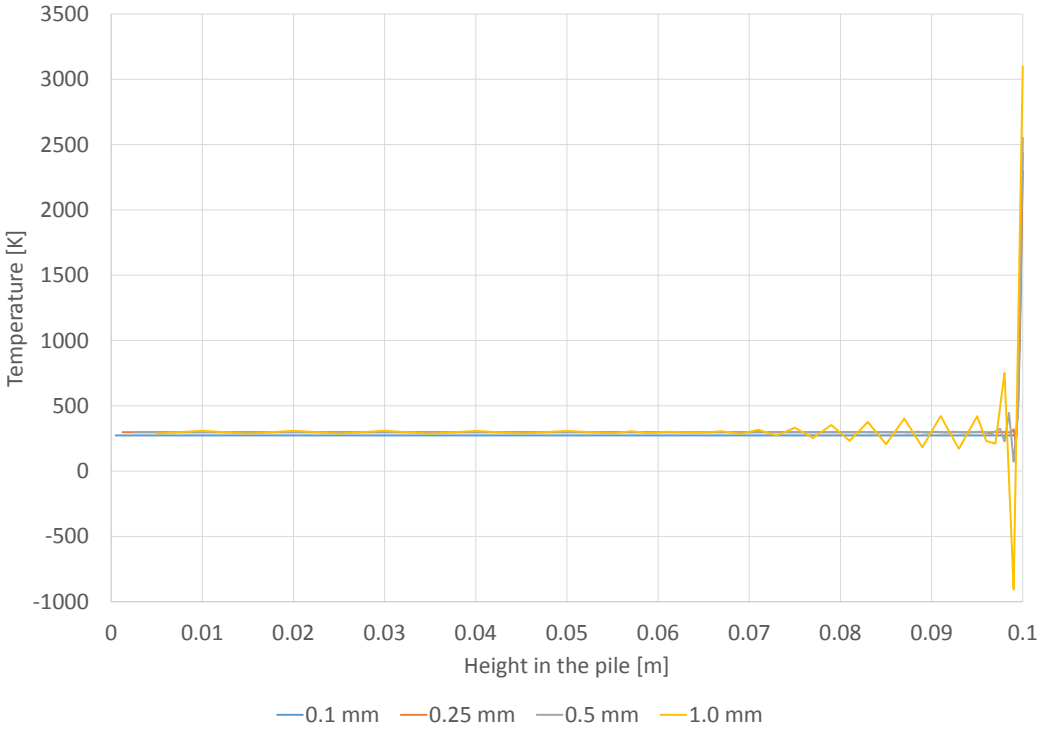

Figure A.5: Spatial temperature distribution in the pile for the different element heights - t=0,01s

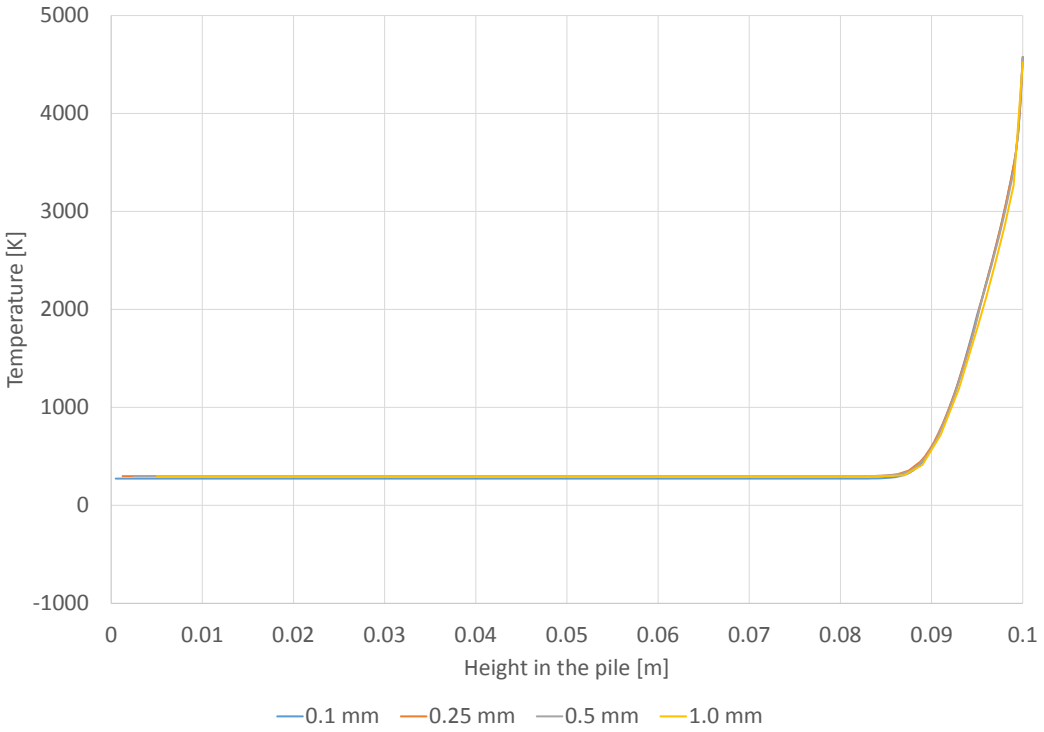

Figure A.6: Spatial temperature distribution in the pile for the different element heights - t=2,0s

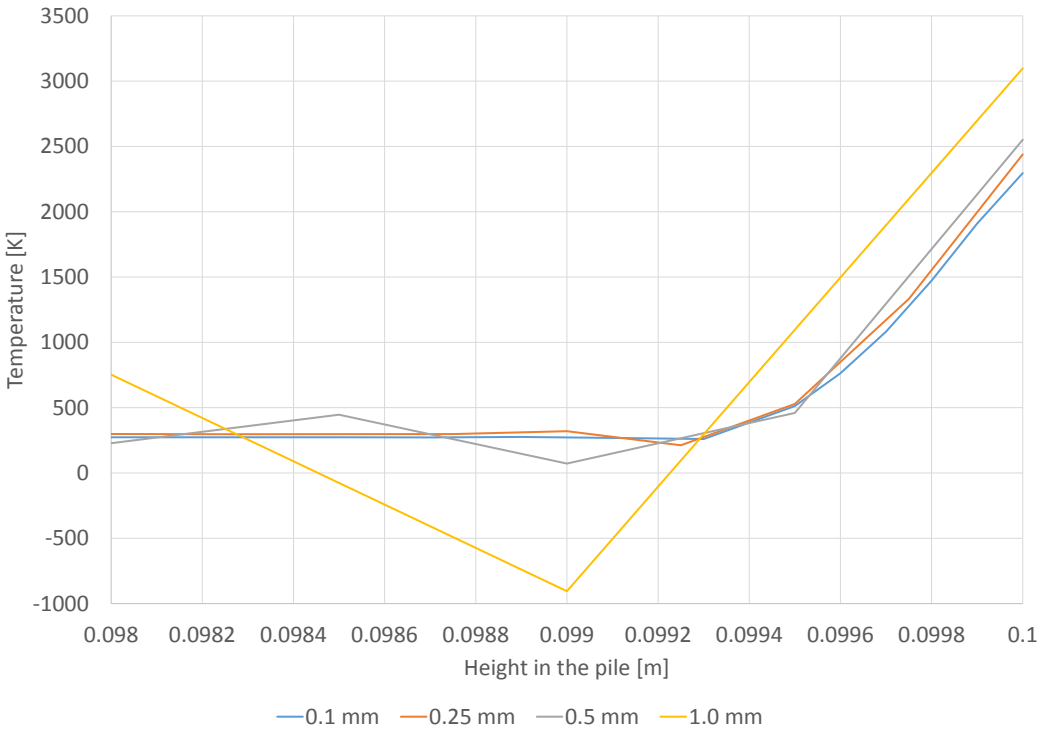

Figure A.7: Spatial temperature distribution in the pile for the different element heights - t=0,01s - Zoom for the top of the pile

A.2 Flux Sensitivity analysis - 3-D

A sensitivity study of the temperature profile obtained in the work-piece, depending on the given flux, was realised for the 3-D model. The sensitivity study was performed for 5 different flux

values. The flux per node values and their corresponding absorptivity coefficients is given in Table A.1.

Table A.1: Flux Sensitivity Analysis

	Flux [W/node]	Applied Flux [W]	Nominal Laser Flux [W]	Absorptivity β
Flux 1	30,29	727,02	1100	0,66
Flux 2	15,15	363,51	1100	0,33
Flux 3	7,57	181,76	1100	0,17
Flux 4	3,79	90,88	1100	0,08
Flux 5	1,89	45,44	1100	0,04

The temperature profile with these value of flux is studied here under for the three nodes presented in Figure A.8 (3-D) with 3 points: first cladding point (1), middle of the first pass (2) and thermocouple (3).

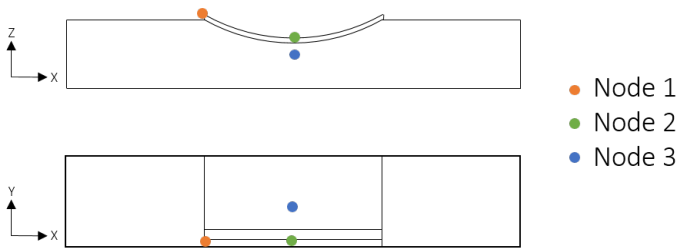

Figure A.8: Location of points 1, 2 and 3 in the work-piece

The results in the different points are given an analysed:

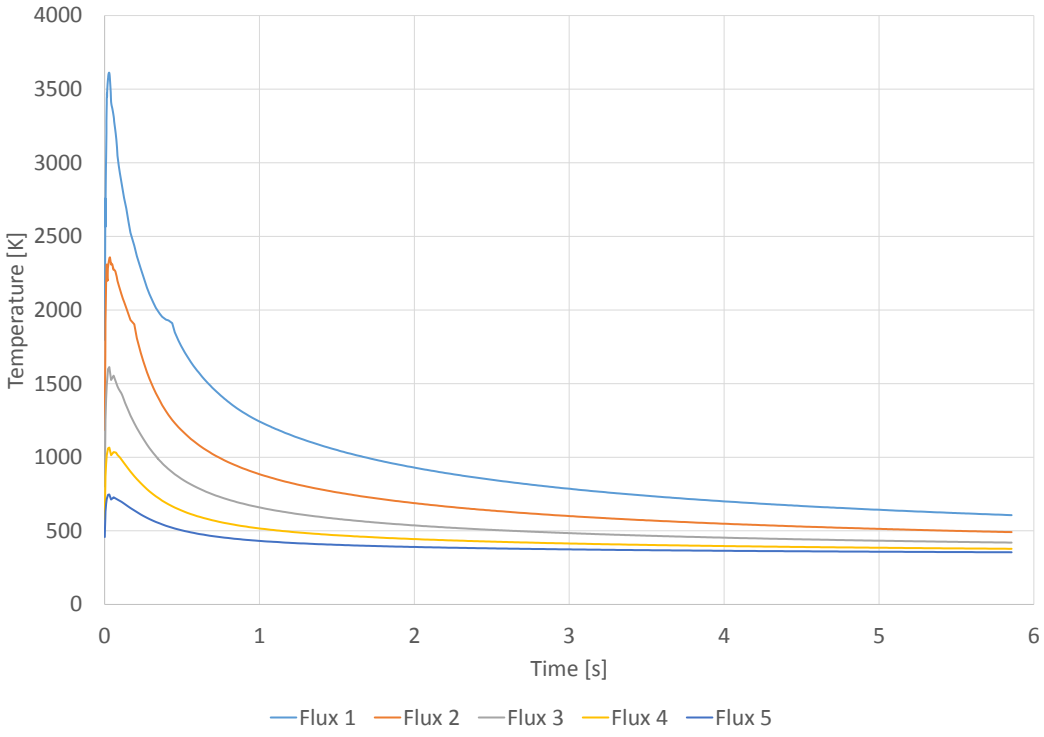

Figure A.9: Node 1 - Sensitivity to flux

Point 1: The temperature curve in Node 1 follows a similar curve with the different flux, as observed in Figure A.9. The highest flux causes numerical oscillation due to a thermal shock. By observing the maximum value of temperature obtained, we can see the relation between the applied flux and maximum temperature at this point. This relation between the maximum temperature observed and the flux applied is presented in Figure A.10.

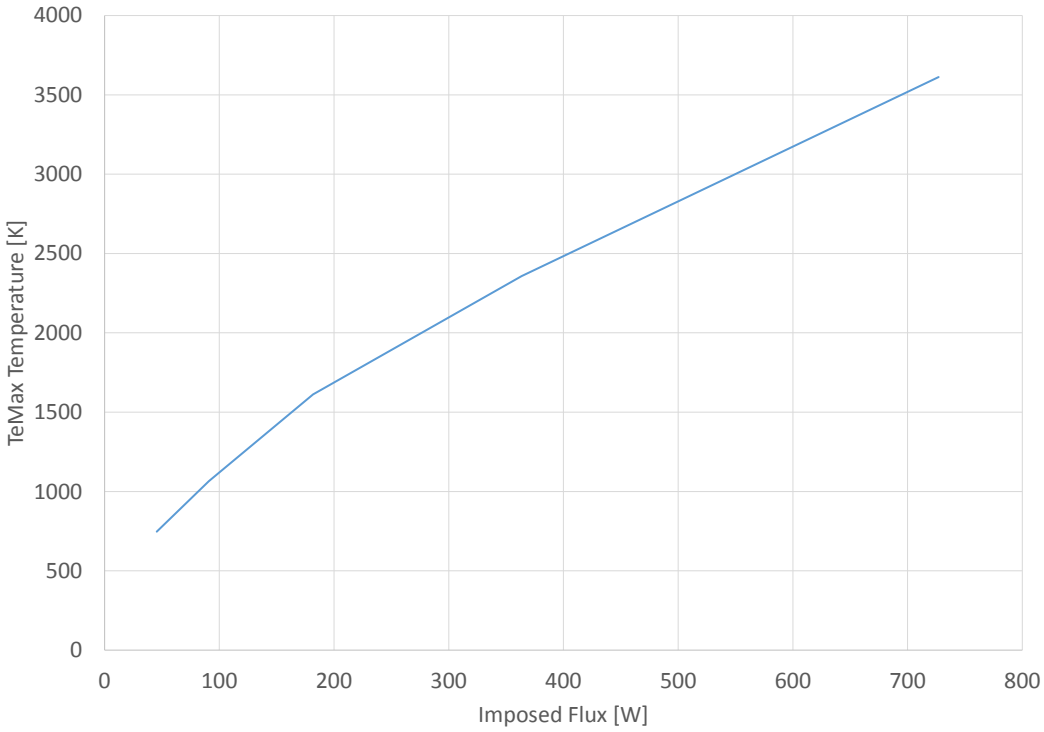

Figure A.10: Node 1 - Sensitivity to flux- Max. temperature

Similar results are obtained from the analysis at point 2:

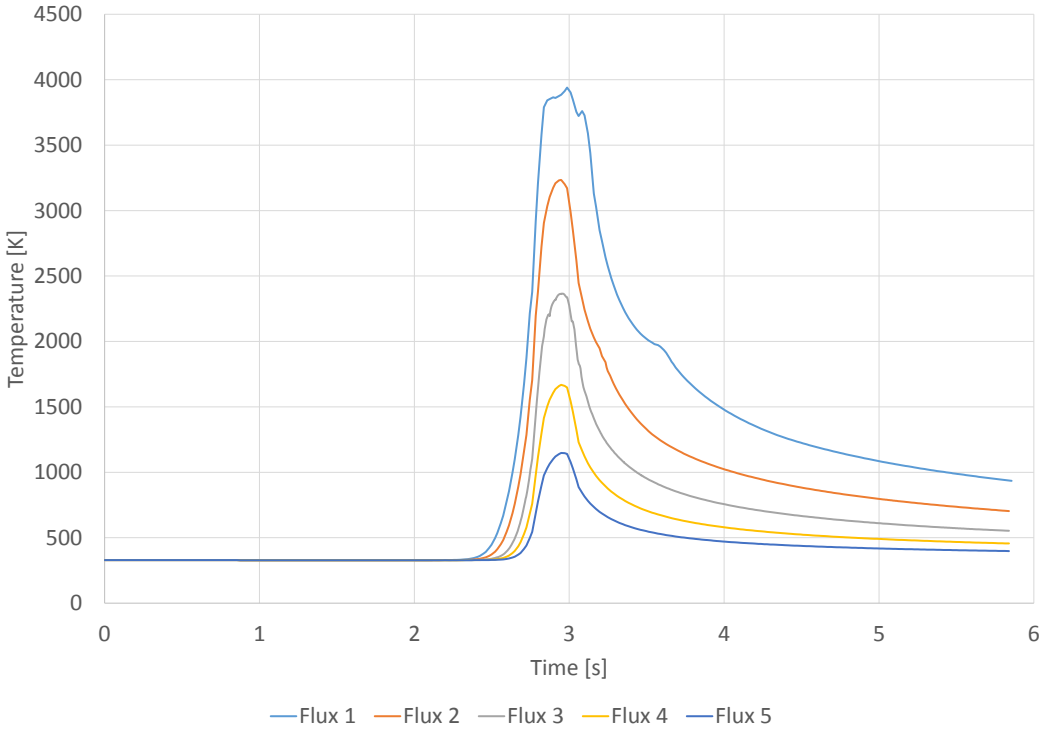

Figure A.11: Node 2 - Sensitivity to flux

The oscillations at this point are even more important. The relation between the maximum temperature observed and the flux applied at point 2 will be used later when modelling the secondary flux in the 2-D model. The physics of the value obtained must also be questioned in regard to the thermo-physical value of Ti6Al4V. As described earlier with Mills data [41]: the liquidus temperature of Ti6Al4V is $1923K$ and the vaporisation temperature is $3533K$. Therefore in node 1 and 2, with the Flux 1, Ti6Al4V will be vapourised. This value used in our numerical model does not reflect the reality as vaporisation, in large quantities, is not observed experimentally.

The analysis at point 3, the thermocouple, will be used for the calibration of the flux in the section 5.7. The following graphs were obtained:

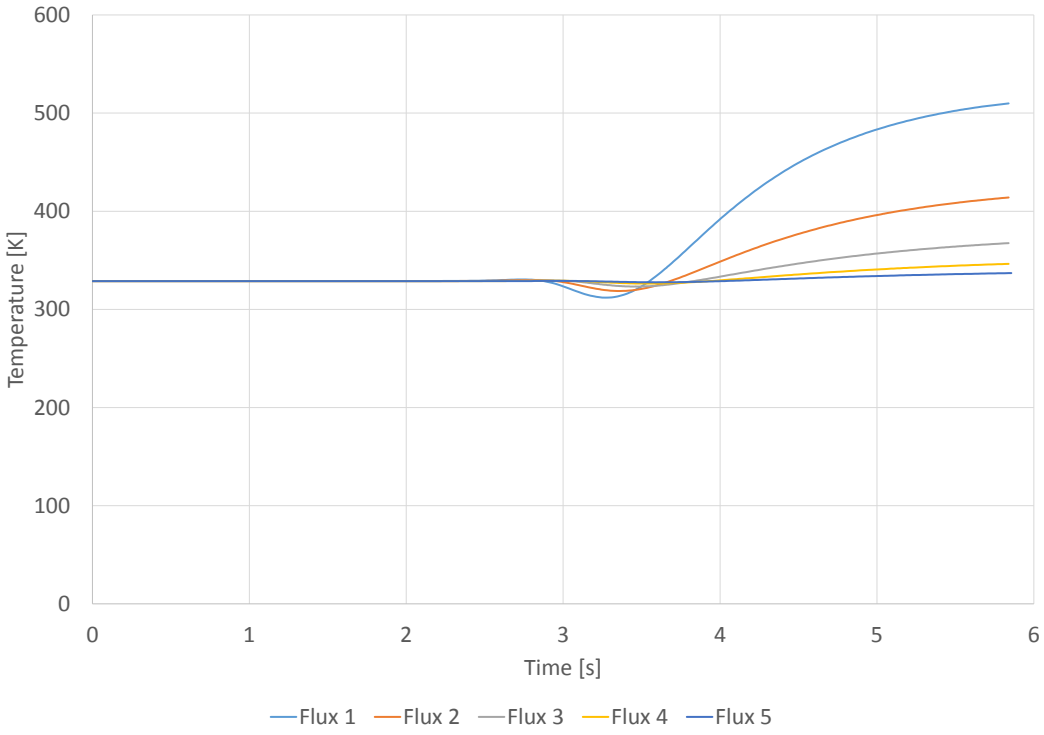

Figure A.12: Node 3 - Sensitivity to flux

The oscillations at the start are explained in detail in section5.2[1].

The maximum temperature analysis of Figure 5.40 shows a linear correlation[2] between the applied flux and the maximum temperature observed at the thermocouple for one-pass printing. This relation is used for the calibration of the flux as described in section 5.7.

A.3 Thermal Expansion Coefficient - Two Definitions

Two main definitions of the thermal expansion coefficient exist in literature and are: the classic thermal expansion coefficient α_c and the partial expansion coefficient α_p. Their definition is given

[1] As a reminder, it is due to a coarse mesh in the Y axis direction
[2] Determination coefficient of $R^2 = 0.999$

here under and based on the article of C.Bouffioux [6]. In this section we will also determined which one is used by the finite element code LAGAMINE based on a simple case.

- The classic thermal expansion coefficient α_c characterises the change in volume at a given temperature T_i with temperature compared to the initial volume at temperature T_0. In most cases, this is the value provided in literature. The mathematical expression of the coefficient is given by:

$$\alpha_{c,i} = \frac{L_i - L_0}{L_0} . \frac{1}{T_i - T_0} \tag{A.1}$$

Where L_i and L_0 are the length considered respectively in i and initially.

- The partial expansion coefficient α_p characterises the change in volume measured between two close temperatures T_{i-1} and T_i. This is the value needed for the LAGAMINE law. The mathematical expression is given by:

$$\alpha_{p,i} = \frac{L_i - L_{i-1}}{L_{i-1}} . \frac{1}{T_i - T_{i-1}} \tag{A.2}$$

Where L_{i-1} is the length considered in $i-1$. Similarly, if two infinitely close temperature T_i and T_{i-1} are considered, the equation A.2 of $\alpha_{p,i}$ can be written:

$$\alpha_p(T) = \frac{1}{L(T)} . \frac{dL}{dT}(T) \tag{A.3}$$

C.Bouffioux provides in [6] the mathematical equation to express α_p, as used in LAGAMINE, as a function of α_c, given in literature. By considering equations A.1 and A.2 the equation becomes:

$$\alpha_{p,i} = \frac{\alpha_{c,i} . (T_i - T_0) - \alpha_{c,i-1} . (T_{i-1} - T_0)}{(T_i - T_{i-1}) . (1 + \alpha_{c,i} . (T_i - T_0)} \tag{A.4}$$

And similarly by considering equations A.1 and A.3:

$$\alpha_{p,i} = \frac{\alpha_{c,i} + (T_i - T_0) . \frac{d\alpha_c}{dT}(T_i)}{1 + \alpha_{c,i} . (T_i - T_0)} \tag{A.5}$$

In order to ensure that LAGAMINE is using the partial thermal expansion coefficient, a numerical study was performed on a simplified case. The numerical experiment involves modelling one single solid element (dimension 10x25 mm) subjected to a steady increase in temperature. The temperature increase will be slow (1°C/20 s.) and will start at a temperature of 25°C up to 1000°C. Convection and radiation are not considered.

By applying a constant value of $\alpha = 1,1.10^{-5}$ $[m.m^{-1}.K^{-1}]$ and observing the thermal deformation of the element, the result obtained is:

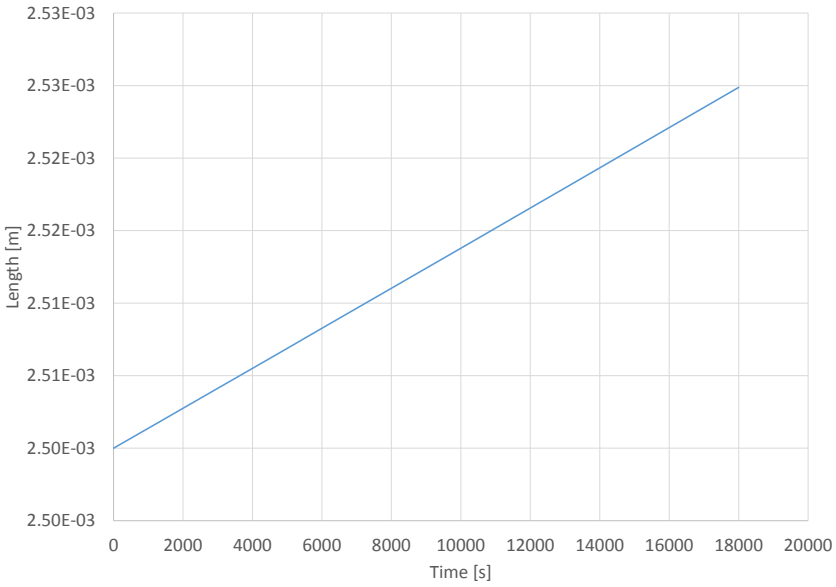

Figure A.13: Change in length of the element with time. Temperature increase of 1°C / 20 seconds.

Based on this change in depth and by applying the equations A.1 and A.2, the corresponding α_p and α_c coefficients are:

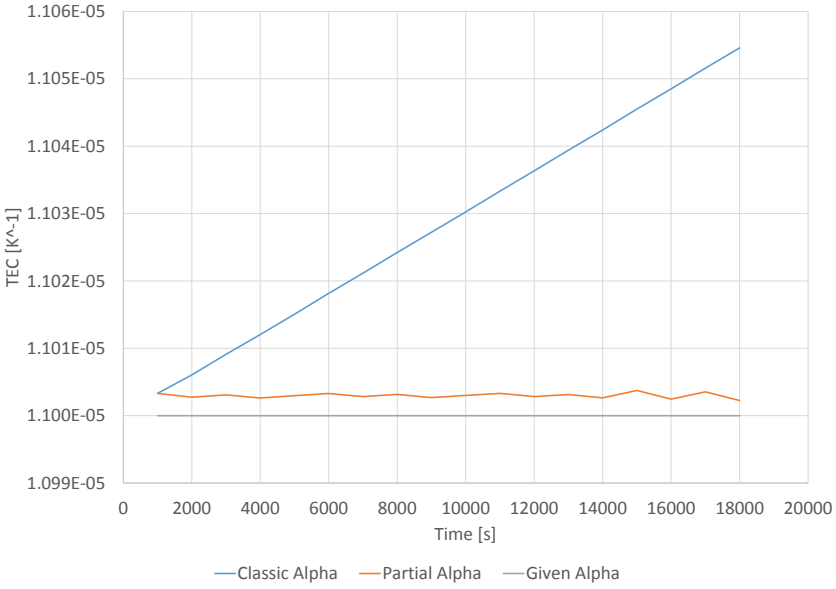

Figure A.14: α_c and α_p computed from Figure A.13 compared to the value of α given in LAGAMINE.

Where Figure A.14 shows that the value used by LAGMINE is the partial thermal expansion coefficient α_p. When looking at thermal expansion coefficients for Ti6Al4V in literature, a special attention will be placed on the definition of this coefficient.

A.4 Influence study - Integration scheme

In this section, the influence of the integration scheme, built in the finite element code LAGAMINE, will be studied. In particular, we will look at the computation time differences with the different schemes. A comparison of the results obtained is also provided.

Depending on the value of the two time integration parameters Θ and β chosen[3], different approximations will be obtained. Different combinations of Θ and β will be tested, each combination corresponding to a well-known integration scheme. The schemes that will be studied are the following:
-Implicit, $\Theta = 1$ and $\beta = 0$.
-Galerkin, $\Theta = 2/3$ and $\beta = 1/6$.
-Crank-Nicolson, $\Theta = 1/2$ and $\beta = 1/4$.

In literature, comparison of these temporal integration scheme is available[9]. The results obtained with the different time-integration schemes are synthesised in Table A.2:

Table A.2: Impact of the time-integration scheme on the computation time

Integration scheme	Computation time [s]	Mean difference with the experimental results [%]
Implicit	5228	1,33
Galerkin	4701	1,37
Crank-Nicolson	No result	No result

No results can be provided for the Crank-Nicolson time-integration scheme as it leads to oscillations at the beginning of the cladding, leading to temperatures outside of the temperature range defined in the law definition. We can see from Table A.2 that the Galerkin scheme is in this specific case more efficient than the implicit scheme. Nevertheless, the results differ slightly and so as not to affect them, it is chosen to keep the implicit time-integration scheme for the following simulation.

[3]The definition of these time-integration parameters can be found in literature

A.5 DESFIN Results

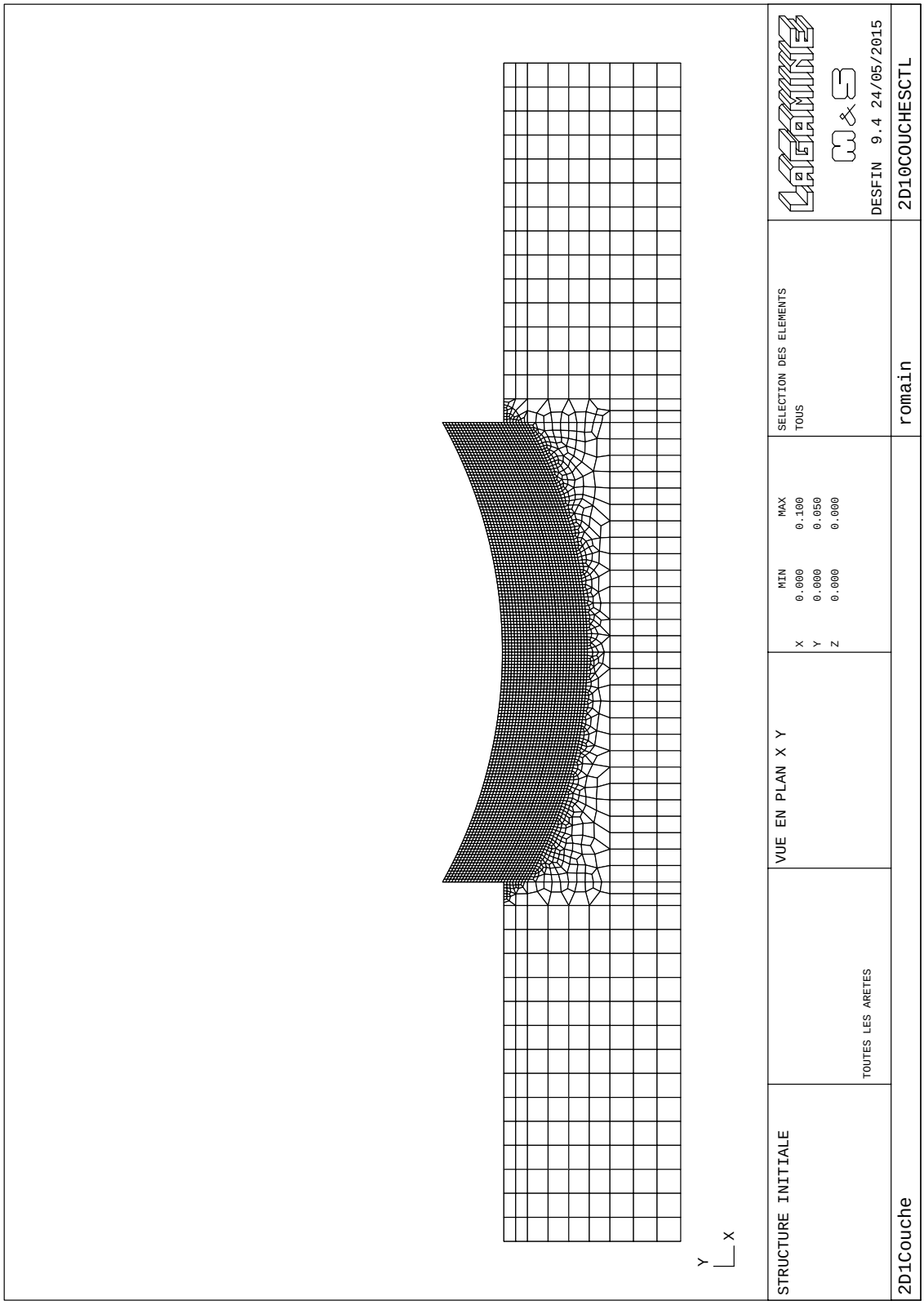

Figure A.15: 2-D model: view from DESFIN, LAGAMINE's viewer

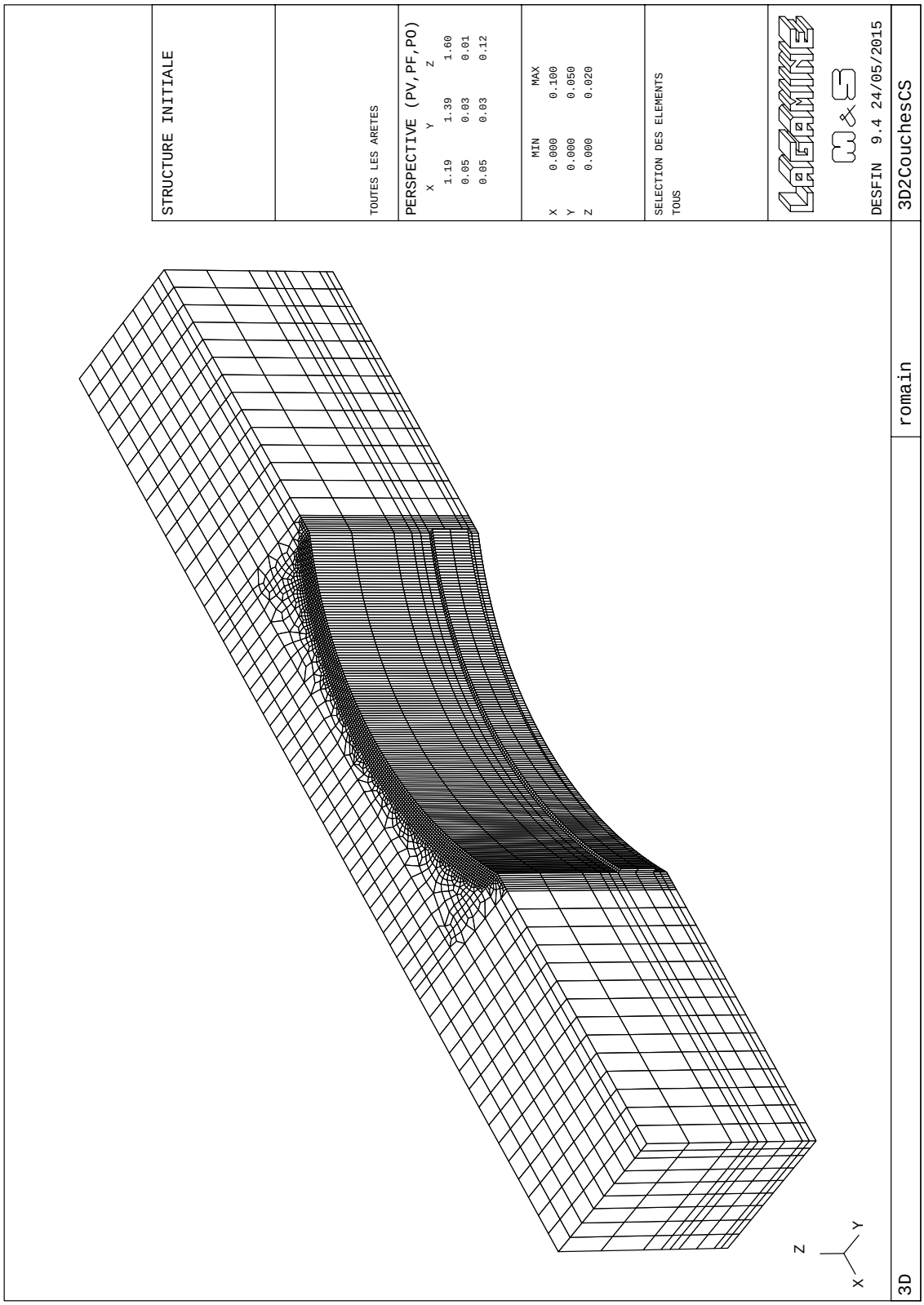

Figure A.16: 3-D model with 2 passes: standard axonometry from DESFIN, LAGAMINE's viewer

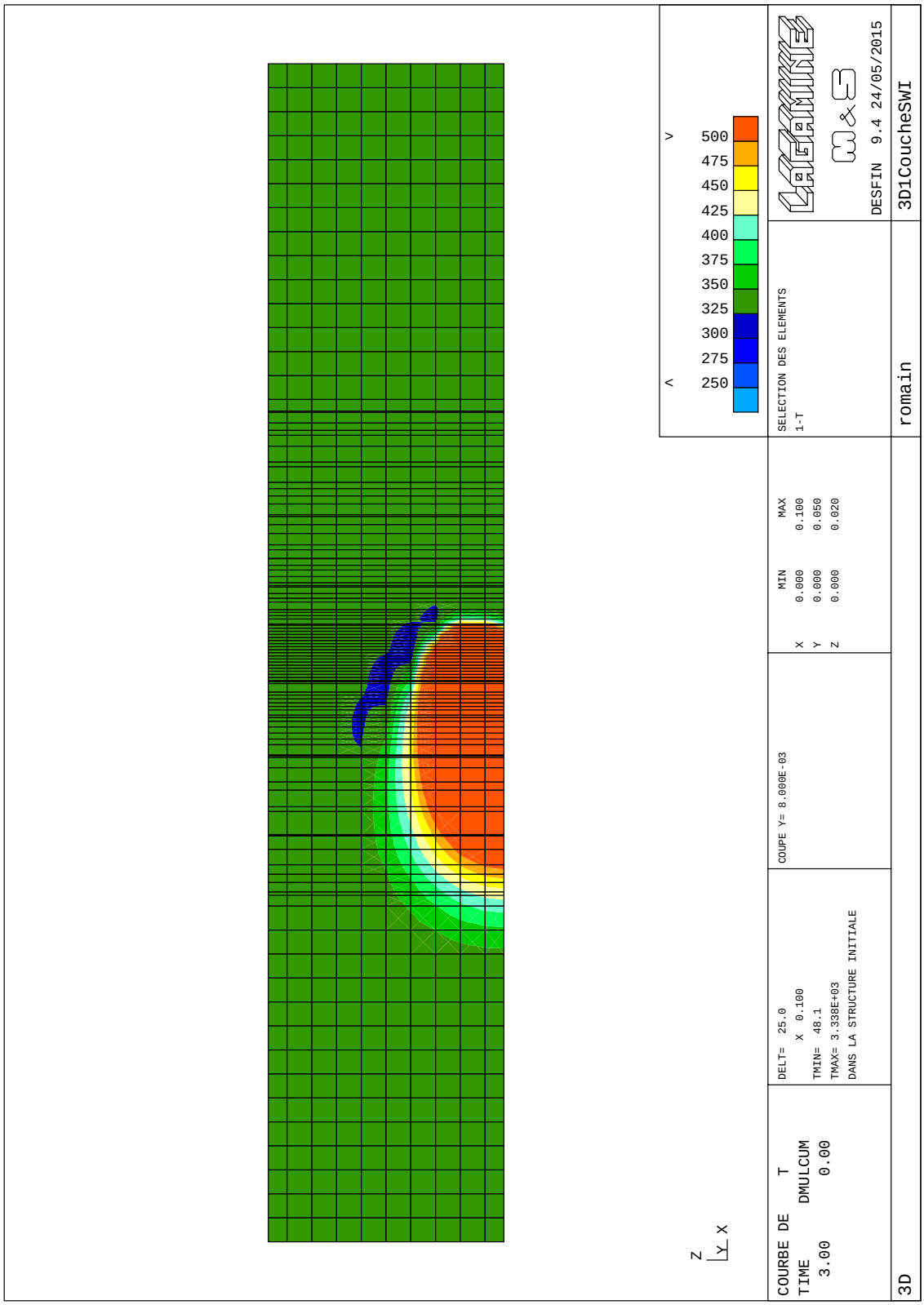

Figure A.17: 3-D model: spatial oscillations in temperature for a horizontal view at a height of $8mm$ and at $t = 3s$

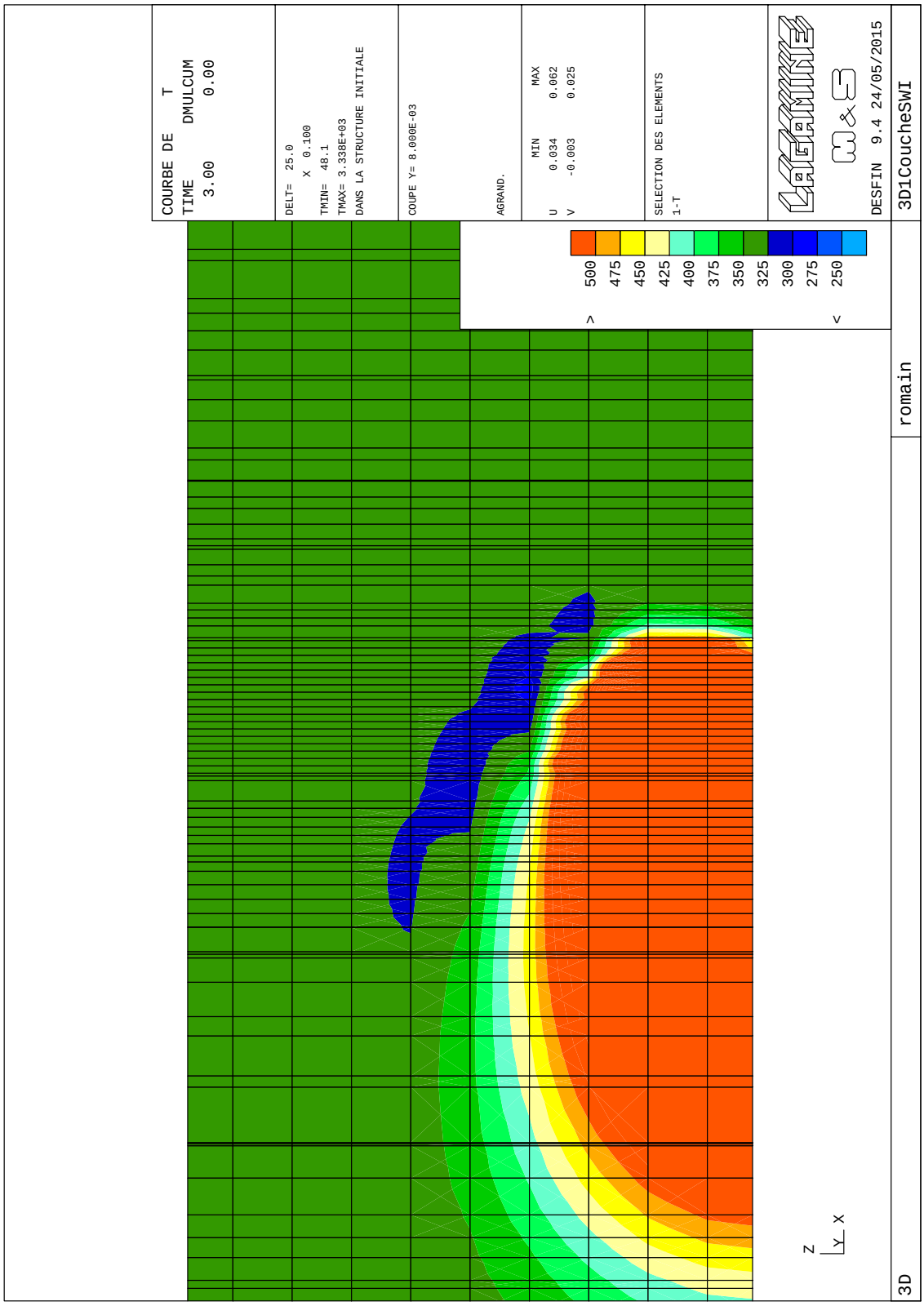

Figure A.18: 3-D model: spatial oscillations in temperature for a horizontal view at a height of $8mm$ and at $t = 3s$. Zoom on the oscillations

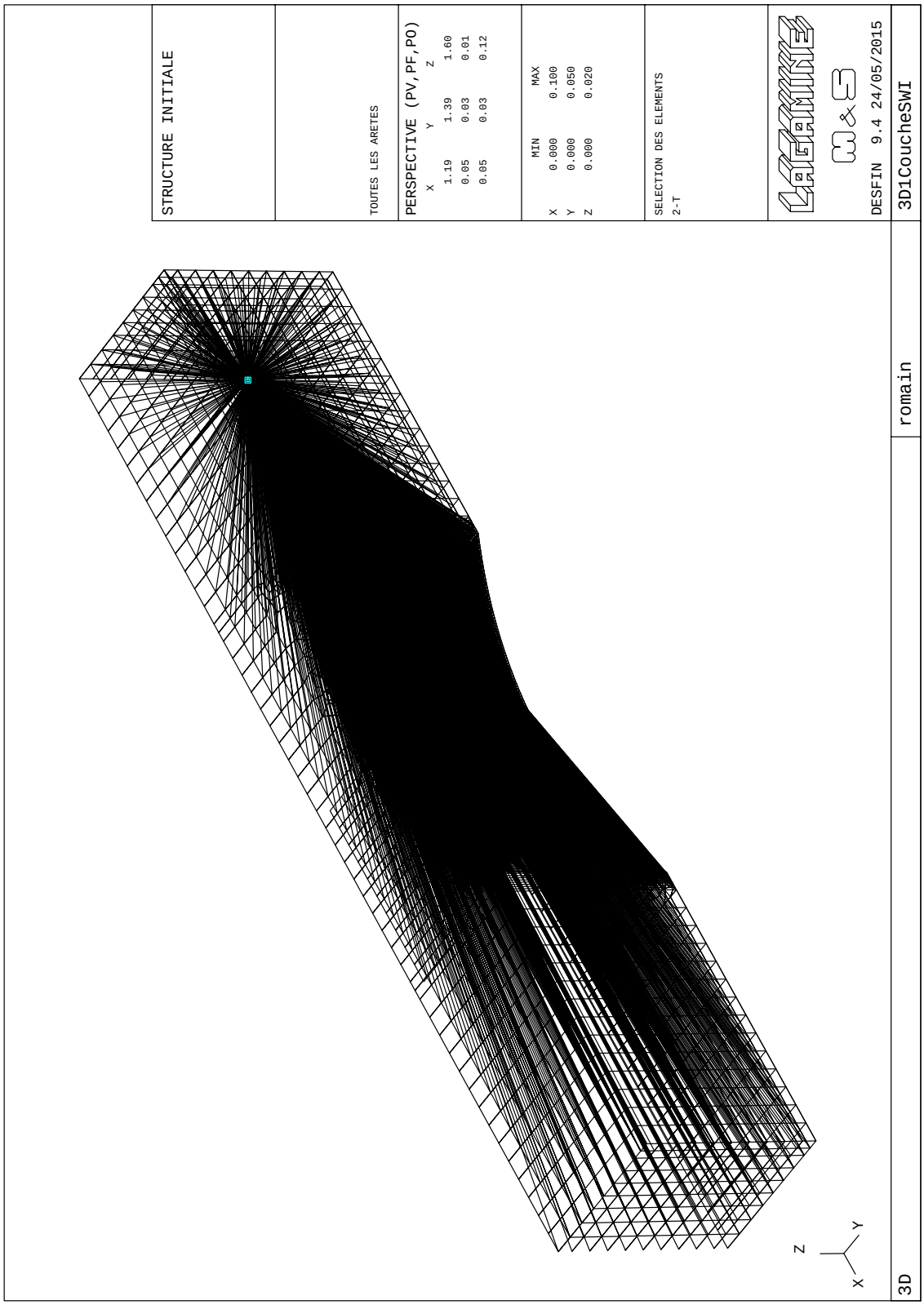

Figure A.19: 3-D model: problem while displaying CORA3 element with DESFIN viewer. All elements look like they have point 1 in common

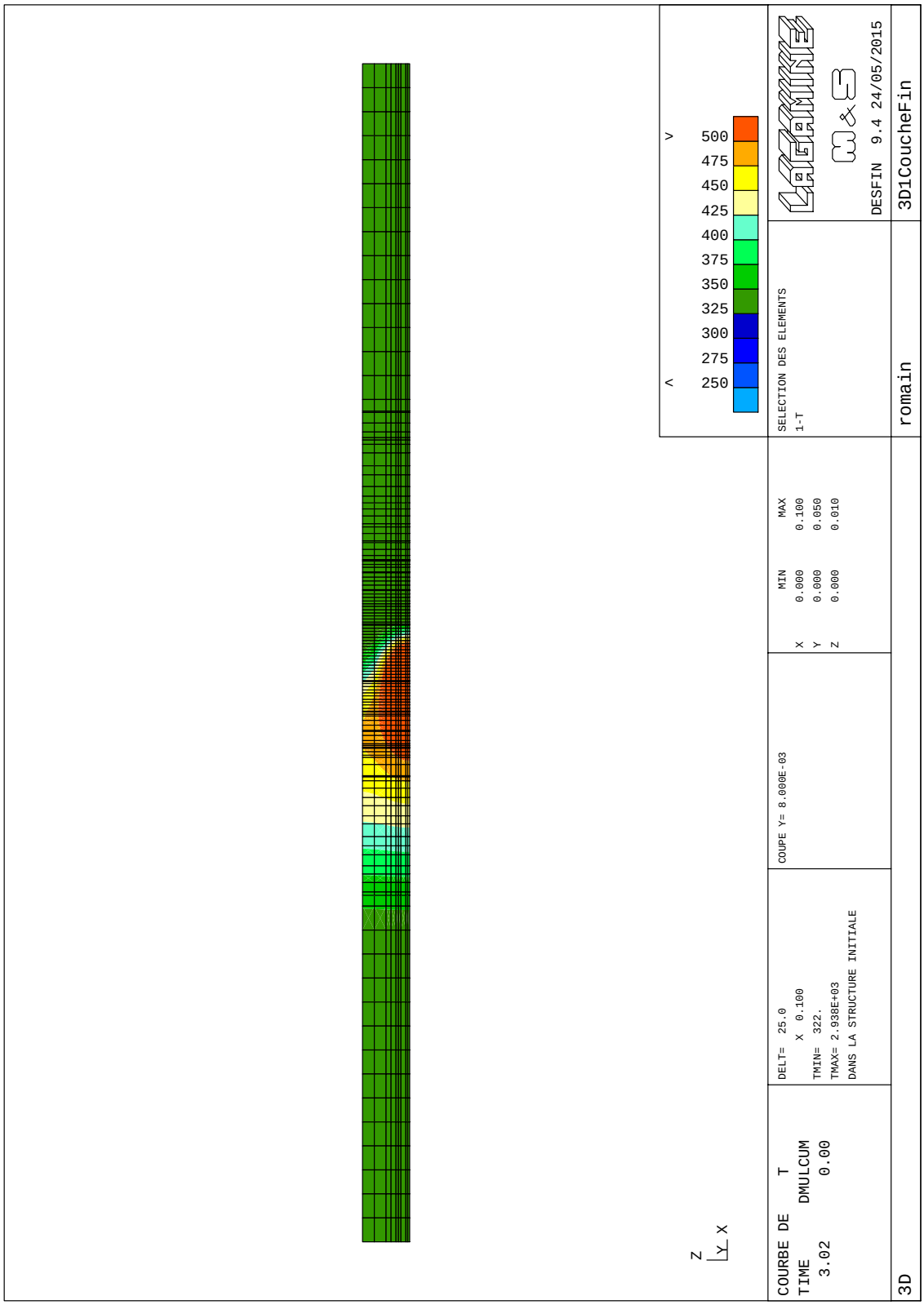

Figure A.20: Modified 3-D model: simulation at height $8mm$ and $t = 3s$. No oscillations observed along the Z axis

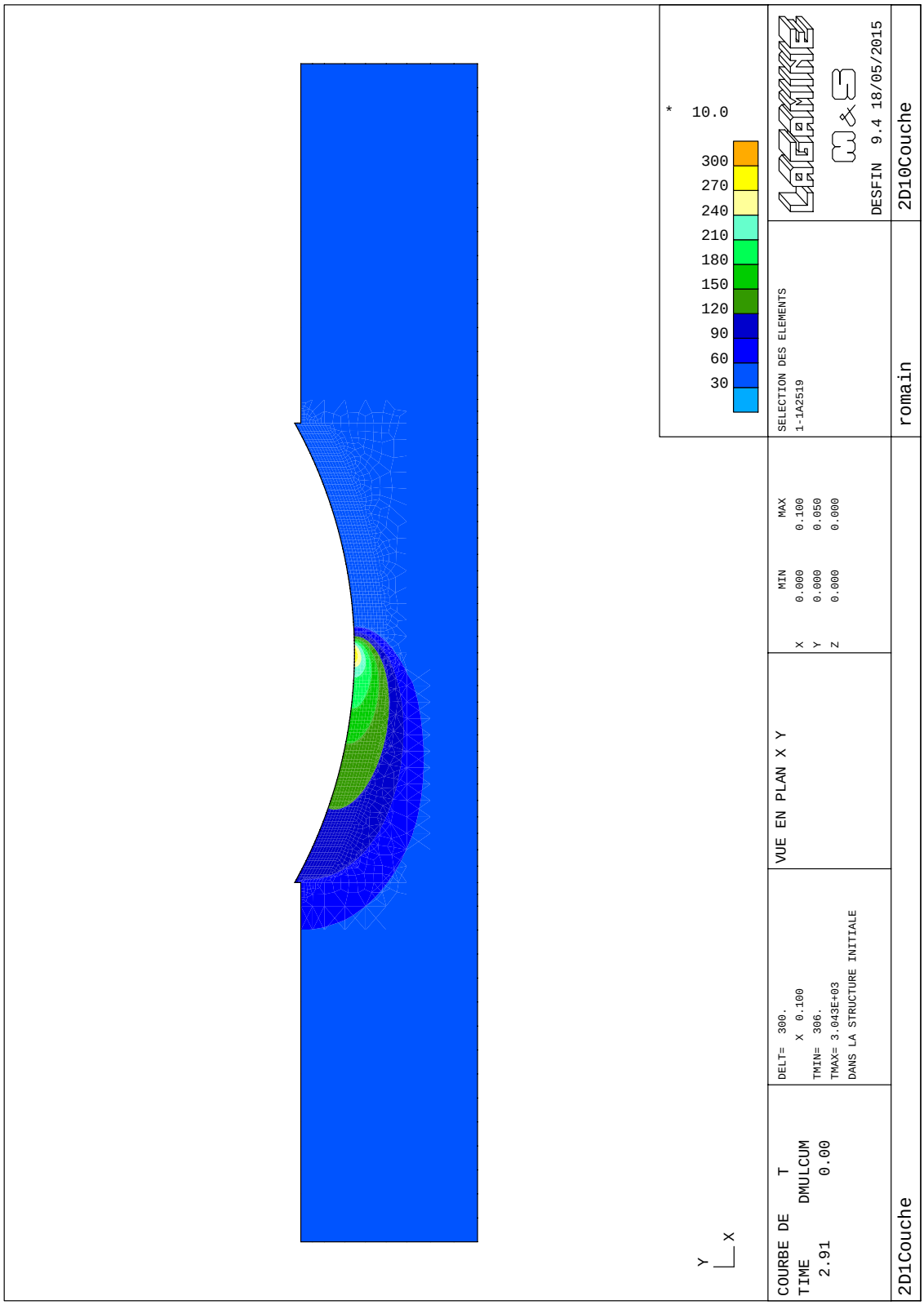

Figure A.21: Temperature profile - Middle of clad 1.

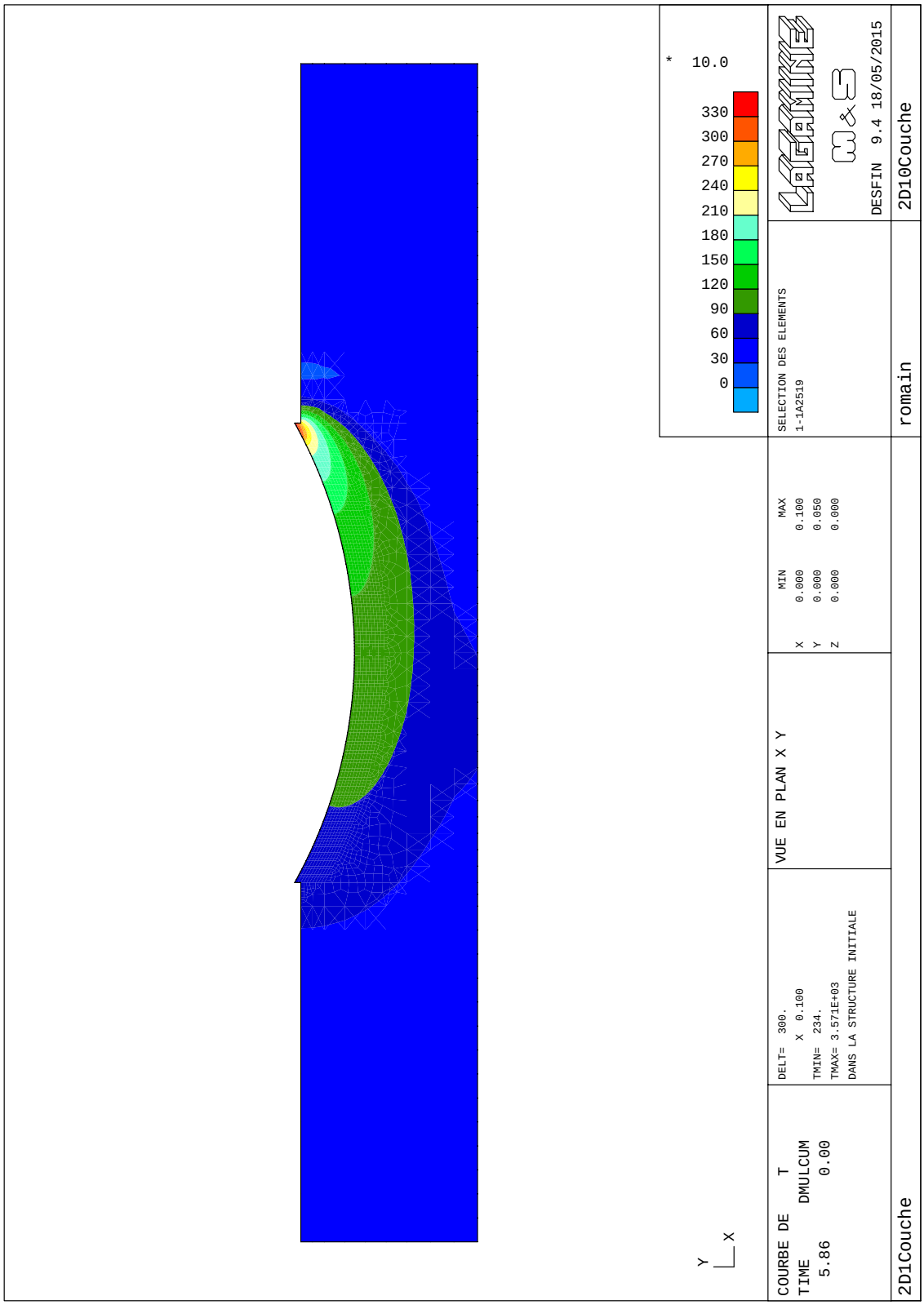

Figure A.22: Temperature profile - End of clad 1.

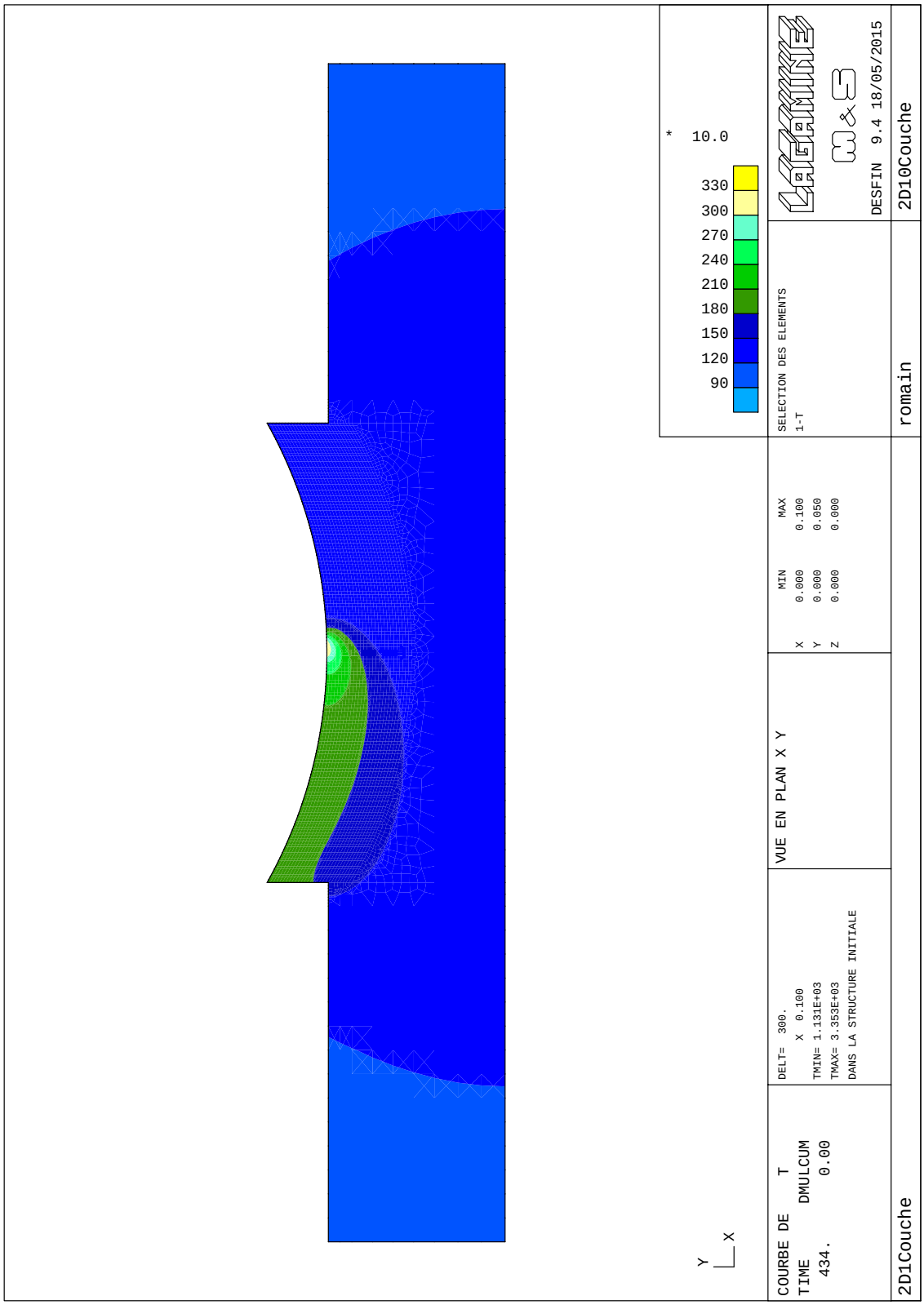

Figure A.23: Temperature profile - Middle of clad 10 - CTL

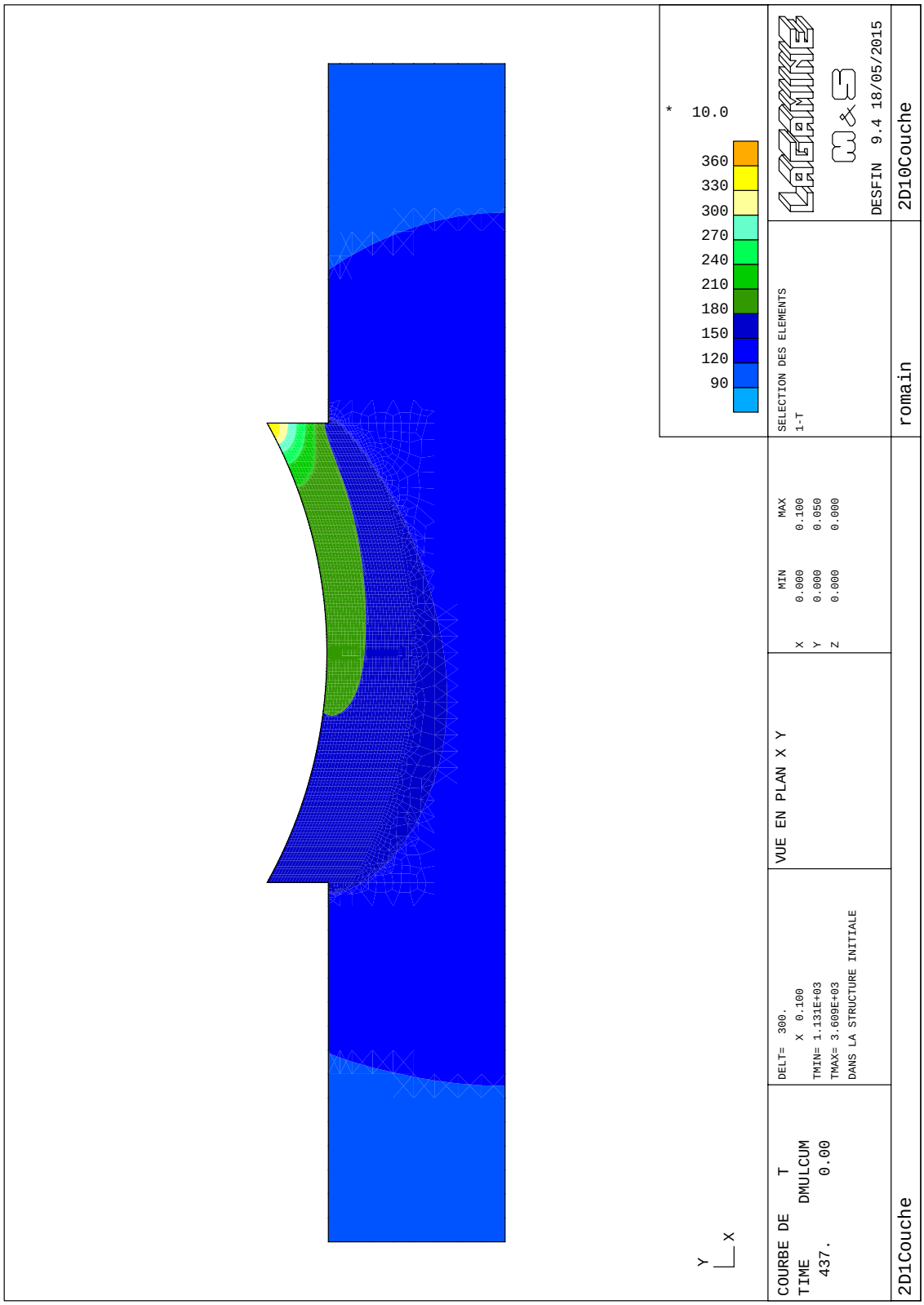

Figure A.24: Temperature profile - End of clad 10 - CTL

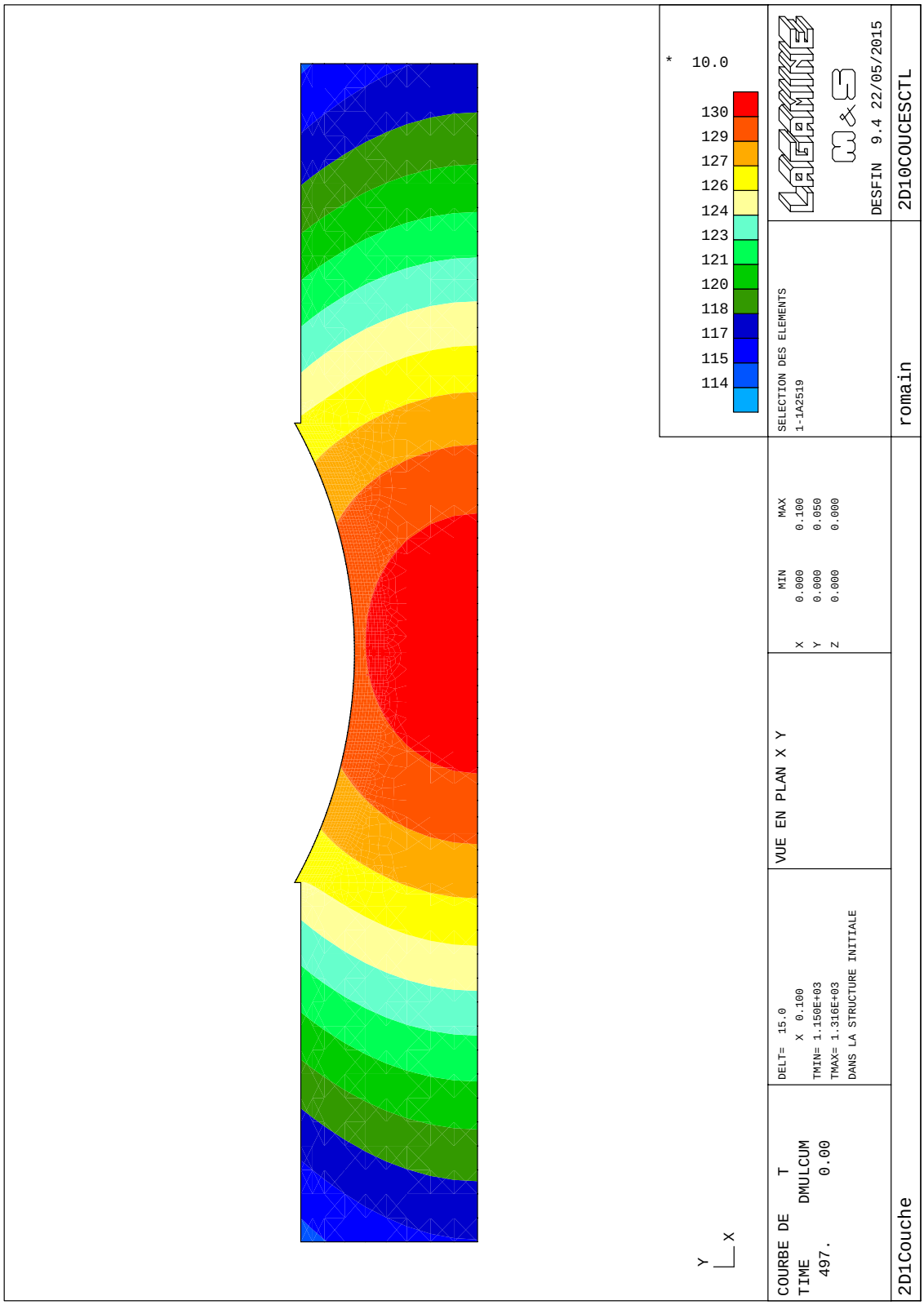

Figure A.25: Temperature profile - End of cooling - CTL

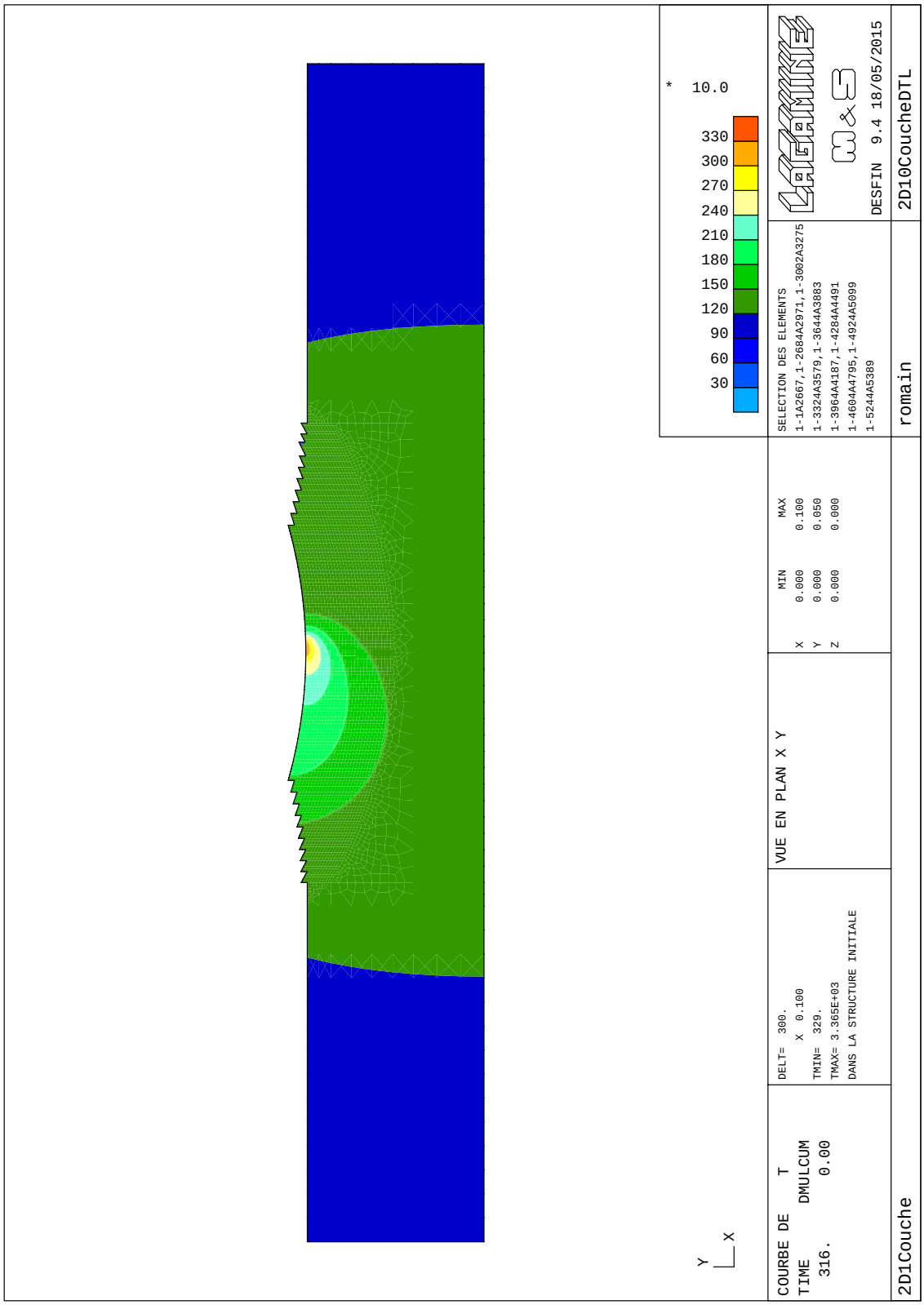

Figure A.26: Temperature profile - Middle of clad 10 - DTL

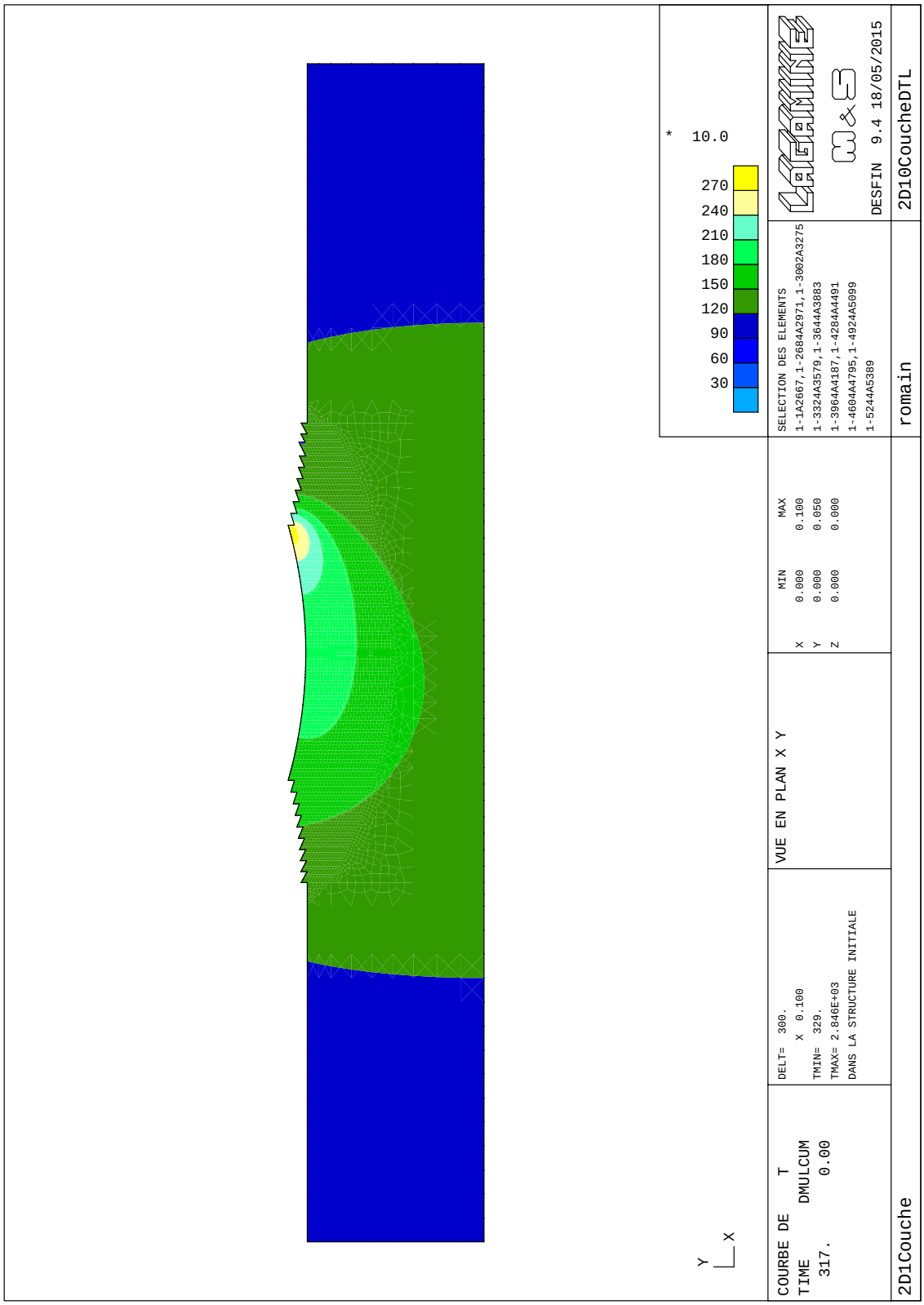

Figure A.27: Temperature profile - End of clad 10 - DTL

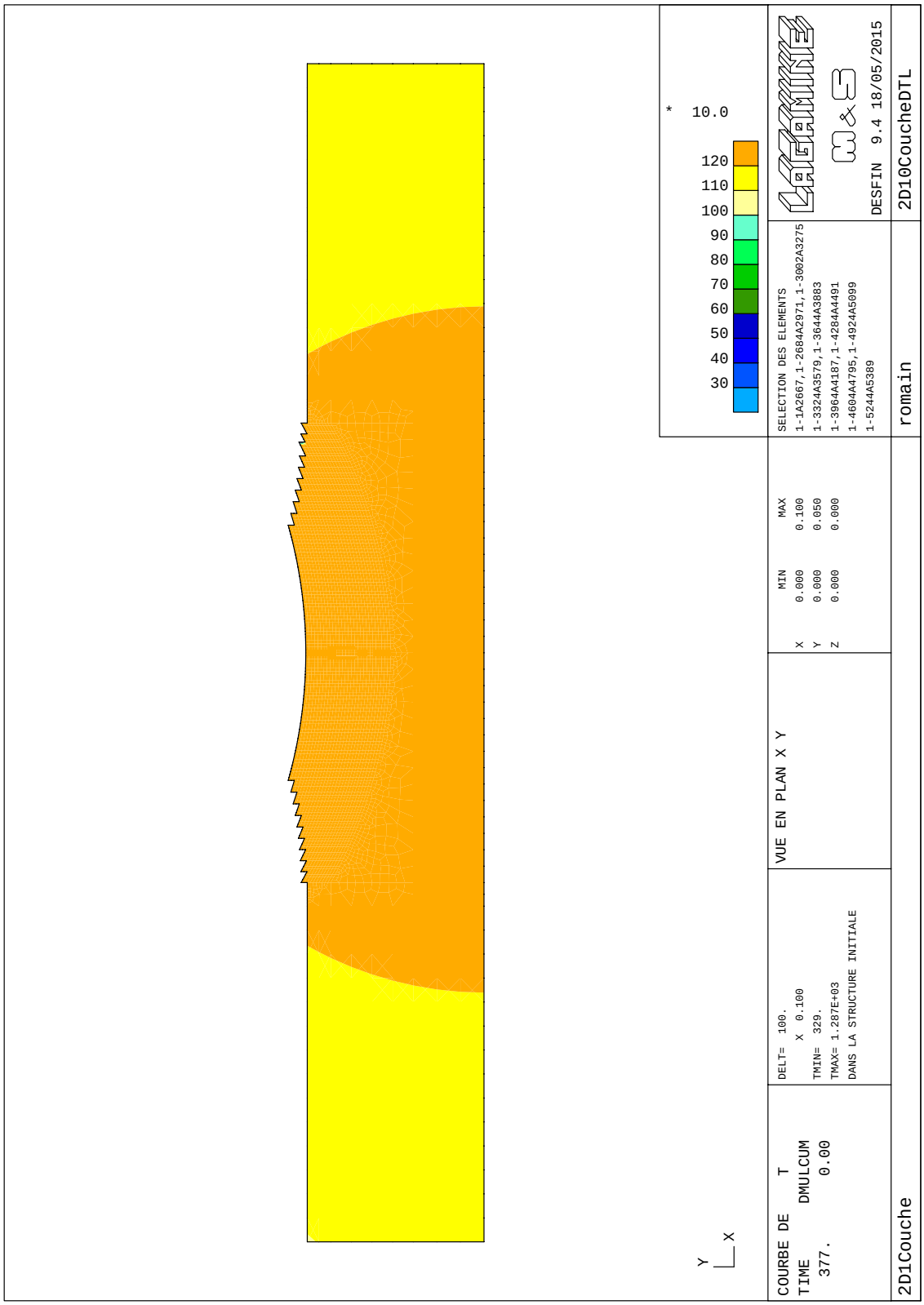

Figure A.28: Temperature profile - End of cooling - DTL

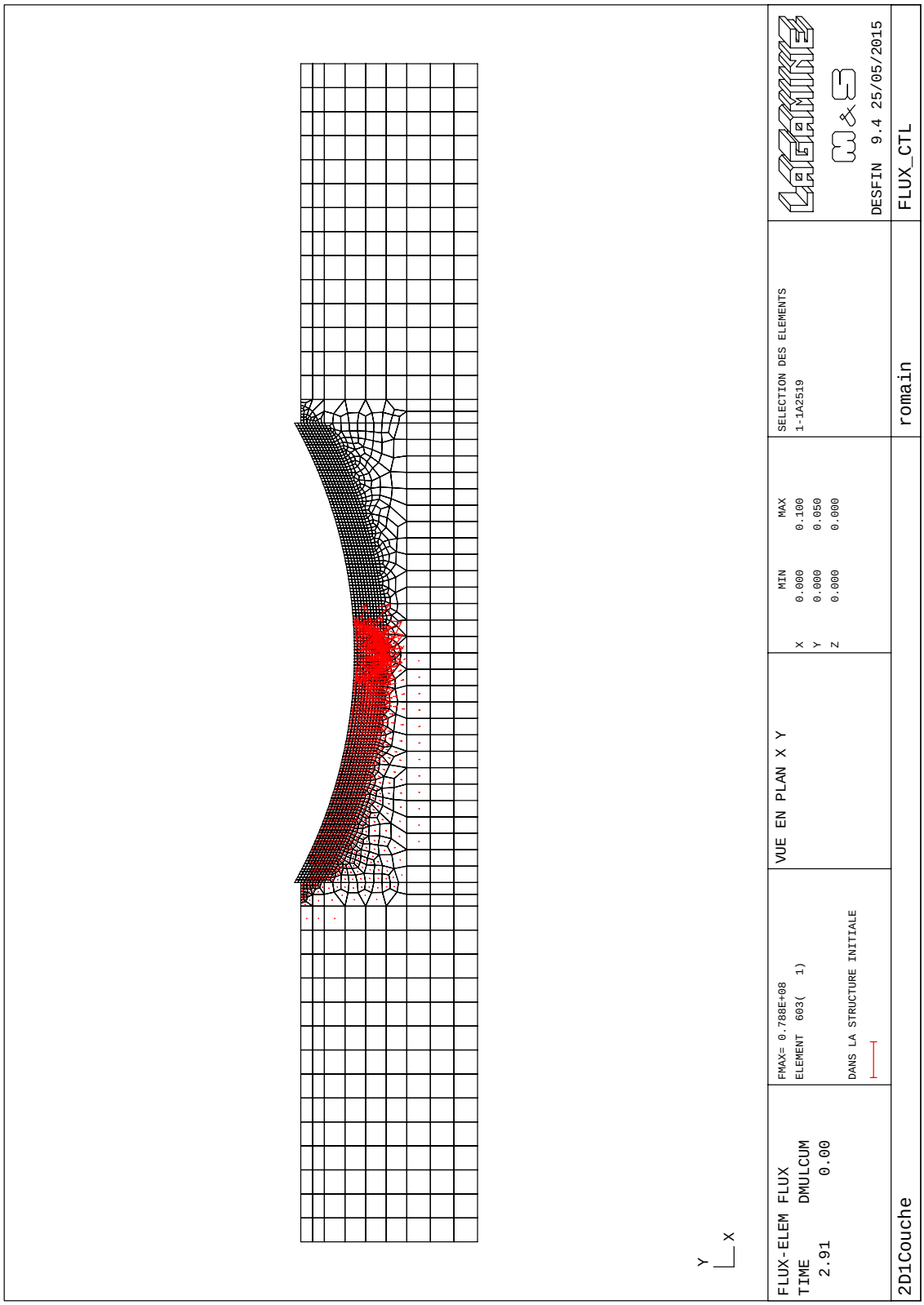

Figure A.29: Flux distribution - Middle of layer 1 - CTL

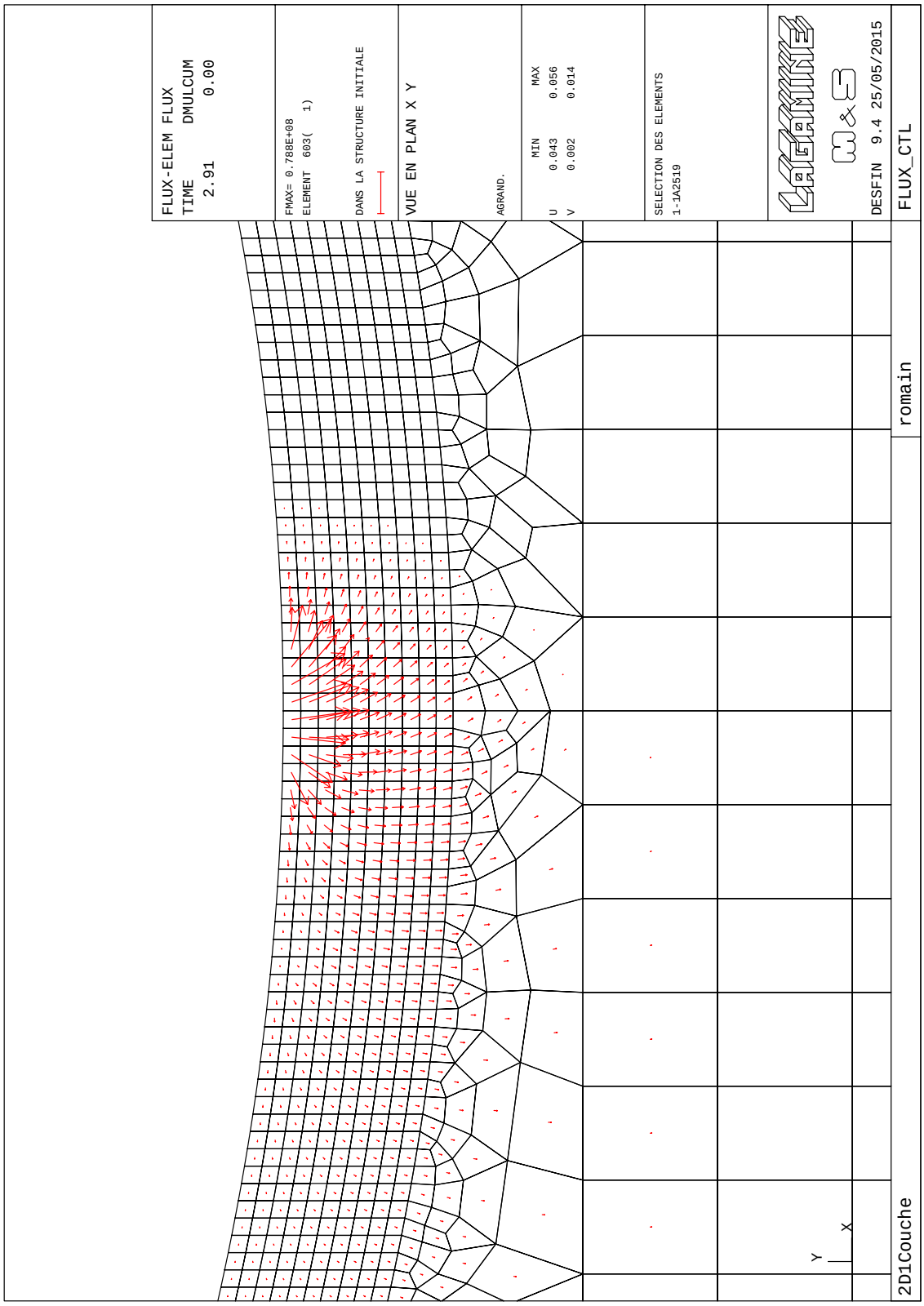

Figure A.30: Flux distribution zoom - Middle of layer 1 - CTL

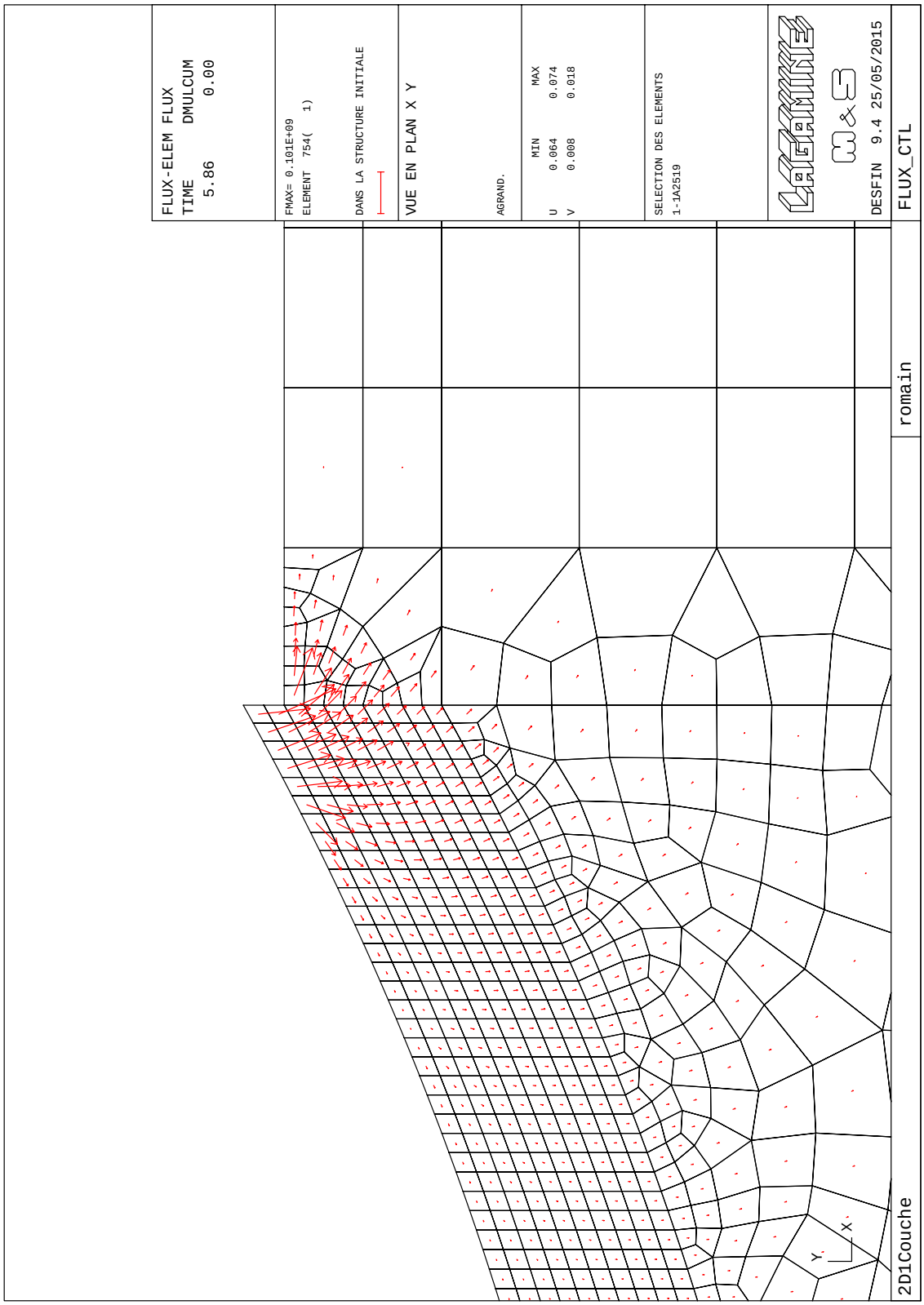

Figure A.31: Flux distribution zoom - End of layer 1 - CTL

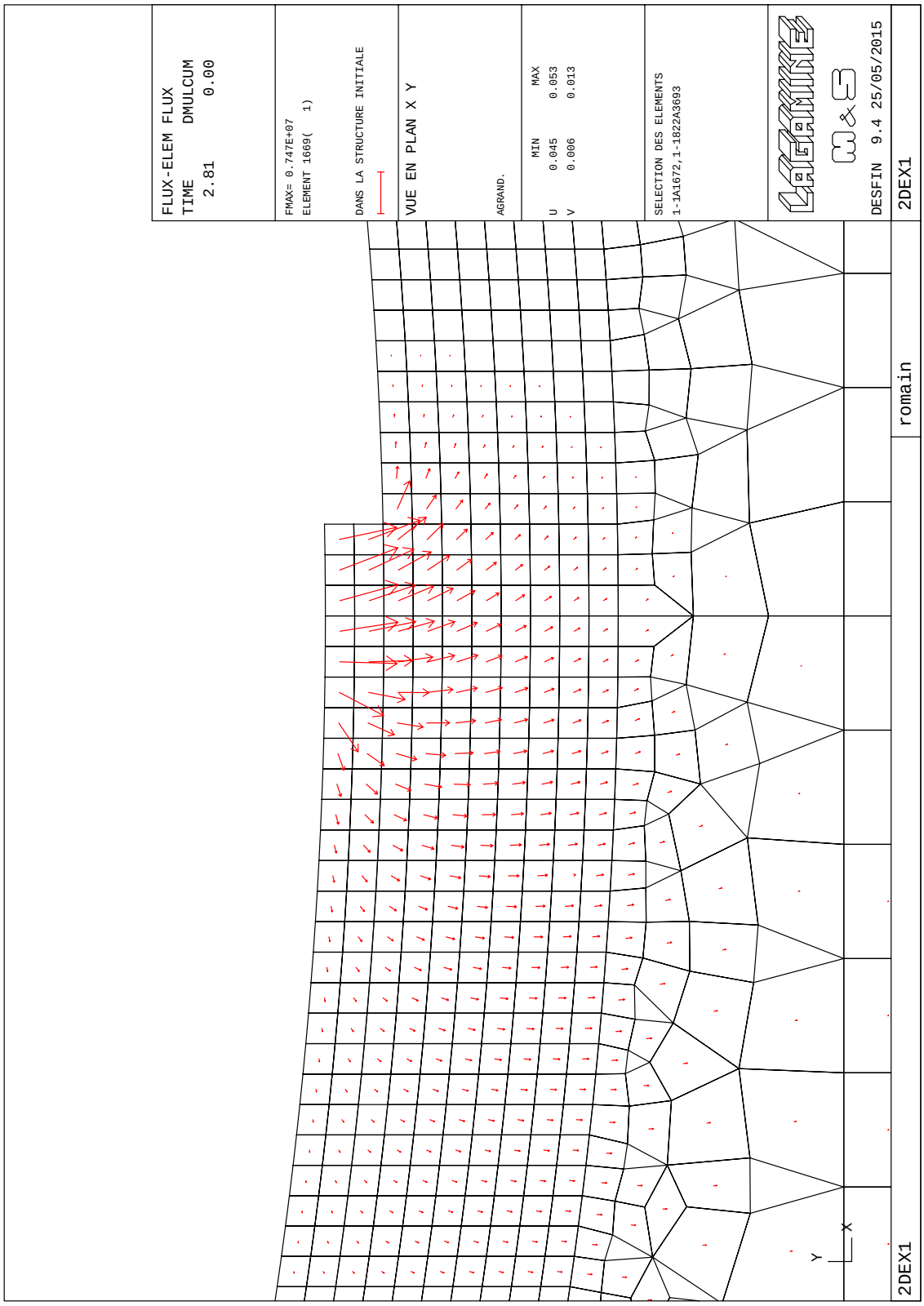

Figure A.32: Flux distribution with element-by-element activation strategy

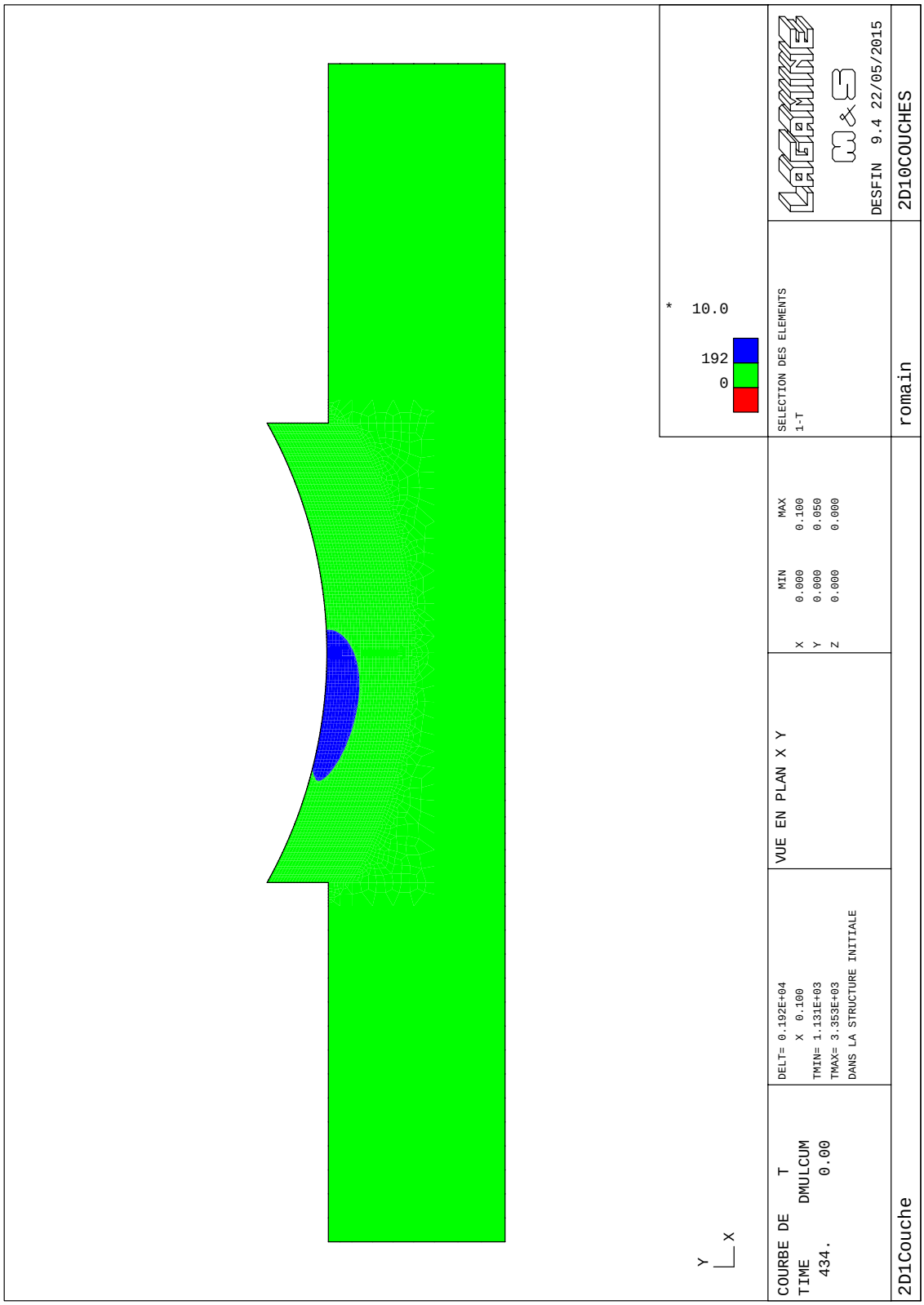

Figure A.33: Thermally affected zone shape - CTL

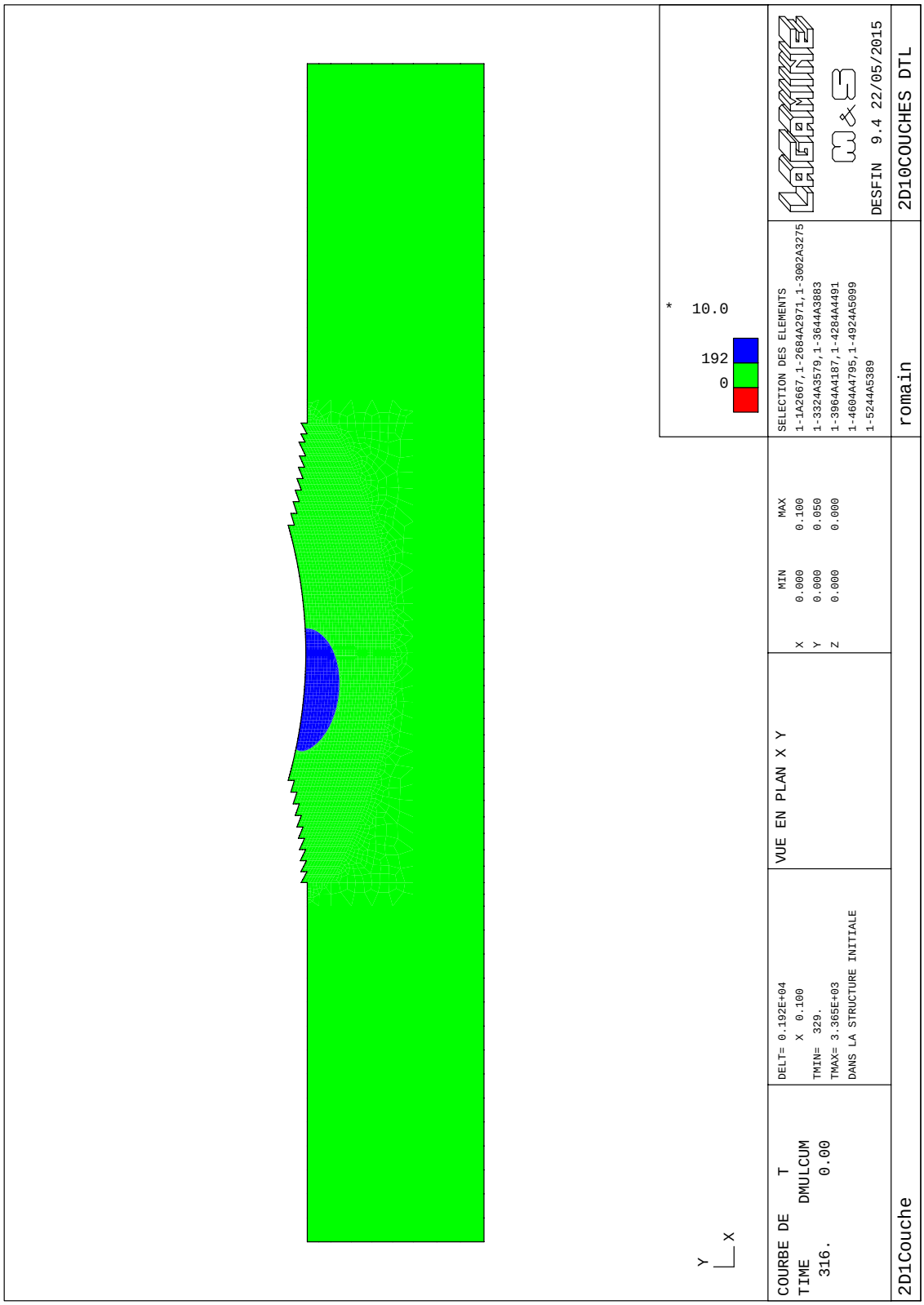

Figure A.34: Thermally affected zone shape -DTL

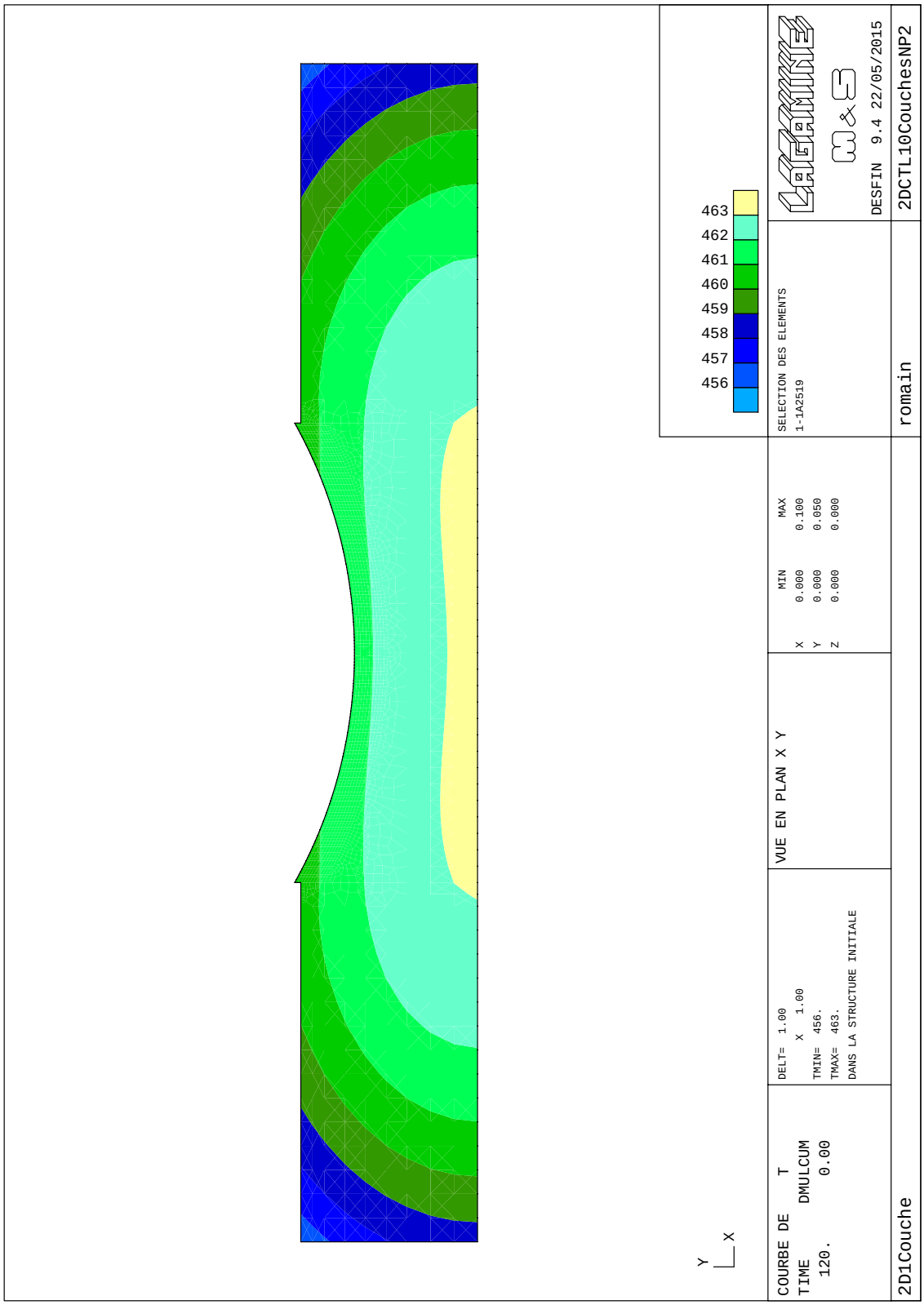

Figure A.35: Temperature profile in the piece after pre-heating at 200°C and cooling for 2 min.

A.6 Limitations potential solutions

A.6.1 Heat transfer through the metallic support

The conduction through the metallic support has not been modelled in our model. The heat flux going through this metallic piece is probably high given the good heat conduction properties of steel. An improved version of the model will need to simulate this energy dissipation.

Sirris has provided a picture of the experiment highlighting this metallic support. It is presented in Figure A.36.

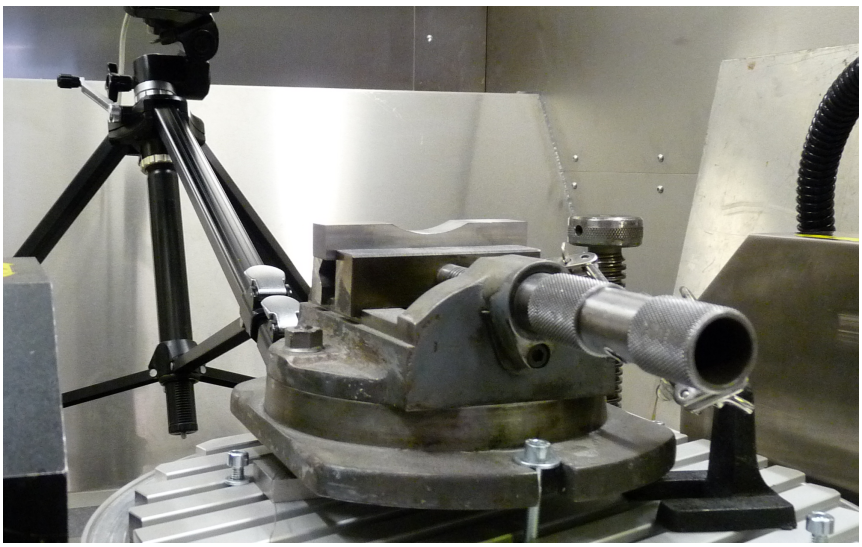

Figure A.36: Picture of the experiment configuration, Sirris

Figure A.36 shows the importance of the metallic support. In order to numerically model it, the best solution will be to design a new geometry modelling the supports and making the link between the work-piece and a large metallic piece used to represent the dissipation in the large metallic tools. The meshing of this geometry will have to be studied carefully in order to have a good coherence at the contact between the support and the work-piece. The meshing of the large metallic piece should be coarse enough to limit the increase in computation time.

The thermal law corresponding to the type of steel constituting the support should be implemented as they will influence the simulation.

Finally, at the contact surface between the support and the workpiece, the convection and radiation elements should be deactivated.

A.6.2 One pass per layer

Solutions exist to improve the 3-D to 2-D simulation to represent the different passes. Among them there is the possibility to simulate the cladding of the other layers using the data from the 3-D model. A second flux can be applied to simulate the printing of the second pass, a third flux to simulate the cladding of the third pass and so on. The more passes modelled, the closer to reality the model will be, but the higher the computation time. The secondary, tertiary, etc. fluxes applied must also determined. One way to do it would be to use the data from the 3-D model.

Figure A.38 is an illustration of that solution for the secondary flux. If in the 3-D model, we look at the temperature profile at three different points as described in Figure A.37and look at the results, we are able to estimate the influence of the printing of the second pass on the point of the first pass. By a rule of thumb we can therefore estimates the value of the secondary flux to simulate the printing of the flux.

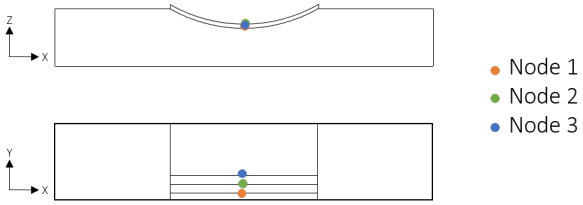

Figure A.37: Position of node 1,2 and 3.

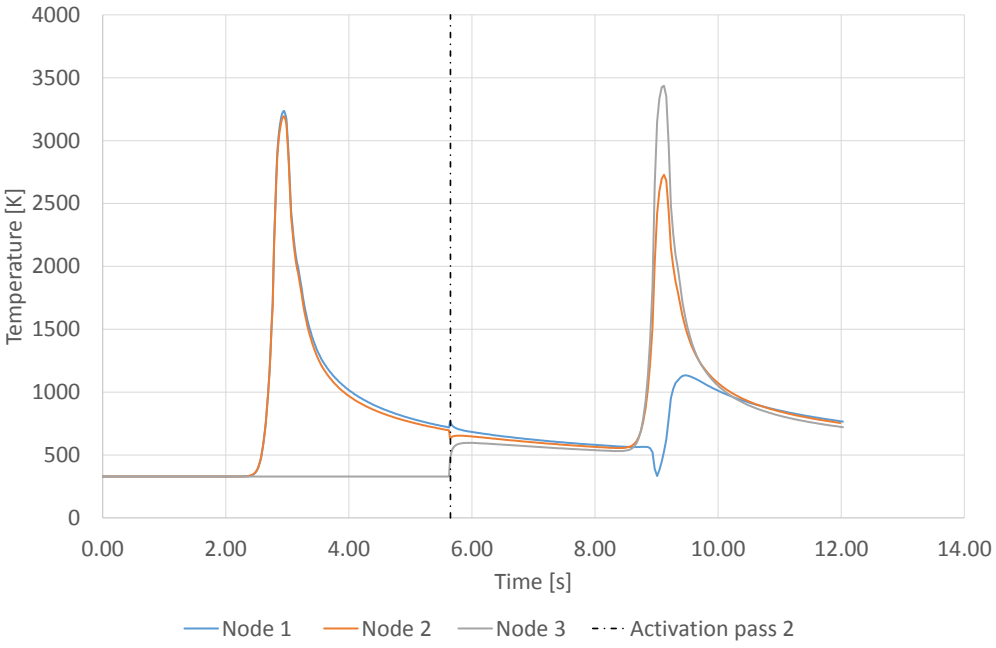

Figure A.38: Temperature profile at node 1,2 and 3 for the cladding of two passes - 3D model.

As we can see on Figure A.38, by studying the variation of temperature at Node 1 during the cladding of the second pass and comparing this with the change in temperature at Node 1 for the cladding of the first pass, we can find a ratio in the temperature peaks for the cladding of pass one and two. We have:

Table A.3: Comparison of the temperature peaks in Node 1 for the cladding of pass one and two.

Pass beeing cladded	Peak intensity [°K]
1	2907,43
2	800,53

Which gives a ratio of 0.28.

This value of temperature ratio can be used as a ratio to apply on the secondary flux. Even if the relation between the temperature at the top of the layer and the value of the flux applied is not perfectly linear (as presented in FigureA.10. A linear relation will be used in this case for the sake of simplicity.

Another solution to tackle this problem is to change the time between layers. The time between layer is the time difference between the printing of two separate layer. In the 2-D and 3-D model, it is currently determined by the laser operating history data. One solution would be to decrease this time in the case of the 2-D model. This strategy will allow the simulation of the energy influx (by decreasing the time during which convection and radiation occurs) due to the printing of the other passes. In an efficient 2-D model, a combination of both solutions, a secondary flux and a reduction of the time between layer should be used.

A.6.3 convection coefficient

Values of the convection coefficient were taken from the literature and are synthesised on Figure 5.32. The value used by Z.Fan and F.Liou[17] is used in the case of our model.

Given the results obtained and presented in chapter 6, and especially the shape of the melt pool, it is obvious than the cooling down of the surface by convection and radiation was underestimated. A new value should then be defined to better represent the reality. In order to change that value consistently, a sensitivity study should be performed for different values of the convection coefficient h and the numerical results should be compared with the experimental data. Relevant experimental data, such as more information on the melt-pool shape will therefore be needed.

On the other hand, an argon flux cool down the surface of the workpiece near the laser beam. This argon flux allow the cooling down of the piece while preventing oxidation. It also locally greatly increase the heat transfer by convection. One way to take that characteristic into account will be to define the convection coefficient as dependent of the temperature. This way, when the laser beam is nearby, the temperature at the surface is high and the convection coefficient will be higher as well. In LAGAMINE, such a time dependent convection and radiation condition can be implemented as such:

Table A.4: Temperature dependant convection coefficient h to take into account the argon flux.

Temperature [°K]	h $[W.m^{-2}.K^{-1}]$
293,15	$h_{Ti6Al4V-Air}$
1877	$h_{Ti6Al4V-Air}$
1923	$h_{Ti6Al4V-Argon}$
3533	$h_{Ti6Al4V-Argon}$

Where the value of $h_{Ti6Al4V-Air}$ and $h_{Ti6Al4V-Argon}$ in $[W.m^{-2}.K^{-1}]$ are still to be determined.

A.6.4 Complete boundary conditions

As shown on Figure A.36, boundary conditions should include convection and radiation under the piece.

Currently, the boundary conditions are presented in Figure 5.33. They should be modified to best represent the operating conditions. FigureA.39 represents this corrected boundary conditions as they should be applied on the 2-D model.

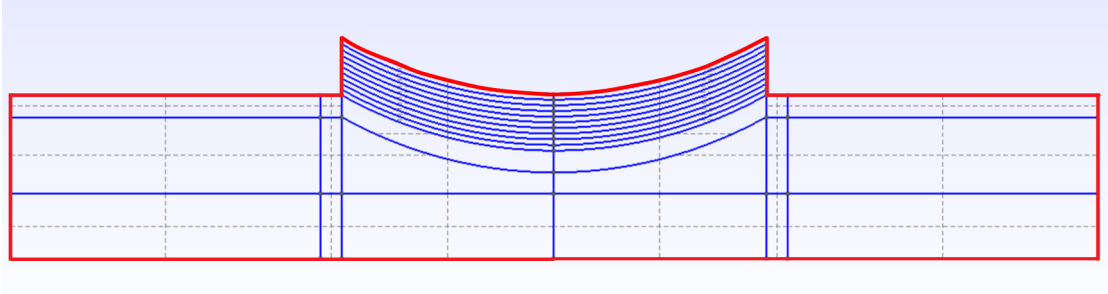

Figure A.39: Corrected boundaries subjected to convection and radiation.

For the 3-D model, the reasoning is similar, the line under the workpiece beeing replaced by a surface.

A.6.5 Calibrations alternatives

The calibration of the flux is performed for the printing of pass one only (3-D model). the criteria is the maximum temperature observed at the thermocouple as detailed in section 5.7.1. The resulting temperature profile at the the thermocouple is presented in Figure 5.41 for 1 pass and in Figure 5.42 for two passes. The error was then quantified.

As Figure 5.42 suggests, the calibrated flux already give inaccurate numerical results for the cladding of two passes. It is therefore not surprising that the difference of value in temperature at the thermocouple become so different after 10 layers of 8 passes each. The difference of temperature at the thermocouple between the numerical model and the experimental results is shown in Figure 5.46 and detailed in section 5.7.2.

The alternatives strategies for calibration proposed are the following:
1. Keep the maximal temperature observed at the thermocouple as a reference but do the simulation of the cladding of 10 passes rather than one. This strategy will imply the definition of a 3-D model able to simulate the cladding of ten passes. Such a simulation will most likely increase the computation time drastically. The computation time being proportional to the duration of the simulation, all other parameters unchanged.
2. A more accurate calibration can be obtained by minimizing the difference between the temperature profile obtained numerically and experimentally. That is computing the difference in all point and minimizing the sum of the square. Such a strategy will provide a much accurate calibration but will require the development of a new calibration tool based on those data. Finally, this second strategy will be more accurate if performed for an higher number of passes, like stated in the first proposed solution.

A.6.6 Activation of element at elevated temperature

One of the problem faced with the activation of element is caused by the temperature at which elements are currently activated. Indeed, with the current model, elements are activated at an initial temperature of $T = T_0 = 328,89$ °K. That is usually way below the minimal temperature in the layer under which these elements are activated, usually situated above 900 °K. This temperature gradient create an heat flux, going from the hot layer already clad and the newly

activated elements. An heat flux going of that amplitude in that directions not physical and it would therefore be useful to avoid it in the model. This heat flux leads to a rapid cooling down of the existing layer compensated by a rapid warming up of the newly activated elements. This phenomenon is particularly visible for the activation of entire layer of element as done for a layer-by-layer activation. It is illustrated in Figure A.38. Where the temperature in node 3, at the extremity of a newly activated element, sharply increase following the activation.

A solution to avoid this unwanted heat transfer would be to increase the temperature of the element activated. In a first approximation, we can consider that the new material arrives in the piece already melted, at a temperature of $T_0 = 1923$°K. This change in the model should allow us to avoid the apparition of an inverted heat flux. However, the use of a new activation temperature requires a new calibration of the flux applied by the heat source. Indeed, an important part of the heat energy is now brought to the piece within the element activated at such an high temperature.

We also note that such a modified activation temperature can only be applied to an element-by-element strategy.

A.7 Most up-to-date model and results

The most up-to-date model uses the design presented in chapter 5 with the application of some of the solutions presented in chapter 7. The corrections applied to the model are the following:

- As described in section A.6.3, the convection coefficient value is increased. It is taken at $h_{Ti6Al4V-Air} = 50\ [W.m^{-2}.K^{-1}]$ [66] and $h_{Ti6Al4V-Air} = 10.h_{Ti6Al4V-Air} = 500\ [W.m^{-2}.K^{-1}]$ to represent the argon flux.
- The boundary conditions are changed as shown in Figure A.39. The heat transfer through convection and radiation under the piece are thus considered.
- A complex pre-heating strategy, such as described in section 6.5 is used. The material is heated at 200°C and then left at an ambient temperature for 5 minutes. This also implies that the newly activated elements are activated at a temperature of 200°C, higher than for the previous model.
- The metallic support and the heat conduction through them is modelled by increasing the heat capacity of the elements at the bottom of the 2-D model. These elements are the one in contact with the metallic support as seen in Figure A.36. By increasing the heat capacity (multiplied by 5), we simulate the absorption of temperature by the support during cladding. The heat transfer via the support by convection and radiation is modelled by multiplying by 5 the convection and radiation in these elements. This simplification allows us to keep the same mesh and same simulation parameters

It is important to note that all the other solutions have not been applied due to time constraints. The calibration of the flux is also kept as performed with the previous model in section 5.7. For a rigorous approach of the corrected model, the calibration should be performed again to find a new value of applied heat flux.

The results presented hereafter contain: the temperature profile at the thermocouple with the corrected model, compared to the temperature profile experimentally obtained. The new melt-pool shape is also highlighted as well as the temperature distribution in the piece, before the cladding operation and at the end of it. Finally, a quick prediction of the micro-structure obtained is performed. The temperature profile at the thermocouple is given in Figure A.40.

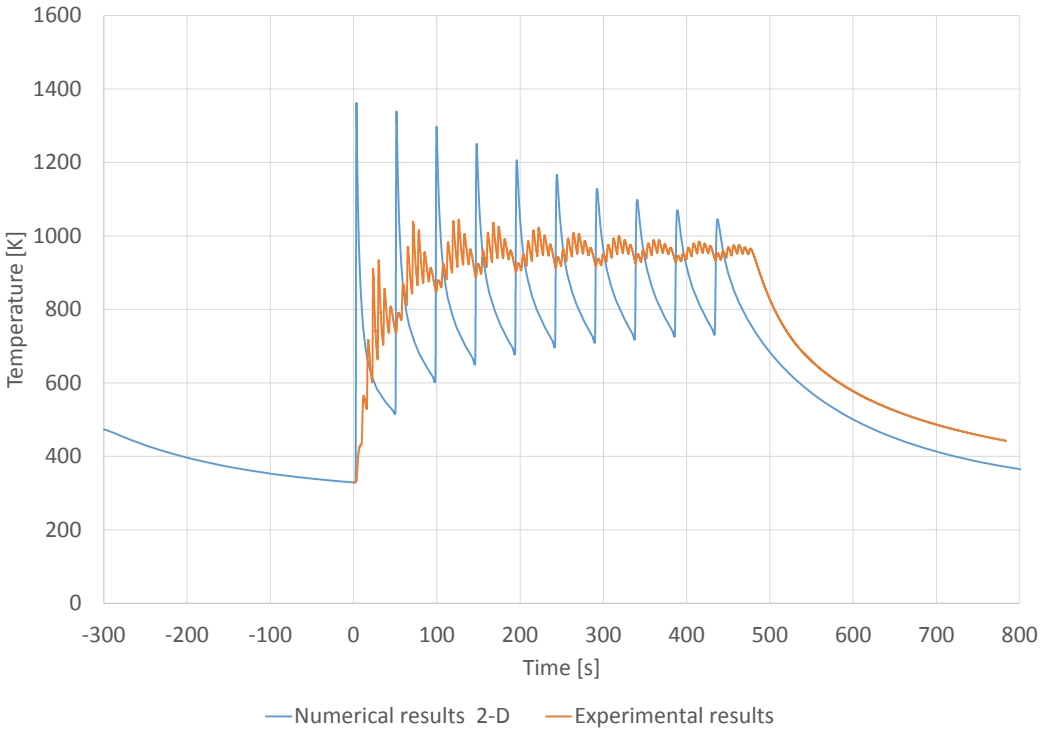

Figure A.40: Temperature profile at the thermocouple for the modified model.

As can be seen in in Figure A.40, the pre-heating model is quite efficient, leading to a temperature at the thermocouple at the start of the cladding of $T = 329,05$ °K where the experimental data gives a temperature at the start of the cladding of $T = 328,89$ °K. The difference in temperature at the thermocouple after the cooling phase is thus 0,05%. The temperature distribution at that point can be seen in Figure A.41. For the rest of the graph, we can see that the profiles obtained are consistent. The 2-D model still models 1 pass per layer, hence that is why each experimental group of peaks are represented by one larger peak in the numerical simulation, but the global temperature profile observed, especially during the cooling phase, is similar.

Temperature distributions at various points is given in the following Figures (A.41 to A.44), generated via DESFIN, LAGAMINE's viewer. As can be seen on these Figures, the shape of the temperature distributions is slightly different to the ones previously obtained. The convection elements at the bottom of the piece tend to dissipate flux that was previously absorbed by the work-piece, leading to overall lower temperatures, especially at the bottom of the substrate. The melt-pool obtained is similar in shape but smaller in size. The size of the melt-pool is still bigger than what is observed experimentally as described by the operator.

The micro-structure prediction, as developed in section 6.4, is applied to the new results. A cooling rate of 82,8°C/s was found at the top of the clad. Such a cooling rate could lead to the apparition of a mixed Widmanstätten and martensite micro-structure according to T.Ahmed [1]. Experimentally, only a Widmanstätten micro-structure was observed at that point. However, the presence of martensite in small quantities is still possible.

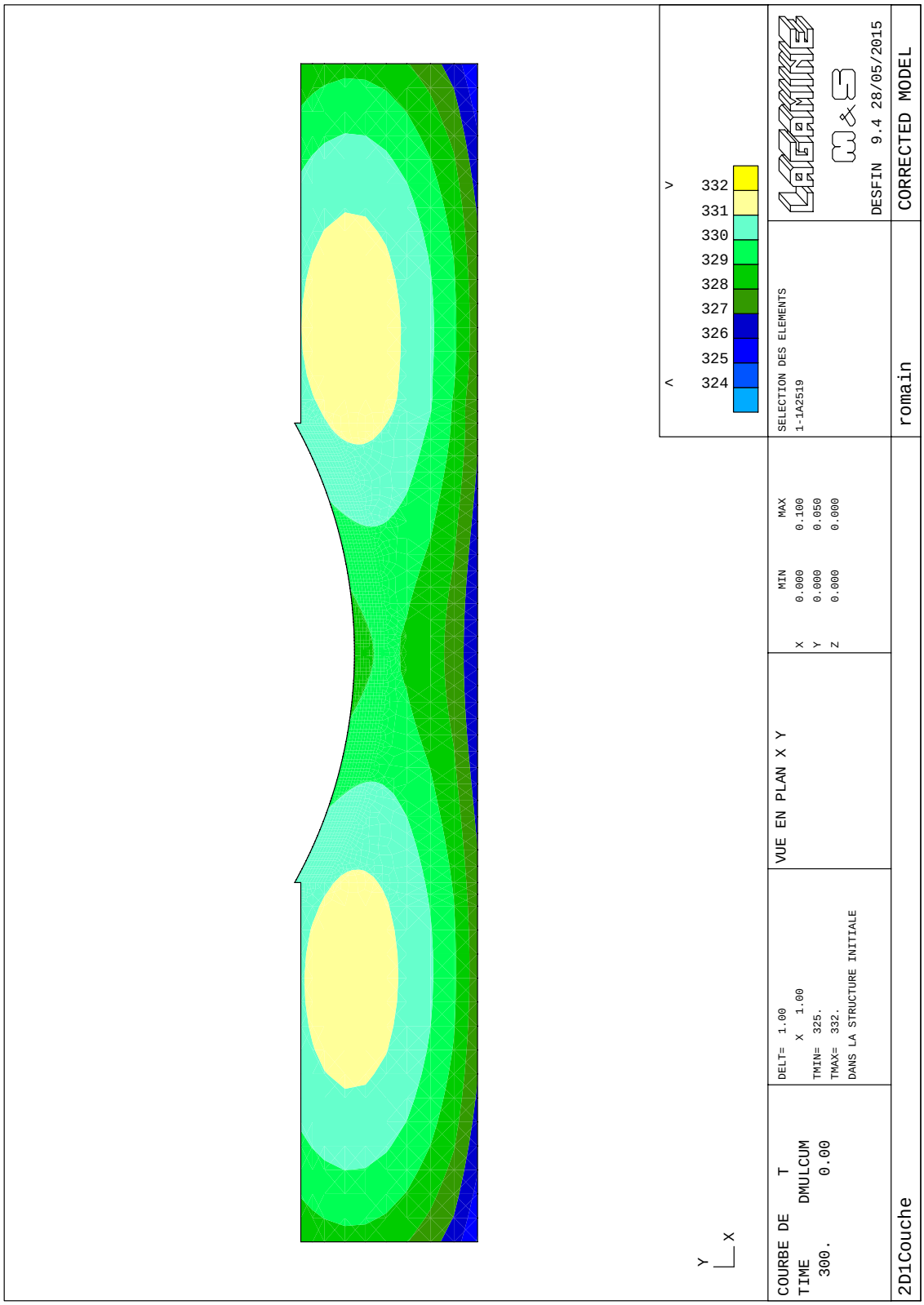

Figure A.41: Numerical temperature distribution just before cladding

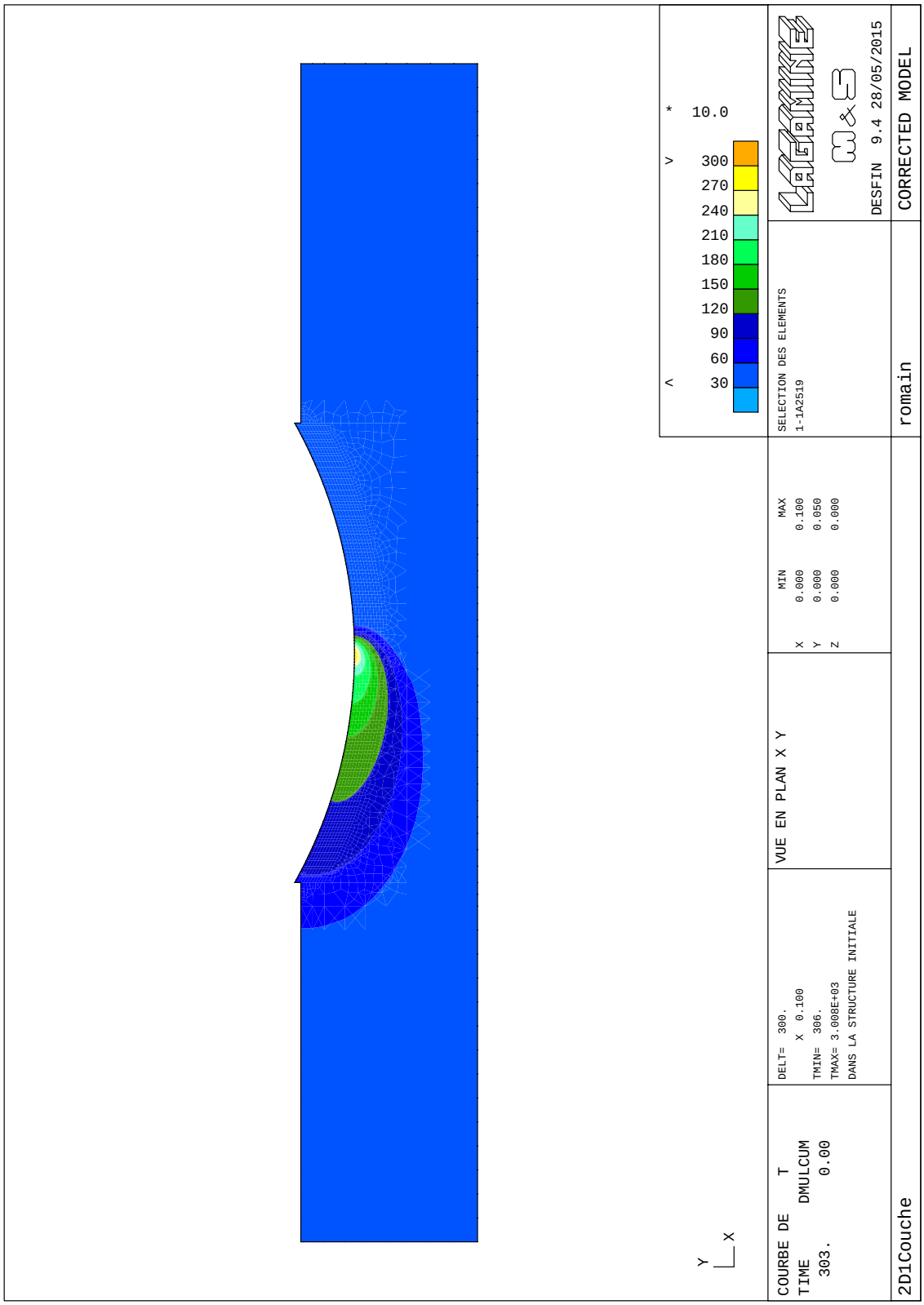

Figure A.42: Numerical temperature distribution at the middle of layer 1

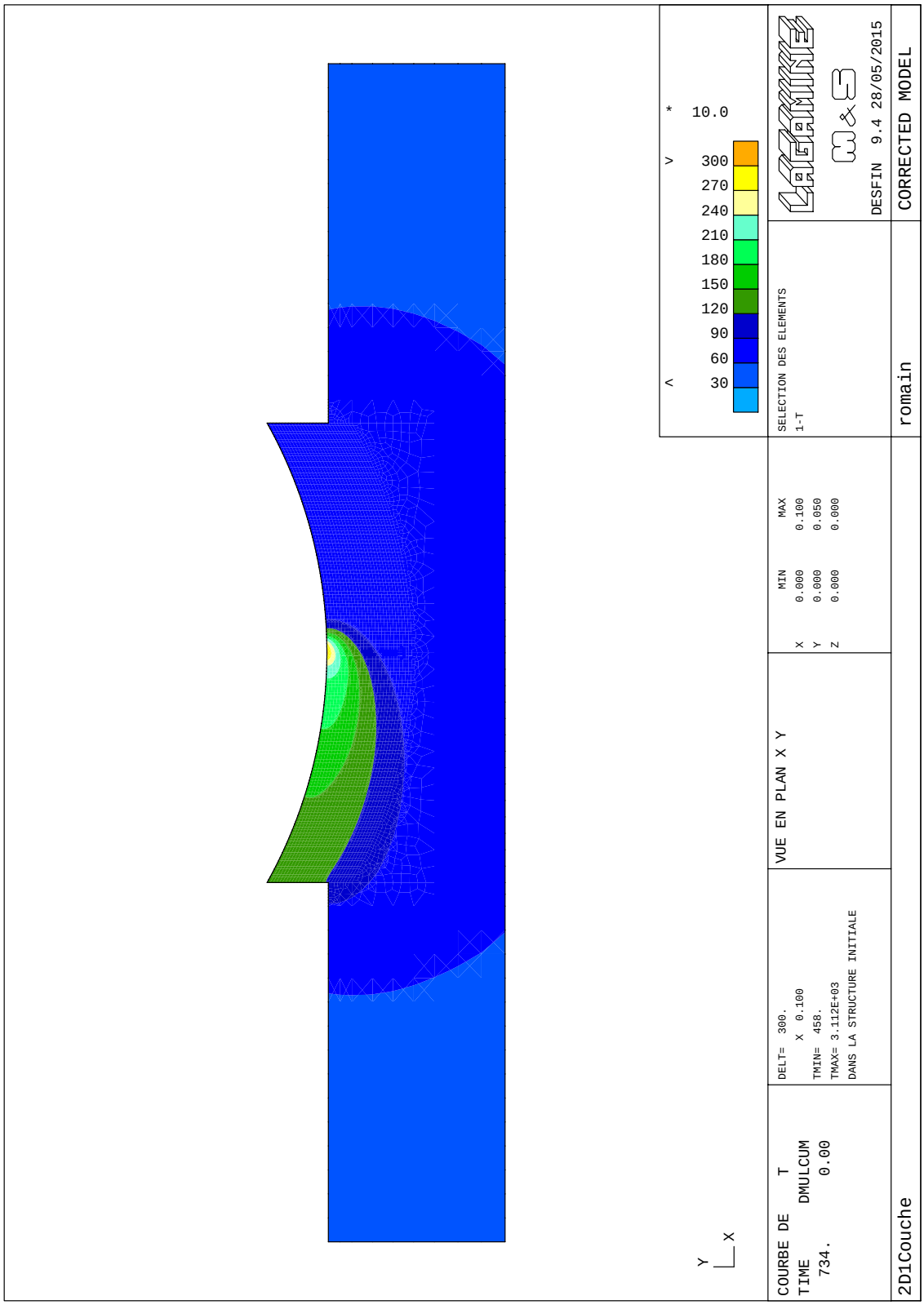

Figure A.43: Numerical temperature distribution at the middle of layer 10

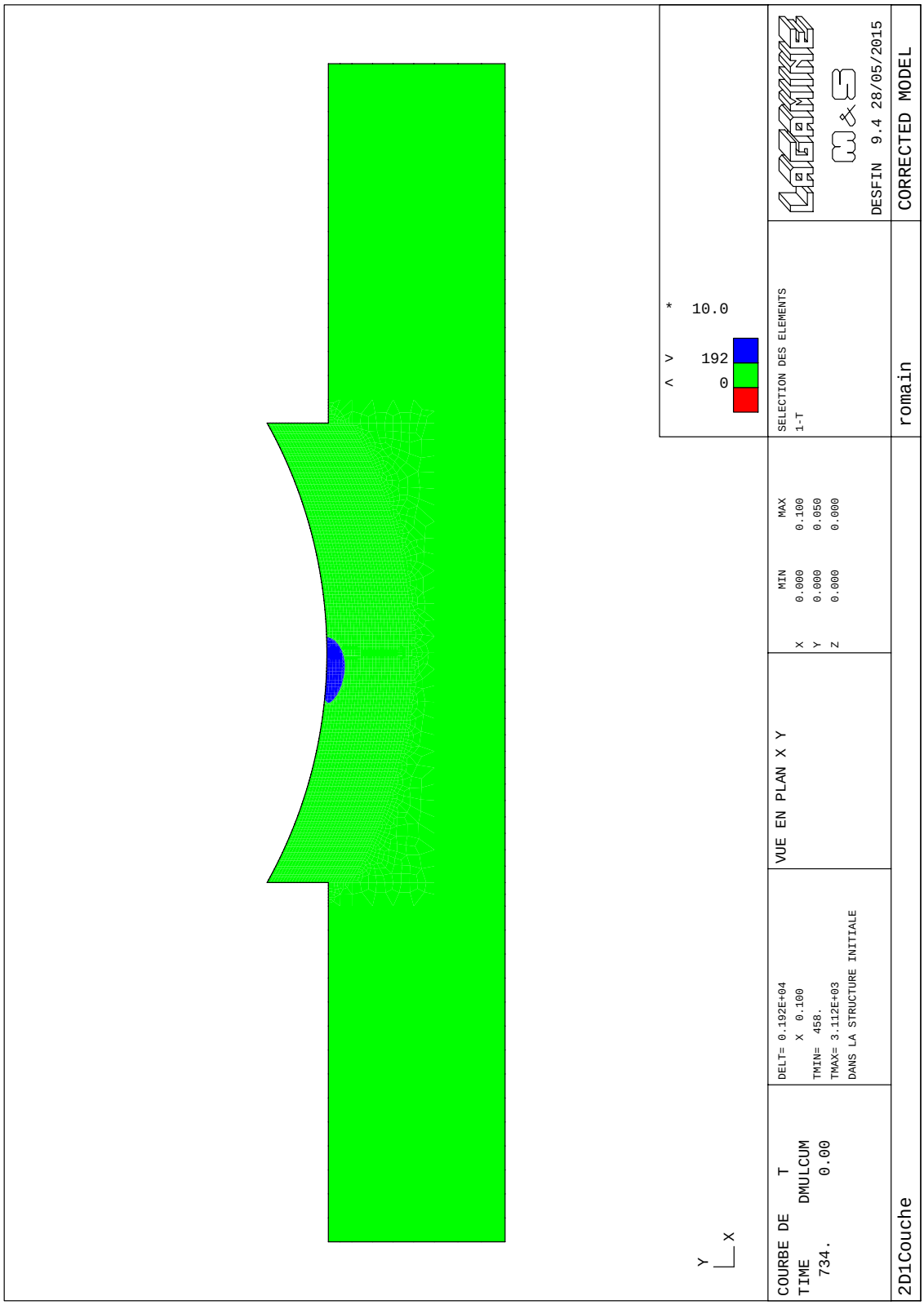

Figure A.44: Shape and size of the melt-pool with the modified model

A.8 Other

A.8.1 Comprehensive example of spatial oscillations

R. Charlier provides a comprehensive example to explain the phenomenon of spatial oscillations[9]. This example is an application of a non-linear finite element model in a porous materials where a pressure solicitation (pressure drop, going from p to p_0) is brutally applied to one of the boundary. Due to the strong curvature of the pressure profile, and by considering a linear approximation inside the element, we obtain the following numerical solution, oscillating around the exact solution of the problem.

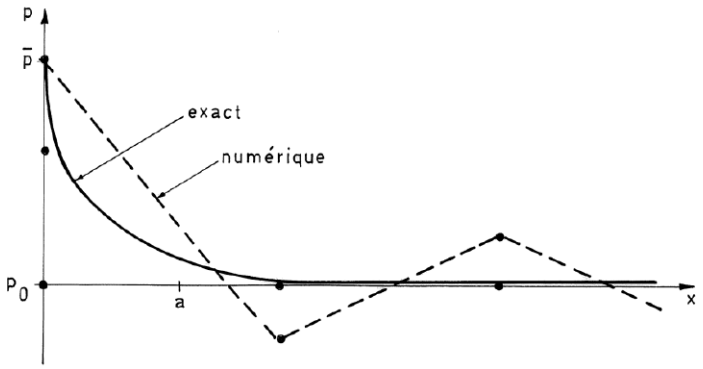

Figure A.45: Comprehensive example of spatial oscillations by R. Charlier [9]

A.8.2 Integration of the Latent heat into heat capacity

Because the model takes as a parameters the apparent heat capacity as a parameter, the Latent heat of fusion L_f $[J.Kg^{-1}]$ and vaporisation L_e $[J.Kg^{-1}]$ should be integrated to the value of the heat capacity c_p $[J.Kg^{-1}.K^{-1}]$.

The apparent heat capacity is thus the addition of the heat capacity $c_{p,0}$ and a value representing the Latent heat of fusion and vaporisation expressed as $c_{p,eq}$, both being expressed in $J.Kg^{-1}.K^{-1}$. The profile of $c_{p,0}$ was determined in the literature as seen in section 5.4 and the calculation of $c_{p,eq}$ is given here under:

$$c_{p,eq} = c_{p,eq,f} + c_{p,eq,e} \tag{A.6}$$

Where $c_{p,eq,f}$ and $c_{p,eq,e}$ are given by;

$$c_{p,eq,f} = \begin{cases} \frac{L_f}{T_l - T_s} = \frac{2{,}86.10^5}{1923-1877} = 6217 \quad J.Kg^{-1}.K^{-1} & \text{if } 1877 \leq T \leq 1923 \\ 0 \quad J.Kg^{-1}.K^{-1} & \text{else} \end{cases} \tag{A.7}$$

$$c_{p,eq,e} = \begin{cases} \frac{L_e}{T_e - T_c} = \frac{9{,}83.10^6}{3533-3483} = 196600 \quad J.Kg^{-1}.K^{-1} & \text{if } 1877 \leq T \leq 1923 \\ 0 \quad J.Kg^{-1}.K^{-1} & \text{else} \end{cases} \tag{A.8}$$

Where L_f $[J.Kg^{-1}]$ and L_e $[J.Kg^{-1}]$ are the Latent heat of fusion and vaporisation. T_l, T_s, T_e and T_c $[K]$ are respectively the liquidus, solidus, evaporation, and condensation temperature [41][7]. The resulting profile of the apparent heat capacity is presented in Figure 5.29.